

NORTHWESTERN UNIVERSITY

Development and Characterization of Pi-stacking Filamentous Polymeric Nanocarriers for
Applications in Nanomedicine

A DISSERTATION

SUBMITTED TO THE GRADUATE SCHOOL

IN PARTIAL FULFILLMENT OF THE REQUIREMENTS

for the degree

DOCTOR OF PHILOSOPHY

Field of Biomedical Engineering

By

Sophia Li

EVANSTON, ILLINOIS

December 2021

ABSTRACT

Development and Characterization of Pi-stacking Filamentous Polymeric Nanocarriers for Applications in Nanomedicine

Sophia Li

Nanocarriers, structures with at least one dimension on the nanoscale (1-1000 nm), have been engineered for delivery of various cargoes. The shape and flexibility of nanocarriers are important parameters that influence their biological performance. Self-assembling polymeric filamentous nanocarriers, known as filomicelles (FM), are of great interest to nanomedicine due to their structural flexibility, extensive systemic circulation time, and amenability to unique “cylinder-to-sphere” morphological transitions for sustained drug delivery. FM self-assembled from the block copolymer poly(ethylene glycol)-*block*-poly(propylene sulfide) (PEG-*b*-PPS) have great potential for drug delivery applications, particularly in immunomodulation. However, current fabrication techniques for FM self-assembly are highly variable and difficult to scale, and the impact of FM flexibility on nanocarrier uptake is not well-understood. In this work, I describe the development and characterization of a pi-stacking filamentous nanocarrier platform with controlled flexibility, enhanced stability, and scalable formation for drug delivery. First, I demonstrate that co-assembly of PEG-*b*-PPS diblocks with tetrablock copolymers composed of PEG-*b*-PPS linked by a pi-stacking perylene bisimide (PBI) moiety permits rapid, scalable, and facile assembly of FM with control over length and flexibility. Secondly, I found that the flexibility of filamentous nanocarriers can be optimized to decrease their internalization by macrophages in vitro, modulate their biodistribution on the cellular and organ level, and increase their systemic circulation times

in vivo compared to (-)PBI-FM without PBI tetrablocks. Lastly, I investigated the potential utility of this FM nanocarrier platform in various biomedical applications, including passive targeting in a melanoma cancer model and as drug delivery vehicles for an anti-parasitic drug. Thus, my work shows that incorporation of pi-stacking moieties allows for rapid, scalable assembly of FM with tunable flexibility and stability for applications in nanomedicine.

ACKNOWLEDGEMENTS

I would like to thank my family near and far for all their love and support. A special thank you goes to my mother, my father, my sister Lauren, and new addition to our family Jake. During all the moments when I doubted myself, you all never stopped believing in me. Thank you for always cheering for me and for brightening my day, whether it was through a phone call, a funny text, or a thoughtful gift.

Thank you to all my friends who would check in on me through thick and thin. To Mallika: I am so glad that you joined the lab the same time I did and became my lab buddy. I am thankful for all the great memories: all those evenings staring at MATLAB code, running to give our final presentation in Stat Mech, making the best cake pops ever, our croissant and coffee breaks, going on bike rides by the lake, etc. I'm not sure how I would have gotten through graduate school without your friendship and support and I'm excited to return to medical school with you. Angela and Julie: you two always lift me up, no matter how far you are. Thank you for all the Facetimes, pig-out sessions, all-you-can-eat hot pot, and fun adventures in Boston, New Haven, and Chicago. I would also like to thank my friends Yufan, Quanquan, Maria, and Shannon for being the best friends one can ask for throughout the years.

I am so grateful for all my wonderful labmates who helped me throughout this journey: Molly, Jacqueline, Chamille, Trevor, Mike, Clayton, and Jen. I want to say a special thank you to the senior lab members and Scott Lab alumni who continue to provide guidance to this day: Sean, Nick, Sijia, Fanfan, Sharan, and Debora. Thank you so much for your patience, sharing your

expertise and wisdom, and answering all my questions. I welcome all the new lab members to the Scott Lab and wish you all the best: Stephanie, Austeja, Sultan, Andrew, and Boaz.

I would like to thank my committee for their advice, guidance, and support: Professor Thomas Hope, Professor Jaehyuk Choi, and Professor Jonathan Rivnay. Thank you for all the thoughtful questions and feedback. I would like to thank Professor Patrick Kiser for his time serving on my committee, and for all his help since I was a rotation student.

Last but not least, I would like to thank my PI, Professor Evan Scott for his mentorship. I am always inspired by your optimism, persistence, creativity, and relentless passion for science. Thank you for always believing in me, reminding me what I am capable of, and showing me the windows of opportunity in science whenever it seemed like I reached a dead-end. Thank you so much for teaching me and helping me grow as a scientist, and for all your support and encouragement over the years.

LIST OF ABBREVIATIONS

ALT	Alanine aminotransferase
AP-1	Activator protein 1
APCs	Antigen-presenting cells
Apt-PAN	Aptamer-PA-nanofibers
BCG	Bacillus Calmette–Guérin vaccine
BCN	Bicontinuous nanospheres
BCP	Block copolymer
BMP-2	Bone morphogenic protein-2
BNZ	Benznidazole
BSA	Bovine serum albumin
CDSA	Crystallization-driven self-assembly
CIJ	Confined impingement jets
CPMV	Cowpea mosaic virus
CPTKMA	Camptothecin methacrylate
Cr	Creatinine
CryoTEM	Cryogenic Transmission Electron Microscopy
DLS	Dynamic Light Scattering
DOX	Doxorubicin
dpi	Days post infection
EPR effect	Enhanced Permeation and Retention effect
f	Hydrophilic weight fraction
FM	Filomicelles
FNP	Flash nanoprecipitation
f _{PEG}	Hydrophilic weight fraction of PEG
Gd	Gadolinium

GMP	Good Manufacturing Practice
GPC	Gel Permeation Chromatography
HER2	Human epidermal growth factor receptor 2
IC50	Half-maximal inhibitory concentration
IO	Iron oxide
IV	Intravenous
L	Length
L _c	Contour length
L _p	Persistence length
LPS	Lipopolysaccharide
MC	Micelles
mPBI-FM	Mixed perylene bisimide-containing filomicelles
mPBI-PS	Mixed perylene bisimide-containing polymersomes
mPEG- <i>b</i> -PAGE	Methoxypoly(ethylene glycol)- <i>b</i> -poly(allyl glycidyl ether)
MPS	Mononuclear phagocyte system
MRI	Magnetic resonance imaging
Mtb	<i>Mycobacterium tuberculosis</i>
NMR	Nuclear Magnetic Resonance
OFETs	Organic field effect transistors
PA	Peptide amphiphiles
PBI	Perylene bisimide
PBS	Phosphate-buffered saline
PDGF-BB	B chain of the platelet-derived growth factor
PDI	Polydispersity index
PDMAEMA- <i>b</i> -PMAEBA	poly((N,N'-dimethylamino)ethyl methacrylate)- <i>block</i> -poly(methacryloxyethoxy)benzaldehyde)

PEG- <i>b</i> -P(CL- <i>r</i> -LA)	poly(ethylene glycol)- <i>block</i> -poly(ϵ -caprolactone- <i>r</i> -lactic acid)
PEG- <i>b</i> -P(CPTKMA-co-PEMA)	poly(ethylene glycol)- <i>block</i> -(poly camptothecin methacrylate-2-(pentamethyleneimino)ethyl methacrylate)
PEG- <i>b</i> -PBCL	poly(ethylene glycol)- <i>block</i> -poly(alpha-benzyl carboxylate epsilon-caprolactone)
PEG- <i>b</i> -PLA	poly(ethylene glycol)- <i>block</i> -poly(lactic acid)
PEG- <i>b</i> -PPS	poly(ethylene glycol)- <i>block</i> -poly(propylene sulfide)
PEG-TAA	Poly(ethylene glycol)-thioacetate
PEMA	2-(pentamethyleneimino) ethyl methacrylate
PEO- <i>b</i> -PB	poly(ethyleneoxide)- <i>block</i> -poly(butadiene)
PEO- <i>b</i> -PBD	poly (ethylene oxide)- <i>block</i> -poly(butadiene)
PEO- <i>b</i> -PCL	poly (ethylene oxide)- <i>block</i> -poly(ϵ -caprolactone)
PEO- <i>b</i> -PEE	poly(ethyleneoxide)- <i>block</i> -poly(ethylethylene)
PISA	Polymerization-induced self-assembly
PRRs	Pattern Recognition Receptors
PS	Polymersomes
PTCDA	Perylene-3,4,9,10-tetracarboxylic dianhydride
PVX	Potato virus X
RAFT	Reversible addition-fragmentation chain-transfer
SAXS	Small angle X-ray scattering
SC	Subcutaneous
SD	Standard deviation
sDCs	Synthetic dendritic cells
SEAP	Secreted embryonic alkaline phosphatase
SEM	Standard error of the mean

SIM	Structured illumination microscopy
SLPhages	Sialyllactose-conjugated filamentous bacteriophages
SRM	Super-resolution microscopy
STEM	Scanning Transmission Electron Microscopy
TEM	Transmission Electron Microscopy
TEMED	Tetramethylethylenediamine
TFH	Thin film hydration
THF	Tetrahydrofuran
TIMT	Temperature-induced morphological transitions
TLR	Toll-like receptor

DEDICATION

I would like to dedicate my thesis to my family, especially my grandfathers, who constantly inspired me to pursue an education, and to be “good, better, then the best.” I would not have gotten this far without all your love and support.

TABLE OF CONTENTS

ABSTRACT	2
ACKNOWLEDGEMENTS	4
LIST OF ABBREVIATIONS	6
DEDICATION	10
TABLE OF CONTENTS	11
LIST OF FIGURES.....	20
LIST OF TABLES	25
CHAPTER 1.....	27
1. Introduction: Dissertation Overview and Review of Literature	27
1.1 Dissertation Overview.....	27
1.1.1. Motivations and Objectives	27
1.1.2. Dissertation Outline	27
1.2 Review of the Literature.....	28
1.2.1 Self-assembled Filamentous Structures.....	28
1.2.2. Synthesis, Self-assembly, and Stability of Polymeric Filaments	32
1.2.2.1 Synthesis of FM-forming BCP.	33
1.2.2.2 Self-assembly Methods for FM.	37

	12
1.2.2.3 “Cylinder-to-sphere” Morphological Transitions of FM.....	38
1.2.3 Characterization of Self-assembled Filaments	41
1.2.4 Techniques to Modulate Filament Length and Flexibility.	41
1.2.5. Advantages of Filaments for Biomedical Applications.....	44
1.2.5.1 High Drug Loading Capacities.	44
1.2.5.2 Morphology-dependent Differences in Circulation Time and Biodistribution.....	45
1.2.5.3 Enhanced Avidity for Active Targeting.....	47
1.2.6 Promising Biomedical Applications of Self-assembled Filaments	50
1.2.6.1 Cancer Nanomedicine.....	50
1.2.6.2 Aerosolized Delivery Systems.....	51
1.2.6.3 Contrast Agent Delivery for Imaging.	52
1.2.6.4 Vaccines.....	53
1.2.6.5 Hydrogels.....	54
Hydrogels for drug delivery.....	54
Hydrogels for tissue engineering.....	55
1.3 Scope of This Work.....	58
CHAPTER 2.....	59
2. Development and Characterization of Scalable Pi-stacking Filamentous Nanocarriers ..	59
2.1 Abstract.....	59

	13
2.2. Introduction	59
2.2.1. Challenges in Self-Assembly of FM	59
2.2.2. Modulation of FM Flexibility	61
2.2.3. Super-resolution Imaging of Filaments	62
2.2.4. Pi-stacking Perylene Bisimide in Self-assembled Nanocarriers.....	63
2.3. Materials and Methods.....	66
2.3.1. Materials	66
2.3.2. Synthesis of Block Copolymers	67
2.3.3. Characterization of Block Copolymers	68
2.3.4. Nanocarrier Fabrication via Thin Film Hydration.....	70
2.3.5. Nanocarrier Fabrication via Flash Nanoprecipitation	70
2.3.6. Small Angle X-ray Scattering.....	71
2.3.7. Transmission Electron Microscopy	71
2.3.8. Cryogenic Transmission Electron Microscopy	72
2.3.9. Scanning Transmission Electron Microscopy (STEM).....	72
2.3.10. Structured Illumination Microscopy (SIM).....	73
2.3.11. Dynamic Light Scattering (DLS)	73
2.3.12. Zeta-potential Measurement	73
2.3.13. Kaiser Test.....	74

	14
2.3.14. UV-Vis Spectroscopy	74
2.4. Results and Discussion.....	74
2.4.1. Synthesis and Formation of PEG- <i>b</i> -PPS FM	74
2.4.2. Synthesis and Characterization of Diblock and Tetrablock Copolymers.....	76
2.4.3 Characterization of Mixed PBI Polymersomes	80
2.4.4 PBI Enhances FM Formation via Thin Film Hydration.....	84
2.4.5 PBI Enhances FM formation via Flash Nanoprecipitation.....	87
2.4.6 PBI Enhances Control over FM Flexibility	93
2.4.7. Zeta-potentials of mPBI-FM	95
2.4.8 Verification of Removal of Amine-functionalized Diblock Copolymer.....	96
2.4.9. Super-resolution Imaging of FM	98
2.4.10. mPBI-FM Undergo “Cylinder-to-Sphere” Transitions upon Oxidation	101
2.4.11. mPBI-FM Fluorescence Intact after Triton-X Incubation.....	105
2.5. Conclusions	106
2.6. Acknowledgments	107
2.7. Publication Information.....	109
CHAPTER 3.....	110
3. Investigation of the Effect of Filament Flexibility on Immune Cell Internalization and Activation	110

3.1. Abstract	110
3.2. Introduction	110
3.2.1. Interaction of PBI Derivatives with Cells.....	111
3.2.2 Effect of Filament Length and Flexibility on Cellular Internalization and Circulation Times	112
3.2.3. Murine Macrophage Activation and Polarization	113
3.2.4 Effect of Nanocarrier Morphology and Flexibility on Immune Cell Activation.....	114
3.3. Materials and Methods.....	115
3.3.1. DNA Intercalation Assay.....	115
3.3.2. Fabrication of DiR-loaded Nanocarriers	115
3.3.3. Cell Culture.....	115
3.3.4. MTT Assay	116
3.3.5. In vitro Uptake Studies	116
3.3.6. Confocal Microscopy	117
3.3.7. Quanti-blue Assay on RAW-blue Cells.....	118
3.3.8. ELISAs	118
3.3.9. Macrophage Surface Receptor Expression.....	118
3.3.10. In vivo Organ-level Biodistribution Study	119
3.3.11. In vivo Cellular-level Biodistribution Study	121

3.3.12. Serum Biomarker Analysis.....	122
3.3.13. Statistical Analysis	122
3.4. Results and Discussion.....	124
3.4.1. Assessment of DNA Intercalation Ability of PBI Tetrablock Copolymers	124
3.4.2. mPBI-FM Shift in Fluorescence after Intracellular Oxidation.....	125
3.4.3. mPBI-FM Flexibility Affects Cell Uptake in Murine Macrophages in vitro	128
3.4.4. PBI Incorporation Modulates FM Biodistribution in vivo	133
3.4.5. Effect of filament flexibility on murine macrophage activation in vitro.....	138
3.4.6. Effect of filament flexibility on serum cytokine levels and biomarkers in vivo	141
3.5. Conclusions	144
3.6. Acknowledgments	145
3.7. Publication Information.....	146
CHAPTER 4.....	147
4. Exploration of Potential Applications of Polymeric Filamentous Nanocarriers	147
4.1. Abstract	147
4.2. Introduction	147
4.2.1. Chagas Disease	148
4.2.2. Nanocarrier Approaches for Chagas Disease Prevention and Treatment.....	150
4.2.3. Nanocarrier Approaches to Improve Cancer Nanomedicine.....	152

4.2.4. Advantages of FM for Advancing Cancer Nanomedicine	154
4.2.5. Nanocarrier Targeting of Tumor-draining Lymph Nodes for Immunomodulation ..	154
4.3. Materials and Methods	156
4.3.1. Fabrication of BNZ-loaded and Vitamin D-loaded Nanocarriers	156
4.3.2. Transmission Electron Microscopy	156
4.3.3. DLS and Zeta-potential Measurement.....	156
4.3.4. Quantification of BNZ Encapsulation Efficiency	157
4.3.5 Cell Culture and Parasite Purification	157
4.3.6. MTT Assay	158
4.3.7. Determination of IC50 for Intracellular Amastigotes.....	159
4.3.8. Chagas Disease in vivo Study	160
4.3.9. BNZ-loaded FM Hydrogel Formation.....	160
4.3.10. Rheology Measurements on FM Hydrogels.....	161
4.3.11. Fabrication of DiR-loaded Nanocarriers	161
4.3.12. Measurement of DiR Encapsulation Efficiency	161
4.3.13. Cancer Biodistribution in vivo Study	161
4.3.14. Statistical Analysis	162
4.4. Results and Discussion.....	163
4.4.1 Characterization of BNZ-loaded and Vitamin D-loaded Nanocarriers	163

4.4.2 Cytotoxicity of BNZ-loaded Nanocarriers	165
4.4.3. Trypanocidal Activity of BNZ-loaded Nanocarriers in vitro	167
4.4.4. Effect of BNZ-loaded MC on Parasitemia and Parasite Load in vivo	169
4.4.5. Characterization of Novel BNZ-loaded PEG- <i>b</i> -PPS FM Hydrogel Platform.....	178
4.4.6. Characterization of DiR-loaded Nanocarriers for Cancer Biodistribution Study.....	184
4.4.7. Nanocarrier Biodistribution after Intratumoral Injection	185
4.5. Conclusions	189
4.6. Acknowledgements	190
CHAPTER 5.....	191
5. Conclusions and Future Directions	191
5.1. Conclusions	191
5.1.1 Rapid, Scalable FM Formation with Tunable Flexibility.....	191
5.1.2. Fluorescence Tracking of “Cylinder-to-sphere” Morphological Transition	192
5.1.3. Investigation of the Effect of FM flexibility on Immune Cell Interactions.....	193
5.1.4 Potential Utility of PEG- <i>b</i> -PPS FM for Drug Delivery.....	193
5.2. Future Directions.....	194
5.2.1. Effect of mPBI-FM Flexibility on Immune Activation.....	194
5.2.2. mPBI-FM Hydrogels for Sustained Delivery of Micelles.....	195
5.2.3. Active Targeting of Immune cells	197

5.2.4. Applications of PEG- <i>b</i> -PPS FM in Cancer Nanomedicine	198
5.2.5. Evaluating Electrical Conductivity of mPBI-FM for Optoelectronics or Regenerative Engineering Applications	199
5.2.6. Characterization of FM in Large Animal Models	199
REFERENCES	201
CURRICULUM VITAE	237

LIST OF FIGURES

Figure 1-1. Filaments of different lengths and flexibilities can be self-assembled from diverse building blocks including block copolymers, peptide amphiphiles, and proteins.

Figure 1-2. Chemical structures of select hydrophilic and hydrophobic polymers that have been used to form amphiphilic block copolymers that self-assemble into FM.

Figure 1-3. Advantages of self-assembled filaments for biomedical applications.

Figure 1-4. Emerging biomedical applications of self-assembled filaments.

Figure 2-1. Scalable self-assembly of mixed perylene bisimide filomicelles (mPBI-FM) using flash nanoprecipitation (FNP).

Figure 2-2. NMR of PEG₁₇PPS₁₉PBIPPS₁₉PEG₁₇ tetrablock copolymer.

Figure 2-3. NMR of PEG₁₇PPS₃₃PBIPPS₃₃PEG₁₇ tetrablock copolymer.

Figure 2-4. Gel permeation chromatography molecular weight distributions of PBI tetrablock copolymer.

Figure 2-5. Morphological transition of PEG₄₅-*b*-PPS₄₄ (-)PBI-FM to micelles during storage at 4°C.

Figure 2-6. mPBI-FM maintain filamentous morphology after storage at 4°C for 1 month.

Figure 2-7. Representative image of mixed PBI formulations formed with FNP.

Figure 2-8. PBI tetrablock copolymer promotes formation of mPBI-FM via FNP.

Figure 2-9. Scanning transmission electron microscopy image of mPBI-FM-A formed via FNP in water.

Figure 2-10. Characterization of the filamentous morphology of mPBI-FM as compared to PEG-*b*-PPS (-)PBI-FM.

Figure 2-11. Image of mPBI-FM and mPBI-PS after Kaiser test.

Figure 2-12. Absorbance spectra of mPBI-FM and mPBI-PS after Kaiser test.

Figure 2-13. Images of DiI-loaded FM formulations entrapped in a polyacrylamide gel and imaged by SIM.

Figure 2-14. mPBI-FM exhibit shifts in fluorescence and “cylinder-to-sphere” morphological transition to micelles after oxidation.

Figure 2-15. Fluorescence emission spectra of mPBI-FM formulations.

Figure 2-16. Emission spectra of mPBI-FM-E before and after incubation with the detergent 0.1% Triton X-100 for 30 min.

Figure 3-1. Fluorescence spectra of PBI tetrablock copolymers after incubation with different base-pair concentrations of double-stranded DNA.

Figure 3-2. mPBI-FM undergo a red to green fluorescence shift in vitro in RAW 264.7 mouse macrophages.

Figure 3-3. Differential cytotoxicity and uptake profiles of mPBI-FM having distinct Lc/Lp in RAW 264.7 murine macrophages.

Figure 3-4. Viability of RAW 264.7 cells after incubation with increased concentrations of mPBI-FM-C and mPBI-FM-D, as measured by the MTT assay (n=4).

Figure 3-5. mPBI-FM loaded with DiR, a near infrared (NIR) dye, are internalized by RAW 264.7 macrophages.

Figure 3-6. PBI incorporation into FM alters nanocarrier biodistribution in vivo.

Figure 3-7. mPBI-FM maintained a filamentous morphology after loading DiR in the FM core. TEM micrographs of negatively stained specimens are displayed.

Figure 3-8. Characterization of whole blood fluorescence using IVIS.

Figure 3-9. Effect on filament flexibility on NF- κ B activation and IL-10 cytokine production in murine macrophages in vitro.

Figure 3-10. Surface marker expression of CD80, CD86, and MHC II on RAW 264.7 macrophages after 24 h incubation with mPBI-FM and mPBI-PS (n=3).

Figure 3-11. Cytokine concentrations in mouse serum collected 24 h after IV injection of DiR-loaded FM nanocarriers in vivo in C57Bl/6 mice (n=3).

Figure 3-12. Biomarker levels in serum collected 24 h after IV injection of DiR-loaded FM nanocarriers in vivo in C57Bl/6 mice.

Figure 4-1. Encapsulation efficiency of BNZ-loaded nanocarriers.

Figure 4-2. TEM images of BNZ-loaded FM formulations.

Figure 4-3. Cytotoxicity profiles of BNZ-loaded and Vitamin D-loaded nanocarriers.

Figure 4-4. IC₅₀ of BNZ-loaded nanocarriers on intracellular amastigotes after 48 h of incubation with infected RAW 264.7 macrophages, H9c2 cardiomyoblasts, and 3T3-L1 adipocytes.

Figure 4-5. Schematic of experimental design of in vivo study to assess effect of BNZ-MC on preventing or treating Chagas disease.

Figure 4-6. Weekly weights of the mice during the study.

Figure 4-7. Blood parasitemia for different BNZ-MC regimens.

Figure 4-8. *T. cruzi* luminescence in the organs of BALB/C mice 25 days post infection for different BNZ-MC regimens.

Figure 4-9. *T. cruzi* luminescence in BALB/c mice as measured on IVIS over 25 days for different BNZ-MC regimens.

Figure 4-10. *T. cruzi* luminescence in BALB/C mice treated with different BNZ regimens over 25 days in relation to baseline parasite load on day 0.

Figure 4-11. Schematic comparing the formation of distinct PEG-*b*-PPS FM hydrogel platforms.

Figure 4-12. Image of hydrogels formed by encapsulating BNZ-loaded FM in crosslinked PEG.

Figure 4-13. Encapsulation efficiency of BNZ for the FM formulations in Table 4-4.

Figure 4-14. Rheology measurements of BNZ-loaded FM hydrogels.

Figure 4-15. Representative fluorescence images of the tumor, tumor-draining inguinal lymph node, lung, spleen, kidney, and liver obtained via IVIS 1 day, 3 days, and 7 days after intratumoral injection in a B16F10 melanoma mouse model in C57BL/6J mice.

Figure 4-16. Organ-level biodistribution of DiR-loaded nanocarriers of various morphologies after intratumoral injection in a B16F10 melanoma mouse model in C57BL/6J mice.

LIST OF TABLES

Table 1-1. Morphological parameters of examples of filamentous nanostructures found in nature.

Table 2-1. Morphology of PEG-*b*-PPS formulations self-assembled via TFH in PBS spanning a range of hydrophilic weight fractions (f_{PEG}).

Table 2-2. Morphology of PEG-*b*-PPS formulations self-assembled via FNP spanning a range of hydrophilic weight fractions (f_{PEG}).

Table 2-3. Morphology of formulations self-assembled via thin film hydration (TFH) with different combinations of PBI tetrablock copolymer and PEG-*b*-PPS diblock copolymer spanning a range of hydrophilic weight fractions (f_{PEG}).

Table 2-4. Morphology of formulations self-assembled via flash nanoprecipitation (FNP) with different combinations of PBI tetrablock copolymer and PEG-*b*-PPS diblock copolymer spanning a range of hydrophilic weight fractions (f_{PEG}).

Table 2-5. Characterization of select mPBI-PS formulations by SAXS.

Table 2-6. Characterization of select mPBI-PS formulations by DLS.

Table 2-7. Composition, formation method, and morphological parameters of key FM formulations in this study.

Table 2-8. mPBI-FM and (-)PBI-FM parameters with parameter uncertainties estimated from flexible cylinder model fits of SAXS scattering profiles in Figure 2-10B.

Table 2-9. Zeta-potential of select mPBI-FM formulations.

Table 2-10. Polydispersity index of mPBI-FM-E at various timepoints after treatment with 5 M H₂O₂ as measured by dynamic light scattering (DLS).

Table 2-11. mPBI-FM-E parameters estimated from flexible cylinder model fit of SAXS scattering profiles in Figure 2-14E for 0 min and 45 min after treatment with 5 M H₂O₂.

Table 2-12. Oxidized mPBI-FM-E parameters estimated from micelle model fit of SAXS scattering profile in Figure 2-14E for the timepoint at 90 min after treatment with 5 M H₂O₂.

Table 3-1. Definitions of cell populations for in vivo cellular biodistribution study.

Table 4-1. Nanocarrier diameter measured by DLS and Zeta-potential.

Table 4-2. IC₅₀ values (μM) of BNZ-loaded nanocarriers after 48 h of incubation on intracellular amastigotes in RAW 264.7 macrophages, H9c2 cardiomyoblasts, and 3T3-L1 adipocytes.

Table 4-3. Treatment groups to assess effect of BNZ-MC on preventing or treating *T. cruzi* infection in a Chagas disease mouse model.

Table 4-4. Composition and formation method of BNZ-loaded FM hydrogels.

Table 4-5. Average diameter and DiR encapsulation efficiency for various PEG-*b*-PPS nanocarrier morphologies.

CHAPTER 1

1. Introduction: Dissertation Overview and Review of Literature

1.1 Dissertation Overview

1.1.1. Motivations and Objectives

The morphology and flexibility of nanoparticles impact their performance *in vivo*, from their biodistribution and circulation time to their internalization and interactions with immune cells. In this work, filamentous polymeric nanocarriers composed of poly(ethylene glycol)-*block*-poly(propylene sulfide) (PEG-*b*-PPS) co-assembled with pi-stacking block copolymers are developed as drug delivery vehicles to investigate the effect of filament flexibility on immune cell interactions and uptake. In addition, these filamentous nanocarriers are explored in different biomedical applications, including in passive targeting and antiparasitic drug delivery.

1.1.2. Dissertation Outline

In Chapter 1, a comprehensive overview of the synthesis and characterization of filamentous polymeric nanoparticles will be provided. In addition, the potential advantages of their unique morphology for biomedical applications ranging from cancer nanomedicine to immunoengineering will be discussed. Chapter 2 will cover my work in the development and characterization of a new pi-stacking filamentous nanocarrier platform with controlled flexibility, enhanced stability and scalable formation compared with PEG-*b*-PPS nanocarriers without pi-stacking chemical moieties. Chapter 3 will discuss my investigation of how the flexibility of filamentous nanocarriers impacts their internalization by macrophages *in vitro* and their biodistribution on a cellular and organ-level *in vivo*. Chapter 4 will explore the potential of the

filamentous nanocarriers in various biomedical applications, including passive targeting of the tumor-draining lymph node in a melanoma cancer model and as drug delivery vehicles for an anti-parasitic drug for Chagas disease. Lastly, Chapter 5 will summarize my work and detail future directions for the development of filamentous nanocarriers for biomedical applications.

1.2 Review of the Literature

1.2.1 Self-assembled Filamentous Structures

Self-assembled filamentous nanostructures can be found throughout nature, from disease-causing agents to essential components of the extracellular matrix and cytoskeleton. These nanofilaments have a wide range of physicochemical properties made possible by their high aspect ratio morphology that enhances their biological function. Filamentous viruses include the Ebola virus in the filovirus family, which causes outbreaks of hemorrhagic fever in humans.¹ Influenza virus, which causes seasonal epidemics in humans, has both spherical and filamentous forms, with the 2009 pandemic strain and human isolates from the upper respiratory tract found to be predominantly filamentous.² Many plant viruses, such as Tobacco Mosaic Virus and Potato Virus X, and M13 bacteriophage are filamentous but not pathogenic to humans, and so are of interest to serve as the basis of self-assembled materials for biomedical applications.^{3, 4} Self-assembled filaments are also found throughout the human body, as exemplified by actin filaments and microtubules that dynamically control cell shape and migration as well as collagen fibrils, which are the primary component of the extracellular matrix. These filaments, with their diverse range of lengths, diameters, and stiffness (**Table 1-1**), have been the inspiration for many biomimetic engineered nanofilaments that serve as biomaterials for tissue engineering and drug delivery.

Table 1-1. Morphological parameters of examples of filamentous nanostructures found in nature. The persistence length (L_p) is the length along a filament where the direction of the filament persists or does not change before the filament bends. It is thus a measure of the flexibility of a filament, where more flexible filaments have length (L) of the filament much greater than L_p , and more rigid filaments have $L_p > L$. The L_p of different filaments found in nature is listed here if experimentally quantified.

	Length	Diameter	Flexibility	References
Ebola virus	1-20 μm	100 nm	Flexible	4
Influenza virus (filamentous form)	20 μm	100 nm	Flexible	2
Tobacco Mosaic Virus	300 nm	18 nm	Rigid	5
Potato Virus X	515 nm	13nm	Flexible	6, 7
M13 Bacteriophage	900 nm	4.5 nm	Semi-flexible $L_p=1\mu\text{m}$	8-10

	Length	Diameter	Flexibility	References
Actin filaments	Up to 100 μm	8 nm	Flexible, $L_p=16.7\mu\text{m}$	11
Microtubules	Up to 100 μm	30 nm	Rigid $L_p=5200\mu\text{m}$	12
Intermediate filaments	2-4 μm	8-12 nm	Flexible, $L_p=1\mu\text{m}$	13

Type 1 collagen monomer	309 nm	1.5 nm	Flexible, $L_p=14.5\text{nm}$	14, 15
Type 1 collagen fiber	14.6 μm	156 nm	Flexible, $L_p=9.11\ \mu\text{m}$	16

Self-assembly is the spontaneous, thermodynamically-driven arrangement of amphiphilic molecules into ordered structures.¹⁷ Amphiphiles, molecules consisting of both hydrophobic and hydrophilic components, spontaneously self-organize when above critical aggregation concentrations under specific solvent conditions to form diverse morphologies, a process that has been reviewed extensively elsewhere.^{17, 18} A range of natural and synthetic molecules, including proteins, peptides, and polymers, have been employed to self-assemble into nanofilaments (**Figure 1-1**). Viral proteins, after extraction from natural sources such as plants or synthesis in vitro, have been studied as building blocks for protein-based filaments that self-assemble around nucleic acid templates.^{8, 19} Peptides can also self-assemble into nanofibers stabilized via π -stacking interactions and/or by forming secondary structures like α -helices and β -sheets via hydrogen bonding.²⁰⁻²⁴ Synthetic nanofilaments can be formed from peptide amphiphiles (PA) fabricated using solid phase chemistry, which generally consist of a hydrophobic lipid tail conjugated to a hydrophilic peptide sequence.²⁵ Similarly, amphiphilic block copolymers (BCP) synthesized via living polymerization techniques, allow the self-assembly of cylindrical “worm-like micelles,” also known as filomicelles (FM).^{26, 27}

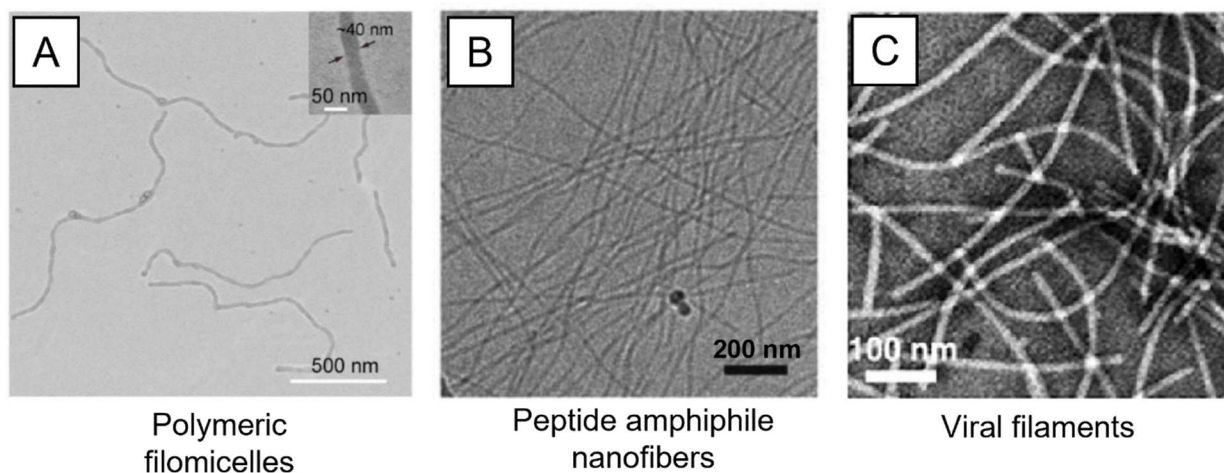


Figure 1-1. Filaments of different lengths and flexibilities can be self-assembled from diverse building blocks including block copolymers, peptide amphiphiles, and proteins. A) Cryogenic transmission electron microscopy (Cryo-TEM) image of polymeric filaments (filomicelles) self-assembled from the block copolymer poly-ethylene glycol-*b*-(poly camptothecin methacrylate-2-(pentamethyleneimino)ethyl methacrylate), or PEG-*b*-P(CPTKMA-co-PEMA). Reproduced with permission from Ke *et al.*, 2020.²⁶ Copyright 2020 Elsevier. B) Cryo-TEM image of nanofibers self-assembled from peptide amphiphiles. Reproduced with permission from Lin *et al.*, 2018.²⁸ Copyright 2018 RSC. C) Transmission electron microscopy (TEM) image of viral filament potato virus X (515 nm by 13 nm) self-assembled from viral proteins. Adapted with permission from Shukla *et al.*, 2017.²⁹ Copyright 2017 Elsevier.

FM, compared to other self-assembled filament systems, have enhanced stability, potential for scalable production, and chemical versatility that make them attractive for biomedical applications. FM have the advantages of requiring chemical synthesis instead of recombinant technology, which is faster and less costly to scale up to Good Manufacturing Practice (GMP)-grade manufacturing.^{7,}

^{19,30} Unlike viral filaments, FM formation does not require extraction from biological organisms, and thus less regulation and optimization is needed to ensure removal of biological impurities.^{7, 19,}
³⁰ Synthetic polymers also have increased stability and processibility compared to peptides and proteins.³¹ Proteins and peptides are sensitive to factors such as pH, temperature, and salt concentrations, leading to challenges in solubility, stability and scalability.³⁰ For example, different salt forms of a peptide may be ideal for small scale manufacturing but not for large scale. Lastly, the chemical versatility of BCP systems have allowed for the development of a variety of biocompatible and biodegradable FM functionalized with bioactive moieties.³²

While much progress in the development of synthetic polymeric filaments for biomedical applications has been made, FM, unlike filaments self-assembled from viral proteins and peptides,^{24, 33-35} have not yet advanced beyond pre-clinical studies. Current challenges for clinical translation of FM include achieving more monodisperse filaments with control over filament length and flexibility, improving the scalability of self-assembly methods, and furthering our understanding of the pharmacokinetics and biodistribution of filamentous nanocarriers in vivo.

1.2.2. Synthesis, Self-assembly, and Stability of Polymeric Filaments

The engineering of FM for biological applications requires the rational design of three different areas: synthesis of the block copolymer, formation of FM via self-assembly, and controlled modulation of FM stability. Amphiphilic BCP that form FM can be synthesized from a variety of hydrophilic and hydrophobic monomers with diverse chemistries allowing for the incorporation of functional groups or prodrugs.³² FM formation then must be explored for each block copolymer system via various self-assembly methods.³² These methods generally exploit a selective solvent

to drive the aggregation or crystallization of the hydrophobic block, and include techniques such as thin film hydration, flash nanoprecipitation, and crystallization-induced self-assembly.^{32, 36, 37} Lastly, as FM often are kinetically controlled systems, FM can undergo cylinder-to-sphere morphological transitions depending on the chemical properties of the BCP and solvent conditions.^{38, 39} By modulating the kinetics of this transition, control over FM stability and thus cargo release can be achieved. Thus, the BCP chemistry, self-assembly method, and FM stability can be optimized to form FM for desired biomedical applications.

1.2.2.1 Synthesis of FM-forming BCP. Polymer engineering has enabled the synthesis of BCP with controlled composition and chain length to form diverse nanostructure morphologies, including FM. Filamentous structures preferentially form when Israelachvili's packing parameter $p = v/(a_0l)$, where v is the volume of the hydrophobic block, a_0 is the area of the hydrophilic head, and l is the length of the hydrophobic block, is $1/3 < p < 1/2$.^{40, 41} Based on this principle, the hydrophilic weight fraction (f) of the BCP is one parameter that has been utilized to predict nanostructure morphologies after self-assembly.^{42, 43} The general trend is that vesicular polymersomes (PS), then FM, then micelles (MC) are observed as f increases, although the exact cutoff points between different morphology regimes depend on the BCP system.^{42, 44} Thus, polymerization techniques that allow the reproducible synthesis of BCP in the desired hydrophilic weight fraction (f) range, along with control over chemical functionality and composition, is needed to synthesize FM-forming BCP.

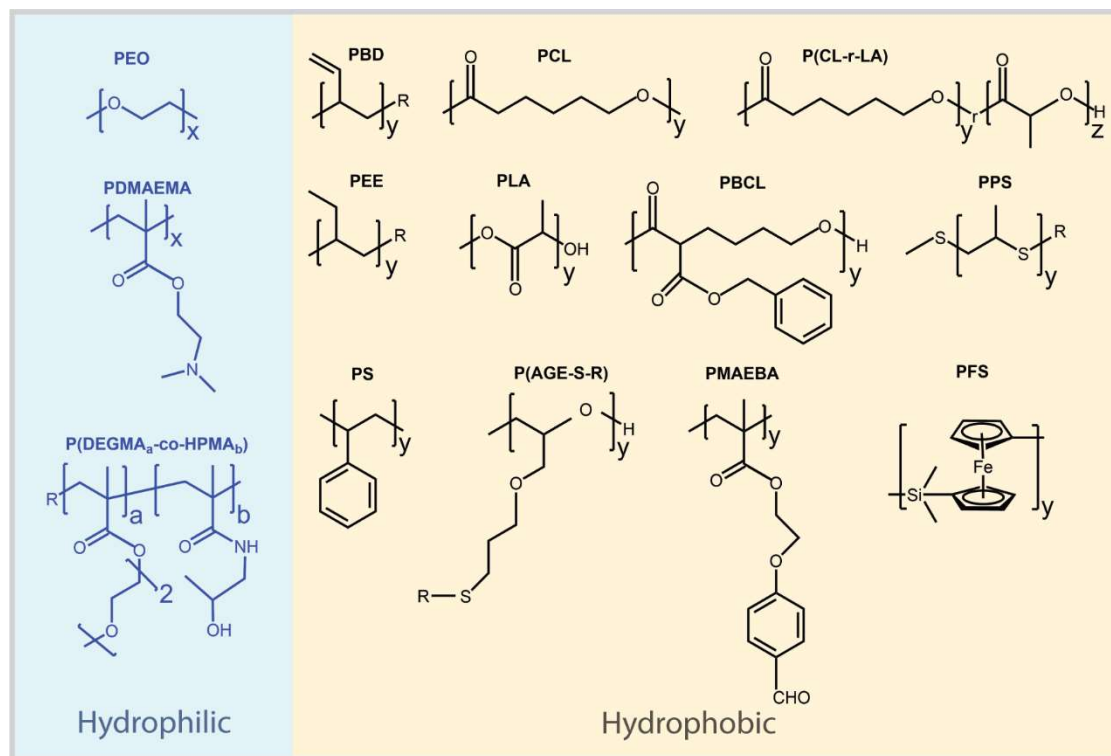


Figure 1-2. Chemical structures of select hydrophilic and hydrophobic polymers that have been used to form amphiphilic block copolymers that self-assemble into FM. PEO: poly(ethylene oxide) or poly (ethylene glycol). PDMAEMA: poly((N,N'-dimethylamino)ethyl methacrylate). P(DEGMA-co-HPMA): poly((di(ethylene glycol) methyl ether methacrylate)co-N-(2-hydroxypropyl) methacrylamide)). PBD: polybutadiene. PCL: poly(ε-caprolactone). P(CL-r-LA): poly(3-caprolactone-r-L,D-lactide). PEE: polyethylethylene. PLA: poly(lactic acid). PBCL: poly(α-benzyl carboxylate-ε-caprolactone). PPS: poly(propylene sulfide). PS: polystyrene. P(AGE-S-R): postalkylated poly(allyl glycidyl ether). PMAEBA: poly(p-(methacryloxyethoxy)benzaldehyde). PFS: poly(ferrocenyl dimethylsilane).

Many amphiphilic BCP used to form FM are synthesized with living anionic polymerization, where polymerization is initiated by anions, generally without spontaneous termination reactions.⁴⁵ Anionic polymerization allows for the synthesis of polymers with low polydispersity in terms of molecular weight and composition.⁴⁶ Some of the most common hydrophilic and hydrophobic polymers used to form FM are shown in **Figure 1-2**. These include poly(ethyleneoxide)-*b*-poly(butadiene) (PEO-*b*-PB) and poly(ethyleneoxide)-*b*-poly(ethylene) (PEO-*b*-PEE), which are inert and have been used to form long FM that are tens of microns in length.²⁷ Other BCP used for FM formation include PEO-*b*-poly(ϵ -caprolactone) (PEO-*b*-PCL), PEG-*b*-poly(lactic acid) (PEG-*b*-PLA), PEG-*b*-poly(ϵ -caprolactone-*r*-lactic acid) (PEG-*b*-P(CL-*r*-LA)), and PEG-*b*-poly(alpha-benzyl carboxylate epsilon-caprolactone) (PEG-*b*-PBCL).⁴⁷⁻⁵⁰ These BCP are attractive for biomedical applications because of their biodegradability and biocompatibility.⁵¹ PEG-*b*-PBCL also contains an aromatic group in its hydrophobic core, which enhances FM formation compared to PEG-*b*-PCL FM, increasing the mass fraction of FM vs. MC formed.⁴⁹ Another BCP that can form FM, poly(ethylene glycol)-*b*-poly(propylene sulfide) (PEG-*b*-PPS), is oxidation sensitive and has shown to be non-toxic and non-immunogenic.^{39, 52} Methoxypoly(ethylene glycol)-*b*-poly(allyl glycidyl ether) (mPEG-*b*-PAGE) is another biocompatible BCP first synthesized with anionic polymerization. In this case, alkyl chains of different lengths were then conjugated to the hydrophobic block via thiol-ene click chemistry, allowing the formation of BCP with different hydrophilic weight fractions from the same initial BCP.⁵³ Anionic polymerization therefore continues to be useful for synthesizing biocompatible BCP for FM self-assembly.

FM-forming BCP have also been synthesized through reversible addition-fragmentation chain-transfer (RAFT) polymerization, which is a living radical polymerization. RAFT polymerization also allows for the synthesis of polymers with controlled molecular weight, versatile end-group functionalization and low molar mass polydispersity.⁵⁴ In one example, PEG with a copolymerized block of thioketal-linked camptothecin methacrylate (CPTKMA) and 2-(pentamethyleneimino) ethyl methacrylate (PEMA), (PEG-*b*-P(CPTKMA-co-PEMA)), formed FM with an average length of 2.5 μm .²⁶ This diblock copolymer is both pH and oxidation responsive and a prodrug of camptothecin, allowing stimuli-responsive drug release of an anti-cancer therapeutic.²⁶ Another BCP-prodrug was made from poly((N,N'-dimethylamino)ethyl methacrylate)-*b*-poly(methacryloxyethoxy)benzaldehyde), or PDMAEMA-*b*-PMAEBA, where the anti-cancer drug doxorubicin was conjugated to the aldehyde groups of PMAEBA, leading to pH-responsive drug release.⁵⁵ This BCP formed short FM with a length of 140 nm and longer FM with a length of 2 μm depending on the hydrophobic chain length.⁵⁵ This synthesis technique also allows for FM to be self-assembled during a one-pot polymerization process. RAFT polymerization is thus especially useful for the synthesis of pro-drug FM for biomedical applications.

In summary, BCP for FM self-assembly can be synthesized by both anionic polymerization and RAFT polymerization to achieve BCP with low polydispersity, different hydrophilic weight fractions, and a variety of hydrophobic and hydrophilic blocks. The engineering and design of FM for biomedical applications starts with consideration of the chemistry of the block copolymer. The BCP used influences the biocompatibility, biodegradability, immunogenicity, drug-loading

capacity, and stimuli-responsiveness of the self-assembled FM. Reproducible formation and stability of the resulting FM and FM “cylinder-to-sphere” transitions also are influenced by the chemistry of the BCP.

1.2.2.2 Self-assembly Methods for FM. The spontaneous self-assembly of filamentous structures versus other morphologies not only depends on the chemical composition and hydrophilic weight fraction of the BCP but also on the formation method, which has to be optimized for each BCP.^{17, 53} Standard self-assembly methods for FM include thin film hydration and co-solvent evaporation.^{32, 50} In thin film hydration, the block copolymer is dissolved in an organic solvent and dried into a thin film that is hydrated with the aqueous solvent under agitation.^{32, 56} In co-solvent evaporation, the block copolymer is first solubilized in an organic solvent suitable for both blocks and then added to an aqueous solvent while mixing, after which the organic solvent is allowed to evaporate or removed by dialysis.^{17, 47, 49} These methods require the optimization of different parameters such as the thickness of the film and hydrophobicity of the block copolymers for thin film hydration, and stirring speed and rate of addition of the organic solvent to the aqueous solvent for co-solvent evaporation.^{26, 57-59} Neither of these methods are highly reproducible or scalable for the assembly of uniform FM without significant contamination of other nanostructures, such as MC and PS. There is thus considerable interest in developing additional methods for improving FM self-assembly.

Emerging self-assembly methods for FM formation include flash nanoprecipitation (FNP), crystallization-driven self-assembly (CDSA), polymerization-induced self-assembly (PISA), and temperature-induced morphological transitions (TIMT).^{32, 37, 60} A rapid and scalable self-assembly

method, FNP involves the dissolution of the block copolymer in a water-miscible organic solvent followed by rapid mixing with an aqueous solvent in a confined impingement jet mixer. So far, PEG-*b*-PPS have been shown to form FM via FNP with $f=0.21$, and this technique may be applicable for FM formation with other BCP systems.³⁷ In CDSA, one of the blocks of the semicrystalline BCP, such as PEO, PLA, or poly(ferrocenylsilanes), crystallizes in a selective solvent to form the FM core.^{32, 61} This method has the advantage of generating FM with highly uniform lengths.^{62, 63} However, CDSA has mainly been used to form FM in organic solvents, and the toxicity of these FM *in vivo* still needs to be assessed. In PISA, micelles are formed *in situ* during the synthesis of the BCP, and as polymerization continues, the micelles undergo a “sphere-to-cylinder” transition into FM.³² RAFT polymerization has been most widely used for PISA to form FM without a second self-assembly step.^{55, 64} However, forming FM in aqueous solutions through PISA is currently limited to certain polymers (polystyrene, poly-2-hydroxypropyl methacrylate, and poly(N-isopropylacrylamide)).³² Lastly, in TIMT, self-assembled spherical nanostructures possessing polystyrene and different polymethacrylate cores undergo a “sphere-to-cylinder” transition upon a change in temperature.^{32, 65} This allows for reversible temperature-dependent “cylinder-to-sphere” transitions of non-toxic FM *in vitro* and the formation of thermoresponsive gels.^{66, 67} While these emerging self-assembly methods are promising for enhancing the reproducibility and scalability of FM formation, more *in vivo* and toxicity studies of FM formed from newer methods such as PISA and CDSA are needed as these FM are evaluated for biomedical applications.

1.2.2.3 “Cylinder-to-sphere” Morphological Transitions of FM. Both thermodynamic considerations and kinetic factors have been shown to affect the final nanostructure and

morphological transitions observed in BCP systems.^{68, 69} The kinetics of chain exchange, which is required to reach equilibrium, is typically slower in aqueous solutions for BCP compared to low molecular weight surfactants, promoting the formation of non-equilibrium structures.^{70, 71} FM are an example of a morphology that can be formed through kinetic trapping depending on the self-assembly method and solvent conditions, which often results in FM being difficult to self-assemble reproducibly and undergoing “cylinder-to-sphere” transitions into micelles over time.^{38, 69, 72} Generally in BCP systems, the boundaries between different morphologies depend on many parameters including the block chain lengths, the excluded volume of the soluble block, the surface free energy per area of the insoluble block, the volume fraction of the monomer in the insoluble block and intercoronal interactions.^{73, 74} Changing these parameters can shift the morphological boundaries, which can induce “cylinder to sphere” morphological transitions.⁶⁵ For example, the volume fraction of the blocks can be changed through thermal deprotection or the addition of core-like homopolymers to the system, leading to the morphological transition.^{75, 76} LaRue *et al.*, also demonstrated that the transition can be induced solely by temperature changes, where polystyrene-*b*-polyisoprene FM transformed into spherical micelles upon heating to 35°C.⁶⁵ This was due to the temperature dependence of the volume of the soluble block and surface free energy of the insoluble block. Additionally, the “cylinder-to-sphere” transition can be induced by changes in the interfacial tension through modulation of the solvent quality or chemical composition,^{38, 72, 74} as FM and MC are respectively favored at higher and at lower interfacial tensions.^{72, 77} In a model system with FM composed of poly(ethylene-alt-propylene)-*b*-poly(ethylene oxide) diblock copolymers in a mixture of dimethylformamide and water, at higher interfacial tension, FM are favored as they have a smaller equivalent core radius and thus reduce the elastic energy of the core

chains, while at lower interfacial tensions, MC reduce the interchain repulsion in the corona and so are favored.⁷² A variety of mechanisms can therefore enable control over the “cylinder-to-sphere” transition in FM.

Currently, there are two proposed kinetic pathways for the “cylinder-to-sphere” transition. The first pathway is driven by Rayleigh instability, where undulations form along the length of the FM, forming an intermediate that resembles a pearl necklace, before the entire FM fragments into MC.⁷⁸ In the second pathway described by Burke and Eisenberg, the ends of the FM bud off, forming MC.⁷⁴ Both of these pathways have been visualized directly by transmission electron microscopy (TEM) in different BCP systems.^{38, 74, 77} While the reasons why a system would undergo one pathway vs. the other is not well understood, the degree of deviation of the FM from the equilibrium state and the magnitude of change in the interfacial tension that was induced may affect the observed kinetic pathway.^{38, 77, 79} The budding mechanism has been seen in BCP systems where there are changes in the interfacial tension over time as f of the BCP increases. For example, in FM formed from PEO-*b*-PCL, hydrolysis of the PCL during “chain end cleavage” increases f , leading to bulb formation and budding of spherical MC.⁴⁸ In a similar mechanism to PEO-*b*-PCL, oxidation of the hydrophobic PPS block in FM formed from (PEG-*b*-PPS) leads to an increase in the hydrophilic weight fraction and spontaneous budding of MC.⁷⁷ When the interfacial tension was changed by a large solvent jump from a 50% to a 70% DMF solvent solution, the Rayleigh instability pathway was observed in poly(ethylene-*alt*-propylene)-*b*-poly(ethylene oxide) FM.⁷⁹ The Rayleigh instability pathway was also observed in poly(2-vinylpyridine)-*b*-poly(ethylene oxide) FM over the course of days under continuous stirring.³⁸ As no change in interfacial tension was induced in this case, the rate and pathway of transition was hypothesized to be due to the

inherent thermodynamic instability of the kinetically trapped FM.³⁸ Thus, both the chemistry of the block copolymer, solvent conditions, and thermodynamic stability of the FM after formation influence the kinetics of the “cylinder-to-sphere” transition.

1.2.3 Characterization of Self-assembled Filaments

Many techniques have been applied to characterize self-assembled filaments. Fluorescence microscopy (for filaments several microns in length), TEM, cryoTEM, and atomic force microscopy have been used to visualize filaments and confirm their morphology.^{56, 65, 77, 80, 81} Filament parameters such as the persistence length, contour length, and core diameter can also be estimated using these techniques with image analysis software, but require many representative images or videos of freely diffusing FM when using fluorescent microscopy for statistical analysis.^{47, 81} Other techniques including small angle X-ray scattering (SAXS) and small-angle neutron scattering have been used to estimate filament parameters by measuring the scattering of the filament population in solution and fitting the scattering data to various cylindrical models.^{27, 77, 82} The above techniques, along with dynamic light scattering, have been used to characterize and provide insight into the mechanisms behind the “cylinder-to-sphere” transitions of FM.^{65, 67, 79, 83} Dynamic oscillatory rheology has also been used to quantify the stiffness and viscoelasticity of concentrated filaments in solution.^{27, 67} Taken together, accurate characterization of self-assembled filaments requires confirmation with multiple orthogonal techniques.

1.2.4 Techniques to Modulate Filament Length and Flexibility.

Filament morphology parameters including their length and flexibility affect their performance in vitro and in vivo, so it is advantageous to develop techniques for engineering

filaments with different lengths and flexibility. As discussed earlier, the hydrophilic weight fraction of the BCP influences the length of the FM, with decreasing hydrophilic weight fractions generally leading to longer FM.⁵⁵ BCP with higher molecular weights are also more amenable to the formation of longer FM that are microns in length.⁵⁰ Shorter FM can also be formed post-self-assembly by fragmentation of longer FM through extrusion through membrane filters, sonication, and ultrasound.^{26, 47} CDSA also allows for length control of FM by modulation of self-assembly conditions, with good solvent conditions leading to long FM and poor solvents leading to short FM because of an increased number of nuclei.⁶³ The length of the FM can also be increased during CDSA by adding more polymer during self-assembly.⁶² The length of FM thus is influenced by formation conditions and post-formation processing methods.

Different approaches to control FM flexibility include modulating the molecular weight of the BCP, increasing the crystallinity of the hydrophobic core, and employing chemical cross-linking. Increasing the molecular weight of the diblock copolymer and thus the diameter increased the stiffness of PEO-*b*-PBD and PEO-*b*-PEE FM.^{81, 84} Increasing the alkyl chain length of mPEG-*b*-PAGE increased the crystallinity of the BCP as measured by differential scanning calorimetry and led to the formation of shorter more rigid rod-like FM.⁵³ This technique has also been used for peptide filaments, as after addition of isomeric hydrocarbons to amphiphilic peptides, the persistence length of peptide filaments was varied without changing the width or morphology.²⁸ Chemical crosslinking, such as of the poly(butadiene) hydrophobic core of FM, also increased the stiffness and stability of FM.^{27, 64, 81} In another example, crosslinking of the FM core with a siloxane led to stiffer FM that were then resistant to dissociation with methanol and surfactants.⁶⁴

While great progress has been made, better understanding of the chemistry and techniques required to modulate filament length and flexibility is still needed.

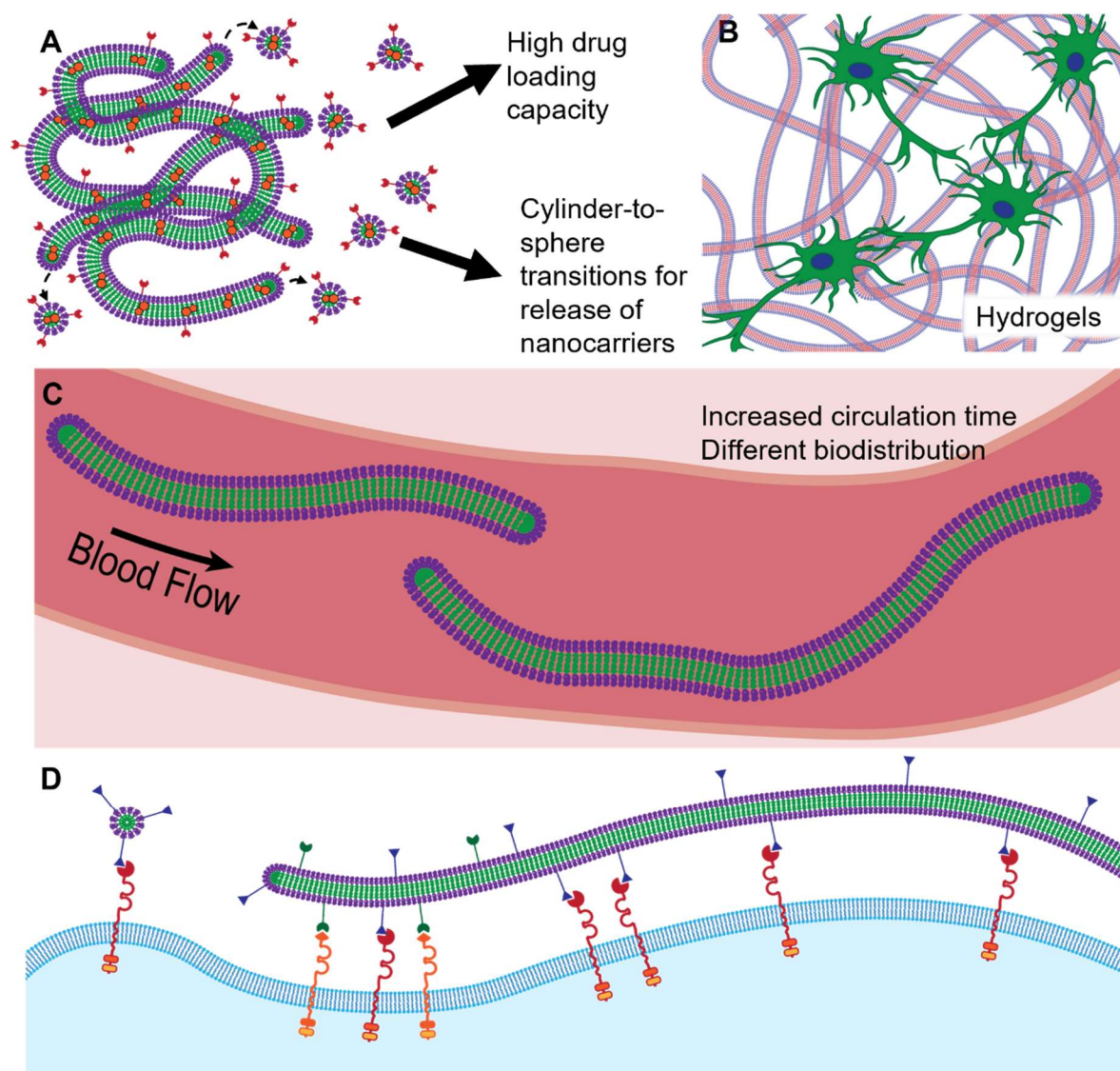


Figure 1-3. Advantages of self-assembled filaments for biomedical applications. A) Self-assembled filaments can be loaded with hydrophobic drugs in their core, and surface functionalized with antigens and contrast agents. Some filaments can undergo controlled

“cylinder-to-sphere” transitions for sustained delivery of spherical nanocarriers. B) Self-assembled filaments can be crosslinked to form hydrogels for tissue regeneration or depots for sustained drug release. C) Filaments have been shown to elongate under flow conditions leading to increased circulation time and differences in biodistribution on an organ and cellular level. D) Filaments, when compared with spherical nanocarriers, can be used to investigate the effects of morphology on endocytosis. Filaments can also be functionalized with different targeting ligands for multivalent targeting with increased avidity because more ligands can be incorporated on its surface due to their high aspect ratio. The flexibility of targeted filaments has also shown to increase receptor clustering.

1.2.5. Advantages of Filaments for Biomedical Applications

Filamentous nanostructures, because of their unique morphology, have certain advantages for biomedicine including high drug loading capacities because of their high internal hydrophobic surface area (**Figure 1-3A**).⁴⁷ The filaments can also be crosslinked to form hydrogels for applications in tissue engineering and sustained drug delivery (Figure 1-3B). The filamentous morphology also leads to differences in circulation time and biodistribution (Figure 1-3C), with FM shown to have increased accumulation in tumors in mice models.⁵⁰ FM also have enhanced avidity for multi-valent and active targeting to cells (Figure 1-3D).⁸⁵ Filamentous nanostructures have thus provided mechanistic insight into the effect of nanostructure morphology, including length, flexibility, and aspect ratio, on the biological performance of materials in vivo.

1.2.5.1 High Drug Loading Capacities. FM show promise for nanomedicine due to their high drug loading capacity, which has been extensively characterized in comparison with spherical

MC. Cai *et al.* found that PEO-*b*-PCL FM had a 2-fold higher drug loading capacity for paclitaxel, a chemotherapeutic, than spherical MC, most likely due to FM having a higher internal hydrophobic surface area compared with MC.⁴⁷ Subsequent studies by the group enhanced this drug loading capacity via incorporation of aromatic groups onto the hydrophobic block of the copolymer and found that these FM were more stable and effective at inducing cancer cell death *in vitro* and *in vivo*.⁴⁹ The ability of FM to load multiple therapeutic cargoes has also been investigated.⁸⁶ Jelonek *et al.* studied the loading of paclitaxel, 17-AAG, and rapamycin within PEG-*b*-PLA FM, and found that individual drug loading efficiencies and release profiles were dependent on drug-drug and drug-polymer interactions, with rapamycin having the lowest loading efficiency. Therefore, careful assessment of how therapeutic cargoes interact with other payloads and the polymer system is important in the design and applications of FM for cancer nanomedicine. Lastly, while the drug loading capacities of FM are often characterized in comparison with spherical MC, some block copolymer FM can actually transition into spherical MC *in vivo* upon application of a particular stimulus.^{77, 79} Karabin *et al.* demonstrated the ability of PEG-*b*-PPS FM to retain encapsulated payloads within released spherical MC following an oxidation-triggered “cylinder-to-sphere” transition.⁷⁷ This property, along with their high drug loading capacity, demonstrates the potential of FM to serve as tools for achieving sustained and controlled drug delivery.

1.2.5.2 Morphology-dependent Differences in Circulation Time and Biodistribution. Self-assembled filaments have been explored as nanocarriers for drug delivery since they exhibit increased systemic circulation times compared to spherical nanoparticles.⁸⁷ A seminal work from Discher’s group established a key connection between the length of FM and systemic circulation

time.⁸⁸ PEG-*b*-PCL FM, up to a length of 8 μm , were able to circulate up to 7 days in rodents following intravenous administration, approximately ten times longer than spherical particles. This increase in circulation time may be due to the elongation of FM under certain flow conditions where the flow rate $> 5 \mu\text{m/s}$, leading to decreased uptake by the mononuclear phagocyte system.^{32, 56, 89} Interestingly, FM longer than 8 μm rapidly fragmented and were cleared quickly. A study comparing the effects of morphology, crosslinking, and folate-conjugation on nanocarrier biodistribution found that folate-conjugated, crosslinked polyethylene glycol methyl ether acrylate-based FM have a characteristic long circulation time, but also high retention in the liver and kidney.⁹⁰ This increase in circulation time has also been confirmed with viral filaments. Le *et al.* developed a flexible, PEGylated potato mosaic virus (PEG-PVX) filament (515 nm in length and 13 nm in width) conjugated with an anticancer drug, doxorubicin (DOX) and found that the circulation time of DOX was increased in vivo.⁹¹

The relationship between the length or aspect ratio of filaments and cellular internalization is inversely proportional. Long or high aspect ratio filamentous nanocarriers exhibit stronger interactions with the cell membrane; however, factors such as greater membrane wrapping time⁹² and steric hindrance²⁶ influence their uptake as compared to their short or low aspect ratio counterparts. In one study, steric hindrance caused by long FM ($\sim 2.5 \mu\text{m}$) at the cell membrane obstructed cellular uptake by macrophages whereas short FM ($\sim 180 \text{ nm}$) were readily internalized via a clathrin and caveolae-mediated and energy-dependent pathway.²⁶ Similarly, Shukla *et al.*, demonstrated that PEGylated tobacco mosaic virus nanorods with a low aspect ratio (AR 3.5) were rapidly phagocytosed by cells while high aspect ratio (AR 16.5) nanorods were trapped at the cell membranes.⁵ The effect of surface charge on cellular internalization of positively-charged long

filaments ($> 10 \mu\text{m}$) self-assembled from GNNQQNY heptapeptide was recently studied.⁹³ However, this strategy enhanced cellular uptake by PC3-Flu cancer cells of vesicle nanocarriers and not of the filaments. In a separate finding, cellular internalization of biotinylated worm micelles made up of PEG-*b*-PEE was proposed to be mediated by a receptor-mediated endocytosis mechanism through packaging of the micelle or fragmentation.⁸⁵

Filaments also exhibit different cellular and organ-level biodistribution *in vivo* compared to spherical particles, allowing for passive targeting of distinct cell types. Yi *et al.*, investigated the cellular and organ-level biodistribution after intravenous administration in mice of PEG-*b*-PPS FM,⁹⁴ which have great clinical potential due to their versatility in fabrication⁹⁵ and surface functionalization,⁹⁶ and non-toxic and non-immunogenic nature.⁸² Interestingly, PEG-*b*-PPS FM were predominantly taken up by neutrophils and monocytes in the blood when compared to their spherical (PS and MC) counterparts. Furthermore, these FM were minimally associated with mononuclear phagocytic cells in the liver, lymph node, and spleen, which allowed enhanced circulation time in the blood. These findings have set a benchmark for the development of new cell-based immunotherapies using FM to treat chronic inflammatory diseases⁹⁷ and cancer^{98, 99} where neutrophils play a vital role. In another study, Dowling and Scott *et al.*, showed that subcutaneous administration of PEG-*b*-PPS FM in mice was able to efficiently target monocytes and plasmacytoid dendritic cells in the lymph node and spleen, respectively, demonstrating the effect of the route of administration on immune cell targeting.¹⁰⁰

1.2.5.3 Enhanced Avidity for Active Targeting. Filaments allow for high targeting avidity due to their high surface area per nanostructure, as ligands can be presented over their entire contour

length. This increased ligand presentation on FM surfaces makes interaction with target cells or tissues more likely, facilitating lengthwise adherence to specific surfaces. As an early example of this principle, Dalhaimer *et al.*, demonstrated the ability of biotinylated FM to “zip-up” lengthwise onto avidin-coated surfaces within 1 second.⁸⁵ Other applications of this concept have decorated FM surfaces with targeting antibodies for more functional studies. Using antibodies specific for endothelial surface markers (ICAM-1, PECAM-1, and thrombomodulin) conjugated onto polyethylene oxide (PEO)-based FM, Shuvaev *et al.*, demonstrated high avidity of the antibody-presenting FM for targeting and binding to vascular endothelium, overcoming the forces of blood flow alignment to anchor and zip up onto target cells.¹⁰¹ As this blood flow alignment is responsible for the uniquely long circulation time of FM, the authors highlighted the importance of careful selection of targeting antibodies to design FM that have both high circulation time and high target avidity.

A unique functional application of antibody-decorated filaments is their utilization as synthetic dendritic cells (sDCs) via engineering of poly(isocyanate peptide) filaments to display anti-CD3 antibodies.¹⁰² These sDCs were hypothesized to bind to and activate T cells via multivalent interactions, where multiple neighboring receptors on a T cell could be engaged by one sDC. T cell activation through subsequent clustering of the engaged receptors is then possible for the filamentous sDCs due to their flexibility. Notably, the sDCs were able to activate T-cells 7-times more efficiently than spherical anti-CD3-labeled controls. Subsequent studies found that both sDC co-stimulatory signal presentation¹⁰³ and higher antibody density¹⁰⁴ contributed to enhanced activation.

Finally, display of molecules on filament surfaces is advantageous for not just cellular targeting, but also for enhanced targeting of disease-associated proteins or viruses. The Stupp group synthesized PA nanofibers conjugated with aptamers specific for the B chain of the platelet-derived growth factor (PDGF-BB), whose blockade is of therapeutic benefit in multiple proliferative disorders.¹⁰⁵ The aptamer-PA-nanofibers (apt-PAN) displayed improved binding with PDGF-BB compared with free aptamers, due to multivalent interactions and cooperative binding. The apt-PANs also displayed increased nuclease resistance compared with free aptamers suggesting that attachment onto the PAN surface slowed down DNA hydrolysis, indicating another advantage of conjugation of targeting moieties onto filament surfaces. A very creative application of ligand-decorated filamentous nanocarriers was shown by Chung *et al.*, who developed sialyllactose-conjugated filamentous bacteriophages (SLPhages) with anti-influenza activity.¹⁰⁶ The native M13 bacteriophage structure had minimal immunogenicity but when decorated with multiple sialyllactose ligands facilitated interactions with influenza virions by allowing the SLPhages to wrap around individual viral particles, achieving subsequent inhibition of viral activity.

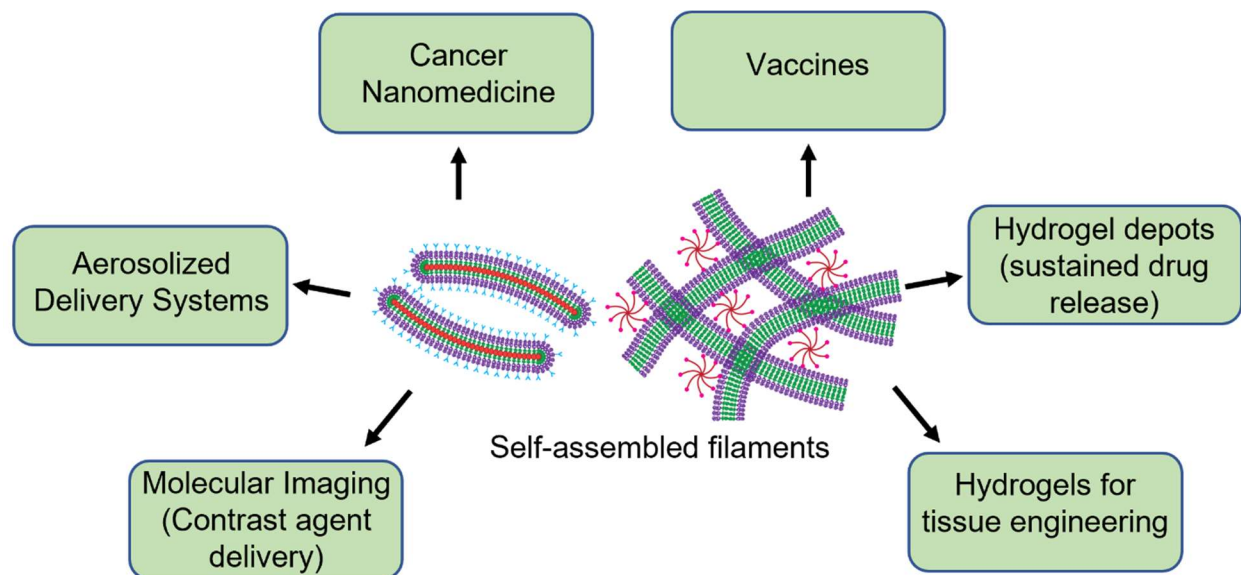


Figure 1-4. Emerging biomedical applications of self-assembled filaments.

1.2.6 Promising Biomedical Applications of Self-assembled Filaments

Over the past few decades, self-assembled filamentous nanostructures, including polymeric FM, peptide nanofibers, and viral protein filaments, have evolved as promising platforms for biomedical applications^{50, 107}, from drug delivery and tissue engineering to molecular imaging (**Figure 1-4**). Here we will provide an overview of what has been achieved with filamentous nanostructures in these emerging biomedical applications. For applications where there are fewer examples of FM, peptide nanofibers and viral protein filaments are highlighted to showcase the promise of polymeric FM systems in these fields.

1.2.6.1 Cancer Nanomedicine. The increased circulation time and increased avidity of self-assembled filaments has been shown to enhance the delivery of chemotherapeutics, as the filaments can achieve both high passive and active accumulation in the tumor.^{32, 50} For example,

FM loaded with an anti-cancer drug, paclitaxel, significantly reduced tumor size compared to free drug in nude mice bearing human tumor xenografts.⁵⁶ Also, a prodrug strategy utilizing PDMAEMA-*b*-PMAEBA nanorods and nanowires to efficiently deliver DOX has been developed.¹⁰⁸ DOX was conjugated to PDMAEMA-*b*-PMAEBA nanorods with an acid-labile imine linkage. The nanorods were able to rapidly release DOX in the acidic endolysosomes of HeLa cells and showed enhanced cytotoxicity as compared to chemically identical vesicles and longer nanowires. Similarly, PEG-PVX viral filaments conjugated with DOX increased the circulation time of DOX *in vivo*, were able to penetrate tumors efficiently, and significantly inhibited tumor growth as compared to free DOX in athymic mice bearing human MDA-MB-231 breast cancer tumors.⁶ Interestingly, the aspect ratio of filaments is important in determining the efficacy of passive vs. active targeting to the tumor. Low aspect ratio tobacco mosaic virus filaments showed greater tumor penetration *in vivo* as they could diffuse through the endothelium, and achieved greater passive targeting.⁵ On the other hand, RGD-labeled viral filaments with a medium aspect ratio achieved greater active targeting, due to the increase in receptor-ligand interactions.⁵ Active targeting of FM has also been explored with folate conjugation of FM, as the folate receptor is overexpressed in multiple carcinoma types.¹⁰⁹ Display of folic acid on betulin-loaded FM was used to achieve targeted drug delivery to folate-receptor positive HeLa cells *in vitro*.¹⁰⁹ Further *in vivo* studies are needed to evaluate the utility of folate-conjugated FM for active tumor targeting and anti-cancer drug delivery.

1.2.6.2 Aerosolized Delivery Systems. Drug delivery into the lung vasculature via inhalation of aerosolized drugs is intriguing due to rapid absorption into the bloodstream and avoidance of first pass metabolism.¹¹⁰ There is much to be learned for the rational design of FM for aerosolized,

intrapulmonary delivery by studying how filamentous viruses survive transmission via respiratory droplets and cross multiple biologic barriers to achieve infection, a concept that is discussed elsewhere.¹¹¹ One interesting, non-biomedical application of aerosolized FM was shown by Mahmud *et al.*, who demonstrated the spray-stability and efficacy of herbicide-loaded PEO-*b*-PCL FM at minimizing pest infestations on plants.¹¹² After spraying, the FM were found to shorten from an initial persistence length of 12 μm to 3-8 μm , but were able to retain encapsulated payloads and minimize plant pest activity. While this study demonstrated the feasibility of drug-loaded FM for withstanding the shear stresses faced during aerosolization, further studies are needed to characterize their drug delivery capability as aerosols for biomedical applications.

1.2.6.3 Contrast Agent Delivery for Imaging. In terms of molecular imaging, filamentous structures have primarily been explored for magnetic resonance imaging (MRI) contrast enhancement through the incorporation of gadolinium-based contrast agents for T1 enhancement or iron oxide (IO) nanoparticles for T2 enhancement. Esser *et al.* formulated Gadolinium (Gd)-DOTA-labeled MC, vesicles, and FM, and found that FM had highest Gd incorporation per polymer and higher r_1 relaxivity (a measure of the efficacy of MRI contrast enhancement).¹¹³ Both results were attributed to the length and larger volume of the FMs. For T2 contrast enhancement, studies have utilized IO nanoparticles stabilized via dextran to form IO nanoworms.¹¹⁴⁻¹¹⁶ These metallic nanoworms have displayed similar properties as FM, such as increased circulation time¹¹⁴ which can be further prolonged via crosslinking of the dextran stabilizer,¹¹⁵ and enhanced targeting peptide display.^{114, 116} Notably, Ahmadi *et al.*, used IO nanoworms functionalized with a synthetic peptide towards somatostatin receptors to achieve efficient *in vivo* targeting and MRI imaging of pancreatic tumors.¹¹⁶ While these studies support the use of filamentous nanocarriers for diagnostic

applications through contrast agent incorporation, their utility for imaging modalities other than MRI needs to be investigated.

1.2.6.4 Vaccines. While synthetic polymeric FMs have not yet been employed extensively for vaccines, the success of peptide nanofibers and viral filaments suggest this may be a fruitful area for further FM development. Filamentous nanostructures have been engineered to induce cellular and humoral immune responses, which are critical for the development of effective vaccines. For example, Chesson *et al.*, developed peptide nanofibers consisting of peptides with *Mycobacterium tuberculosis* (Mtb)-specific CD4⁺ and CD8⁺ T cell epitopes.¹¹⁷ Co-assembly of these peptide nanofibers with a Toll-like receptor agonist, Pam2cys, allowed greater expansion (8-fold) of multifunctional-CD8⁺ T cells in the lungs of immunized mice. Furthermore, these nanofibers when injected as a booster dose in Bacillus Calmette–Guérin vaccine (BCG)-primed mice showed enhanced protection against aerosol Mtb challenge as compared to only BCG vaccinated mice. Analogously, Si *et al.*, engineered peptide nanofibers for an influenza vaccine using influenza acid polymerase (PA) CD8⁺ epitope peptide and β -sheet forming Q11 peptides.¹¹⁸ Intranasal administration of PAQ11 nanofibers in mice stimulated greater antigen-specific CD8⁺ T cell responses in lung draining lymph nodes than subcutaneously immunized mice. Despite the absence of CD4⁺ epitopes or an adjuvant, PAQ11 nanofibers were able to elicit tissue-resident memory cells in the lungs, which expanded rapidly in response to influenza infection. In another study, the vaccine performance of icosahedral cowpea mosaic virus (CPMV) and filamentous potato virus X (PVX) was compared.²⁹ The CPMV and PVX nanoparticles conjugated to human epidermal growth factor receptor 2 (HER2) epitope peptides were able to induce antigen-specific cellular and antibody responses. However, icosahedral CPMV particles outperformed the filamentous PVX

particles, which is attributed to lower uptake of high aspect ratio PVX particles by dendritic cells and B cells.

1.2.6.5 Hydrogels. Following crosslinking via a variety of methods and chemistries, self-assembled filaments can serve as the basis for hydrogels that mimic natural ECM, which is notably composed primarily of collagen filaments.¹¹⁹ Such filamentous scaffolds are advantageous for their high surface area for cellular and molecular interactions as well as for their controllable porosity.^{120, 121} Furthermore, these structures are advantageous because many of the attractive qualities of filaments such as high drug and antigen loading efficiency, multivalent functionality, and tunable composition can be incorporated into the hydrogel.

Hydrogels for drug delivery. This approach was demonstrated through the use of PEG-*b*-PPS FM cross-linked via vinyl sulfone-thiol linkages into a hydrogel, or ‘FM-depot’.^{77, 82} The oxidation-sensitive PPS component of the block copolymer triggers a “cylinder-to-sphere” transition of FM into MC under physiological conditions. This capability presents a novel form of hydrogel degradation via the release of monodisperse nanoscale MC, in contrast to standard bulk or surface degradation of hydrogels that respectively result in the release of large nonuniform fragments or small molecule metabolites. Depending on the extent of cross-linking, these gels can be designed to release MC from hours to several weeks.⁷⁷ When paired with surface-conjugated ligands, these particles can be designed for targeted cellular uptake followed by release of drug payloads via PPS-mediated endosomal escape.^{77, 122} Additionally, this hydrogel system can be injected *in situ* for easy administration and improved localized delivery.⁸² Incorporating these elements into FM-depots allows for the release of highly tailored MC for optimal cell targeting *in vivo*.⁸² Yi *et al.*

demonstrated the first application of this delivery system to test the regulatory effects of Vitamin D3 payloads designed to inhibit NF- κ B mediated inflammation in atherosclerotic mice.⁸² In this work, the advantages of the sustained release of drug-loaded MC versus bulk delivery of MC is demonstrated by significant increases in regulatory T cell populations. This highlights the use of this system to greatly improve sustained drug payload delivery to specific cell populations, with the potential for sustained modulation of immune cell function in chronic disease.

Authimoolam *et al.* synthesized FM hydrogels composed of PEG-*b*-PLA.¹²³ Layers containing a mix of biotinylated FMs and drug-loaded MC are alternated and crosslinked with layers of streptavidin-conjugated poly(acrylic acid). This results in a mucin-like hydrogel network containing a releasable MC drug payload. Capping the mucin-like hydrogel with a biotin-poly(acrylic acid)-streptavidin matrix allowed for modulation of MC release rates and protection of the hydrogel. The use of a capping layer also allows for incorporation into delivery systems as a patch, which possesses advantages for regenerative medicine applications and localized delivery.

Hydrogels for tissue engineering. FM hydrogels are also beginning to be explored for the application of tissue engineering, as they have the advantages of controlled chemical composition and purity without contamination from biological components. Canton *et al.*, demonstrated that a thermoresponsive poly(glycerol monomethacrylate)-poly(2-hydroxypropyl methacrylate) FM hydrogel maintained the viability and pluripotency of human pluripotent stem cells and human embryos for over a week.¹²⁴ The hydrogel was designed to mimic natural mucins, as it is rich in hydroxyl groups and had a similar elasticity. This demonstrates the non-toxicity and potential of

FM hydrogels for cell encapsulation, opening the door for the engineering of other FM hydrogel systems.

While FM hydrogels have not been studied as extensively for tissue engineering, self-assembled PA hydrogels demonstrate the potential for FM in this area. These PA systems incorporate functional peptide sequences into the gel structure allowing for improved biocompatibility and cell signaling¹²⁵, the ability to bind biomolecules before or after injection¹²⁶, and fine-tuned degradation and disassembly.¹²⁷ The synthesis process allows for control over the peptide sequence, allowing modulation of various biochemical and physical properties and incorporation of unnatural and modified peptides.¹²⁸ PA hydrogels can be tailored for different regenerative applications such as osteogenesis,^{129, 130} neuronal differentiation,^{131, 132} and supporting other specialized cell growth.^{126, 133-135} Additionally, the fibers of these gels can be aligned in an organized fashion, contributing to their impact on cell growth and differentiation as scaffold materials.¹³² An example application of PA hydrogels is their use for bone regeneration. Lee *et al.* utilized PA hydrogels to deliver bone morphogenic protein-2 (BMP-2) in a regenerative model of spinal arthrodesis. They reduced the amount of BMP-2 necessary for regenerative effects by 10-fold. They also observed improved bone fusion in PA gels without BMP-2, demonstrating the bioactive benefits of these gels. Both properties are attractive in the design of future biomaterials for regenerative applications.

PA hydrogels have also shown to be unique and potent scaffold materials for cell types that are historically difficult to work with. Edelbrock *et al.*, investigated the use of brain-derived neurotrophic factor (BDNF) mimetic peptide bearing PA hydrogels.¹³⁶ BDNF protein has had

limited success as a biologic due to poor pharmacological properties.¹³⁷ To circumvent this issue, a receptor targeting peptide sequence was incorporated into the PAs. This approach was beneficial as there was no need to develop a conjugation scheme which might affect the binding properties of BDNF, and the supramolecular structure was more easily controlled. The hydrogel produced an effective BDNF-like signal via the TrkB receptor found on neuronal cells, leading to enhanced maturation while promoting cell infiltration into the hydrogel.¹³⁶

1.2.7 Summary

A century after Staudinger coined “polymerization,” polymer science has allowed us to better understand, rationally design, and engineer novel nanostructures. Self-assembled filaments, inspired by filamentous viruses and protein filaments found in nature, can be engineered from different building blocks, including amphiphilic block copolymers, peptides and peptide amphiphiles, and viral proteins. Compared to filaments self-assembled from biological building blocks of peptide amphiphiles and viral proteins, synthetic polymeric filaments self-assembled from block copolymers, or FM, have the advantage of less expensive GMP manufacturing due to the relative ease of removing biological impurities, and enhanced stability in different conditions. Methods of FM self-assembly vary and are optimized based on the BCP. Different chemistries have been developed to form filaments that range in width, length and flexibility, mirroring the variety of physiological filaments. Because of their unique morphology, self-assembled filaments have demonstrated benefits including altered biodistribution and increased circulation times, enhanced avidity with versatile surface functionalization, high drug loading capacities, and the ability to form hydrogels. Looking toward the future, self-assembled filaments have great potential

to further our knowledge on the effects of nanostructure morphology on biological behavior, along with advancing many biomedical fields, including drug delivery, immunotherapies, vaccine development, regenerative medicine, and diagnostic imaging.

1.3 Scope of This Work

Filamentous nanocarriers have various advantages for nanomedicine, including increased circulation time and “cylinder-to-sphere” morphological transitions for sustained drug delivery. However, current nanocarriers utilized as drug delivery vehicles have largely had a spherical morphology, due to challenges in the scalable formation and characterization of filamentous nanocarriers. PEG-*b*-PPS filamentous nanocarriers have great potential for drug delivery applications, particularly in immunomodulation and sustained drug delivery. In order to translate PEG-*b*-PPS filamentous nanocarriers into the clinic, certain questions need to be explored. Can PEG-*b*-PPS filamentous nanocarriers be formed more reproducibly in a scalable fashion? Can the flexibility and stability of PEG-*b*-PPS filamentous nanocarriers be controlled? How does the flexibility of PEG-*b*-PPS filamentous nanocarriers affect their interactions with immune cells and biodistribution in vivo in healthy and diseased mice models? I aimed to answer these questions in the research covered in this dissertation to advance filamentous nanocarriers further toward clinical translation.

CHAPTER 2

2. Development and Characterization of Scalable Pi-stacking Filamentous Nanocarriers

2.1 Abstract

Self-assembling filomicelles (FM) are of great interest to nanomedicine due to their structural flexibility, extensive systemic circulation time, and amenability to unique “cylinder-to-sphere” morphological transitions. However, current fabrication techniques for FM self-assembly are highly variable and difficult to scale. Here, I demonstrate that tetrablock copolymers composed of poly(ethylene glycol)-*b*-poly(propylene sulfide) (PEG-*b*-PPS) diblocks linked by a pi-stacking perylene bisimide (PBI) moiety permit rapid, scalable, and facile assembly of FM via the flash nanoprecipitation (FNP) technique. Co-assembling the tetrablocks and PEG-*b*-PPS diblocks at different molar ratios resulted in mixed PBI-containing FM (mPBI-FM) with tunable length and flexibility. While PEG-*b*-PPS diblocks form FM within a narrow range of hydrophilic weight fractions, incorporation of pi-stacking PBI groups expanded this range to increase favorability of FM assembly. Furthermore, the aggregation-dependent fluorescence of PBI shifted during oxidation-induced “cylinder-to-sphere” transitions of mPBI-FM into micelles, resulting in a distinct emission wavelength for filamentous versus spherical nanostructures. Thus, incorporation of pi-stacking allows for rapid, scalable assembly of FM with tunable flexibility and stability.

2.2. Introduction

2.2.1. Challenges in Self-Assembly of FM

Despite numerous advantages for nanomedicine, therapeutic application of FM has been limited by challenges in their scalable and reproducible fabrication. FM fabrication requires both the synthesis of specific copolymer block lengths and optimization of self-assembly conditions (solvent, mixing parameters, extrusion, etc.), with mixtures of nanostructures instead of uniform FM often being the result.^{32, 37, 50} The morphology of self-assembled nanostructures depends on the weight fraction of the hydrophilic block, and this variable has been adjusted to self-assemble PEG-*b*-PPS copolymers into diverse nanostructures, including micelles (MC), polymersomes (PS), and bicontinuous nanospheres (BCN), with FM formation typically being restricted to a narrow range of hydrophilic weight fractions.^[1, 9, 12, 15a, 15b, 15c, 15d] Two established procedures for FM self-assembly are co-solvent evaporation^{49, 56, 109} and thin film hydration (TFH),^{77, 81} each of which presents distinct challenges for reproducible self-assembly and can result in significant batch-to-batch structural variability,^{26, 48, 57-59} polydisperse formulations and difficulties for reproducible scale-up.^{56, 58, 138}

In co-solvent evaporation, the block copolymer is dissolved in an organic solvent and added to an aqueous solvent. The mixture is then slowly stirred for 2 days in order for the organic solvent to evaporate.⁴⁹ This method is challenging for reproducible self-assembly of FM as the parameters of organic solvent addition speed, stirring speed, and evaporation speed have to be optimized for different block copolymers. FM co-solvent evaporation methods vary and require either slow addition of the organic solvent,²⁶ controlled gentle stirring to avoid FM fragmentation,⁵⁷ or slow evaporation of the organic solvent to minimize FM degradation.⁴⁸ In thin film hydration, the block copolymers are dissolved in an organic solvent such as chloroform or dichloromethane.^{39, 81} After removal of the organic solvent through evaporation, a thin film of

polymer is formed on a glass vessel that is then hydrated with an aqueous solvent with agitation of the vessel. Reproducible self-assembly with thin film hydration is difficult because parameters such as the thickness of the thin film, the hydrophobicity and composition of the block copolymers, and the speed of agitation have to be optimized.^{58, 59, 139} Thin film hydration also often leads to polydisperse formulations, where extrusion is then required to obtain monodisperse nanocarrier populations.^{56, 58} Both of these established self-assembly fabrication methods can take days and are challenging to scale up reproducibly.¹³⁸

To this end, flash nanoprecipitation (FNP) has emerged as a scalable fabrication technique for the reproducible and rapid assembly of diverse soft nanostructures from amphiphilic block copolymers.^{37, 140, 141} FNP employs confined impingement jet mixers to impinge an aqueous solution with a water-miscible organic solvent containing the amphiphilic block copolymers and any hydrophobic payloads into an aqueous reservoir (**Figure 2-1a**).^{142, 143} Supersaturation under these turbulent mixing conditions leads to precipitation of the hydrophobic payloads and coprecipitation of the block copolymer to form nanoscale assemblies.¹⁴⁰ Although typically limited to the assembly of solid core nanoparticles, FNP has been recently demonstrated to form a wide range of nanostructure morphologies, including PS, BCN, lamellar colloids, Janus colloids and nanorods.^{37, 144-147} To the best of our knowledge, PEG-*b*-PPS remains the first and only block copolymer to predominantly form FM via FNP; however, PEG-*b*-PPS only forms FM when the PEG hydrophilic weight fraction (f_{PEG}) is 0.21, so the synthesis of FM polymer remains challenging as there is less room for error in the chain lengths of the blocks.³⁷

2.2.2. Modulation of FM Flexibility

In addition to a need for improved methods of scalable FM formation, enhanced modulation of FM flexibility and contour lengths is necessary. The length and flexibility of FM are key properties that influence their performance *in vivo*. FM longer than 1 μm in length have achieved circulation times that are 3 times longer than spherical particles.⁵⁶ Nanocarrier flexibility also impacts cellular internalization, as stiffer particles have generally demonstrated increased uptake into immune cells.¹⁴⁸ Having FM with different flexibilities allows for the mimicry of different physiological filaments such as actin cytoskeletons, and the formation of filamentous hydrogels possessing varying elasticities and internal structure biomimetic of the extracellular matrix.^{81, 148}

2.2.3. Super-resolution Imaging of Filaments

Fluorescence microscopy has been used to image FM that are tens of microns in length.^{38, 56, 89} However, PEG-*b*-PPS FM, which are generally 1 μm in length or less, are difficult to visualize by standard fluorescence microscopy techniques, such as confocal or wide-field microscopy. These methods generally have an optical resolution of about half the wavelength of emitted light, or around 250 nm at best.¹⁴⁹ Super-resolution microscopy (SRM) techniques can bypass this diffraction limit and can increase the resolution closer to nanometer scales.¹⁵⁰ In addition, SRM has the advantages of enabling imaging under biologically relevant conditions and sample preservation.¹⁵⁰ While SRM has been utilized to image biological structures such as influenza virus filaments and actin filaments,^{151, 152} the imaging of flexible FM with SRM techniques remains to be explored.

Structured illumination microscopy (SIM) is a variant of SRM with an around 100 nm spatial resolution.¹⁵³ In SIM, an interference pattern is generated by a diffraction grating and utilized to shift the sample's spatial frequency spectrum collected by wide-field illumination. The final image is then generated through mathematical reconstruction.^{150, 153} While SIM provides lower resolution than other SRM techniques, SIM is faster, has higher signal-to-noise ratios, and enables gentler imaging, making it ideal for live cell imaging or imaging under physiologically relevant conditions.^{153, 154}

2.2.4. Pi-stacking Perylene Bisimide in Self-assembled Nanocarriers

Utilizing the intermolecular noncovalent interactions of pi-electronic molecules is an effective strategy for promoting self-assembly of various nanoscale morphologies.¹⁵⁵ PBI conjugated to melamine units self-organized into ribbonlike nanofibers in alkanes via pi-stacking interactions.¹⁵⁶ Amphiphilic PBI block copolymers was shown to self-assemble into MC, vesicles, or short rod aggregates (<50 nm in length) depending on the shape of the polymer.¹⁵⁷

I hypothesized that incorporation of a PBI pi-stacking linker into a self-assembling copolymer will enhance the reproducibility of FM fabrication under the turbulent mixing conditions of FNP over a range of hydrophilic weight fractions, stabilize FM morphological properties and allow control over FM flexibility. The Scott Lab previously engineered PEG-*b*-PPS-PBI-PPS-*b*-PEG (PBI tetrablock copolymers) that co-assembled with PEG-*b*-PPS (f_{PEG} of 0.24) to form vesicular PS via TFH.^[25] PBI exhibits a shift in fluorescence emission from a range of 600-800 nm when in aggregated form due to excimer formation, to a band at 500-600 nm when free in solution.¹⁵⁷ Additionally, PEG-*b*-PPS nanocarriers are oxidation sensitive due to the

presence of the hydrophobic PPS block, which allows for controlled morphological transitions and disassembly of nanocarriers upon photo-oxidation or physiological oxidation from cellular reactive oxygen species.^{39, 158-160} Thus, these PS containing PBI tetrablock copolymers (mPBI-PS) exhibit bioresponsive fluorescence, with a fluorescence shift from 640 nm emission when intact to 550 nm emission when disassembled upon oxidation in endolysosomes inside cells, demonstrating their applicability as an immunotheranostic tool for studying intracellular delivery.¹⁵⁸

In this chapter, I aimed to improve the scalability and reproducibility of nanofabrication of FM. I hypothesized that the co-assembly of PBI tetrablock copolymers with PEG-*b*-PPS diblock copolymers would enable the rapid, scalable formation of mixed pi-stacking PBI-containing FM (mPBI-FM) instead of polymersomes over a range of hydrophilic weight fractions (**Figure 2-1**). I reasoned that pi-stacking by PBI would enhance FM stability and improve control over the formation of FM with a range of flexibilities. I further hypothesized that the introduction of PBI would allow for the tracking of “cylinder-to-sphere” morphological transitions of FM to micelles by monitoring shifts in fluorescence emission caused by PBI disaggregation (**Figure 2-1D**).

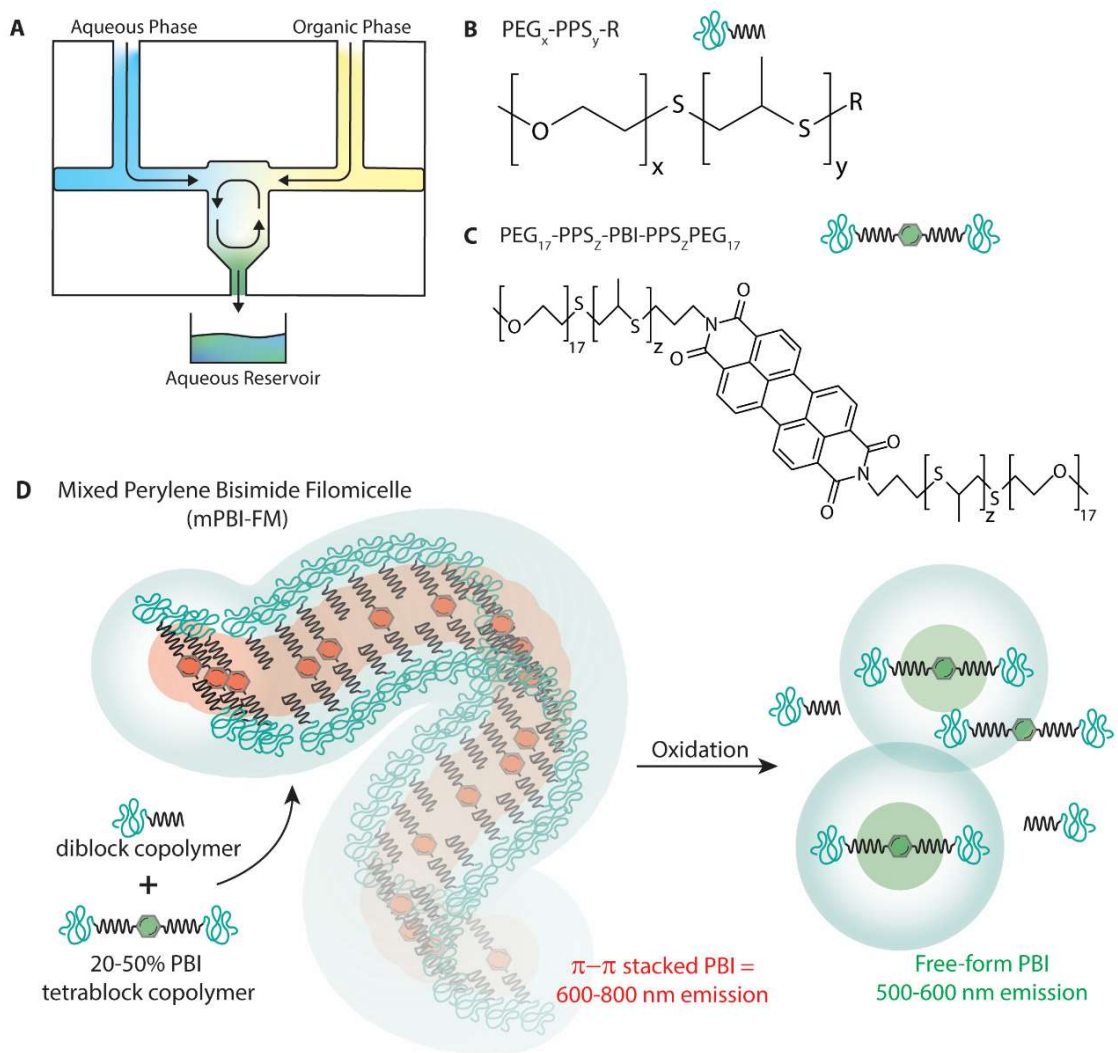


Figure 2-1. Scalable self-assembly of mixed perylene bisimide filomicelles (mPBI-FM) using flash nanoprecipitation (FNP). a) Schematic of the FNP method. The block copolymer is dissolved in the organic phase and impinged against the aqueous phase (water or saline) in a confined impingement jet mixer into an aqueous reservoir, resulting in the final FM structure. b) Chemical structure of polyethylene glycol-*b*-polypropylene sulfide (PEG-*b*-PPS) diblock copolymer where R is a phthalimide or a benzyl group and x in PEG_x is the chain length of either

17 or 45 units. c) Chemical structure of PBI tetrablock copolymer. d) Schematic of mPBI-FM co-assembled from diblock and tetrablock copolymers at different ratios and their inducible transition into micelles upon oxidation. When assembled as cylindrical FM, π - π interactions between PBI result in a fluorescence emission from 600-800 nm, which shifts to a band from 500-600 nm after an oxidation-mediated morphological transition into MC.

2.3. Materials and Methods

2.3.1. Materials

The following reagents were obtained commercially from Sigma-Aldrich: poly (ethylene glycol) methyl ether MW 2000 (product 202509), poly (ethylene glycol) methyl ether MW 750 (product 202495), methanesulfonyl chloride (product 471259), triethylamine (product T0886), potassium carbonate (product 791776), thioacetic acid (product T30805), 0.5 M sodium methoxide solution (product 403067), benzyl bromide (product B17905), benzyl mercaptan (product B25401), (N-(3-bromopropyl)phthalimide (product B80003), dichloromethane (product 320269), tetrahydrofuran (product 437638), anhydrous dimethylformamide (product 227056), ethanol (product 459844), methanol (product 179337), diethyl ether (product 346136), anhydrous hydrazine (product 215155), hydrochloric acid (product 320331), pyridine (product 270970), perylene-3,4,9,10-tetracarboxylic dianhydride (PTCDA) (product P11255), isothiocyanate polymer bound resin (product 538604), deuterated chloroform (product 151823), 10X Phosphate-buffered saline (product D1408), Sephadex LH-20 (product LH20100) and 0.2 μ m nylon syringe filters (product WHA67891302). Fetal bovine serum (product A3160601) was ordered from Thermo Fisher Scientific. DiR (product D12731) was ordered from Fisher Scientific. Propylene

sulfide was ordered from TCI Chemicals (product P0321). 1 mL Luer slip syringes (product 4010.200V0) were ordered from Air-Tite. Electron microscopy grids (product FCF400-Cu-50 for TEM and product LC200-U for CryoTEM) were ordered from Electron Microscopy Sciences.

2.3.2. Synthesis of Block Copolymers

PEG-*b*-PPS diblock copolymers were synthesized as previously described.^[12, 45] Briefly, for PEG₄₅-*b*-PPS, linear mPEG (MW=2000) was functionalized with the mesylate leaving group. Benzyl mercaptan, after activation by the base sodium methoxide, initiated the ring-opening polymerization reaction with propylene sulfide. The reaction was then endcapped with PEG₄₅-mesylate. For PEG₁₇-*b*-PPS, linear mPEG (MW =750) was functionalized to form PEG-mesylate, which was reacted with thioacetic acid to form PEG-thioacetate (PEG-TAA). PEG-TAA, upon activation with the base sodium methoxide, initiates a ring-opening polymerization reaction with propylene sulfide. The reaction is then endcapped with either benzyl bromide or *N*-(3-bromopropyl) phthalimide.

PEG-*b*-PPS-PBI-PPS-*b*-PEG was synthesized as previously described.^[25] Briefly, PEG₁₇-*b*-PPS endcapped with *N*-(3-bromopropyl)phthalimide was heated with hydrazine in 95% ethanol under reflux for over 6 h at 90°C. Hydrochloric acid was then added, and the reaction continued for at least 2 more h. The phthalhydrazide salt was removed via filtration and the filtrate was concentrated and precipitated in diethyl ether at -20°C overnight. The resulting PEG₁₇-*b*-PPS-NH₂ was dissolved in pyridine and reacted with perylene-3,4,9,10-tetracarboxylic dianhydride (PTCDA) while stirring in a 35 mL high pressure vessel in an oil bath at 150°C for over 72 h. Afterwards, the vessel was removed from heat and isothiocyanate polymer bound resin was added and the

reaction was stirred overnight to remove any unreacted amines. The resin was removed through filtration with filter paper and washed with tetrahydrofuran (THF). The filtrate was then centrifuged to spin down unreacted PBI and the pyridine was removed from the resulting supernatant by rotary evaporation. The product was resuspended in THF, filtered through a 200 nm nylon syringe filter, and then precipitated in cold diethyl ether at -20°C overnight. After desiccation, the product was dialyzed in first in methanol, then in 1% hydrochloric acid, and lastly in water and lyophilized.

2.3.3. Characterization of Block Copolymers

The structure of the block copolymers was characterized with ^1H NMR on a Bruker Avance III HD system with a TXO Prodigy probe.

PEG₁₇-*b*-PPS₃₃-PBI-PPS₃₃-*b*-PEG₁₇: ^1H NMR (500 MHz, CDCl₃, δ): 8.74-8.56 (d, 4H, CH_{aromatic}, PBI), 3.70-3.60 (m, 68H, CH₂-CH₂, PEG backbone), 3.57-3.52 (m, 2H, CH₂), 3.40-3.36 (s, 3H; OCH₃, PEG), 3.05-2.81 (m, 66H, CH₂, PPS), 2.71-2.51 (m, 33H, CH, PPS), 2.15-2.03 (m, 2H, CH₂), 1.42-1.28 (m, 99H, CH₃, PPS);

PEG₁₇-*b*-PPS₁₉-PBI-PPS₁₉-*b*-PEG₁₇: ^1H NMR (500 MHz, CDCl₃, δ): 8.71-8.57 (d, 4H, CH_{aromatic}, PBI), 3.64-3.54 (m, 68H, CH₂-CH₂, PEG backbone), 3.50-3.48 (m, 2H, CH₂), 3.33-3.30 (s, 3H; OCH₃, PEG), 2.93-2.77 (m, 38H, CH₂, PPS), 2.64-2.50 (m, 19H, CH, PPS), 2.23-2.19 (m, 2H, CH₂), 1.34-1.25 (m, 57H, CH₃, PPS);

PEG₁₇-*b*-PPS₃₂-PBI-PPS₃₂-*b*-PEG₁₇: ^1H NMR (500 MHz, CDCl₃, δ): 8.76-7.99 (d, 4H, CH_{aromatic}, PBI), 3.71-3.59 (m, 68H, CH₂-CH₂, PEG backbone), 3.57-3.53 (m, 2H, CH₂), 3.41-3.37 (s, 3H;

OCH₃, PEG), 3.02-2.81 (m, 64H, CH₂, PPS), 2.78-2.51 (m, 32H, CH, PPS), 2.12-2.03 (m, 2H, CH₂), 1.43-1.28 (m, 96H, CH₃, PPS);

PEG₁₇PPS₄₁ benzyl: ¹H-NMR (500 MHz, CDCl₃, δ): 7.38–7.31 (d, 4H, ArH), 3.73–3.60 (s, 68H, PEG backbone), 3.42-3.39 (s, 3H, O–CH₃), 3.01–2.73 (m, 82H, CH₂, PPS), 2.71–2.54 (m, 41H, CH), 1.47–1.31 (d, 123H, CH₃).

PEG₁₇PPS₁₉ phthalimide: ¹H-NMR (500 MHz, CDCl₃, δ): 7.92-7.81 (m, 2H, ArH), 7.77–7.67 (m, 2H, ArH), 3.68–3.61 (s, 68H, PEG backbone), 3.57-3.53 (m, 2H, CH₂), 3.39-3.37 (s, 3H, O–CH₃), 2.99–2.81 (m, 38H, CH₂, PPS), 2.68–2.56 (m, 19H, CH, PPS), 2.02-1.93 (m, 2H, CH₂), 1.44–1.31 (d, 57H, CH₃, PPS).

PEG₁₇PPS₃₄ phthalimide: ¹H-NMR (500 MHz, CDCl₃, δ): 7.88-7.82 (m, 2H, ArH), 7.75–7.69 (m, 2H, ArH), 3.67z–3.61 (s, 68H, PEG backbone), 3.57-3.53 (m, 2H, CH₂), 3.39-3.37 (s, 3H, O–CH₃), 2.98–2.84 (m, 68H, CH₂, PPS), 2.69–2.54 (m, 34H, CH, PPS), 2.02-1.94 (m, 2H, CH₂), 1.44–1.31 (d, 102H, CH₃, PPS).

PEG₄₅PPS₄₉ benzyl: ¹H-NMR (500 MHz, CDCl₃, δ): 7.31–7.29 (d, 4H, ArH), 3.63–3.62 (s, 180H, PEG backbone), 3.37-3.35 (s, 3H, O–CH₃), 2.93–2.82 (m, 98H, CH₂), 2.65–2.56 (m, 49H, CH), 1.38–1.33 (d, 147H, CH₃).

PEG₄₅PPS₄₇ benzyl: ¹H-NMR (500 MHz, CDCl₃, δ): 7.31–7.29 (d, 4H, ArH), 3.63–3.61 (s, 180H, PEG backbone), 3.37-3.34 (s, 3H, O–CH₃), 2.92–2.81 (m, 94H, CH₂), 2.65–2.56 (m, 47H, CH), 1.39–1.32 (d, 141H, CH₃).

PEG₄₅PPS₄₅ benzyl: ¹H-NMR (500 MHz, CDCl₃, δ): 7.34–7.31 (d, 4H, ArH), 3.68–3.60 (s, 180H, PEG backbone), 3.39–3.36 (s, 3H, O–CH₃), 2.98–2.79 (m, 90H, CH₂, PPS), 2.69–2.54 (m, 45H, CH, PPS), 1.43–1.29 (d, 135H, CH₃, PPS).

PEG₄₅PPS₄₄ benzyl: ¹H-NMR (500 MHz, CDCl₃, δ): 7.36–7.33 (d, 4H, ArH), 3.68–3.65 (s, 180H, PEG backbone), 3.42–3.38 (s, 3H, O–CH₃), 2.99–2.85 (m, 88H, CH₂, PPS), 2.70–2.59 (m, 44H, CH, PPS), 1.44–1.36 (d, 132H, CH₃, PPS).

The purity was assessed by gel permeation chromatography (GPC). Waters Styragel THF columns were used with a THF mobile phase running at a flow rate of 0.6 mL min⁻¹ with refractive index and UV/vis detectors (ThermoFisher Scientific).

2.3.4. Nanocarrier Fabrication via Thin Film Hydration

The desired block copolymers for that formulation were added to a 2 mL clear glass vial (ThermoFisher Scientific) and dissolved in around 2 mL of dichloromethane. After desiccation overnight, a thin film of polymer formed around the edges of the vial. Milli-Q water or 1x Phosphate-buffered saline (PBS) was added for a final polymer concentration of 10 mg mL⁻¹ and the films were hydrated by gentle agitation overnight with a Stuart SB3 rotator. The hydrated solution was then filtered through a 200 nm nylon filter to remove any residual free PBI aggregates.

2.3.5. Nanocarrier Fabrication via Flash Nanoprecipitation

Nanocarrier self-assembly via flash nanoprecipitation was performed as previously described using a confined impingement jets (CIJ) mixer.^[14a, 21b] Briefly, the desired block copolymers (total mass of 10 mg) were dissolved in 0.5 mL of the organic solvent THF and placed in a 1 mL plastic Luer Slip syringe. 0.5 mL of the aqueous solvent (Milli-Q water or 1x PBS) was

placed in another 1 mL syringe. The two syringes were then secured in the mixer and the aqueous and organic solutions were impinged against each other at approximately 1 mL s^{-1} , leading to turbulent mixing of the two solutions. The resulting supersaturated solution flowed out of the CIJ mixer into a 1 mL reservoir of the same aqueous solvent in a 20 mL glass scintillation vial. The sample was desiccated for 4 h to remove the THF and then filtered through a 200 nm nylon filter to remove any residual free PBI aggregates.

2.3.6. Small Angle X-ray Scattering

Small angle X-ray scattering (SAXS) experiments were performed at the DuPont-Northwestern-Dow Collaborative Access Team (DND-CAT) beamline at Argonne National Laboratory's Advanced Photon Source (Argonne, IL, USA) with 10 keV (wavelength $\lambda = 1.24 \text{ \AA}$) collimated X-rays. Silver behenate, a diffraction standard was utilized for q-range calibration. All the samples were measured in the q-range 0.001 to 0.5 \AA^{-1} . For oxidation studies, mPBI-FM (2.5 mg mL^{-1} final concentration) were incubated in $5 \text{ M H}_2\text{O}_2$ and measurements were taken at 0 min, 45 min, and 90 minutes. The data reduction was performed in PRIMUS 2.8.2 software, which includes subtraction of background solvent buffer scattering from the sample scattering. FM and oxidized FM were confirmed after fitting with the flexible cylinder and polymer micelle model fits, respectively, using SasView. PS samples were confirmed after fitting with the core-shell-sphere model or vesicle model fits.

2.3.7. Transmission Electron Microscopy

After 400 mesh formvar/carbon coated copper grids were glow-discharged, 3 μL of the sample ($5\text{--}10 \text{ mg mL}^{-1}$ concentration) were applied to the grid. The grid was then gently blotted, washed 2x for 5 seconds each in Milli-Q water, submerged in 1.5% uranyl formate stain for 15-20 seconds,

and then blotted and allowed to air-dry. Images were collected with a Jeol 1400 120 kV transmission electron microscope at a range of 5000-30,000 x nominal magnification. Micrographs were acquired using a Gatan 4k x 4k Ultrascan CCD camera and Gatan Digital Micrograph software.

2.3.8. Cryogenic Transmission Electron Microscopy

200 mesh Lacey carbon grids were glow-discharged for 30 seconds in a PELCO easiGlow Glow Discharge Cleaning System at 15mA with a chamber pressure of 0.24 mBar. 4 uL of the desired sample was applied to the grid. The grid was then plunge-frozen into liquid ethane in a FEI Vitrobot Mark III cryo-plunge freezing device for 5 seconds with a blot offset of 0.5 mm to capture the sample in vitreous ice. Grids were then loaded into a Gatan 626.5 cryo-transfer holder and imaged at -172°C in a JEOL JEM-1230 LaB6 emission transmission electron microscope operating at 100kV at a range of 2,500-10,000 x nominal magnification. Data was collected on a Gatan Orius 2k x 2k camera with Digital Micrograph software (Gatan). Image J was used for any further image processing including the addition of scale bars.

2.3.9. Scanning Transmission Electron Microscopy (STEM)

After 400 mesh formvar/carbon coated copper grids were glow-discharged, 3-5 uL of the nanocarrier sample (8 mg mL^{-1} concentration) were applied to the grid. After 2-3 minutes, the grid was gently blotted. Another 3 uL of nanocarriers were applied to the grid for 3 minutes, then the grid was blotted again and left to air dry. Images were collected with a JEOL 7900FLV Field Emission Gun 30 kV scanning electron microscope at a range of 10,000-33,000 x nominal magnification. Low kV STEM images were taken with the Lower Electron Detector.

2.3.10. Structured Illumination Microscopy (SIM)

PEG₄₅-*b*-PPS₄₇ was loaded with 0.0625% w/w of the hydrophobic dye DiI and formed via TFH. PEG₄₄-*b*-OES₇ was loaded with 0.0625% w/w DiI and formed FM via FNP. The formulations were filtered with a LH20 column to remove free DiI. The 10% polyacrylamide gel was formed from a monomer mixture consisting of 3.75 mL of 40% electrophoresis grade acrylamide, 0.5 mL of 10% tetramethylethylenediamine (TEMED), 3mL of 5xPBS, and 7.75 mL distilled water, that was then mixed with 2% ammonium persulfate. The ratio of monomer mixture to 2% ammonium persulfate was 10:1. The FM were encapsulated at a final concentration of 0.175 mg mL⁻¹ and 0.35 mg mL⁻¹ in MatTek 35 mm glass bottom dishes and imaged with a Nikon Structured Illumination Super-Resolution Microscope with up to 115 nm resolution.

2.3.11. Dynamic Light Scattering (DLS)

mPBI-FM (0.5 mg polymer mL⁻¹) were incubated in 5 M H₂O₂ in PBS and DLS measurements were taken with a Zetasizer Nano (Malvern Instruments) with a 4mW He-Ne 633 laser at 0 h, 0.5 h, 2 h, and 48 h. The number average size and polydispersity index were calculated. After 2 h the mPBI-FM were spin concentrated using an Amicon Ultra-4 Centrifugal Filter unit (Millipore Sigma) with a 10 kDa molecular weight cutoff to remove H₂O₂ and was saved for characterization by TEM.

2.3.12. Zeta-potential Measurement

mPBI-FM were diluted in 0.1x PBS to a final concentration of 0.1 mg mL⁻¹ and zeta-potential measurements were taken with a Zetasizer Nano (Malvern Instruments). For each sample, 3 separate measurements were taken.

2.3.13. Kaiser Test

2 drops of potassium cyanide, ninhydrin, and phenol solutions¹⁶¹ were added to 100 μL of mPBI-FM or mPBI-PS nanocarriers (0.5mg mL^{-1}). After heating at 110°C for 5 minutes, the color of the samples were compared with the negative control (H_2O) and the positive controls of 0.5 mg mL^{-1} and 5 mg mL^{-1} bovine serum albumin (BSA). After the solution cooled to room temperature, the absorbance spectra were measured from 300 nm to 800 nm on the SpectraMax M3 (Molecular Devices).

2.3.14. UV-Vis Spectroscopy

Fluorescence measurements were taken in a quartz cuvette with a Shimadzu RF-6000 Spectrofluorometer. For serum stability studies, mPBI-FM (0.5mg mL^{-1}) were incubated in 50% fetal bovine serum (FBS) for 24 h with shaking at 1000 rpm at 37°C . The emission spectra from 500 nm to 800 nm before and after oxidation were measured at an excitation wavelength of 485 nm. For oxidation kinetic studies, mPBI-FM ($0.5\text{ mg polymer mL}^{-1}$) was incubated in $20\ \mu\text{M H}_2\text{O}_2$ and the emission at 550 nm and 640 nm (excitation at 485 nm) was measured every 15 minutes for 12 h.

2.4. Results and Discussion

2.4.1. Synthesis and Formation of PEG-*b*-PPS FM

I first endeavored to synthesize PEG-*b*-PPS diblock copolymer that can form FM as described by Karabin *et al.*³⁹ I synthesized diblock copolymer with a range of f_{PEG} , made nanocarrier formulations via TFH and FNP, and characterized the morphology using TEM, cryoTEM, and/or SAXS. A subset of these formulations self-assembled via TFH and FNP is

shown in **Table 2-1** and **Table 2-2**, respectively. PEG-*b*-PPS FM were thus difficult to synthesize and form reproducibly as I found that block copolymers in a very narrow range of f_{PEG} ($f_{\text{PEG}}=0.36$) formed FM via TFH with PBS. None of the PEG-*b*-PPS diblock copolymers with f_{PEG} ranging from 0.35-0.39 formed FM with FNP and instead predominantly formed spherical structures (MC and/or PS).

Table 2-1. Morphology of PEG-*b*-PPS formulations self-assembled via TFH in PBS spanning a range of hydrophilic weight fractions (f_{PEG}). The morphology was characterized by TEM, cryoTEM and/or SAXS. MC= micelles, PS=polymersomes, FM= filomicelles.

Diblock copolymer	f_{PEG}	Morphology
PEG ₄₅ PPS ₄₉ benzyl	0.34	MC
PEG ₄₅ PPS ₄₈ benzyl	0.35	MC
PEG ₄₅ PPS ₄₇ benzyl	0.35	MC
PEG ₄₅ PPS ₄₅ benzyl	0.36	FM
PEG ₄₅ PPS ₄₆ benzyl	0.36	MC
PEG ₄₅ PPS ₄₄ benzyl	0.37	PS
PEG ₄₅ PPS ₄₁ benzyl	0.38	PS
PEG ₄₅ PPS ₄₂ benzyl	0.38	MC
PEG ₄₅ PPS ₄₀ benzyl	0.39	MC
PEG ₄₅ PPS ₃₉ benzyl	0.39	MC

Table 2-2. Morphology of PEG-*b*-PPS formulations self-assembled via FNP spanning a range of hydrophilic weight fractions (f_{PEG}). The morphology was characterized by TEM, cryoTEM and/or SAXS. MC= micelles, PS=polymersomes.

Diblock copolymer	Aqueous Solvent	f_{PEG}	Morphology
PEG ₄₅ PPS ₄₇ benzyl	H ₂ O	0.35	MC
PEG ₄₅ PPS ₄₅ benzyl	PBS	0.36	MC or PS
PEG ₄₅ PPS ₄₄ benzyl	H ₂ O	0.37	MC or PS
PEG ₄₅ PPS ₄₂ benzyl	H ₂ O	0.38	MC
PEG ₄₅ PPS ₃₉ benzyl	PBS	0.39	MC

2.4.2. Synthesis and Characterization of Diblock and Tetrablock Copolymers

To assess whether the incorporation of pi-stacking moieties with PEG-*b*-PPS diblock copolymers can enhance the reproducibility of FM formation, I synthesized PBI tetrablock copolymers with different PPS chain lengths and thus different f_{PEG} to characterize mPBI-FM self-assembly.^[25] Briefly, PEG-*b*-PPS diblock copolymer (Figure 2-1b) was synthesized via ring-opening polymerization of propylene sulfide and end-capped with *N*-(3-bromopropyl) phthalimide. The phthaloyl group was replaced with an amine group through hydrazinolysis, resulting in PEG-*b*-PPS-NH₂. Perylene-3,4,9,10-tetracarboxylic dianhydride (PTCDA) was then used to bridge two PEG-*b*-PPS-NH₂ block copolymers to form a PBI tetrablock copolymer (Figure 2-1c).

The incorporation of PBI into the tetrablock copolymers was verified by NMR, by assessing the presence of aromatic proton peaks of PBI at 8.6 ppm (**Figures 2-2 and 2-3**, and by gel permeation chromatography (GPC) via an increase in the molecular weight distribution compared to PEG-*b*-PPS diblock copolymers (**Figure 2-4**). A higher molecular weight secondary peak was observed during GPC analysis of the PEG-*b*-PPS diblock copolymer (Figure 2-4). This is most likely due to PEG-*b*-PPS dimerization during synthesis to form a tetrablock copolymer.^[28] The chromatogram of the PBI tetrablock copolymer had a secondary peak of a lower molecular

weight, most likely from unreacted diblock copolymer. These minor diblock and tetrablock side products are of the same size as the tetrablocks and diblocks used to fabricate the nanocarriers and thus do not impact the final assembled morphology.

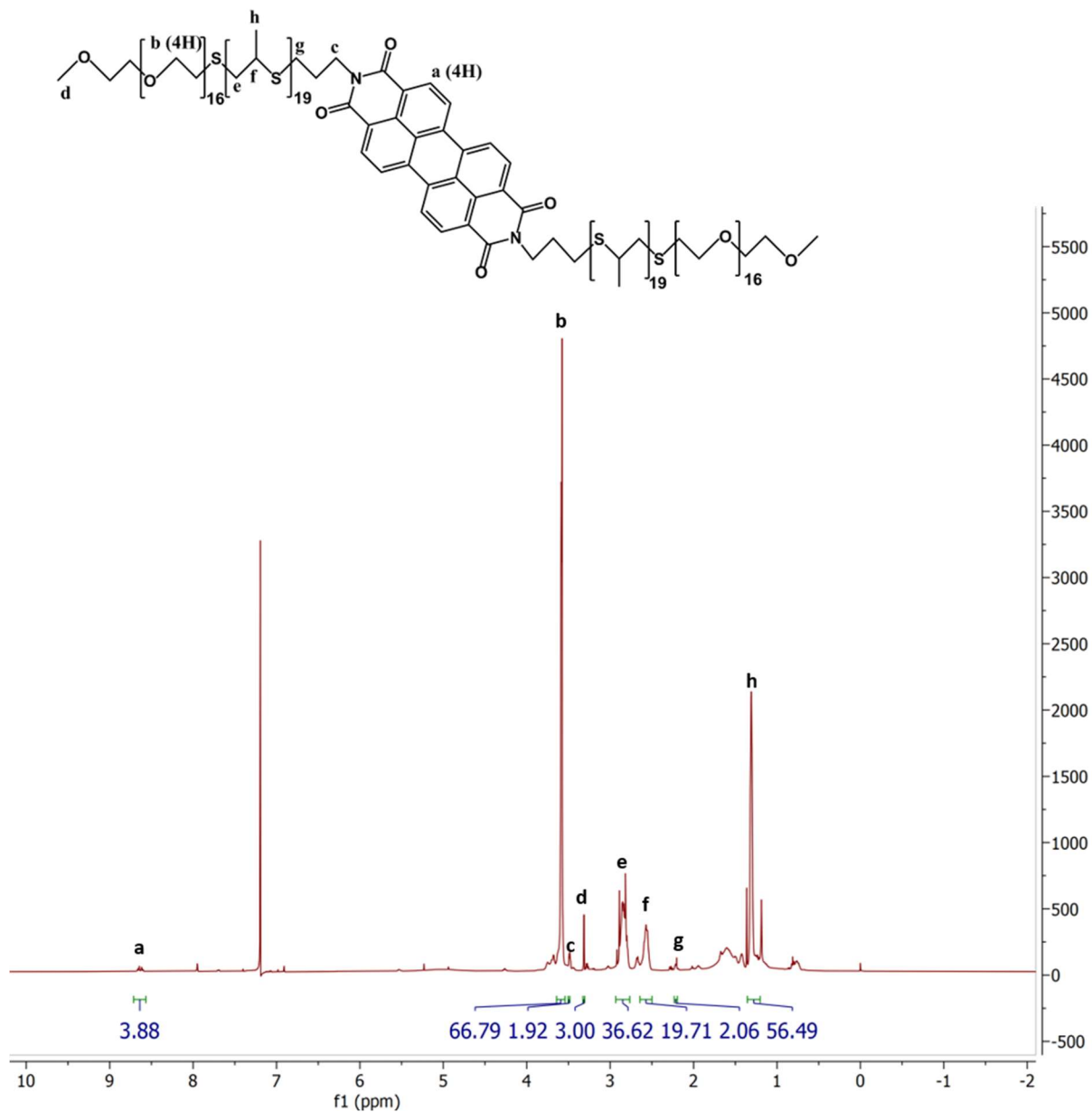


Figure 2-2. NMR of PEG₁₇PPS₁₉PBIPPS₁₉PEG₁₇ tetrablock copolymer.

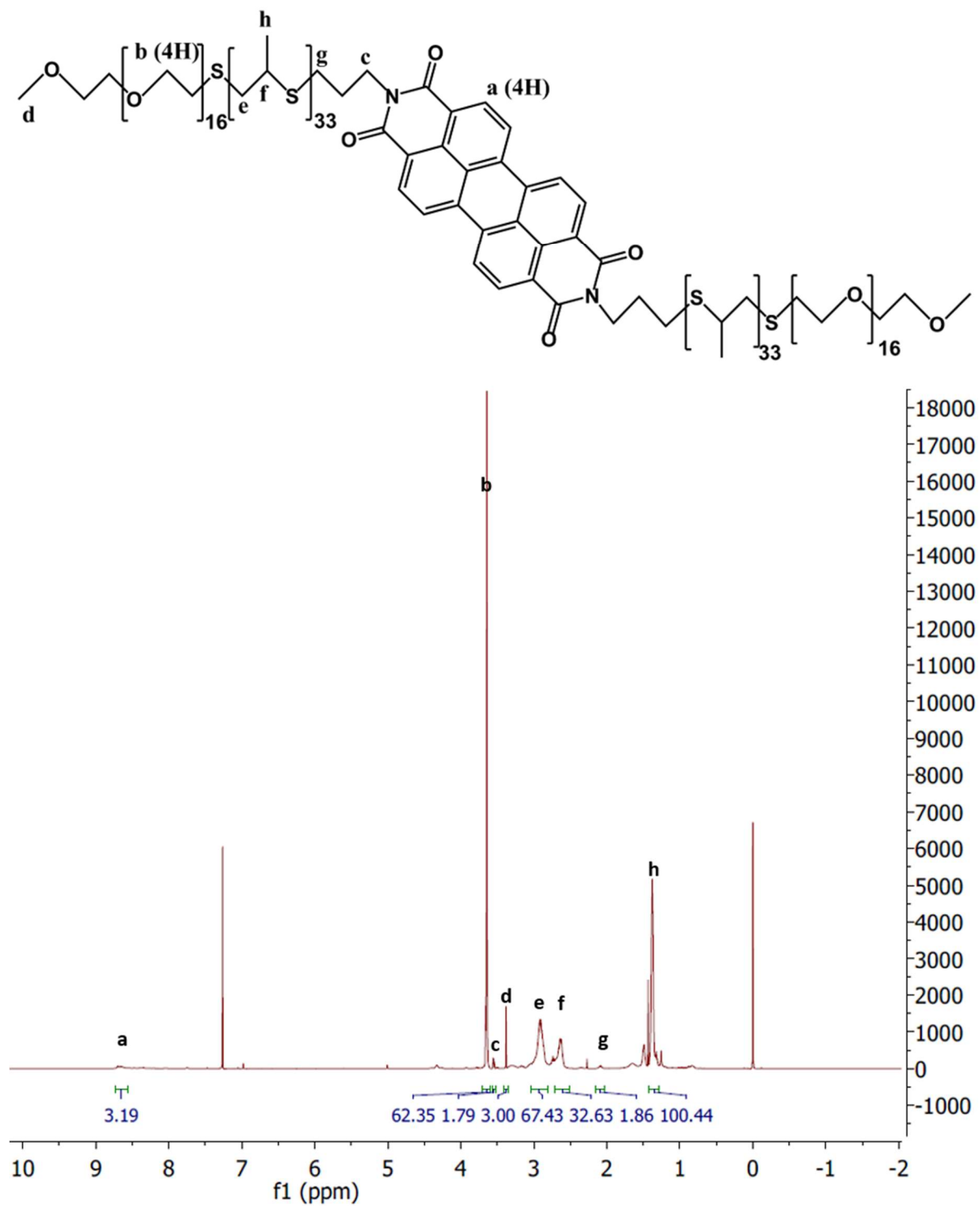


Figure 2-3. NMR of PEG₁₇PPS₃₃PBIPPS₃₃PEG₁₇ tetrablock copolymer.

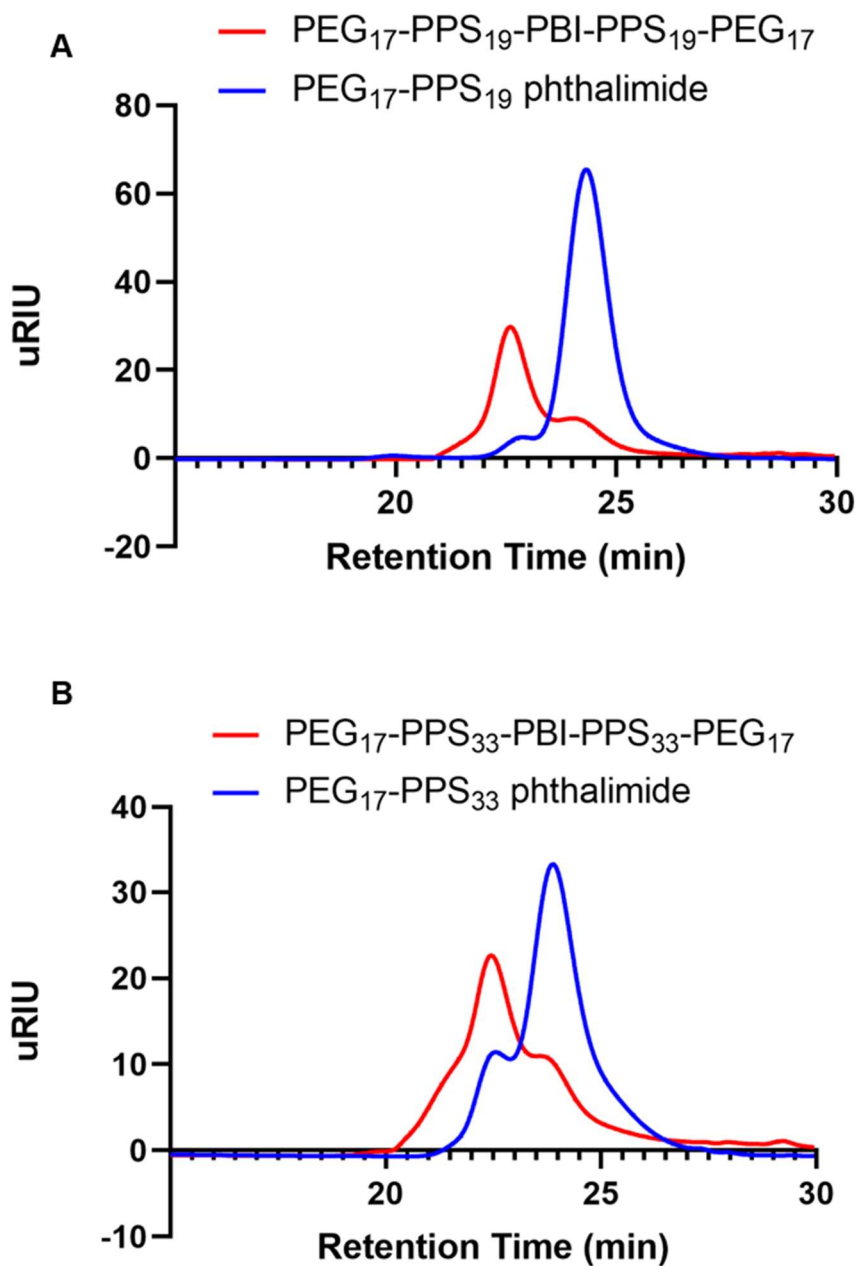


Figure 2-4. Gel permeation chromatography molecular weight distributions of PBI tetrablock copolymer. A) PEG₁₇PPS₁₉PBIPPS₁₉PEG₁₇ tetrablock copolymer and PEG₁₇PPS₃₃ phthalimide diblock copolymer B) PEG₁₇PPS₃₃PBIPPS₃₃PEG₁₇ tetrablock copolymer and PEG₁₇PPS₃₃ phthalimide diblock copolymer.

2.4.3 Characterization of Mixed PBI Polymersomes

The co-assembly of PBI tetrablock copolymers with PEG-*b*-PPS diblock copolymers into mixed PBI polymersomes (mPBI-PS) was first described by the Scott Laboratory by Du *et al.*, where PS were formed from a 1:1 molar ratio of PEG₁₇-PPS₂₈-PBI-PPS₂₈-PEG₁₇/PEG₁₇-*b*-PPS₂₈ ($f_{\text{PEG}} = 0.24$) via TFH.¹⁵⁸ I found that mPBI-PS are also formed in the f_{PEG} range of 0.2 to 0.22 via TFH (**Table 2-3**). I further demonstrated for the first time that mPBI-PS can be formed via FNP in the f_{PEG} range of 0.2 to 0.21 (**Table 2-4**). Various mPBI-PS formations were characterized by SAXS after fitting to the core-shell model (**Table 2-5**) and/or by dynamic light scattering (DLS) (**Table 2-6**). PS were formed that ranged from 11 nm to 59 nm in diameter, which is in a similar size range as the mPBI-PS described by Du *et al.*, which had a diameter of 60 nm with a polydispersity index (PDI) of 0.22 as measured by DLS.¹⁵⁸

Table 2-3. Morphology of formulations self-assembled via thin film hydration (TFH) with different combinations of PBI tetrablock copolymer and PEG-*b*-PPS diblock copolymer spanning a range of hydrophilic weight fractions (f_{PEG}). The morphology was characterized by TEM and/or SAXS. Polymersomes = PS, Filomicelles= FM.

PPS length of tetrablock polymer	Diblock copolymer	Molar fraction of tetrablock polymer	Solvent	Overall f_{PEG}	f_{PEG} of tetrablock copolymer	f_{PEG} of diblock copolymer	Morphology
33	PEG ₁₇ PPS ₄₁ benzyl	0.5	PBS	0.2	0.22	0.19	PS and FM
33	PEG ₁₇ PPS ₃₄ phthalimide	0.5	H ₂ O	0.21	0.22	0.21	FM

33	PEG ₁₇ PPS ₃₄ phthalimide	0.5	PBS	0.21	0.22	0.21	PS and FM
32	PEG ₁₇ PPS ₃₇ phthalimide	0.5	H ₂ O	0.21	0.22	0.2	PS
32	PEG ₁₇ PPS ₃₇ phthalimide	0.5	PBS	0.21	0.22	0.2	PS
32	PEG ₁₇ PPS ₃₄ phthalimide	0.33	H ₂ O	0.22	0.22	0.21	PS and FM
19	PEG ₁₇ PPS ₁₉ phthalimide	0.5	H ₂ O	0.31	0.31	0.31	PS
19	PEG ₁₇ PPS ₁₉ phthalimide	0.5	PBS	0.31	0.31	0.31	FM
19	PEG ₄₅ PPS ₄₉ benzyl ^a	0.27	H ₂ O	0.33	0.31	0.34	FM
19	PEG ₄₅ PPS ₄₇ benzyl	0.27	PBS	0.34	0.31	0.35	FM
19	PEG ₄₅ PPS ₄₄ benzyl ^a	0.28	H ₂ O	0.35	0.31	0.37	FM
19	PEG ₄₅ PPS ₄₅ benzyl	0.2	PBS	0.35	0.31	0.36	FM

a) diblock copolymer alone does not predominantly form FM with TFH.

Table 2-4. Morphology of formulations self-assembled via flash nanoprecipitation (FNP) with different combinations of PBI tetrablock copolymer and PEG-*b*-PPS diblock copolymer spanning a range of hydrophilic weight fractions (fPEG). The morphology was characterized with TEM, cryoTEM, and/or SAXS. Polymersomes = PS, Filomicelles= FM, Micelles=MC.

PPS length of tetrablock polymer	Diblock Polymer	Molar fraction of tetrablock polymer	Solvent	Overall fPEG	fPEG of tetrablock copolymer	fPEG of diblock copolymer	Morphology
33	PEG ₁₇ PPS ₄₁ benzyl	0.5	PBS ^a	0.2	0.22	0.19	PS
33	PEG ₁₇ PPS ₃₄ phthalimide	0.5	PBS ^a	0.21	0.22	0.21	PS
32	PEG ₁₇ PPS ₃₇ phthalimide	0.5	H ₂ O	0.21	0.22	0.2	FM
32	PEG ₁₇ PPS ₃₇ phthalimide	0.5	PBS	0.21	0.22	0.2	PS
32	PEG ₁₇ PPS ₃₄ phthalimide	0.5	H ₂ O	0.22	0.22	0.21	FM
19	PEG ₁₇ PPS ₁₉ phthalimide	0.5	H ₂ O	0.31	0.31	0.31	FM
19	PEG ₁₇ PPS ₁₉ phthalimide	0.5	PBS	0.31	0.31	0.31	FM
32	PEG ₄₅ PPS ₄₅ benzyl	0.2	H ₂ O	0.32	0.22	0.36	FM
19	PEG ₄₅ PPS ₄₅ benzyl	0.2	H ₂ O	0.35	0.31	0.36	FM
No tetrablock	PEG ₄₅ PPS ₄₅ benzyl	0	PBS	0.36	N/A	0.36	MC and PS

a) FNP was performed using 4 impingements. Otherwise, FNP was performed with a single impingement.

Table 2-5. Characterization of select mPBI-PS formulations by SAXS.

PS	Tetrablock copolymer	Diblock copolymer	Molar % of tetrablock copolymer	Final f_{PEG}	Core radius (nm)	Shell thickness (nm)	Diameter	Chi ²	Formation method
mPBI-PS type A	PEG ₁₇ PPS ₃₃ PBI PPS ₃₃ PEG ₁₇	PEG ₁₇ PPS ₃₄ phthalimide	50%	0.21	6.5	3.5	20	0.002 ^a	FNP in H ₂ O*
mPBI-PS type B	PEG ₁₇ PPS ₃₃ PBI PPS ₃₃ PEG ₁₇	PEG ₁₇ PPS ₄₁ benzyl	50%	0.20	18.5	5.1	47.2	0.006 ^a	FNP in H ₂ O*
mPBI-PS type C	PEG ₁₇ PPS ₃₃ PBI PPS ₃₃ PEG ₁₇	PEG ₁₇ PPS ₄₁ benzyl	50%	0.20	8.2	3.5	23.3	0.002 ^a	TFH in PBS
mPBI-PS type D	PEG ₁₇ PPS ₃₂ PBI PPS ₃₂ PEG ₁₇	PEG ₁₇ PPS ₃₇ phthalimide	50%	0.21	12.8	8.3	42.1	0.22 ^b	TFH in PBS

*FNP was performed with 4 impingements

a) Core-shell-sphere model fit

b) Vesicle model fit

Table 2-6. Characterization of select mPBI-PS formulations by DLS.

PS	Tetrablock copolymer	Diblock copolymer	Molar percent of tetrablock copolymer	Final f_{PEG}	Number average diameter \pm SD (nm)	PDI	Formation method
mPBI-PS type A	PEG ₁₇ PPS ₃₃ PBIPPS PPS ₃₃ PEG ₁₇	PEG ₁₇ PPS ₃₄ phthalimide	50%	0.21	11 \pm 3	0.07	FNP in H ₂ O*
mPBI-PS type B	PEG ₁₇ PPS ₃₃ PBIPPS PPS ₃₃ PEG ₁₇	PEG ₁₇ PPS ₄₁ benzyl	50%	0.20	59 \pm 33	0.32	FNP in H ₂ O*
mPBI-PS type C	PEG ₁₇ PPS ₃₃ PBIPPS PPS ₃₃ PEG ₁₇	PEG ₁₇ PPS ₄₁ benzyl	50%	0.20	30 \pm 10	0.11	TFH in PBS

mPBI-PS type D	PEG ₁₇ PPS ₃₂ PBIPPS 32PEG ₁₇	PEG ₁₇ PPS ₃₇ phthalimide	50%	0.21	49±16	0.11	TFH in PBS
mPBI-PS type E	PEG ₁₇ PPS ₃₃ PBIPPS 33PEG ₁₇	PEG ₁₇ PPS ₃₄ phthalimide	50%	0.21	46±21	0.21	TFH in PBS
(-)PBI- PS	N/A	PEG ₁₇ PPS ₄₁ benzyl	0%	0.19	239±115	0.23	FNP in PBS*

*FNP was performed with 4 impingements

2.4.4 PBI Enhances FM Formation via Thin Film Hydration

I first verified the self-assembly of PBI tetrablock copolymers into mPBI-FM using the established method of TFH.^[12] Consistent with our past studies, FM composed solely of PEG-*b*-PPS diblock copolymers ((-)PBI-FM) predominantly form FM by TFH when the hydrophilic weight fraction (f_{PEG}) is 0.35-0.38, and these assemblies are unstable when stored in solution as the FM transitioned to micelles after 1 month in PBS at 4° C (**Figure 2-5**).^[12] To assess the impact of PBI pi-stacking on FM stability, PEG-*b*-PPS diblock copolymers were synthesized and co-assembled with different 20-50 mol % of PBI tetrablock copolymer to make mixed PBI FM (mPBI-FM) (Figure 2-1d; **Table 2-3**). The overall f_{PEG} was calculated using a weighted average of the individual f_{PEG} of the tetrablock and diblock copolymer, and ranged from 0.2 to 0.35 for the mPBI-FM. The thin films were hydrated with phosphate-buffered saline (PBS) or water. The molar fraction of tetrablock copolymer used was less than 0.5 for all formulations in this study, since strong aggregation of PBI can result in significant decreases in fluorescence intensity and complete quenching of fluorescence.^[29] Previous work with mPBI-PS reported that formulations with 50 mol% PBI tetrablock copolymer have a maximum fluorescence emission intensity at a wavelength

of 640 nm, with the intensity decreasing with increasing mol % of PBI tetrablock copolymer.^[25] Furthermore, past studies with self-assemblies composed solely of amphiphilic PBI-linked copolymers only reported the formation of short rod aggregates instead of flexible filaments.^[26] Collectively, these past investigations demonstrate that co-assembling different ratios of diblock to tetrablock copolymers may yield a versatile nanocarrier assembly platform to generate modular FM, allowing for the fine-tuning of physicochemical properties of the nanocarrier and the potential to incorporate diverse functional groups or targeting ligands.^[12]

Here, different mPBI-FM formulations with overall f_{PEG} ranging from 0.21 to 0.35 self-assembled into FM using TFH (Table 2-3). Typically, FM self-assembly by TFH has been limited to amphiphilic block copolymers within a narrow range of f_{PEG} . For example, FM formed from poly(ethylene oxide)-*b*-poly(ϵ -caprolactone) (PEO-*b*-PCL) in water required a minimum f_{PEG} of 0.36 to form FM, as the PEO chains are unable to stabilize the assemblies when they are shorter, leading to polymer precipitation.^[1, 18b] Considering that PEG-*b*-PPS (-)PBI-FM formation by TFH requires polymers within a narrow f_{PEG} of 0.35-0.38,^[12] my results suggest that the incorporation of PBI facilitates FM assembly by broadening the f_{PEG} range that is acceptable for filament formation. I found that in a lower f_{PEG} range from 0.19-0.21, FM formation was promoted when water instead of PBS was the solvent, most likely due to increased steric stabilization of the hydrophilic block.^[14a] mPBI-PS were formed in this f_{PEG} range via the TFH method after rehydration with PBS, consistent with previous work by the Scott Lab with PBI-containing tetrablock copolymers.^[25] I also demonstrated that mPBI-FM formed with TFH are more stable in aqueous solution compared to (-)PBI-FM. Unlike (-)PBI-FM formed from PEG₄₅-*b*-PPS₄₄, mPBI-

FM nanostructures maintain a predominantly filamentous morphology after one month in water at 4° C, as observed by cryogenic transmission electron microscopy (cryoTEM) (**Figure 2-6**).

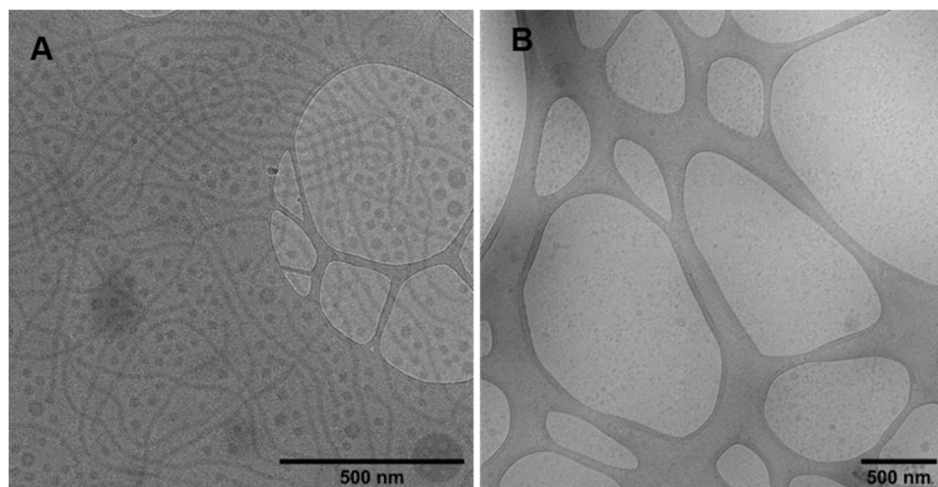


Figure 2-5. Morphological transition of PEG₄₅-*b*-PPS₄₄ (-)PBI-FM to micelles during storage at 4°C. A) CryoTEM image of (-)PBI-FM after formation by TFH in PBS. B) CryoTEM images of (-)PBI-FM after storage at 4°C for 1 month in PBS, showing predominantly micelles.

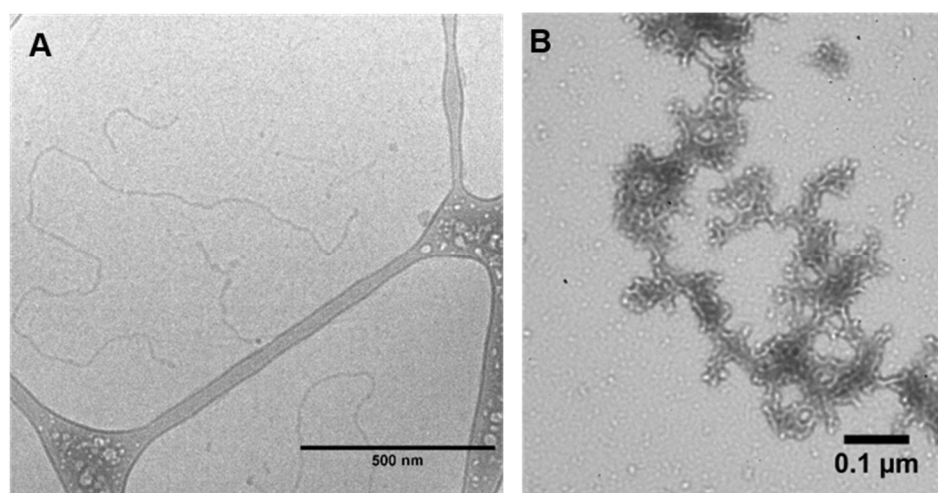


Figure 2-6. mPBI-FM maintain filamentous morphology after storage at 4°C for 1 month. A) CryoTEM images of mPBI-FM-E formed by thin film hydration (TFH) after storage at 4°C for 1

month in water, showing predominantly FM. B) CryoTEM images of mPBI-FM-C formed by FNP after storage at 4°C for 1 month in PBS, showing predominantly FM.

2.4.5 PBI Enhances FM formation via Flash Nanoprecipitation

Previously, nanostructure stability issues have prevented the use of FNP for the reliable fabrication of FM self-assembled from amphiphilic diblock copolymers, which has restricted their formation methods to more traditional, yet less scalable techniques such as TFH.^[9, 12, 13, 30] A formulation of PEG₁₇-*b*-PPS₃₈ diblock copolymer ($f_{\text{PEG}}=0.21$) with water as the aqueous solvent was the first block copolymer shown to predominantly form FM via FNP.^[14a] However, PEG-*b*-PPS diblock copolymers with f_{PEG} between 0.30 and 0.38 primarily formed micelles via FNP, most likely due to the turbulent mixing conditions requiring longer hydrophobic block chain lengths for stable FM formation.^[14a] Since the incorporation of pi-stacking PBI enhances FM stability, I hypothesized that PBI tetrablock copolymers would promote the self-assembly of FM under the turbulent mixing conditions of flash nanoprecipitation (FNP). I thus prepared formulations from different mixtures of diblock copolymer and PBI tetrablock copolymer (20-50 mol%) via FNP (**Table 2-4**). The resulting formulations were clear solutions having different shades of red depending on the f_{PEG} of the PBI tetrablock copolymer used (**Figure 2-7**). Using FNP, I found mPBI-FM self-assembled from polymers having an overall f_{PEG} of 0.22-0.35, which greatly expands the range of acceptable f_{PEG} that reliably form FM (Table 2-4). For example, PEG₄₅-*b*-PPS₄₅ ($f_{\text{PEG}}=0.36$) only forms FM via TFH and forms spherical nanostructures via FNP, as characterized by TEM (**Figure 2-8**). In contrast, when 20 mol% of PBI tetrablock copolymer is mixed with PEG₄₅-*b*-PPS₄₅, mPBI-FM successfully form via FNP (Figure 2-8). Interestingly, these mPBI-FM nanostructures also exhibit enhanced storage stability in solution, as observed by the

presence of filaments after over one month of storage in PBS at 4° C (Figure 2-6). mPBI-FM formed from FNP also maintained a filamentous structure after dehydration, with rigid rods ranging in length from 100 nm to 600 nm observed on scanning transmission electron microscopy (Figure 2-9). The inclusion of pi-stacking PBI tetrablock copolymer therefore permits the reproducible self-assembly of FM nanostructures via FNP, a scalable nanofabrication method, over a wide range of f_{PEG} ratios, and enhances the stability of the resulting suspensions in storage.

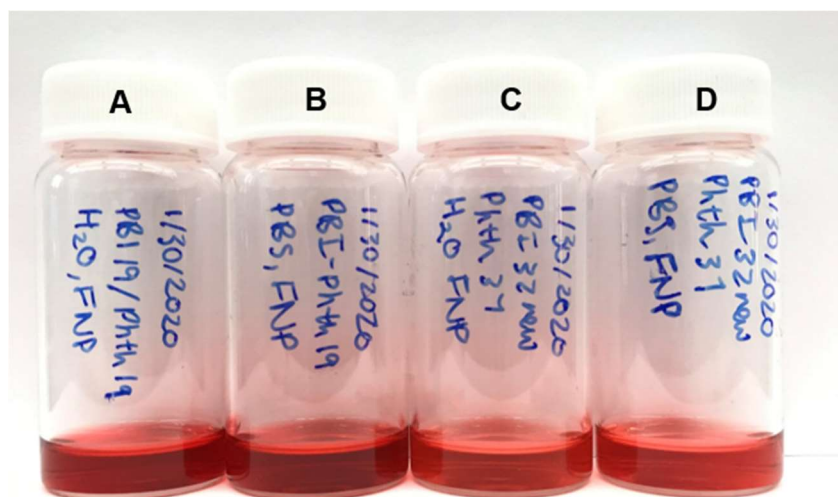


Figure 2-7. Representative image of mixed PBI formulations formed with FNP. A) 1:1 molar ratio of PBI tetrablock polymer with PPS length of 19 units and PEG₁₇-*b*-PPS₁₉ phthalimide formed in H₂O. B) 1:1 molar ratio of PBI tetrablock polymer with PPS length of 19 units and PEG₁₇-*b*-PPS₁₉ phthalimide formed in PBS. C) 1:1 molar ratio of PBI tetrablock polymer with PPS length of 32 units and PEG₁₇-*b*-PPS₃₇ phthalimide formed in H₂O. D) 1:1 molar ratio of PBI tetrablock polymer with PPS length of 32 units and PEG₁₇-*b*-PPS₃₇ phthalimide formed in PBS.

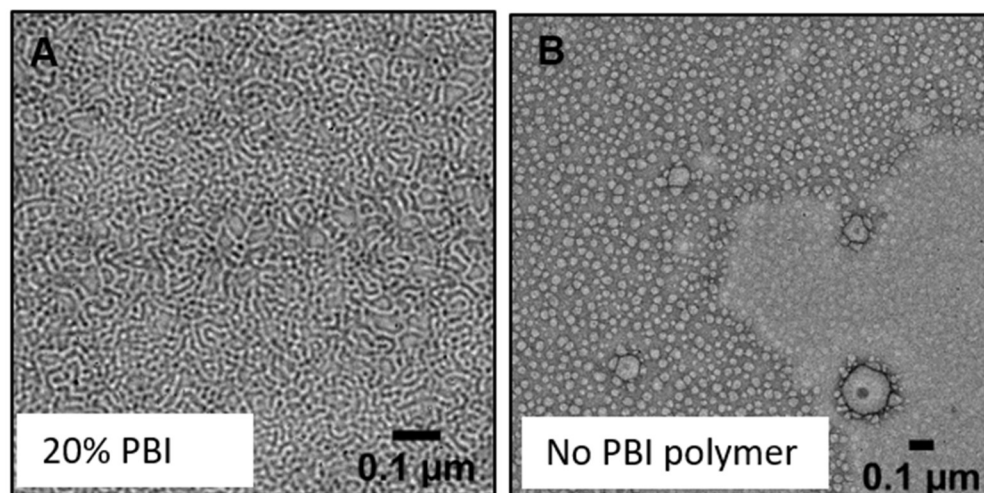


Figure 2-8. PBI tetrablock copolymer promotes formation of mPBI-FM via FNP. A) TEM image of mPBI-FM-C, consisting of PEG₄₅-*b*-PPS₄₅ benzyl mixed with PBI 19 tetrablock copolymer (20 mol percent, overall $f_{\text{PEG}}=0.35$) formed in H₂O. C) PEG₄₅-*b*-PPS₄₅ benzyl with no PBI polymer added forms spherical structures instead of FM in PBS, as seen on TEM.

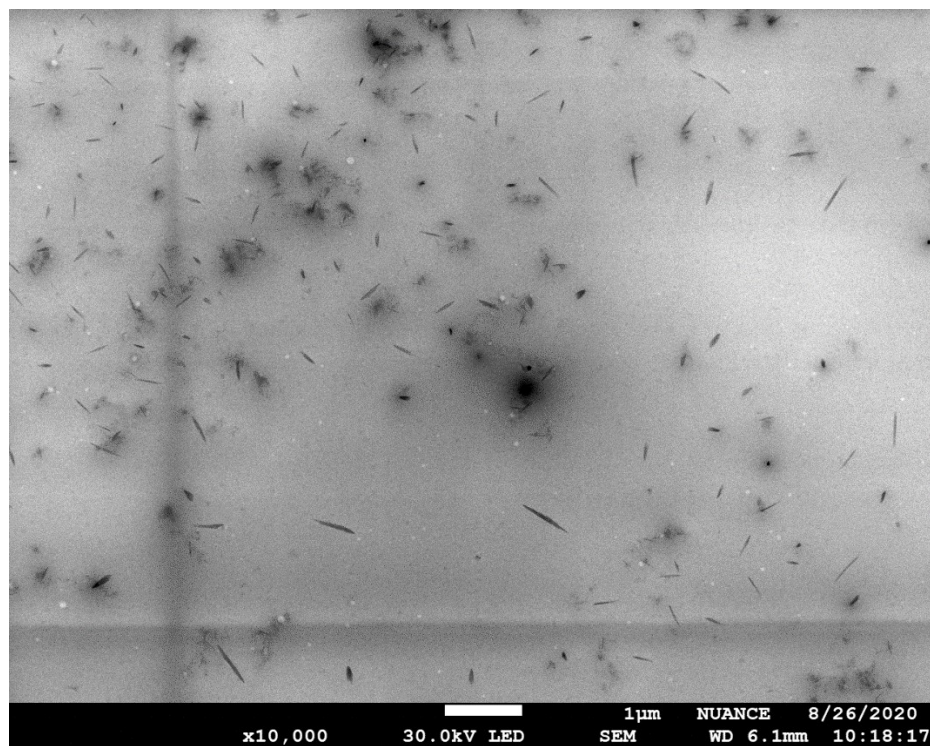


Figure 2-9. Scanning transmission electron microscopy image of mPBI-FM-A formed via FNP in water. mPBI-FM-A consists of 1:1 molar ratio of PBI tetrablock polymer with PPS length of 19 units and PEG₁₇-*b*-PPS₁₉ phthalimide.

Figure 2-10. Characterization of the filamentous morphology of mPBI-FM as compared to PEG-*b*-PPS (-)PBI-FM. a) Transmission electron microscopy (TEM) images of mPBI-FM formulations and (-)PBI-FM listed in Table 1. Formulations prepared by FNP have a blue border, whereas formulations formed by thin film hydration (TFH) have a black border. b) Small angle X-ray scattering (SAXS) and flexible cylinder model fits for the FM formulations listed in Table 2-7.

Table 2-7. Composition, formation method, and morphological parameters of key FM formulations in this study. Formulations were prepared using TFH or FNP with different mixtures of PBI tetrablock copolymer and PEG-*b*-PPS diblock copolymer spanning a range of hydrophilic weight fractions (f_{PEG}). The formulations are presented in order of increasing contour length to persistence length ratio (L_c/L_p), with a higher L_c/L_p corresponding to increasing flexibility. The morphological parameters were characterized by SAXS, with the parameter uncertainties from the flexible cylinder model fit included.

FM	Tetrablock copolymer	Diblock copolymer	Molar % of tetrablock copolymer	Final f_{PEG}	Contour Length L_c (nm)	Persistence Length L_p (nm)	L_c/L_p	Formation method
mPBI-FM type A	PEG ₁₇ PPS ₁₉ PBI PPS ₁₉ PEG ₁₇	PEG ₁₇ PPS ₁₉ phthalimide	50%	0.31	191.2 ± 15.2	58.0 ± 9.0	3.3	FNP
mPBI-FM type B	PEG ₁₇ PPS ₁₉ PBI PPS ₁₉ PEG ₁₇	PEG ₁₇ PPS ₁₉ phthalimide	50%	0.31	423.5 ± 144.9	123.3 ± 25.8	3.4	TFH
mPBI-FM type C	PEG ₁₇ PPS ₁₉ PBI PPS ₁₉ PEG ₁₇	PEG ₄₅ PPS ₄₅ benzyl	20%	0.35	337.5 ± 41.4	61.3 ± 14.1	5.5	FNP

mPBI-FM type D	PEG ₁₇ PPS ₁₉ PBI PPS ₁₉ PEG ₁₇	PEG ₄₅ PPS ₄₇ benzyl	20%	0.34	1012.4 ± 274.1	112.4 ± 23.1	9.0	TFH
mPBI-FM type E	PEG ₁₇ PPS ₃₃ PBI PPS ₃₃ PEG ₁₇	PEG ₁₇ PPS ₃₄ phthalimide	50%	0.21	936.3 ± 123.2	53.6 ± 18.6	18	TFH
(-)PBI-FM	N/A	PEG ₄₅ PPS ₄₅ benzyl	0%	0.36	1022.4 ± 168.5	46.8 ± 5.8	22	TFH*

*(-)PBI-FM only predominantly forms FM with TFH, but not with FNP.

2.4.6 PBI Enhances Control over FM Flexibility

Since pi-stacking PBI enhances the stability of FM, I next assessed whether the incorporation of PBI alters the flexibility of the cylindrical nanostructures. In addition to observing a filamentous morphology by TEM, I characterized 5 different mPBI-FM formulations and (-)PBI-FM with Small Angle X-Ray Scattering (SAXS) (**Figure 2-10**). A flexible cylinder model was fit to the scattering data to estimate FM parameters, including the contour length and the persistence length (**Table 2-7 and 2-8**). In the flexible cylinder model, the FM is modeled as a chain of stiff rods, each with a length L_p , or the persistence length.^[31] The contour length (L_c) is the estimated total length of the chain. As the persistence length decreases compared to the contour length, or as L_c/L_p increases, the chain becomes more flexible.^[32] I organized the FM formulations in order of increasing L_c/L_p , (Figure 2-10; Table 2-7). The (-)PBI-FM formulation was included for the purpose of comparison.

Table 2-8. mPBI-FM and (-)PBI-FM parameters with parameter uncertainties estimated from flexible cylinder model fits of SAXS scattering profiles in Figure 2-10B.

FM Parameters	mPBI-FM A	mPBI-FM B	mPBI-FM C	mPBI-FM D	mPBI-FM E	(-)PBI-FM
Contour Length, L_c (nm)	191.2 ± 15.2	423.5 ± 144.9	337.5 ± 41.4	1012.4 ± 274.1	936.3 ± 123.2	1022.4 ± 168.5
Kuhn length (nm)	115.9 ± 17.9	246.5 ± 51.5	122.5 ± 28.2	224.8 ± 46.2	107.1 ± 37.2	93.5 ± 11.5
Persistence length, L_p (nm)	58.0 ± 9.0	123.3 ± 25.8	61.3 ± 14.1	112.4 ± 23.1	53.6 ± 18.6	46.8 ± 5.8
L_c/L_p	3.3	3.4	5.5	9.0	18	22
Radius (nm)	5.1	8.6 ± 2.1	7.2 ± 1.4	13.8 ± 1.4	12.2 ± 7.7	11.2
Aspect ratio	19	25	23	37	38	46
Chi ²	0.02	0.03	0.009	0.04	0.01	0.13

As observed by the L_c/L_p ratios (Table 2-7), the (-)PBI-FM were most flexible whereas the incorporation of PBI decreased FM flexibility. Generally, increasing the molar percent of PBI tetrablock copolymer in the formulation decreased filament flexibility, most likely due to increased pi-stacking (Table 2-7). The formation method also affected FM flexibility. mPBI-FM formed with FNP were shorter and less flexible than mPBI-FM with the same polymer composition formed via TFH (Table 2-7). The nucleation and precipitation of the block copolymer that occurs in supersaturated conditions in FNP is known to provide control over particle size, and may have led to shorter FM.^[20a] Forming FM with shorter contour lengths previously required fragmentation of

longer FM after self-assembly with repeated extrusion through a membrane or sonication.^[6b, 18a]

Here, my results demonstrate the formation of shorter FM through self-assembly via FNP.

In addition, by incorporating different molar fractions of PBI tetrablock copolymer and varying the formation method and self-assembly parameters, I created a library of FM nanostructures that have identical surface chemistries but differ in their flexibility. This not only demonstrates the utility of PBI incorporation for controlling FM flexibility, but also provides a library for examining the relationship between nanocarrier flexibility and various performance metrics that are important for drug delivery. Furthermore, this library minimizes influences from crosslinking strategies reported elsewhere in the literature. Previous studies with PEO-*b*-PCL and PEO-*b*-PBD FM modulated FM flexibility by increasing the molecular weight of the polymer while keeping f_{PEG} constant or utilizing free-radical polymerization to crosslink the FM after formation, respectively.^[17, 18b, 33] My platform for modulating FM flexibility through the co-assembly of pi-stacking polymers does not require chemical crosslinking after formation or the synthesis of multiple diblock copolymers with a specific f_{PEG} , as FM flexibility can be modulated by incorporating different ratios of a pi-stacking tetrablock copolymer with a diblock copolymer.

2.4.7. Zeta-potentials of mPBI-FM

The zeta-potentials for the mPBI-FM were negative or near neutral (**Table 2-9**), similar to the zeta-potentials reported for previous PEG-*b*-PPS nanocarriers.^{94, 162}

Table 2-9. Zeta-potential of select mPBI-FM formulations. (n=3 different measurements)

mPBI-FM	Zeta potential (mV±SD)
mPBI-FM type A	0.1±0.4
mPBI-FM type B	-9.1±6.4
mPBI-FM type C	-6.3±0.7
mPBI-FM type D	-1.3±0.8
mPBI-FM type E	-9.4±0.5
(-)PBI-FM	-6.5±0.3

2.4.8 Verification of Removal of Amine-functionalized Diblock Copolymer

For the reaction to synthesize PBI tetrablock copolymer, two PEG₁₇-*b*-PPS-NH₂ diblock copolymers are bridged by PTCDA to form the tetrablock copolymer. As primary amines are cationic and can exhibit toxicity,¹⁶³ to verify the removal of amine-functionalized PEG-*b*-PPS from the mixed PBI formulations through the work-up procedure, the Kaiser test was performed on a representative mPBI-FM and mPBI-PS formulation. The Kaiser (ninhydrin) test is a sensitive test for primary amines utilized in solid phase peptide synthesis to determine whether amino acid coupling reactions are complete.¹⁶¹ Ninhydrin reacts with the primary amine group to form a blue color. mPBI-FM-E and mPBI-PS-A were found to have levels of amines comparable to the negative control of H₂O, and no blue color was detected (**Figure 2-11**). Samples with bovine serum albumin (BSA) served as a positive control. Absorbance spectra of the samples after the Kaiser test also verified there was no peak at 600 nm for mPBI-FM and mPBI-PS, compared to the BSA positive controls (**Figure 2-12**).

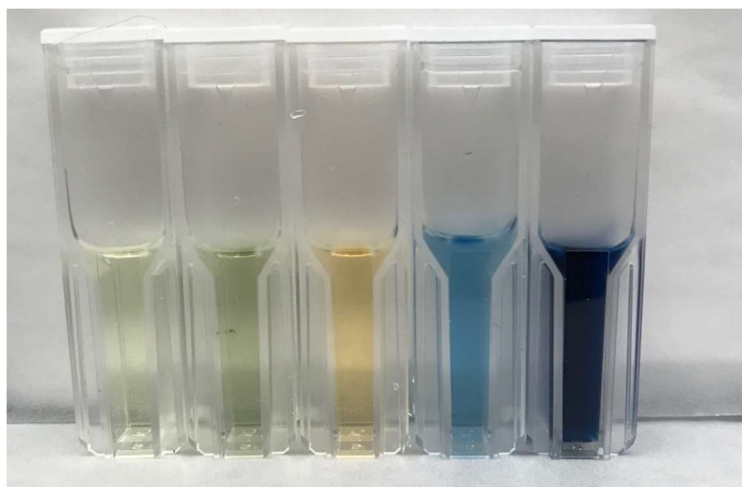


Figure 2-11. Image of mPBI-FM and mPBI-PS after Kaiser test. From left to right: H₂O (negative control), mPBI-FM-E, mPBI-PS-C, 0.5 mg/mL BSA, 5 mg/mL BSA. The BSA served as the positive control.

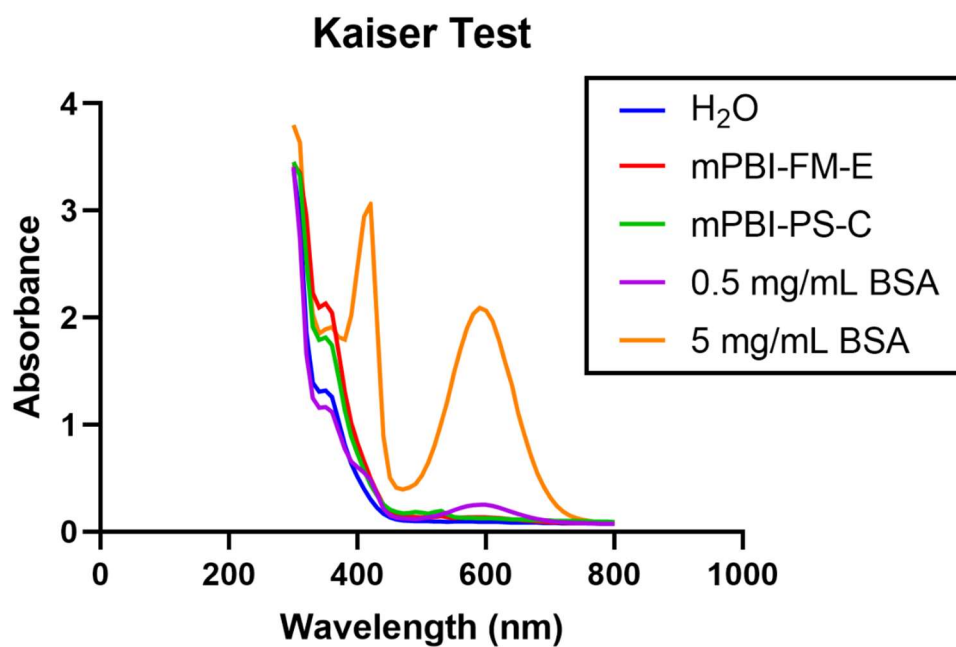


Figure 2-12. Absorbance spectra of mPBI-FM and mPBI-PS after Kaiser test. A 600 nm absorbance peak corresponds to the blue color observed when primary amines are present.

2.4.9. Super-resolution Imaging of FM

Standard techniques to characterize the morphology of PEG-*b*-PPS FM include cryoTEM, TEM, and SAXS. cryoTEM and SAXS allows verification of FM morphology in a frozen-hydrated state and in solution, respectively.³⁹ However, both of these techniques are time-intensive, require extensive training and/or specialized equipment, and are low throughput. I therefore explored whether super-resolution microscopy techniques can be used to assess the morphology of PEG-*b*-PPS FM.

(-)PBI-FM were loaded with the hydrophobic fluorescent dye DiI and encapsulated into a 10% polyacrylamide gel. DiI-loaded poly(ethylene glycol)-*b*-oligo(ethylene sulfide) (PEG₄₄-*b*-OES₇) FM were also prepared for comparison.¹⁶⁴ PEG₄₄-*b*-OES₇ forms stable FM at a very high f_{PEG} of 0.83 because of the crystallinity of the OES block.¹⁶⁵ The entrapped FM were then imaged with interference-based structured illumination microscopy (SIM). A few isolated filaments and clusters of filaments were observed for the (-)PBI-FM sample (**Figure 2-13**). However, background fluorescence was observed and the majority of the image consisted of punctate fluorescence. For the PEG₄₄-*b*-OES₇ sample, clusters of small rods were observed, but individual filaments were difficult to be distinguished. These results demonstrate that imaging of FM with SIM is possible; however, the method of sample preparation requires further optimization. During imaging, the acrylamide gel was contracting leading to slight movement, which reduced image

quality. Potential approaches to improving image quality include keeping the gel hydrated while imaging, washing the gel with PBS to remove micelles in the formulation, and further decreasing FM concentration. While clusters of FM should be able to be resolved with further optimization, the resolution of SIM is most likely not high enough to resolve individual FM, especially FM shorter than 1 μm , so other super-resolution microscopy imaging techniques should also be explored.

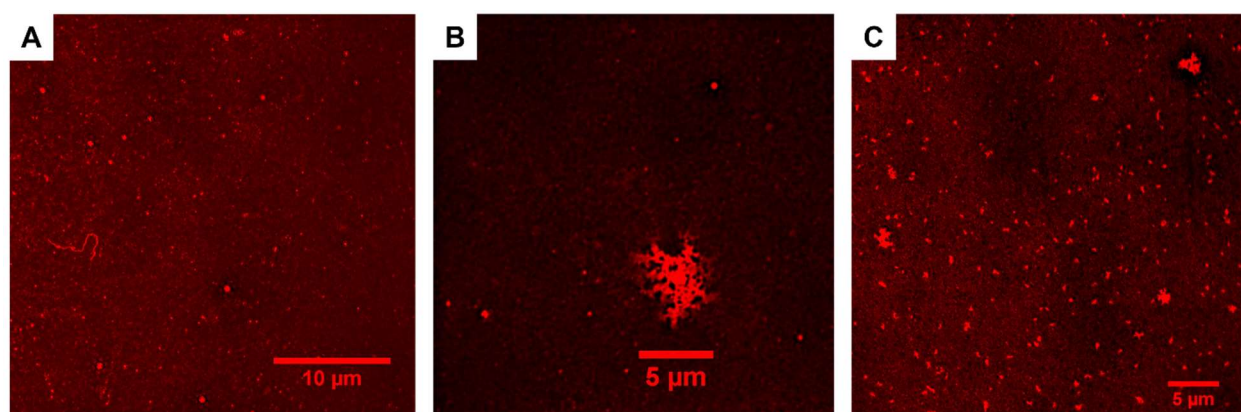


Figure 2-13. Images of DiI-loaded FM formulations entrapped in a polyacrylamide gel and imaged by SIM. a) DiI-loaded (-)PBI-FM at a concentration of 0.175 mg/mL. b) DiI-loaded (-)PBI-FM at a concentration of 0.34 mg/mL. c) DiI-loaded PEG₄₄-*b*-OES₇ at a concentration of 0.175 mg/mL.

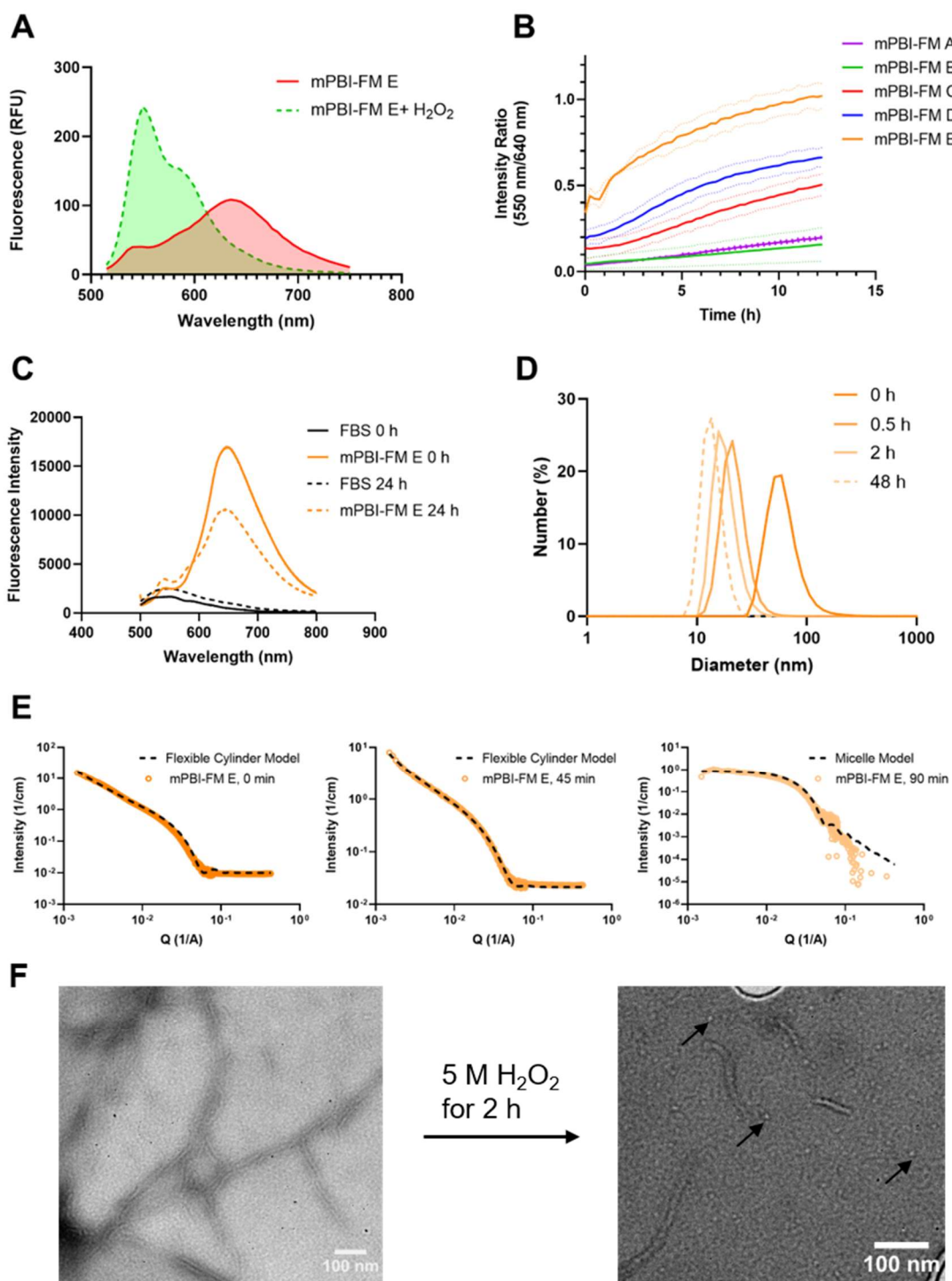


Figure 2-14. mPBI-FM exhibit shifts in fluorescence and “cylinder-to-sphere” morphological transition to micelles after oxidation. a) Emission spectra of mPBI-FM-E before and after oxidation with 5 M H₂O₂ for 2 h. b) Changes in the intensity ratio (emission at 550 nm /emission at 640 nm) of mPBI-FM types A through E after treatment with a physiological concentration (20 μM) of H₂O₂ over 12 h (n=2). The mean (solid line) and standard deviation (dotted lines) are displayed. c) Emission spectra of mPBI-FM-E before and after incubation in 50% fetal bovine serum for 24 h at 37° C. d) Dynamic light scattering (DLS) of mPBI-FM-E treated with 5 M H₂O₂ over 48 h. e) SAXS and model fit of mPBI-FM-E at timepoints of 0 minutes, 45 minutes, and 90 minutes after oxidation with 5 M H₂O₂. At 0 minutes and 45 minutes, mPBI-FM-E best fits the flexible cylinder model. At 90 minutes, the SAXS scattering profile best fit a micelle model. f) TEM images of mPBI-FM-E before and after treatment with 5M H₂O₂ for 2 h at 25°C. Examples of micelles are marked with the black arrows.

2.4.10. mPBI-FM Undergo “Cylinder-to-Sphere” Transitions upon Oxidation

The fluorescence emission spectrum of PBI shifts depending on its concentration and level of aggregation.^[29] The Scott Lab previously leveraged this property to form immunotheranostic mPBI-PS that shift in fluorescence emission in response to oxidation-mediated disassembly.^[25] Since PEG-*b*-PPS (-)PBI-FM are capable of undergoing morphological transitions from FM to MC upon oxidation,^[12] I investigated the effect of oxidation on the fluorescence emission spectra and morphology of mPBI-FM.

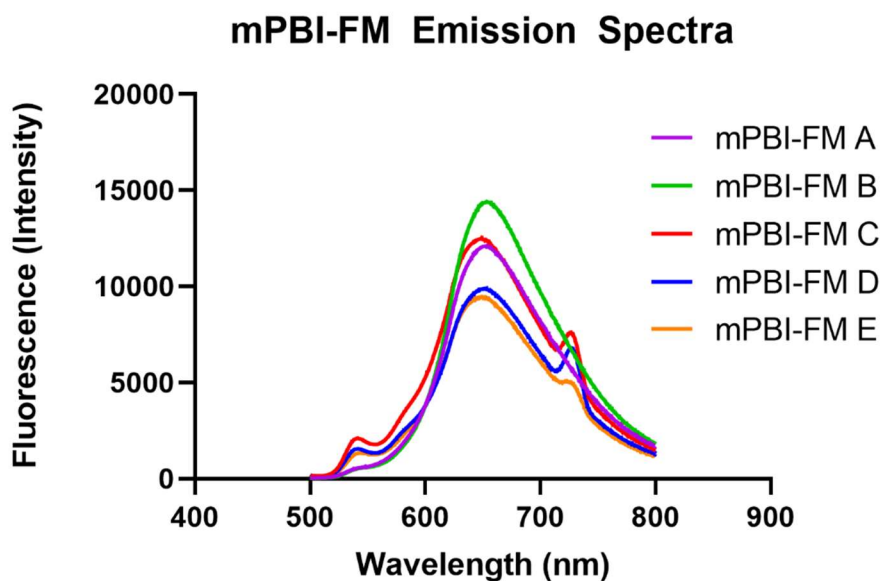


Figure 2-15. Fluorescence emission spectra of mPBI-FM formulations. The plot displays emission spectra acquired for mPBI-FM types A-E at a polymer concentration of 0.5 mg/mL in PBS after excitation at 485 nm.

Table 2-10. Polydispersity index of mPBI-FM-E at various timepoints after treatment with 5 M H₂O₂ as measured by dynamic light scattering (DLS).

Time in 5 M H ₂ O ₂	Polydispersity index (PDI)
0 min	0.22
30 min	0.09
2 h	0.07

48 h 0.06

Table 2-11. mPBI-FM-E parameters estimated from flexible cylinder model fit of SAXS scattering profiles in Figure 2-14E for 0 min and 45 min after treatment with 5 M H₂O₂.

Parameters	0 min	45 min
Length (nm)	1011.1	815.9
Radius (nm)	6.2	11.8
Chi ²	0.008	0.009

Table 2-12. Oxidized mPBI-FM-E parameters estimated from micelle model fit of SAXS scattering profile in Figure 2-14E for the timepoint at 90 min after treatment with 5 M H₂O₂.

Parameters	90 min
Core radius (nm)	8.46
Radius of gyration (nm)	7.05
Diameter (nm)	31.02
Chi ²	0.001

Before oxidation, mPBI-FM had a similar emission spectra to that of the previously reported mPBI-PS^[25] with a peak in the emission spectra at 640 nm after excitation at 485 nm (**Figure 2-14A; Figure 2-15**). Following oxidation with 5 M H₂O₂ for 2 h, the fluorescence emission spectra of mPBI-FM shifted to a peak at 550 nm (Figure 2-14A), which indicates that the

pi-stacking of PBI is disrupted under these conditions. Since the concentration of intracellular reactive oxygen species is generally below 100 μM ,^[34] I studied the kinetics of this fluorescence shift at a physiological concentration of H_2O_2 (20 μM) by measuring the ratio of the fluorescence emission intensity at 550 nm over 640 nm for 12 h. An increase in the 550 nm/640 nm fluorescence intensity ratio was observed over time for mPBI-FM types A-E with 20 μM H_2O_2 , with the largest increase observed for mPBI-FM-E (Figure 2-14B). To assess the stability of mPBI-FM for in vivo applications, I measured the fluorescence emission spectra before and after incubation with fetal bovine serum (FBS) of mPBI-FM-E for 24 h at 37° C. The peak in emission at 640 nm indicated that pi-stacking was maintained after 24 h (Figure 2-14C). Thus, mPBI-FM are likely to be stable after exposure to physiologically relevant fluids such as blood in vivo.

I next assessed whether this shift in fluorescence emission corresponds to a morphological transition of the mPBI-FM upon oxidation. I conducted these studies using mPBI-FM-E, which had the greatest shift in fluorescence after oxidation with physiological levels of H_2O_2 . I first tracked their apparent hydrodynamic diameter and polydispersity index with dynamic light scattering (DLS) after treatment with 5 M H_2O_2 for 48 h. DLS is most useful for characterizing the hydrodynamic diameter and polydispersity index of spherical structures, so I measured relative shifts in these parameters to monitor the “cylinder-to-sphere” morphological transition.^[34] A decrease in the apparent hydrodynamic diameter and polydispersity index of the mPBI-FM solution was observed over 48 h of oxidation (Figure 2-14D, **Table 2-10**). This result suggests that the abundance of small monodisperse spherical structures in the solution was increasing over time, which is consistent with mPBI-FM transitioning into spherical MC upon oxidation. Furthermore, I monitored the morphology of mPBI-FM-E with SAXS at different timepoints after treatment

with 5 M H₂O₂. After 0 minutes and 45 minutes of oxidation, mPBI-FM-E maintained a filamentous morphology as the scattering profiles best fit a flexible cylinder model (Figure 2-14E). However, the contour length shortened from over a micron to 815.9 nm after 45 minutes of oxidation, further suggesting that the cylinders were budding into MC (Table 2-11). After 90 minutes of oxidation, changes in the scattering profile were observed and best fit a micelle model, which confirmed that the mPBI-FM were undergoing a morphological transition into a population of predominantly MC (Figure 2-14E). The morphological parameters of mPBI-FM-E in this degradation study, as modeled by SAXS, are presented in Table 2-11 and 2-12. Their morphological transition to MC was further confirmed by TEM. After 2 h of treatment with 5 M H₂O₂, FM fragments and micelles (marked by arrows) were observed (Figure 2-14F). I therefore concluded that mPBI-FM undergo shifts in fluorescence and a morphological transition to MC after oxidation as aggregation and pi-stacking of the PBI is disrupted. The fluorescence shifts correlate with the kinetics observed through TEM, SAXS, and DLS. These unique features of mPBI-FM further enable the characterization of “cylinder-to-sphere” transition kinetics by monitoring fluorescence emission without requiring loading of additional fluorescent dyes or using more low-throughput characterization techniques.

2.4.11. mPBI-FM Fluorescence Intact after Triton-X Incubation

Besides oxidation, I assessed whether the addition of a surfactant can disrupt mPBI-FM nanostructures. Generally, polymer bilayers are solubilized by detergents, which can lead to disruption of the nanocarrier morphology.¹⁶⁶ Addition of 0.1% Triton X-100 for 10 minutes has been utilized to disrupt PEG-*b*-PPS PS to release enzymes encapsulated in the nanocarriers.³⁷

Interestingly, the fluorescence emission peak at 640 nm of mPBI-FM-E did not change after addition of the surfactant, 0.1% Triton X-100 for 30 min (**Figure 2-16**). This suggests that the addition of detergent did not disrupt PBI pi-stacking at this timepoint, and that the pi-stacking enhanced the stability of the nanocarriers, making them less sensitive to detergents compared to PEG-*b*-PPS PS. However, further characterization with TEM imaging of mPBI-FM after longer incubation times with Triton-X is needed to confirm that the addition of detergent did not disrupt mPBI-FM morphology.

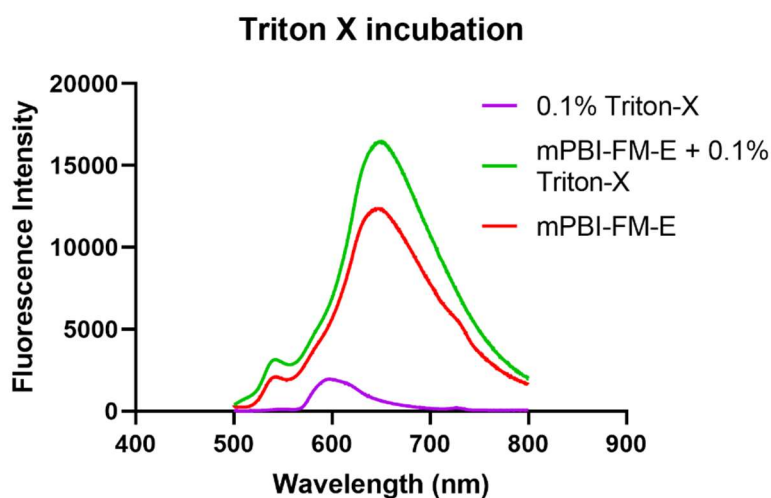


Figure 2-16. Emission spectra of mPBI-FM-E before and after incubation with the detergent 0.1% Triton X-100 for 30 min.

2.5. Conclusions

While FM nanocarriers have great potential as delivery vehicles for medicine due to their unique filamentous morphology, reproducible and scalable formation of FM has remained challenging. Taken together, I have developed a filamentous pi-stacking nanomaterial, which

allow for rapid, scalable self-assembly of FM via FNP and permitted control over FM flexibility. Scalable FM formation via FNP and control over flexibility was achieved by co-assembling PBI tetrablock copolymers containing pi-stacking moieties with diblock copolymers, a strategy that is potentially applicable across different BCP systems. The pi-stacking ability of these polymers enhanced the stability and shelf-life of the resulting mPBI-FM, as the mPBI-FM maintained their filamentous morphology after a month in storage at 4° C. PBI incorporation also increased the acceptable f_{PEG} range of BCP that forms FM via TFH and FNP ($f_{\text{PEG}}=0.22$ to 0.35). Depending on the overall f_{PEG} of the BCP, ratio of PBI tetrablock copolymers incorporated, and self-assembly method, mPBI-FM with varying flexibilities and contour lengths were formed. The mPBI-FM were less flexible than (-)PBI-FM in all cases. Incorporation of PBI also offered a high-throughput method to evaluate the oxidation-induced “cylinder-to-sphere” morphological transition of mPBI-FM by monitoring changes in fluorescence emission dependent on the extent of PBI aggregation.

2.6. Acknowledgments

I would like to acknowledge the support for my training by the National Institutes of Health Training Grant (T32GM008449) through Northwestern University’s Biotechnology Training Program, and by the National Institutes of Health Training Grant (T32GM008152) through the Northwestern Medical Scientist Training Program.

I would like to acknowledge Lauren Li for her assistance designing and producing the graphics and artwork for Figure 2-1. I would like to acknowledge Eric W. Roth for his assistance with CryoTEM imaging, Nathaniel Kabat for his assistance with STEM imaging, and Constadina

Arvanitis for her assistance with SIM. This work made use of the BioCryo facility of Northwestern University's NUANCE Center, which has received support from the Soft and Hybrid Nanotechnology Experimental (SHyNE) Resource (NSF ECCS-1542205); the MRSEC program (NSF DMR-1720139) at the Materials Research Center; the International Institute for Nanotechnology (IIN); and the State of Illinois, through the IIN. It also made use of the CryoCluster equipment, which has received support from the MRI program (NSF DMR-1229693). This work was supported by the Northwestern University Keck Biophysics Facility and a Cancer Center Support Grant (NCI CA060553). We acknowledge staff and instrumentation support from the Structural Biology Facility at Northwestern University, the Robert H Lurie Comprehensive Cancer Center of Northwestern University and NCI CCSG P30 CA060553. This work made use of the IMSERC NMR facility at Northwestern University, which has received support from the Soft and Hybrid Nanotechnology Experimental (SHyNE) Resource (NSF ECCS-1542205), Int. Institute of Nanotechnology, and Northwestern University. Structured illumination microscopy was performed on a Nikon N-SIM system, purchased through the support of NIH 1S10OD016342-01. This research used resources of the Advanced Photon Source, a U.S. Department of Energy (DOE) Office of Science User facility operated by Argonne National Laboratory under Contract NO. DE-AC02-06CH11357. SAXS experiments were performed at the DuPont-Northwestern-Dow Collaborative Access Team (DND-CAT) located at Sector 5 of the Advanced Photon Source (APS). DND-CAT is supported by Northwestern University, The Dow Chemical Company, and DuPont de Nemours, Inc. This research used resources of the Advanced Photon Source, a U.S. Department of Energy (DOE) Office of Science User Facility operated for the DOE Office of Science by Argonne National Laboratory under Contract No. DE-AC02-06CH11357. This work

benefited from the use of the SasView application, originally developed under NSF Award DMR-0520547. SasView also contains code developed with funding from the EU Horizon 2020 programme under the SINE2020 project Grant No 654000.

2.7. Publication Information

Sections of this chapter have been published, with the citation below:

Li, S.; Bobbala, S.; Vincent, M. P.; Modak, M.; Liu, Y.; Scott, E. A., Pi-Stacking Enhances Stability, Scalability of Formation, Control over Flexibility, and Circulation Time of Polymeric Filamentous Nanocarriers. *Advanced NanoBiomed Research* **2021**, 2100063.

CHAPTER 3

3. Investigation of the Effect of Filament Flexibility on Immune Cell Internalization and Activation

3.1. Abstract

The shape and flexibility of nanocarriers affect their cellular internalization, circulation time, and transport through the body. Co-assembling the pi-stacking PBI tetrablocks and PEG-*b*-PPS diblocks at different molar ratios resulted in mixed PBI-containing FM (mPBI-FM) with tunable length and flexibility, allowing the investigation of the effect of filament flexibility on immune cell uptake and macrophage activation. The flexibility of the filamentous nanocarriers affected their cytotoxicity profile, with the most rigid mPBI-FM exhibiting the greatest toxicity in murine macrophages in vitro. The flexibility of mPBI-FM was also optimized to decrease uptake by macrophages in vivo, leading to increased circulation time compared to (-)PBI-FM without PBI tetrablocks after intravenous administration in mice. Lastly, filament flexibility affected macrophage activation, with the most rigid mPBI-FM eliciting the greatest upregulation of surface markers characteristic of classically activated macrophages. Thus, FM flexibility can be engineered to enhance passive targeting of immune cell subtypes, increase systemic circulation times, and to induce immune cell activation.

3.2. Introduction

This chapter concerns the investigation of how filament flexibility affects interactions with immune cells, particularly macrophages, which are largely involved in nanocarrier clearance in vivo. To provide some background, the concepts of 1) how the chemical properties of PBI derivatives affect their cellular interaction, 2) how macrophages are activated and involved in

nanocarrier clearance and 3) how nanocarrier flexibility or elasticity affects cellular interactions and immune cell activation is briefly summarized.

In this chapter, to better understand how the tunable physical properties of FM influence their performance as drug delivery vehicles, I examined the relationship between mPBI-FM flexibility and their uptake by cells *in vitro*, as well as their organ and cellular level biodistribution *in vivo*. I also investigated how FM flexibility affected activation of murine macrophages *in vitro* and serum cytokine and biomarker levels *in vivo*.

3.2.1. Interaction of PBI Derivatives with Cells

The fluorescent dye PBI has been utilized as pigments in nonpolar solvents for industrial applications such as automotive finishes, due to their chemical inertness and thermal stability, since the 1950s.¹⁶⁷ More recently, PBI derivatives with enhanced water solubility have been developed for biological applications, especially as photostable fluorescent dyes. Increased solubility of PBI has been achieved by introducing hydrophilic groups or polymers at the imide positions or bay region.¹⁶⁸ The size, shape, electric charges and chemical composition of these PBI constructs have been found to influence their cellular interactions and toxicity.¹⁶⁹ PBI constructs have been synthesized as DNA intercalators, and PBI constructs with a small molecular weight, highly polar substituents, and increased number of charges from the addition of amines were able to enter the cell nucleus and inhibit the growth of HeLa cancer cells more effectively.^{169, 170} Conversely, attaching two amphiphilic diblock copolymers to PBI to form a tetrablock copolymer led to the formation of mPBI-PS that exhibited no cellular toxicity *in vitro* in RAW 264.7 macrophages.¹⁵⁸ These mPBI-PS served as immunotheranostic tools to visualize and quantify

nanoparticle disassembly upon internalization.¹⁵⁸ These examples illustrate how the chemical properties and ability of PBI constructs to form supramolecular structures can be engineered for different biomedical applications.

3.2.2 Effect of Filament Length and Flexibility on Cellular Internalization and Circulation Times

The effect of polymeric filament length and flexibility on cellular internalization is not well understood. Many studies have focused on spherical particles, where generally stiffer particles demonstrate increased uptake in immune cells.¹⁴⁸ For filamentous nanostructures, the impact of length and flexibility in vitro depends on the nanomaterial system. Mullner *et al.* found that cylindrical polymer brushes with a length of 1.2 μm had almost 3 times higher cellular association with RAW 264.7 macrophages compared to 250 nm brushes.¹⁷¹ Cylindrical polymer brushes that were made more rigid through the addition of a PCL core, when compared with more flexible brushes, were found to have similar cell association with RAW 264.7 macrophages in vitro.¹⁷¹ In contrast, Geng *et al.* found that longer and more flexible self-assembled FM (3 μm) were internalized by activated human macrophages at lower rates in vitro compared to 1.8 μm FM.⁵⁶ These studies suggest that filaments with a length between 1-2 μm are internalized by macrophages at higher rates.

Filament length has had varying effects with regards to circulation times in vivo. Increasing the aspect ratio of cylindrical polymer brushes increased plasma clearance and increased uptake in the spleen and liver after intravenous administration in rats.¹⁷¹ Conversely, longer degradable PEG-*b*-PCL FM ranging from 2-18 μm in length exhibited increased circulation times in vivo; however, these FM fragmented over time due to shear forces, so the persistent circulation observed

was not only due to the FM length.⁵⁶ Indeed, inert PEG-*b*-PEE FM that had a starting length of 3.5 μm had similar circulation times as 8 μm degradable FM. With respect to filament flexibility, in general decreasing the flexibility shortened circulation times. Increasing the rigidity of the polymer brushes led to rapid clearance from plasma, with a greater uptake of the brushes observed in the liver.¹⁷¹ Similarly, increasing the rigidity of degradable PEG-*b*-PEE FM led to shorter circulation times in rats.⁵⁶ Of note, if the persistence length of the filamentous nanostructures is not measured, it is difficult to compare the effect of filament flexibility across different nanomaterial platforms. Further studies, especially with systematic characterization of the persistence length of the nanomaterials, are thus needed to better elucidate how the properties of filamentous nanostructures affect their biological performance in vivo.

3.2.3. Murine Macrophage Activation and Polarization

Macrophages are a member of the innate immune system and engulf pathogens to present antigens to the adaptive immune system. In response to various stimuli and the local tissue environment, macrophages become activated and differentiate into diverse populations with different immune effector functions, including the secretion of pro or anti-inflammatory cytokines.¹⁷² While there is a spectrum of macrophage populations, the phenotype of murine macrophages has generally been categorized into a two categories on different ends of this spectrum.¹⁷³ Macrophages that are activated by proinflammatory cytokines and pathogen-associated molecular patterns (PAMPs), such as IFN- γ and LPS, are known as classically activated or M1 macrophages.¹⁷⁴ These macrophages are pro-inflammatory, ready to quickly defend against an infection, and have enhanced phagocytic and intracellular bactericidal activity, as evidenced by their production of nitric oxide.¹⁷³ In contrast, alternatively activated macrophages or M2

macrophages have an anti-inflammatory phenotype and are activated by anti-inflammatory cytokines such as IL-4 and IL-13, parasitic infections, and danger signals known as damage-associated molecular patterns (DAMPs).¹⁷³ M2 macrophages resolve the inflammatory response to promote tissue repair and wound healing and may be more vulnerable to intracellular infection.¹⁷⁴ They have induced arginase activity leading to production of ornithine, and typically secrete the anti-inflammatory cytokine IL-10.¹⁷⁴ M2 macrophages have been further classified into four different subtypes with different effector functions that include promoting angiogenesis, regulating the immune response, and removal of debris.¹⁷²

3.2.4 Effect of Nanocarrier Morphology and Flexibility on Immune Cell Activation

Nanocarrier shape and flexibility not only influence their cellular uptake, but also their ability to activate immune cells.¹⁷⁵ For rod-like nanostructures, the general trend is that shorter rods induce less of an immune response. Rod-shaped aluminum oxide nanoparticles with a longer aspect ratio more effectively induced expression of CD80 and CD86 on splenocytes after intravenous injection in ICR mice, compared to shorter rods.¹⁷⁶ In RAW 264.7 macrophages, longer cylindrical glyconanoparticles of 215 nm induced a greater inflammatory response with increased IL-6 secretion compared to shorter cylindrical nanoparticles (99 nm in length).¹⁷⁷ In another study by Sato *et al.*, longer carbon nanotubes (825 nm) induced greater inflammation than shorter carbon nanotubes (220 nm) as quantified by histology after subcutaneous injection in rats.¹⁷⁸ While the length effect of rods has been characterized, the effect of flexibility of polymeric filamentous nanostructures on immune cell activation has not been studied and needs to be investigated.¹⁷⁵

3.3. Materials and Methods

3.3.1. DNA Intercalation Assay

5 μM of PBI tetrablock copolymer was incubated at 25°C in 1xPBS with 0, 5, 10, and 15 μM of dsDNA. The DNA consisted of plasmid DNA (pL-CRISPR.EFS.tRFP, Plasmid # 57819 from Addgene) extracted from DH5 alpha competent cells with the ZymoPURE II Plasmid Maxiprep Kit (Zymo Research). The fluorescence spectra were measured after excitation at 485 nm with the Shimadzu RF-6000 Spectrofluorometer.

3.3.2. Fabrication of DiR-loaded Nanocarriers

0.5 weight % of DiR (50 μg DiR/ 10 mg polymer) was added to the organic solvent during nanocarrier fabrication with either FNP or TFH as described in Chapter 2, sections 2.3.4 and 2.3.5. After formation, the formulations were filtered in a Sephadex LH-20 (Sigma-Aldrich) column to remove free DiR. The nanocarriers were spin-concentrated to the desired concentration using Amicon Ultra-4 Centrifugal Filter Units (Millipore Sigma). Nanocarrier fabrication and purification were performed under sterile conditions for *in vivo* studies.

3.3.3. Cell Culture

The RAW 264.7 murine macrophage cell line was obtained from the American Type Culture Collection (ATCC, Rockville, MD, USA). The cells were cultured in DMEM supplemented with 10% fetal bovine serum, 100 IU mL⁻¹ of penicillin and 100 μg mL⁻¹ streptomycin at 37°C in a humidified incubator with 5% CO₂ and 95% air. RAW-Blue macrophages (InvivoGen) were cultured in DMEM supplemented with 10% fetal bovine serum, 100 IU mL⁻¹ of penicillin, 100

$\mu\text{g mL}^{-1}$ streptomycin, $100 \mu\text{g mL}^{-1}$ Normocin and $200 \mu\text{g mL}^{-1}$ Zeocin (every other passage) at 37°C in a humidified incubator with 5% CO_2 and 95% air.

3.3.4. MTT Assay

RAW 264.7 cells were seeded at a density of 30,000 cells in $100 \mu\text{L}$ of media per well in a 96-well plate and let to adhere overnight. Nanocarriers were then added to each well for final concentrations of 0, 0.0625, 0.125, 0.25 and 0.5 mg mL^{-1} . After 24 h, $12 \mu\text{L}$ of 5 mg mL^{-1} of MTT (thiazol blue tetrazolium bromide) was added per well, and the cells were incubated at 37°C for 4 h. The media was removed and $150 \mu\text{L}$ of DMSO was added to each well to dissolve the formazan crystals. The absorbance was measured at 570 nm. The absorbance of any cell debris at 630 nm was subtracted from the absorbance at 570 nm, and the percent cell viability was determined by normalizing the absorbance by the negative control (PBS-treated cells).

3.3.5. In vitro Uptake Studies

mPBI-FM (no dye): RAW 264.7 cells were seeded at a density of 1.3×10^5 cells/well on a 24-well plate and cultured overnight. The cells were incubated in media with 0.5 mg mL^{-1} of mPBI-FM for 4 hr and 24 h timepoints. Cells incubated in media only were used as a control. The media was discarded and the cells were washed three times with 1 x PBS. The cells were harvested, stained with Zombie NIR Fixable Viability Dye (BioLegend), and fixed in 4% paraformaldehyde. Cells incubated in media only were left unstained or stained with Zombie NIR dye only as controls. The samples were analyzed on a LSR Fortessa flow cytometer (BD Biosciences) and the data was analyzed with Cytobank Community software.

DiR-loaded mPBI-FM: RAW 264.7 cells were seeded at a density of 1.3×10^5 cells/well on a 24 well plate and cultured overnight. The cells were incubated in media with 0.25 mg mL^{-1} of DiR-loaded FM for 4 hr and 24 h timepoints. Cells incubated in media only were used as a control. The media was discarded, and the cells were washed three times with 1 x PBS. The cells were harvested, stained with Zombie Violet Fixable Viability Dye (BioLegend), and fixed in 4% paraformaldehyde. Cells incubated in media only were left unstained or stained with Zombie Violet dye only as controls. The samples were analyzed on a 3-laser Aurora Spectral Flow Cytometer (Cytek). After spectral mixing was performed using Spectroflo software, the data was analyzed with Cytobank Community software.

3.3.6. Confocal Microscopy

mPBI-FM (no dye): RAW 264.7 cells were seeded at a density of 2×10^5 cells/well and cultured for 24 hours. The cells were then incubated in 0.5 mg mL^{-1} of mPBI-FM for 4 h and 24 h timepoints. Cells incubated in media only were used as controls. The cells were then washed three times with 1 x PBS, stained with NucBlue Live Ready Probes Reagent (ThermoFisher Scientific), and imaged with a Leica TCS SP8 confocal microscope with a 63x (NA=1.4) objective.

DiR-loaded mPBI-FM: RAW 264.7 cells were seeded at a density of 2×10^5 cells/well and cultured for 24 h. The cells were then incubated in 0.25 mg mL^{-1} of DiR-loaded FM for 24 h. Cells incubated in media only were used as controls. The cells were then washed three times with 1 x PBS, stained with LysoTracker Blue DND-22 (ThermoFisher Scientific) at 1:2000

dilution for 2 h, and imaged with a Leica TCS SP8 confocal microscope with a 63x (NA=1.4) objective.

3.3.7. Quanti-blue Assay on RAW-blue Cells

RAW-blue cells (100,000 cells/well) were incubated with nanocarriers (final concentration 0.5 mg mL⁻¹) or LPS (1 µg mL⁻¹) for 24h. Cell supernatant was then incubated with QUANTI-Blue solution (InvivoGen) at 37°C for up to 6 h. The absorbance was then measured at 620-655 nm.

3.3.8. ELISAs

The Mouse Th1/Th2 Uncoated ELISA kit (Invitrogen) was utilized. Briefly, ELISA plates were coated with the capture antibody overnight at 4°C. The wells were then washed 3 times with Wash Buffer (1xPBS, 0.05% Tween-20), blocked with ELISA/ELISPOT diluent for 1 hour at room temperature, then the plate was washed again. The sample or standards were added to the wells. Standard curves were included in duplicate and 1:10 and 1:2 dilutions of the samples were performed. The plate was then incubated at room temperature for 2 h, washed 5 times, incubated with detection antibody at room temperature for 1 h, washed 5 times, incubated with Streptavidin-horse radish peroxidase at room temperature for 30 min, washed 5 times, incubated with TMB solution for 15 minutes, and then Stop solution was added. The absorbance was then measured at 450 nm.

3.3.9. Macrophage Surface Receptor Expression

RAW 264.7 cells were seeded overnight at a concentration of 2×10^5 cells/well. The cells were then incubated with nanocarriers at a final concentration of 0.25 mg mL⁻¹ or LPS (1 µg mL⁻¹

¹) for 24 h. The cells were then washed with PBS and single cell suspensions were prepared. For cellular staining, the cells were washed with 1xPBS, FcR binding was blocked with anti-mouse CD16/32 (BioLegend), and then stained with Zombie Violet dye (Biolegend) for 20 min at 4°C. After a wash with 1xPBS, the cells were then stained with the antibody cocktail (Biolegend) for 45 minutes, and fixed. The antibody cocktail consisted of FITC CD80 (#104706), PE/Dazzle 594 MHC II (#107648), and APC/Fire 750 CD86 (#105046). Unstained samples, single-colored controls, and full panel controls were prepared for spectral unmixing. Flow cytometry was performed with the Cytex Aurora 3-laser Spectral Flow Cytometer.

3.3.10. In vivo Organ-level Biodistribution Study

Male, 90-day old C57BL/6J mice (The Jackson Laboratory) were fed a standard diet. All in vivo experiments were conducted according to protocols approved by the Institutional Animal Care and Use Committee at Northwestern University. 150 μ L of 1x PBS (control group) or DiR-loaded FM (mPBI-FM-C, mPBI-FM-D, or (-)PBI-FM at 5 mg mL⁻¹ concentration) were administered by retroorbital intravenous injection to the mice. The PBS control group had 3 mice while the FM experimental groups had 7 mice. 6 h after injection, 150 μ L of whole blood was collected through retro-orbital bleeding in the opposite eye for serum analysis. 24 h after injection, the mice were sacrificed and whole blood was collected into Eppendorf tubes through cardiac puncture. After whole-body perfusion with heparinized PBS, the liver, spleen, kidneys, lungs, brain, and heart were collected into a petri dish for each mouse. The organs and tubes of whole blood were imaged by the IVIS in vivo imaging system (PerkinElmer) with an excitation wavelength of 745 nm, emission wavelength of 800 nm, and exposure time of 0.5 seconds. The

liver, kidneys, and spleen were saved to prepare single-cell suspensions for flow cytometry, and the whole blood was saved for serum analysis.

IVIS data was analyzed using Living Image software (PerkinElmer). A circular region of interest (ROI) was drawn over each organ, and a background ROI was drawn in an empty area of the petri dish for each mouse. For the whole blood tubes, the tubes from each group were imaged together, and a background ROI was drawn in an empty area of the image for each group. The radiant efficiency, RE, $((p/s/cm^2/sr)/(\mu W/cm^2))$ was determined for each ROI. The adjusted radiant efficiency was obtained by subtracting from the RE of the organ the RE of the background, which was defined as average RE of the background ROI multiplied by the area of the organ ROI and a factor calculated as the RE of the organ / (average RE x area of the organ ROI). To calculate the relative biodistribution of each FM among the different organs and whole blood, for each mouse the adjusted RE for all the organs and whole blood were summed to calculate a total RE. The adjusted radiant efficiency for each organ in that mouse was divided by this sum to obtain the percentage of the total radiant efficiency for each organ. For the images of the organs, the color scale minimum was adjusted until the plate autofluorescence disappeared for all images and the images were displayed with the same logarithmic color scale for each organ.

Serum fluorescence analysis: Whole blood was spun down at 3000 rpm for 25 min at 4°C and the supernatant was collected as the serum. For each sample, the serum was diluted 1:40 and the DiR fluorescence spectra was measured with a Shimadzu RF-6000 Spectrofluorometer with excitation wavelength of 745 nm and emission wavelengths of 750 nm to 900 nm. The serum

fluorescent intensity for each mouse sample was multiplied by the dilution factor. The serum fluorescence was then normalized by the initial fluorescence of each FM formulation before injection as follows. The integrated fluorescent intensity (area under the curve) of the DiR emission peak from 765 nm to 815 nm was calculated for each FM formulation mPBI-FM-C, mPBI-FM-D, and (-)PBI-FM at 0.25 mg mL^{-1} and divided by the lowest integrated fluorescent intensity to obtain a normalization factor that was applied for each FM group. The integrated fluorescent intensity of the control group (PBS injection) was then subtracted to account for background fluorescence.

3.3.11. In vivo Cellular-level Biodistribution Study

Single-cell suspensions were prepared from the liver, spleen, and kidneys for flow cytometry as previously described.⁹⁴ For cellular staining, the cells were washed with 1xPBS, FcR binding was blocked with anti-mouse CD16/32 (BioLegend), and then stained with Zombie Aqua dye (Biolegend) for 20 min at 4°C. After a wash with 1xPBS, the cells were then stained with the antibody cocktail (Biolegend) for 45 minutes, and fixed. The antibody cocktail consisted of BV421 CD45 (#103133), BV605 Ly-6C (#128035), BV785 CD11b (#101243), PE/Dazzle 594 F4/80 (#123146), PerCP/Cy5.5 CD11c (#117328), FITC CD3 (#100204), Alexa-fluor 700 Ly6-G (#127622), and APC MHC-II (#107614). Unstained samples, single-colored controls, and full panel controls were prepared for spectral unmixing. Flow cytometry was performed as above with the Cytex Aurora 3-laser Spectral Flow Cytometer. A minimum of 500,000 single cell events were recorded for spleen samples, 300,000 single cell events for the kidney samples, and 100,000 single cell events for the liver samples. Live, single cells were gated using FSC, SSC, and Zombie Aqua viability dye. The percentage of DiR positive cells was determined using

a 2% false positive rate set by gating against cells from the PBS-injected control group. The gating strategy and cell markers for the various cell populations is shown in **Table 3-1**. Data for a cell population was only reported if the cell count was greater than 100 for that population.

3.3.12. Serum Biomarker Analysis

Serum creatinine was measured with the Mouse Creatinine Assay Kit (Crystal Chem #80350). Serum alanine aminotransferase was measured with the Alanine Transaminase Assay kit (ScienCell Research Laboratories #8478).

3.3.13. Statistical Analysis

Any pre-processing of data including normalization and background subtraction are described above in the relevant methods subsection. Unless otherwise noted in the figure captions, the mean was presented with error bars representing the SEM. Statistical significance was determined by ANOVA with *post hoc* Tukey's test to correct for multiple comparisons for data with a normal distribution and equal variances. All statistical analyses used a 5% significance level and were performed with GraphPad Prism software (version 9.0.2).

Table 3-1. Definitions of cell populations for in vivo cellular biodistribution study. Gates for all cell populations were set on population of live single cells using FSC, SSC, and Zombie Aqua viability stain (Zombie Aqua low).

Organ	Cell Type	Markers for Flow cytometry
Spleen	Non-immune cells	CD45-

	T cells	CD45+, CD3+
	Macrophages	CD45+, CD3-, Ly6C-, CD11b+, F4/80+
	Dendritic cells	CD45+, CD3-, Ly6C-, CD11b-, CD11c+, IA/IE+
	Patrolling Monocytes	CD45+, CD3-, CD11b+, Ly6C ^{lo} , SSC ^{lo}
Liver	Non-immune cells	CD45-
	T cells	CD45+, CD3+
	Macrophages and Kupffer cells	CD45+, CD3-, Ly-6G-, CD11c-, CD11b+, F4/80+
	Dendritic Cells	CD45+, CD3-, Ly-6G-, CD11c+, IA/IE+
	Monocytes	CD45+, CD3-, Ly-6G-, CD11c-, CD11b+, F4/80-
	Neutrophils	CD45+, CD3-, Ly-6G+
Kidneys	Non-immune cells	CD45-
	T cells	CD45+, CD3+
	Macrophages (CD11c+)	CD45+, CD3-, Ly-6G-, F4/80+, CD11b+, CD11c+
	Macrophages (CD11c-)	CD45+, CD3-, Ly-6G-, F4/80+, CD11b+, CD11c-
	Dendritic Cells	CD45+, CD3-, Ly-6G-, F4/80-, CD11c+, IA/IE+
	Granulocytes	CD45+, CD3-, Ly-6G+

3.4. Results and Discussion

3.4.1. Assessment of DNA Intercalation Ability of PBI Tetrablock Copolymers

To assess whether PBI tetrablock copolymers can intercalate DNA, the fluorescence of the PBI tetrablocks after incubation with different concentrations of DNA was assessed. The fluorescence intensities of PEG₁₇PPS₁₉PBIPPS₁₉PEG₁₇ and PEG₁₇PPS₃₂PBIPPS₃₂PEG₁₇ tetrablocks did not substantially decrease after incubation with concentrations of up to 15 μ M of DNA (**Figure 3-1**). PBI derivatives that intercalate well with DNA exhibit a dose-dependent decrease in the fluorescent intensity as the DNA concentration increases.¹⁶⁹ Xu *et al.*, observed an almost 4-fold decrease in fluorescence after incubation of their PBI DNA intercalator with 15 μ M of dsDNA.¹⁶⁹ These results demonstrate that PBI tetrablock copolymer do not intercalate DNA, most likely due to the steric hindrance of the large PEG-*b*-PPS diblocks attached to the PBI. The PBI tetrablock copolymer is thus unlikely to localize in nuclei and inhibit cellular growth.

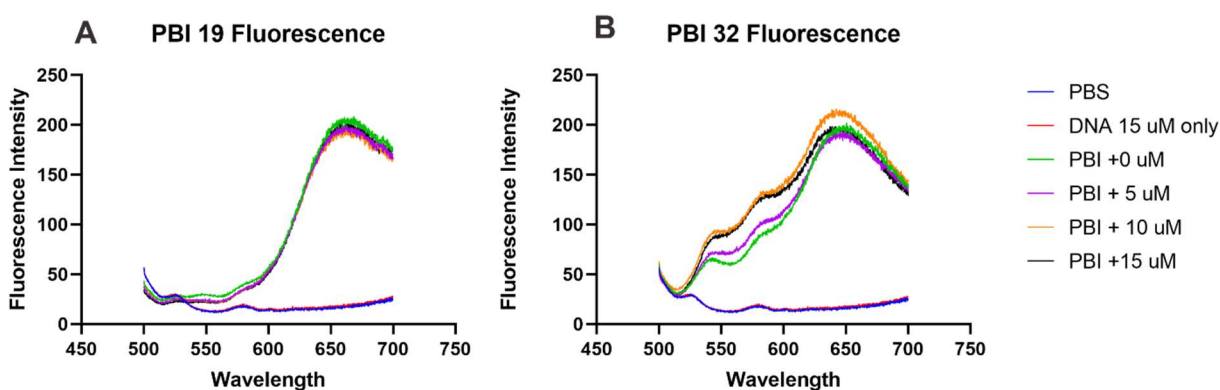


Figure 3-1. Fluorescence spectra of PBI tetrablock copolymers after incubation with different base-pair concentrations of double-stranded DNA.

3.4.2. mPBI-FM Shift in Fluorescence after Intracellular Oxidation

In previous studies, mPBI-PS exhibited a shift in fluorescence in vitro after oxidation-induced disassembly within the endolysosome.¹⁵⁸ I therefore studied whether the shift in fluorescence of mPBI-FM can also be observed under physiological oxidation conditions in vitro in RAW 264.7 murine macrophages. The shift in fluorescence of mPBI-FM-E after uptake in murine macrophages was quantified through flow cytometry after incubation with the nanocarriers for 4 h and 24 h timepoints, as compared to unstained controls and cells stained with Zombie Fixable Viability Dye. The percent uptake of mPBI-FM into the macrophages increased from 4 h to 24 h, as 41% of the cells were positive for red fluorescence at 24 hours (**Figure 3-2A**). At 24 hours, 6 percent of the cells were positive for green fluorescence as well as red fluorescence, demonstrating that mPBI-FM can undergo oxidation and morphological transition in vitro (Figure 3-2A). The median fluorescence intensity of red and green fluorescence also increased over time from 4 to 24 hours as more of the mPBI-FM were endocytosed and oxidized (**Figure 3-2B**). This shift in fluorescence upon cellular uptake and oxidation in vitro was further confirmed by confocal microscopy imaging of the cells at 4 and 24 h timepoints. At 4 hours, red and to a lesser extent green fluorescence could be observed intracellularly as discrete puncta, and at 24 hours, more green fluorescence was observed intracellularly (**Figure 3-2C**). These studies demonstrate that the morphological transition of mPBI-FM after oxidation in vitro can be observed by measuring the shift in fluorescence emission from red to green fluorescence.

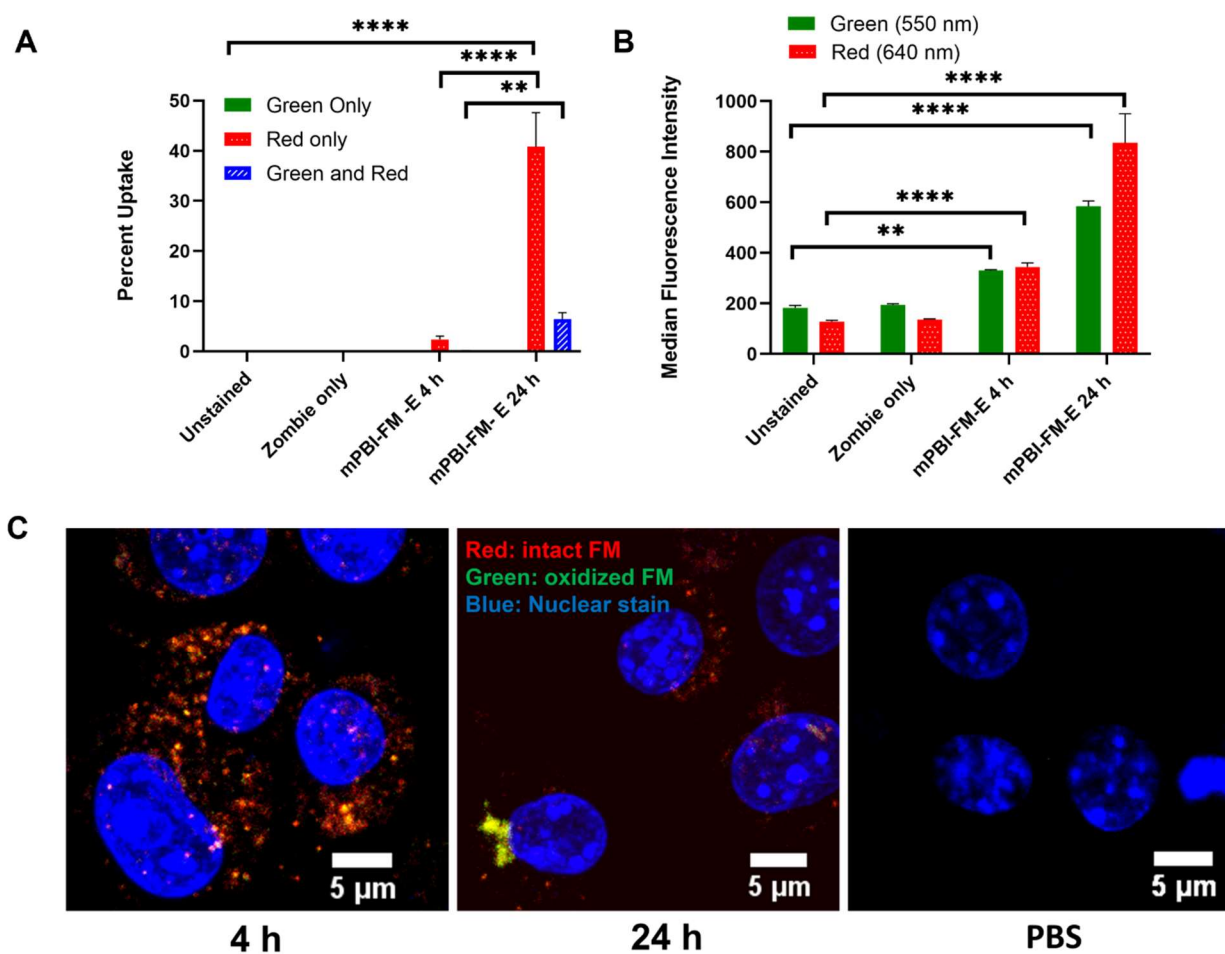


Figure 3-2. mPBI-FM undergo a red to green fluorescence shift in vitro in RAW 264.7 mouse macrophages. a) Percent uptake and b) median fluorescence intensity of mPBI-FM-E (0.5mg/mL) by RAW 264.7 cells after incubation for 4 h and 24 h as measured by flow cytometry, compared to controls that were unstained or stained with Zombie Aqua Viability Dye (n=3). Statistical significance was determined by ANOVA with post hoc Tukey's test to correct for multiple comparisons with a 5 percent significance level (**p<0.01, ****p<0.0001) The mean is displayed together with error bars representing the standard deviation. c) Confocal microscopy images of RAW 264.7 macrophages incubated with mPBI-FM-E for 4h and 24 h as compared to a control

incubated with PBS. Intact FM had red fluorescence, oxidized FM had green fluorescence, and areas of overlap of red and green are shown in yellow.

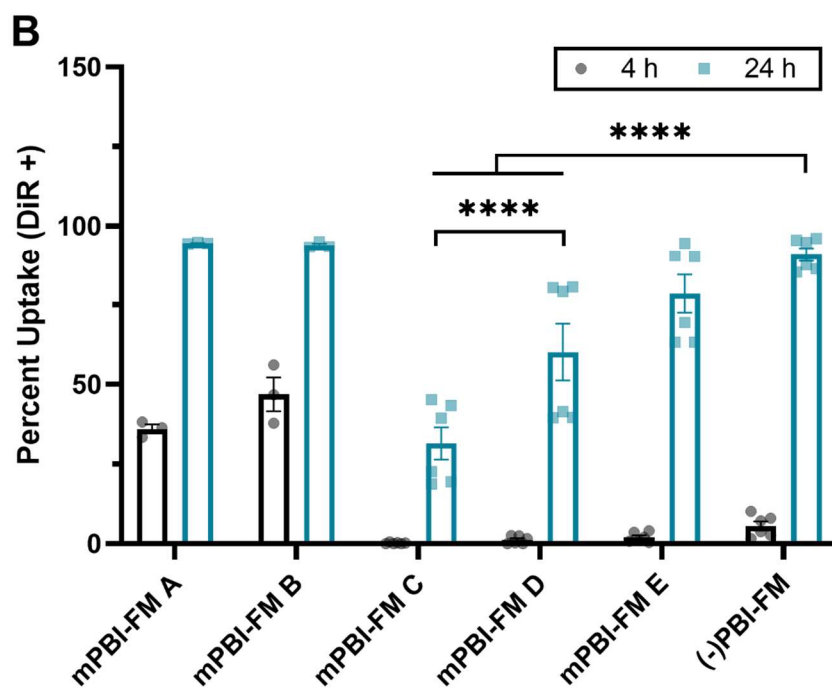
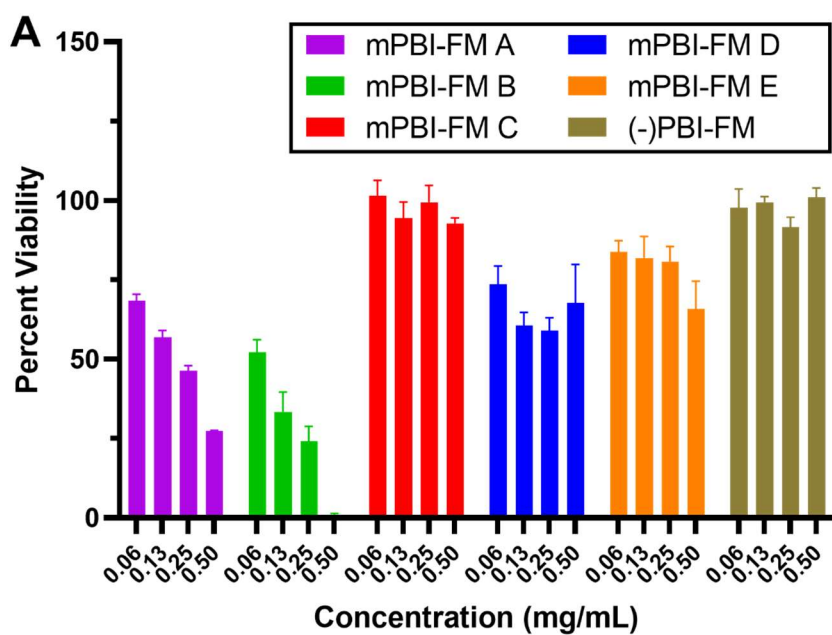


Figure 3-3. Differential cytotoxicity and uptake profiles of mPBI-FM having distinct Lc/Lp in RAW 264.7 murine macrophages. FM formulations from Table 2-7 are ordered in terms of increasing flexibility. (-)PBI-FM is included for comparison. a) Viability of RAW 264.7 cells after incubation with different FM formulations for 24 h as measured by the MTT assay (n=4). The viability was compared to cells treated with PBS (100% viability). b) Percent cell uptake (DiR+ live cells) by RAW 264.7 cells after incubation for 4 h and 24 h with DiR-loaded FM formulations in Table 2-7 (0.25 mg mL^{-1}) as measured by flow cytometry (n=3-6). Statistical significance was determined by ANOVA with post hoc Tukey's test to correct for multiple comparisons with a 5 percent significance level (* $p < 0.05$, **** $p < 0.0001$). The mean is displayed together with error bars representing the SEM.

3.4.3. mPBI-FM Flexibility Affects Cell Uptake in Murine Macrophages in vitro

Taking advantage of my ability to form FM with a range of flexibilities, I conducted a systematic investigation into whether FM flexibility affects cytotoxicity and cellular internalization. I first assessed viability of the macrophages after incubation with the FM formulations in Table 2-7 at different concentrations up to 0.5 mg mL^{-1} for 24 h using an MTT (methyl-thiazolyl-tetrazolium) assay. Dose-dependent cytotoxicity was observed with the least flexible FM, mPBI-FM-A and mPBI-FM-B, while the more flexible FM, particularly mPBI-FM-C and (-)PBI-FM, were found to be non-toxic (**Figure 3-3A**). Of note, the most rigid FM (types A and B) contained 50 mol% of PBI tetrablock copolymer compared to 20 mol% for types C and D. To confirm that the cytotoxicity observed is due to FM rigidity and not the concentration of PBI tetrablock copolymer the cells are exposed to, macrophage viability was again assessed with mPBI-FM-C and mPBI-FM-D, but at the same concentration of PBI tetrablock copolymer as

mPBI-FM-A and mPBI-FM-B (**Figure 3-4**). The percent viability was not dependent on the dose of the mPBI-FM, so the cytotoxicity observed with mPBI-FM-A and mPBI-FM-B was not related to the amount of PBI tetrablock copolymer in the formulation (Figure 3-4), but to the properties of the FM. The cytotoxicity observed with the most rigid FM may be similar to cytotoxicity observed with multiwalled carbon nanotubes (MWCNTs) which are generally very rigid with $L_c/L_p < 1$.¹⁷⁹ It is known that MWCNTs having thin and rigid physical properties exhibit cytotoxic effects in mouse macrophage cell lines.^{180, 181}

I then assessed cellular uptake of the FM at a concentration of 0.25 mg mL^{-1} with RAW 264.7 macrophages through flow cytometry at 4 h and 24 h incubation timepoints. The FM were loaded with DiR, a hydrophobic NIR dye, to enable fluorescence detection and tracking of the nanocarriers. The percentage of FM positive (FM+) cells increased from 4 h to 24 h for all formulations (Figure 3-3B). In addition to this consistent time-dependent increase in FM uptake, the level of nanocarrier internalization was found to differ for the different FM types examined. The least flexible, cytotoxic mPBI-FM-A and mPBI-FM-B exhibited high levels of cell uptake (Figure 3-3B). For mPBI-FM types C to E and (-)PBI-FM, cell uptake increased with increasing FM flexibility (Figure 3-3B). Interestingly, mPBI-FM-C and mPBI-FM-D, having moderate flexibilities of L_c/L_p of 5.5 and 9.0 respectively, were internalized by macrophages at a significantly lower rate compared to mPBI-FM-E and (-)PBI-FM ($p < 0.05$). Confocal microscopy revealed that the FM were internalized by the macrophages and were not merely associated with the cell surface (**Figure 3-5**). These results are comparable to previous studies with FM self-assembled from PEG-*b*-polyethylenethylene (PEG-*b*-PEE), where FM nanocarriers having a length greater than $3 \mu\text{m}$, or a L_c/L_p of 6, led to decreased phagocytosis in an activated human

macrophage cell line after a 24 h incubation period in static culture.⁵⁶ PEG-*b*-PEE FM less than 3 μm in length ($L_c/L_p < 6$) were phagocytosed at a greater rate by the activated human macrophages.⁵⁶ In summary, these studies demonstrate that differences in flexibility affect the cytotoxicity and cell uptake profiles of FM in vitro. The least flexible FM (mPBI-FM types A and B) were cytotoxic, while FM in the middle range of flexibilities studied here (mPBI-FM types C and D) reduced nanocarrier uptake by macrophages.

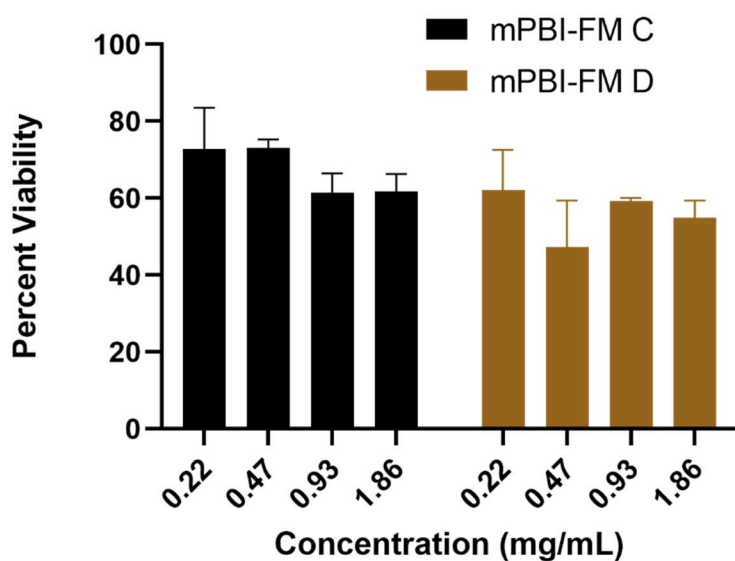


Figure 3-4. Viability of RAW 264.7 cells after incubation with increased concentrations of mPBI-FM-C and mPBI-FM-D, as measured by the MTT assay (n=4). The viability was normalized by cells treated with PBS (100% viability).

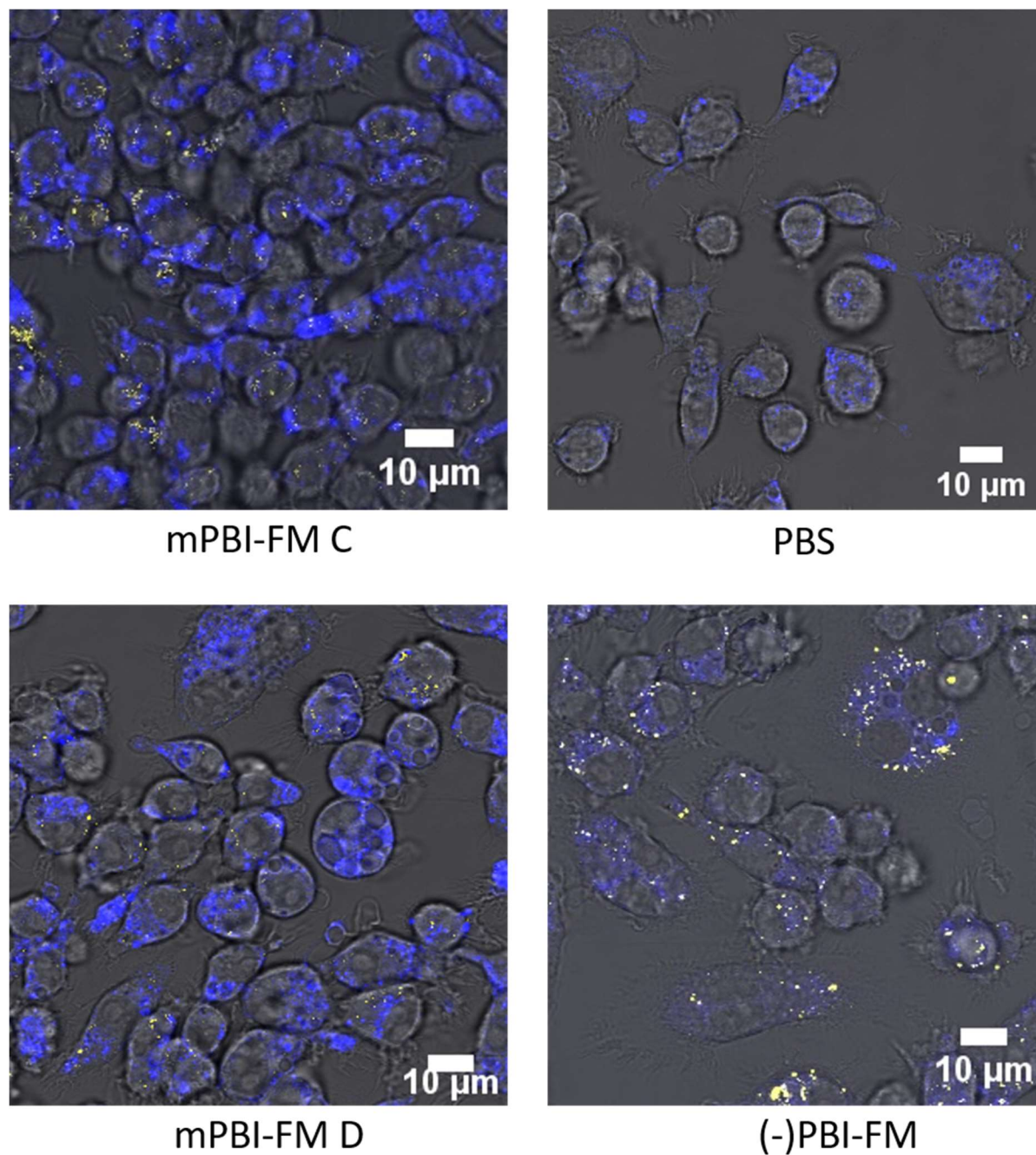


Figure 3-5. mPBI-FM loaded with DiR, a near infrared (NIR) dye, are internalized by RAW 264.7 macrophages. Confocal images were obtained after 24 h of incubation with the nanocarriers (polymer concentration of 0.25 mg/ mL) with (-)PBI-FM and PBS as controls. Lysosomes are

labeled with Lysotracker (blue) and DiR is shown in yellow. Colocalization of Lysotracker and DiR is white.

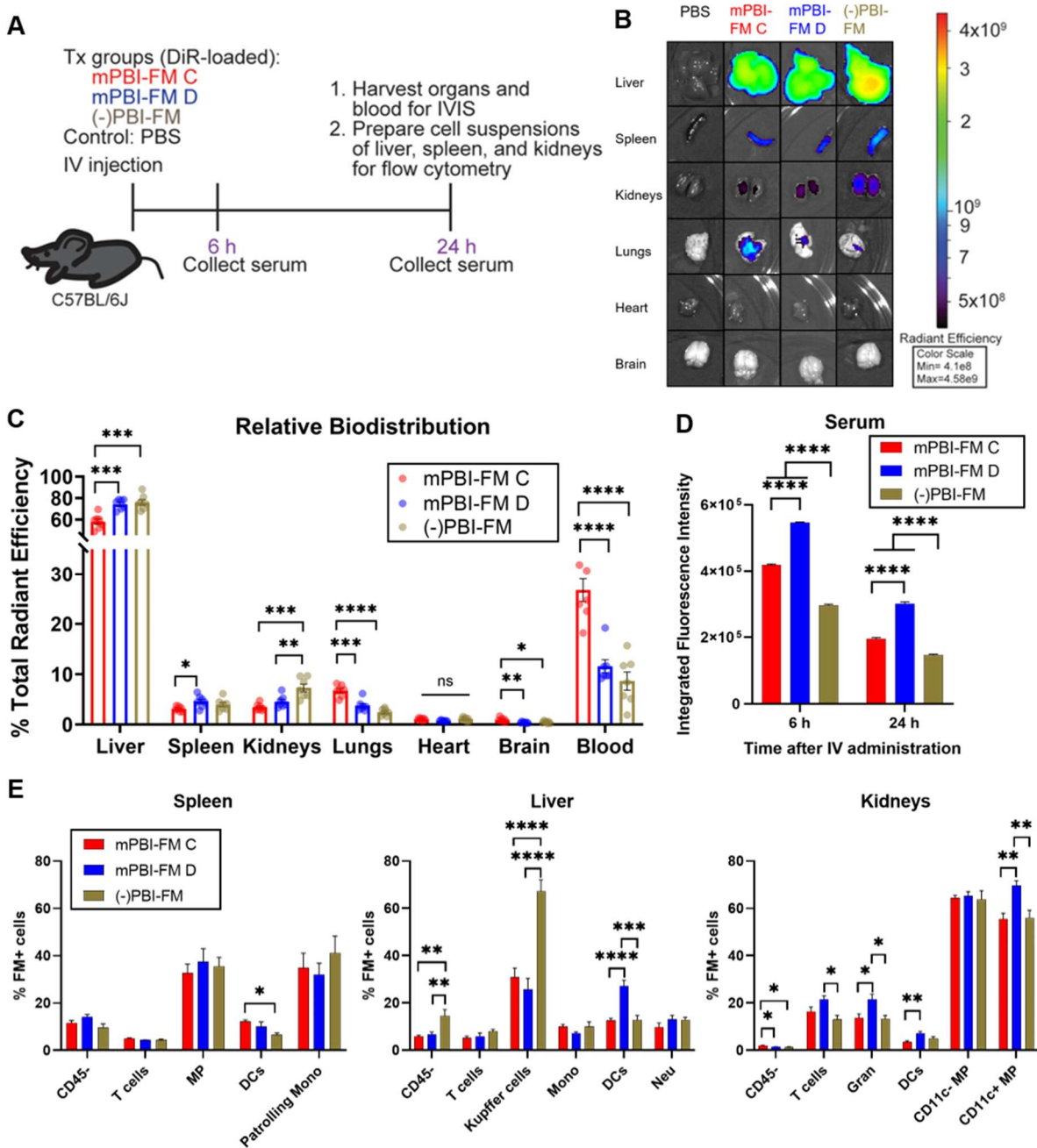


Figure 3-6. PBI incorporation into FM alters nanocarrier biodistribution in vivo. a)

Schematic of the experimental design of in vivo studies. mPBI-FM-C, mPBI-FM-D, and (-)PBI-FM loaded with NiR dye DiR were administered intravenously in C57BL/6J mice (n=7). Mice injected with PBS were included as controls (n=3). Serum was collected 6 h and 24 h after injection. At 24 h, organs and whole blood were collected for IVIS, and the liver, spleen and kidneys were processed for cellular-level biodistribution analysis by flow cytometry. b) Representative fluorescence images obtained via IVIS for the liver, spleen, kidneys, lungs, heart and brain 24 h after IV injection. c) Relative biodistribution of each FM for each organ and whole blood, as the percentage of the total adjusted RE. d) Integrated fluorescence intensity of DiR in the serum at 6 h and 24 h post-injection. e) FM association with various immune cell populations (DiR positive cells) in the spleen, liver, and kidneys. Within each organ or timepoint, statistical significance was determined by ANOVA with post hoc Tukey's test to correct for multiple comparisons with a 5 percent significance level (*p<0.05, **p<0.01, ***p<0.001, ****p<0.0001). The mean is displayed, with error bars representing the SEM.

3.4.4. PBI Incorporation Modulates FM Biodistribution in vivo

As mPBI-FM types C and D led to decreased cell uptake in RAW 264.7 macrophages in vitro, I hypothesized that these mPBI-FM formulations would have decreased uptake in the mononuclear phagocyte system (MPS) resulting in increased circulation times in vivo compared to (-)PBI-FM. The MPS, a network of phagocytic cells including blood monocytes, tissue macrophages, and dendritic cells, is important for clearance of nanoparticles and filamentous

viruses.^{56,182} I therefore investigated the biodistribution of these FM at the organ and cellular levels in a common mouse model (**Figure 3-6A**). I injected C57Bl/6J mice intravenously with DiR-loaded mPBI-FM-C, mPBI-FM-D, (-)PBI-FM or PBS, which served as the negative control. The FM maintained their morphology after DiR loading as confirmed by TEM (**Figure 3-7**).

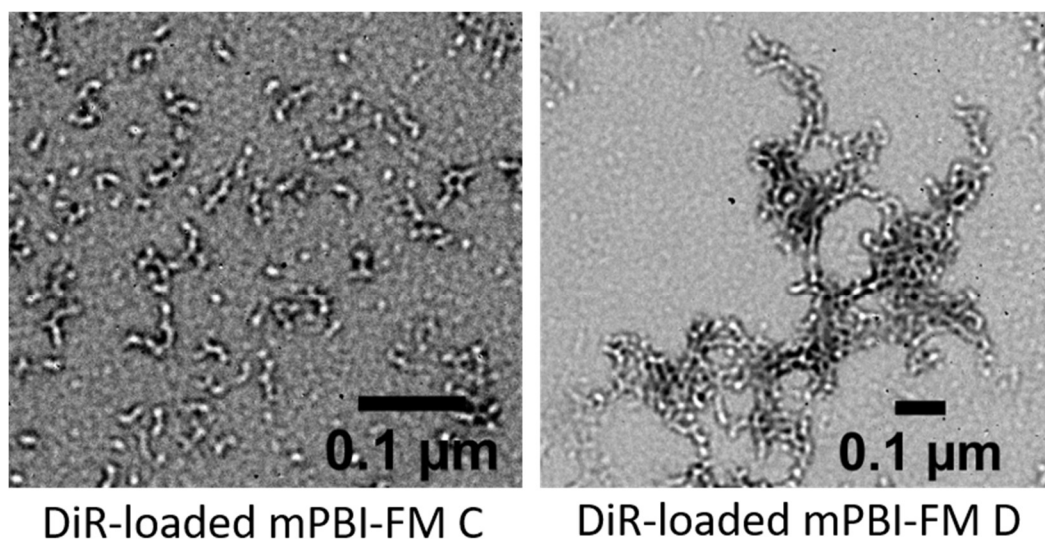


Figure 3-7. mPBI-FM maintained a filamentous morphology after loading DiR in the FM core. TEM micrographs of negatively stained specimens are displayed.

At the organ-level, I assessed the relative biodistribution of the FM among the different organs, which accounts for any inherent differences in fluorescence of the three FM formulations prior to injection. Fluorescence images of representative organs are displayed in **Figure 3-6B**, with images of collected whole blood presented in **Figure 3-8**. For each mouse, the adjusted radiant efficiency of the liver, spleen, kidneys, lungs, heart, brain, and whole blood were summed to determine the total radiant efficiency, and the percentage of the total radiant efficiency for each

organ was calculated (Figure 3-6C). (-)PBI-FM had a similar biodistribution as seen in previous studies with the most uptake observed in the liver.⁹⁴ For all the FM formulations, after the liver, the blood had the highest fluorescence levels, ranging from 9-27% of the total radiant efficiency. mPBI-FM-C, which was less flexible, had statistically significant differences in relative biodistribution compared to mPBI-FM-D and (-)PBI-FM 24 h after intravenous injection. mPBI-FM-C had significantly less accumulation than mPBI-FM-D in the spleen (Figure 3-6C). Compared to both mPBI-FM-D and (-)PBI-FM, significantly less accumulation of mPBI-FM-C was observed in the liver, while a higher percentage of mPBI-FM-C was observed in the lungs, brain, and blood (Figure 3-6C). A statistically significant increase in fluorescence was also observed in the serum with mPBI-FM-C and mPBI-FM-D compared to (-)PBI-FM (Figure 3-6D). Both mPBI-FM-C and mPBI-FM-D had significantly less accumulation in the kidneys compared to (-)PBI-FM, suggesting reduced renal clearance (Figure 3-6C). The oxidation of PPS in PEG-*b*-PPS block copolymers into more hydrophilic sulfoxides and sulfones leads to nanocarrier disassembly allowing for kidney clearance of the block copolymer.¹⁸³ Based on our in vitro analyses in oxidative conditions, the enhanced stability of mPBI-FM after oxidation compared to (-)PBI-FM (Figure 2-6) most likely reduced oxidation-induced nanocarrier disassembly in vivo leading to decreased clearance by the kidneys.

These results demonstrated that incorporation of PBI into FM can shift the biodistribution of nanocarriers away from the liver, kidneys, and spleen and increase FM in circulation to 27% of the total radiant efficiency 24 h after intravenous injection. The less flexible mPBI-FM-C ($L_c/L_p=5.5$) had increased persistence in circulation compared to the more flexible (-)PBI-FM ($L_c/L_p=22$). These findings regarding circulation time are similar to previous in vivo studies in rats by

Geng *et al.* utilizing FM that are much longer (2 to 18 μm), but have similar diameters and L_c/L_p to the FM in the present study.⁵⁶ Geng *et al.*, found that inert PEG-*b*-PEE FM with $L_c/L_p = 7$ persisted in circulation for up to a week, while degradable PEG-*b*-PCL FM with L_c/L_p ranging from 8 to 36 disappeared from circulation more quickly.⁵⁶ FM flexibility thus is an important parameter that influences circulation time and organ-level biodistribution *in vivo*. Developing nanocarriers with increased circulation time has implications for diverse fields including cancer nanomedicine, where decreased clearance by the MPS enhances nanocarrier accumulation in solid tumors.¹⁸⁴

To better understand how modulation of FM flexibility through PBI incorporation affects clearance by the MPS *in vivo*, I assessed FM biodistribution on a cellular level among various CD45+ immune cell populations along with CD45- cells in the liver, spleen, and kidneys 24 h after intravenous injection (Figure 3-6E). For the three FM formulations, the cell populations with the most nanocarrier uptake in each organ were generally macrophages. In the spleen, preferential uptake for the FM with levels similar to splenic macrophages was also observed in the reservoir of patrolling monocytes.¹⁸⁵ However, there were clear preferences in uptake dependent on FM flexibility on the cellular level. mPBI-FM-C, the least flexible FM, was not preferably internalized by any cell population, aside from some enhanced uptake by dendritic cells (DCs) in the spleen ($p < 0.05$) when compared to (-)PBI-FM. This corresponds with the mPBI-FM-C having the lowest accumulation on the organ level in the spleen, liver, and kidneys. In contrast, (-)PBI-FM with the highest flexibility had significantly higher uptake compared to both mPBI-FM types in CD45- cells and Kupffer cells in the liver. mPBI-FM-D, with an intermediate flexibility, had significantly increased uptake by DCs in the liver. This increase in uptake in DCs and decrease in uptake in

Kupffer cells in the liver may explain how there was no significant decrease in uptake at the organ level in the liver for mPBI-FM-D compared to (-)PBI-FM (Figure 3-6C). In the kidneys, immune cell populations generally preferred mPBI-FM-D compared to mPBI-FM-C and (-)PBI-FM, with significant increases observed in granulocytes and CD11c⁺ macrophages. mPBI-FM-D also had significantly higher uptake in T cells in the kidney compared to the more flexible (-)PBI-FM, and kidney DCs preferred mPBI-FM-D over the less flexible mPBI-FM-C. This suggests that the flexibility of mPBI-FM-D is optimal for uptake by multiple immune cell populations in the kidney.

Overall, differences in cellular biodistribution were observed between the three FM formulations, demonstrating that changes in the flexibility of FM having identical surface chemistry influences their cellular interactions. Notably, mPBI-FM-C and mPBI-FM-D had significantly reduced clearance by Kupffer cells in the liver. As Kupffer cells encompass the majority of tissue resident macrophages and play an important role in nanoparticle clearance,¹⁸⁴ ¹⁸⁶ this most likely led to the bioavailability increases observed for mPBI-FM-C and mPBI-FM-D in the blood. Furthermore, these nanocarriers demonstrate passive targeting of immune cells, as mPBI-FM-D had increased uptake in DCs in the liver and multiple immune populations in the kidneys, including granulocytes and DCs. These observations are intriguing, since they suggest the flexibility of nanocarriers can be modified to passively target immune cell subpopulations that play key roles in disease. For example, liver DCs are important in promoting tolerance, so immunomodulation of these cells can be effective in preventing liver transplant rejection.¹⁸⁷

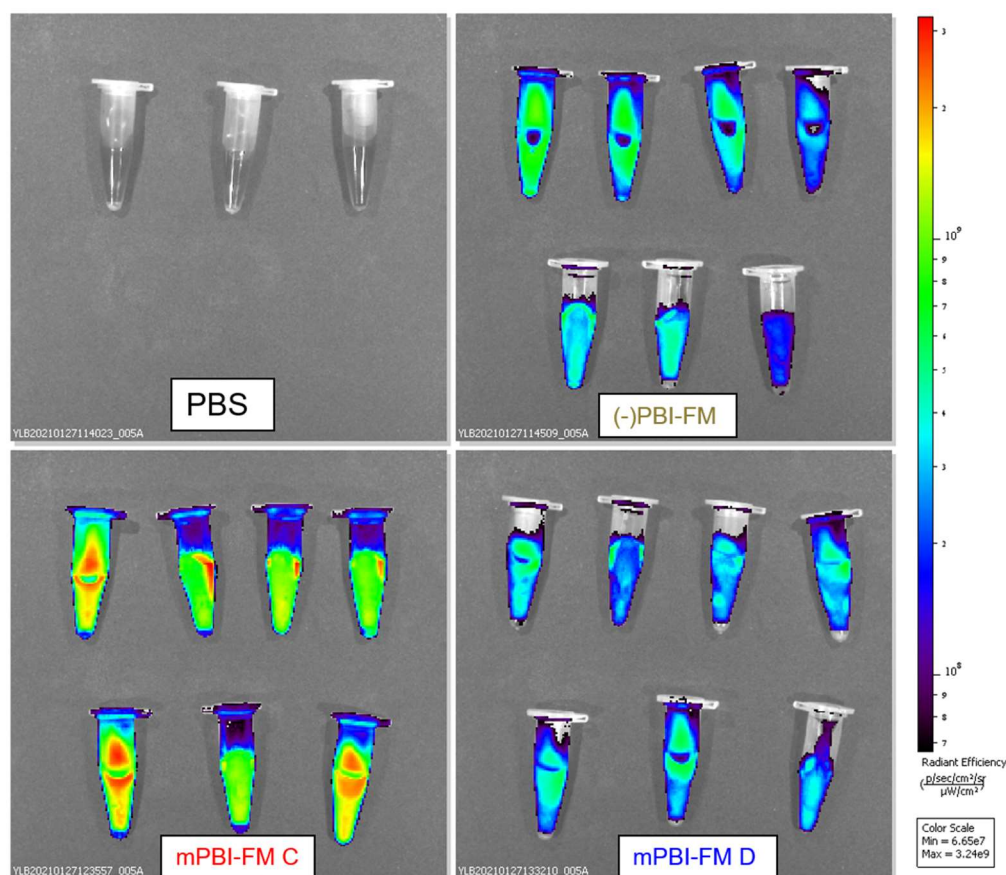


Figure 3-8. Characterization of whole blood fluorescence using IVIS. Fluorescence images of whole blood samples collected 24 h after intravenous administration of DiR-loaded FM nanocarriers in C57Bl/6 mice. A PBS treatment group was included as a negative control.

3.4.5. Effect of filament flexibility on murine macrophage activation in vitro

I investigated whether filament flexibility had an effect on murine macrophage activation in vitro by measuring NF- κ B activation, quantifying surface marker expression, and assessing cytokine release after RAW 264.7 cells were incubated with mPBI-FM types A through E. (-)PBI-FM, (-)PBI-PS, and mPBI-PS-A were included for comparison, and lipopolysaccharide (LPS), a

Toll-like receptor 4 (TLR4) agonist, was utilized as the positive control. I used the Quanti-Blue assay to measure NF- κ B activation of RAW-Blue cells, which are murine RAW 264.7 macrophages modified with a secreted embryonic alkaline phosphatase (SEAP) reporter construct induced by NF- κ B and activator protein 1 (AP-1). I found that none of the mPBI-FM formulations, similar to PBS and (-)PBI-FM and (-)PBI-FM PS, induced NF- κ B activation in RAW-blue cells after incubation for 24 h compared to the positive control of 1 μ g/mL of LPS (**Figure 3-9A**). This demonstrates that mPBI-FM do not activate microbial pattern-recognition receptors (PRRs) expressed by RAW-Blue cells including TLRs, NOD-like receptors, RIG-I-like receptors and C-type lectin receptors, and did not elicit a strong inflammatory response in vitro. Similarly, high levels of IL-10, a cytokine expressed by macrophages after recognition of PRRs, was only produced by RAW 264.7 macrophages after incubation with the positive control of LPS, with none of the nanocarrier formulations inducing IL-10 secretion (Figure 3-9B). As IL-10 expression is induced by TLR signaling (TLR2, TLR3, TLR4, and TLR9) and C-type lectin receptors,¹⁸⁸ these results further suggest that mPBI-FM do not induce TLR and C-type lectin receptor signaling in murine macrophages. Interestingly, incubation with mPBI-FM and mPBI-PS formulations led to upregulation of CD80 and MHC II in RAW 264.7 macrophages compared to the PBS control (**Figure 3-10**). The most rigid mPBI-FM (types A and B) also led to the most upregulation of CD86, while mPBI-FM-E, mPBI-PS-A, and (-)PBI PS slightly upregulated CD86 compared to the PBS control (Figure 3-10). While NF- κ B activation was not observed, low IL-10 secretion and upregulation of MHC II and the costimulatory molecules CD80/CD86 suggest that mPBI-FM, particularly the most rigid types A and B, can activate macrophages toward the classically-activated macrophage phenotype and are not inducing polarization toward an anti-inflammatory

regulatory macrophage phenotype.¹⁷⁴ In addition, FM flexibility affects macrophage surface marker expression levels, as mPBI-FM with intermediate flexibility (types C and D) generally showed lower levels of CD80, CD86, and MHC II compared to the most rigid mPBI-FM types A and B. Further assessment of secretion of proinflammatory cytokines such as TNF- α , IL-6, and IL-1 β , and quantification of nitric oxide production can shed more light on whether mPBI-FM are inducing activation of pro-inflammatory, M1-like macrophages or a distinct mixed M1/M2 phenotype.¹⁷⁴

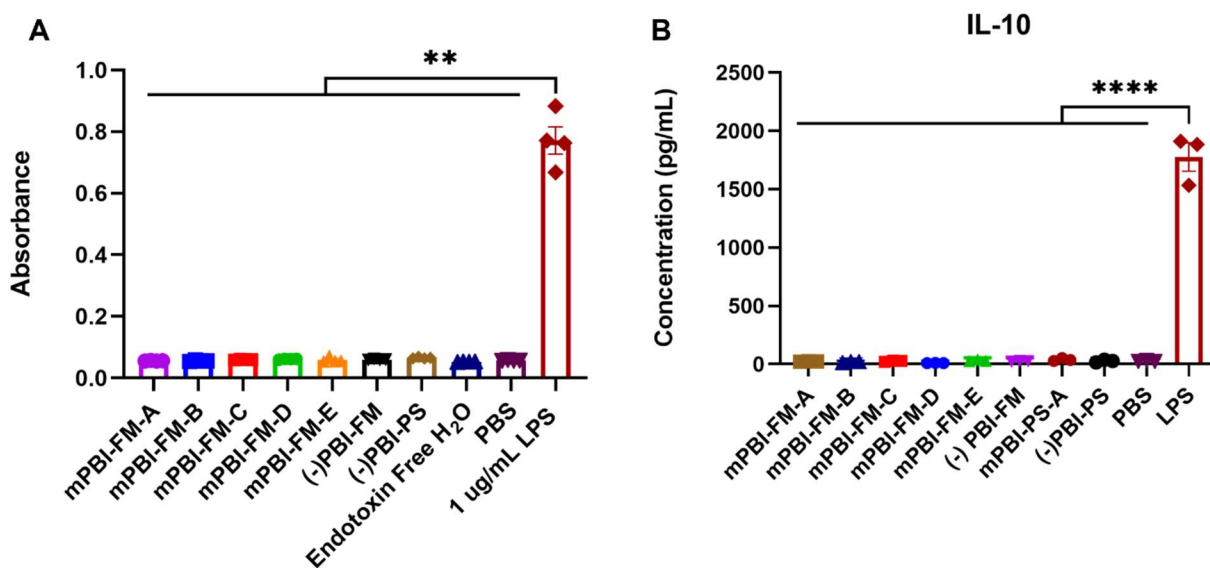


Figure 3-9. Effect on filament flexibility on NF- κ B activation and IL-10 cytokine production in murine macrophages in vitro. a) NF- κ B activation of RAW-Blue cells (modified RAW 264.7 cells) after incubation with 0.5 mg mL^{-1} of different mPBI-FM formulations for 24 h as measured by the Quanti-Blue Assay (n=4). Statistical significance was determined by Brown-Forsythe and Welch ANOVA tests with post hoc Dunnett's test to correct for multiple comparisons with a 5 percent significance level (**p<0.01). b) IL-10 cytokine release in vitro by RAW 264.7 cells after

24 h of incubation with mPBI-FM formulations (n=3). 1 $\mu\text{g}/\text{mL}$ of LPS served as the positive control. Statistical significance was determined by one-way ANOVA with post hoc Tukey's test to correct for multiple comparisons with a 5 percent significance level (****p<0.0001). The mean is displayed, with error bars representing the SEM for both A and B.

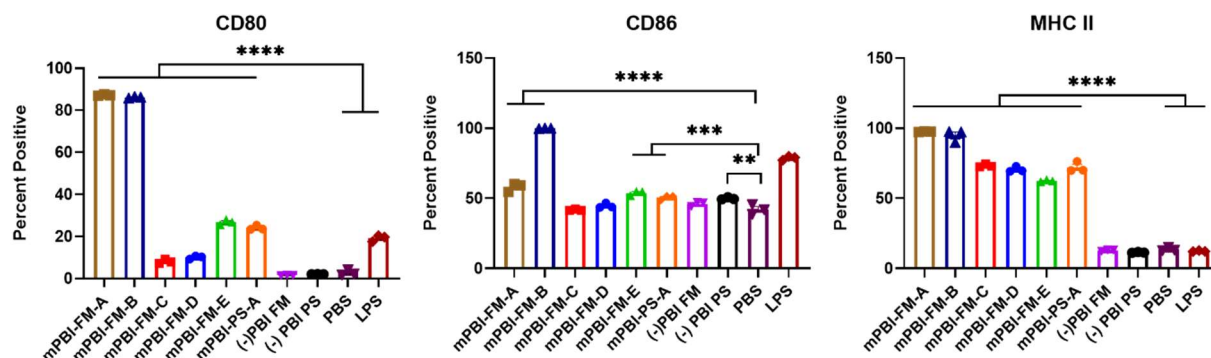


Figure 3-10. Surface marker expression of CD80, CD86, and MHC II on RAW 264.7 macrophages after 24 h incubation with mPBI-FM and mPBI-PS (n=3). (-)PBI-FM and (-)PBI-PS were included for comparison. 1 $\mu\text{g mL}^{-1}$ of LPS served as the positive control. Statistical significance was determined by one-way ANOVA with post hoc Tukey's test to correct for multiple comparisons with a 5 percent significance level (**p<0.01, ***p<0.001, ****p<0.0001). The mean is displayed, with error bars representing the SEM.

3.4.6. Effect of filament flexibility on serum cytokine levels and biomarkers in vivo

To assess the effect of filament flexibility on immune cell activation, the serum was collected 24 h after intravenous administration of DiR-loaded FM nanocarriers, and cytokine levels of IL-10, IFN- γ , IL-2, and IL-4 were measured to evaluate whether a Th1 or Th2 immune response

had been elicited. None of the mice injected with FM (mPBI-FM-C, mPBI-FM-D, or (-)PBI-FM) had a significant difference in cytokine levels compared to the PBS or free DiR control mice (**Figure 3-11**). These results demonstrate that a strong Th1 or Th2 response was not elicited by FM administration at this time point and suggests that mPBI-FM types C and D of medium flexibility, similar to PEG-*b*-PPS nanocarriers, are non-immunogenic after intravenous administration in vivo.^{39, 189, 190}

The serum biomarkers of alanine aminotransferase (ALT) and creatinine (Cr) for hepatotoxicity and renal toxicity respectively, were also measured 24 h after intravenous administration of DiR-loaded FM. No significant elevations in ALT and Cr were observed compared to the control group of mice injected with PBS (**Figure 3-12**), suggesting that the FM, similar to PEG-*b*-PPS nanocarriers developed previously,^{77, 190} did not lead to hepatotoxicity and renal toxicity in vivo at this timepoint.

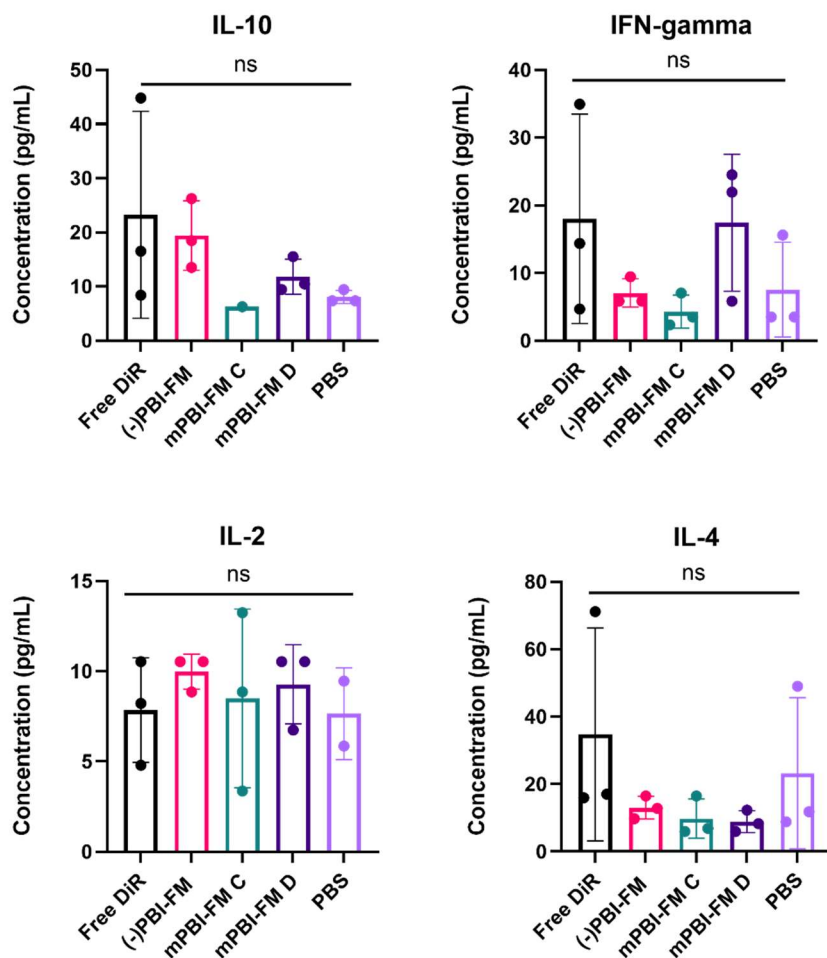


Figure 3-11. Cytokine concentrations in mouse serum collected 24 h after IV injection of DiR-loaded FM nanocarriers in vivo in C57Bl/6 mice (n=3). Statistical significance was determined by ANOVA with post hoc Tukey's test to correct for multiple comparisons with a 5 percent significance level. The mean is displayed, with error bars representing the standard deviation.

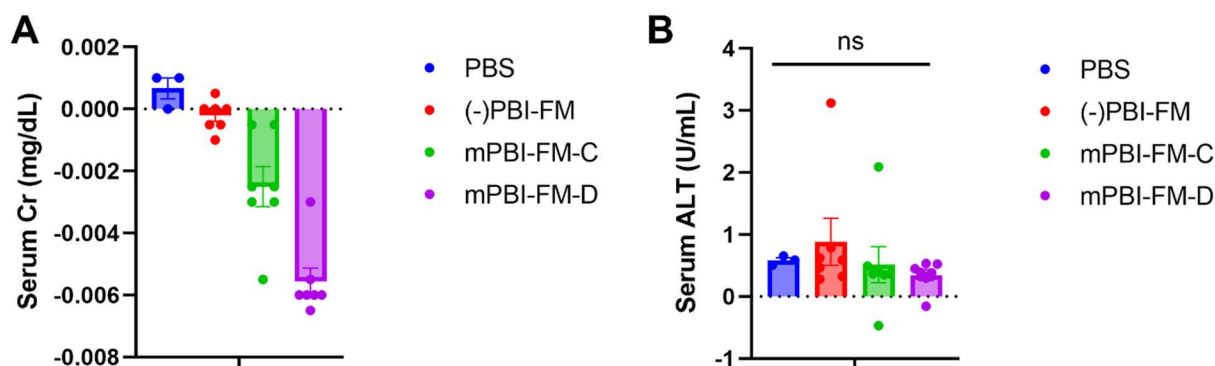


Figure 3-12. Biomarker levels in serum collected 24 h after IV injection of DiR-loaded FM nanocarriers in vivo in C57Bl/6 mice. A) Serum creatinine (Cr), a biomarker for renal toxicity. B) Serum alanine aminotransferase (ALT), a biomarker for hepatotoxicity. Statistical significance was determined by ANOVA with post hoc Tukey's test to correct for multiple comparisons with a 5 percent significance level. The mean is displayed, with error bars representing the SEM.

3.5. Conclusions

As nanocarrier elasticity affects cellular internalization, with softer spherical nanoparticles generally reducing internalization in immune cells,^{148, 191} this ability to modulate FM flexibility can be harnessed to control FM cellular interactions. Control over flexibility was achieved by co-assembling PBI tetrablock copolymers containing pi-stacking moieties with diblock copolymers, a strategy that is potentially applicable across different block copolymer systems.

The flexibility of FMs affected their cytotoxicity, with the greatest toxicity observed for the most rigid mPBI-FM. The mPBI-FM with an optimal flexibility of L_c/L_p from 5.5 to 9 were selected for their decreased toxicity and decreased uptake by murine macrophages in vitro. Notably,

the selected mPBI-FM loaded with the hydrophobic NIR dye DiR exhibited different biodistribution profiles at both an organ level and cellular level *in vivo*, including significantly decreased uptake in Kupffer cells, resulting in increased circulation time compared to (-)PBI-FM. As the flexibility and length of FM affect their performance *in vivo*, my work enabling the formation of FM with a range of flexibilities allows for better understanding of morphology-dependent differences on biodistribution and improved rational design of nanocarriers for biomedical applications. The loading and delivery of a model hydrophobic small molecule DiR by mPBI-FM *in vitro* and *in vivo* also demonstrates the potential of these filamentous nanocarriers for drug delivery.

While increased levels of key Th1 and Th2 cytokines were not observed in the serum after intravenous administration of mPBI-FM types C and D *in vivo*, my work with RAW 264.7 murine macrophages *in vitro* suggests that mPBI-FM, particularly the most rigid types, may activate macrophages as upregulation of MHC II and costimulatory molecules CD80/CD86 were observed. Further studies can elucidate the activation profile of macrophages after treatment with mPBI-FM with varying flexibilities.

3.6. Acknowledgments

Imaging work was performed at the Northwestern University Center for Advanced Molecular Imaging generously supported by NCI CCSG P30 CA060553 awarded to the Robert H. Lurie Comprehensive Cancer Center. Microscopy was performed at the Biological Imaging Facility at Northwestern University, graciously supported by the Chemistry for Life Processes Institute, the NU Office for Research and the Rice Foundation. This work was supported by the

Northwestern University – Flow Cytometry Core Facility supported by Cancer Center Support Grant (NCI CA060553).

3.7. Publication Information

Sections of this chapter have been published, with the citation below:

Li, S.; Bobbala, S.; Vincent, M. P.; Modak, M.; Liu, Y.; Scott, E. A., Pi-Stacking Enhances Stability, Scalability of Formation, Control over Flexibility, and Circulation Time of Polymeric Filamentous Nanocarriers. *Advanced NanoBiomed Research* **2021**, 2100063.

CHAPTER 4

4. Exploration of Potential Applications of Polymeric Filamentous Nanocarriers

4.1. Abstract

Filamentous nanocarriers have advantages for nanomedicine, as their unique morphology enables increased circulation time, high drug loading capacities, and enhanced avidity for drug delivery compared to spherical nanocarriers. In addition, FM are amenable to “cylinder to sphere” morphological transitions for sustained drug delivery. In this chapter, I explore applications of PEG-*b*-PPS FM in improving antiparasitic drug delivery and in passive targeting of tumor-draining lymph nodes for applications in cancer nanomedicine. I loaded PEG-*b*-PPS nanocarriers of both spherical and filamentous morphologies with benznidazole (BNZ), an anti-parasitic drug for Chagas disease, and assessed the cytotoxicity and trypanocidal activity of these drugs in vitro. I also developed a new method to form BNZ-loaded FM hydrogels and began assessing the feasibility of sustained release BNZ systems for Chagas disease prophylaxis. In a different application of cancer nanomedicine, I investigated the biodistribution of different nanocarrier morphologies after intratumoral injection in vivo, including their accumulation in the tumor-draining lymph node. These studies lay the groundwork for PEG-*b*-PPS FM as nanocarriers in two different applications: infectious disease and cancer.

4.2. Introduction

In this chapter, I explore potential applications of FM in two mouse disease models: Chagas disease and a B16F10 melanoma model. The concepts introduced in this chapter include background on Chagas disease, why nanocarrier approaches are needed for prevention and

treatment of Chagas disease, and why nanocarriers are advantageous for cancer nanomedicine, particularly for the application of targeting tumor-draining lymph nodes for immunomodulation.

4.2.1. Chagas Disease

Chagas disease, or American trypanosomiasis, is a neglected tropical disease caused by the obligate intracellular protozoan parasite, *Trypanosoma cruzi*, and usually transmitted by triatomine insect vectors.¹⁹² Chagas disease affects more than 6 million people globally with an incidence of 30,000 new infections per year.¹⁹³ While the disease is currently endemic in 21 countries mostly in Latin America, the CDC estimates that more than 300,000 people are currently infected in the United States.^{194, 195} Cases in the United States are predominantly from imported chronic infections of *T. cruzi*, with some local transmission cycles in the southern United States.¹⁹⁵

Transmission of Chagas disease occurs when feces from the infected vector (triatomine insects) enter through the bite site, a skin abrasion, or the mucosa of a mammalian host.¹⁹⁵ Mammalian reservoirs for *T. cruzi* include opossums, dogs, and rodents. *T. cruzi* infection can also be spread through blood transfusions, organ transplantation, consumption of food contaminated by the vector, and congenitally from the mother to fetus.¹⁹⁶ During the *T. cruzi* life cycle, the parasite has three distinct developmental forms: amastigotes, epimastigotes, and nonreplicative trypomastigotes.¹⁹⁷ Infective metacyclic trypomastigotes, after entry to the body through the feces of the triatomine reduviid bug, invade nucleated cells in a vacuole that fuses with a lysosome. The acidic pH within the vacuole causes the trypomastigote to differentiate into the intracellular amastigote form which migrates to the cytosol in 8-16 hours.¹⁹⁸ In the cytosol, the amastigotes undergo asexual replication for 4-6 days to form pseudocysts, which are

predominantly found in cardiac, smooth, and skeletal muscles and the cells of the mononuclear phagocyte system. The amastigotes then differentiate into trypomastigotes that are released into the blood stream or lymphatic system after cell lysis. The blood-feeding triatomine bugs then ingest the trypomastigotes, where they differentiate into epimastigotes after transformation to an intermediate spheromastigote form in the midgut. This differentiation is induced by decreasing levels of glucose during blood digestion. The epimastigotes replicate by binary fission in the hindgut and then travel to the rectum, where they differentiate into infective metacyclic trypomastigotes.¹⁹⁵

The clinical manifestations of Chagas disease include an acute phase, which begins 1-2 weeks after infection and lasts for 8 weeks, followed by indeterminate (asymptomatic) and chronic phases.¹⁹⁵ During the acute phase, an abscess known as a chagoma at the site of infection and unilateral eyelid swelling known as the Romaña sign can be observed.¹⁹⁹ The eyelid swelling is caused by parasite entry through the conjunctiva or allergic reactions to triatomine antigens.²⁰⁰ In rare cases, severe symptoms such as myocarditis, pericardial effusion, or meningoencephalitis can occur with a high risk of mortality, and are more common with oral transmission.^{201,202} However, most patients are asymptomatic or have mild symptoms such as fever, and thus most infections are not diagnosed during the acute phase. In the indeterminate phase, parasitemia levels fall and become undetectable by light microscopy. An estimated 20 to 30% of patients will develop chronic Chagas cardiomyopathy over the following years to decades, with a high risk of mortality.¹⁹² Clinical manifestations include palpitations, syncope, pulmonary emboli, and arrhythmias.²⁰³ While less common, chronic disease can also involve the gastrointestinal tract,

where patients may present with a range of symptoms including dysphagia, esophageal reflux, weight loss, constipation, bowel ischemia, and megacolon.²⁰⁴

4.2.2. Nanocarrier Approaches for Chagas Disease Prevention and Treatment

T. cruzi infection is life-long without treatment.¹⁹⁵ The two trypanocidal drugs available for treatment of Chagas disease are nifurtimox and benznidazole (BNZ). Benznidazole was FDA-approved in 2017 for the treatment of children ages 2-12 and nifurtimox was approved by the FDA in 2020 for the treatment of children from birth to 18 years of age.^{205, 206} Both drugs are available in oral formulations. For BNZ, the dose for adults and pediatric patients is 5-7 mg/kg and 8-10 mg/kg daily, respectively, for 30-60 days.²⁰⁷ The dose of nifurtimox is 8-10mg/kg daily for adults, 12.5-15 mg/kg for adolescents, and up to 20 mg/kg for pediatric patients for at least 60 days.²⁰⁸ While both treatments are effective, with an 80-90% cure rate during the acute phase of infection,²⁰⁹ patients experience serious side effects, which can lead to discontinuation of treatment. These side effects include rash, edema, fever, and polyneuropathy for BNZ and headache, amnesia, psychiatric symptoms, weight loss, anorexia, and nausea for nifurtimox.²⁰⁵ Both of these drugs are generally poorly soluble in water leading to decreased bioavailability, requiring large daily doses. BNZ is a Class II or IV drug with reduced solubility according to the Biopharmaceutical Classification System, and has a log P of 0.7.²¹⁰ Nifurtimox is a Class III drug with high solubility and low permeability and a calculated log P (CLog P) of 0.02.²¹¹

Nanocarrier approaches for delivery of antitrypanosomal drugs can decrease systemic toxicity of the drugs by altering their biodistribution, increasing circulation time, and improving drug solubility, stability, and permeability.^{205, 212} The trypanocidal activity can also be enhanced

by passive and/or active targeting and intracellular delivery of nanocarriers to specific tissues or cells to increase local effective drug concentrations.²¹³ Because their size and morphological properties resemble that of viruses, nanocarriers generally have enhanced uptake in immune cells, facilitating immunomodulation for disease prevention and treatment.²¹⁴ Nanocarriers can also be engineered to enable sustained release of a drug, reducing dosing frequency. Lastly, nanomedicines may overcome antimicrobial drug resistance, by delivering the drug through different mechanisms and thus avoiding mechanisms of resistance such as efflux pumps.²¹⁵

Different nanoparticle platforms have been explored for the delivery of BNZ and nifurtimox, including polymeric nanoparticles, liposomes, oil nanoemulsions, nanocrystals, and mesoporous silica nanoparticles, with varying efficacy in mice models.^{212, 216} Previous work in the Scott Lab demonstrated that BNZ-loaded PS self-assembled from the triblock copolymer (PEG₁₇-*b*-PPS₆₀-*b*-PEG₁₇) had enhanced potency against intracellular amastigotes compared to free BNZ in H9c2 cardiomyoblasts.²¹⁷ Two doses a week apart of 1.5 mg/kg BNZ-PS led to decreased blood parasitemia comparable to the 100 mg/kg oral BNZ control with no detectable hepatotoxicity. In addition, 1.5 mg/kg BNZ-PS significantly decreased heart inflammation compared to 100 mg/kg oral BNZ. This study demonstrated that PEG-*b*-PPS nanocarriers can enhance the potency of BNZ in vivo while reducing cardiac inflammation and hepatotoxicity.

These findings are especially relevant in the context of chronic Chagas disease, particularly for chronic Chagas cardiomyopathy, where the clinical benefit of BNZ treatment is less clear.²¹⁸ BNZ treatment does not reduce the development of cardiac disease in patients with cardiomyopathy but does reduce progression from the indeterminate form of Chagas disease to

cardiomyopathy.²¹⁸⁻²²⁰ As Chagas cardiomyopathy is thought to involve parasite persistence in cardiac tissue and inflammation induced by the parasite and self-antigens, improved therapies that both eradicate parasites and decrease inflammation is needed.

PEG-*b*-PPS nanocarriers have proven to be advantageous for immunomodulation, as the nanocarriers themselves are non-immunogenic, providing a “blank slate” platform for delivery of immunomodulatory drugs.²²¹ PEG-*b*-PPS self-assembles into nanocarriers of various morphologies with preferential uptake by different immune cells, allowing for passive targeting of immune subtypes, such as antigen-presenting cells.⁹⁴ PEG-*b*-PPS nanocarriers have been utilized to deliver the anti-inflammatory drugs Vitamin D and celestrol for treatment of atherosclerosis, leading to reduced inflammatory cells and plaque area in mice.^{222, 223} Sustained release of Vitamin D from a PEG-*b*-PPS FM depot also induced high levels of regulatory T cells in an ApoE-/- mouse model of atherosclerosis.⁸² Thus, a combined approach utilizing PEG-*b*-PPS to deliver both anti-parasitic drugs and anti-inflammatory agents has great potential for the prevention and treatment of chronic cardiomyopathy in Chagas disease.

4.2.3. Nanocarrier Approaches to Improve Cancer Nanomedicine

Nanocarrier formulations have already been used clinically for cancer nanomedicine and are effective in decreasing the systemic toxicity of chemotherapeutics.²²⁴ For example, Doxil, the PEGylated liposomal formulation of doxorubicin, is known as the first nanoformulation approved by the FDA for AIDS-related Kaposi’s sarcoma, ovarian cancer, metastatic breast cancer, and multiple myeloma.²²⁵ The main advantage of Doxil over free doxorubicin is its ability to modify the biodistribution of the drug to reduce side effects, particularly cardiac toxicity. Nanocarriers

also have the advantages of allowing for encapsulation of multiple drugs, increasing drug accumulation in the tumor through both passive and active targeting, and enabling stimuli-responsive drug release at the tumor site.²²⁴

Besides enhancing tumor delivery of chemotherapeutics, nanocarriers have been used to improve the imaging of tumors for cancer diagnosis and stratification. The enhanced permeation and retention effect, where tissues have increased vascular permeability, is highly heterogeneous depending on the tumor and the patient.²²⁶ Nanocarriers can thus provide imaging assistance to assess nanocarrier biodistribution and tumor accumulation in preclinical models, as well as stratify patients and characterize the extent of the EPR effect for the specific tumor in the clinic. In a complementary approach, nanocarriers can enhance delivery of immunotherapies that can stimulate the immune system to mount antitumor responses.²²⁷ Nanocarriers have been used to target the adaptive immune system through T cell activation, polarizing tumor-associated macrophages toward a more anti-tumor (M1-like) phenotype, and promoting immunogenic cell death to recruit T cells to the tumor.²²⁸ The innate immune system can also be targeted by nanocarriers by activating Pattern Recognition Receptors (PRRs), receptors that detect the presence of pathogens through pathogen-associated molecular patterns (PAMPs) and cellular damage through damage-associated molecular patterns (DAMPs).^{229, 230} This leads to a type I interferon response that also increases T cell migration to the tumor. In another approach to target innate immunity, nanocarriers can deliver drugs to bone-marrow myeloid cells to boost their antitumor response by inducing metabolic and epigenetic changes in the cells to activate the innate immune memory known as “trained immunity.”²²⁸ An effective cancer nanotherapy will most

likely require a combination of these approaches, and ramp up the immune system while delivering chemotherapeutics to the tumor.

4.2.4. Advantages of FM for Advancing Cancer Nanomedicine

Nanocarrier properties, including their size, shape, charge, and surface chemistry, affect their ability to reach and penetrate tumors.²²⁴ Filamentous nanocarriers, as summarized in Chapter 1, have many advantages for nanomedicine, including improving chemotherapeutic delivery to tumors *in vivo* because of their increased systemic circulation times compared to spherical particles, high drug loading capacities, ability to penetrate tumors more deeply than spherical particles, and enhanced avidity for targeted tumor delivery.^{32, 36} FM, because of their unique morphology, have also been shown to target sites of metastases, such as the lungs in a metastatic breast cancer model after intravenous injection.²³¹ Thus, FM have been used to improve treatment of cancer including in models for malignant glioma, lung cancer, and breast cancer.²³²⁻²³⁴

4.2.5. Nanocarrier Targeting of Tumor-draining Lymph Nodes for Immunomodulation

One approach in cancer immunotherapy is to target immunomodulatory drugs to the tumor-draining lymph nodes. Lymph nodes are sites of the adaptive immune response and thus contain specific immune cell subtypes including dendritic cells, macrophages, B cells, and T cells.²³⁵ Targeting lymph nodes is useful in the context of cancer vaccines, where antigens and co-stimulatory agents are delivered to antigen-presenting cells (APCs), such as dendritic cells and macrophages, to activate the adaptive immune response.²³⁶ In the case of a tumor draining lymph node, the lymph node already contains tumor antigen, so delivery of an adjuvant can induce an immune response against the tumor.²³⁶ Immunomodulatory drugs can also be delivered directly to

lymphocytes to regulate their activation and function. In addition, lymph node targeting allows for targeting and eradication of lymph node-resident cancers such as lymphomas and metastases.²³⁷

Different nanocarrier platforms have been explored for targeted delivery to the lymph nodes, including micelles, dendrimers, liposomes, inorganic nanoparticles, and sustained release hydrogels.²³⁷ The nanocarriers can be targeted to the lymph node via different mechanisms: through lymphatic uptake, by targeting peripheral APCs that then migrate into the lymph nodes, targeting circulating lymphocytes, and through the bloodstream.²³⁶ Nanocarriers with increased flexibility (flexible macromolecules vs. rigid spheres), increased diffusivity through the ECM, and with a size of 10-100 nm are most efficiently taken up into the lymphatic system.²³⁸ Targeting lymphatic uptake is especially of interest for targeting tumor draining lymph nodes, as transport through the afferent lymph can increase accumulation in the draining lymph node by a 1000-fold compared to transport through systemic circulation.²³⁹ Many different APCs reside in the periphery, including cutaneous dendritic cells and Langerhans cells in the skin, lung APCs and mucosal APCs, which can be targeted through intradermal delivery, pulmonary delivery, and oral delivery respectively.²⁴⁰⁻²⁴² For targeting circulating lymphocytes, lymphocytes can be removed, covalently attached to nanocarriers, and returned to “backpack” the cargo to the lymph nodes.²⁴³ To target the lymph node through the bloodstream, nanocarriers can target T cells which are able to transmigrate through high endothelial venules into the lymph nodes.²³⁶ The bloodstream also can target lymph node tumors as metastatic lymph nodes generally have enhanced permeability due to changes in vasculature.²⁴⁴

4.3. Materials and Methods

4.3.1. Fabrication of BNZ-loaded and Vitamin D-loaded Nanocarriers

BNZ-loaded nanocarriers were formed with 0.5 mg of BNZ (Cayman Chemicals # 29090) added for 10 mg of polymer. BNZ-PS, and BNZ (-)PBI-FM were self-assembled via TFH, as described in Chapter 2. BNZ-PS were extruded 5 times through a 0.2 μM membrane after formation. BNZ-MC and BNZ-mPBI-FM-C were formed via FNP with 1 impingement in PBS and H₂O respectively. For Vitamin D-MC, 100 ng of active Vitamin D₃ or calcitriol (Cayman Chemicals # 71820) was added to 1.5 mg of polymer and Vitamin D-MC were self-assembled via FNP in PBS with 1 impingement. Zeba spin columns with a 7 kDa MW cutoff were utilized to remove free BNZ and Vitamin D.

4.3.2. Transmission Electron Microscopy

After 400 mesh formvar/carbon coated copper grids were glow-discharged, 3 μL of the sample (5-10 mg mL⁻¹ concentration) were applied to the grid. The grid was then gently blotted, washed 2x for 5 seconds each in Milli-Q water, submerged in 1.5% uranyl formate stain for 15-20 seconds, and then blotted and allowed to air-dry. Images were collected with a Jeol 1400 120 kV transmission electron microscope at a range of 5000-30,000 x nominal magnification. Micrographs were acquired using a Gatan 4k x 4k Ultrascan CCD camera and Gatan Digital Micrograph software.

4.3.3. DLS and Zeta-potential Measurement

DLS and zeta-potential measurements were taken with a Zetasizer Nano (Malvern Instruments) with a 4mW He-Ne 633 laser. For DLS, samples were diluted 1:100 in PBS. The number average diameter and polydispersity index were calculated. For zeta-potential

measurements, samples were diluted in 0.1x PBS to a final concentration of 0.1 mg mL⁻¹. For each sample, 3 separate measurements were taken.

4.3.4. Quantification of BNZ Encapsulation Efficiency

Unfiltered sample and filtered sample were incubated in a cocktail of 95% acetonitrile and 5% water overnight with shaking. The samples were then diluted 1:10 and the absorbance was measured at 325 nm. The cocktail (95% acetonitrile and 5% water) was used as the blank and this background absorbance was subtracted. The encapsulation efficiency was calculated as absorbance of filtered sample/absorbance of unfiltered sample multiplied by 100.

4.3.5 Cell Culture and Parasite Purification

The RAW 264.7 murine macrophage cell line was obtained from the American Type Culture Collection (ATCC, Rockville, MD, USA). The cells were cultured in DMEM (Gibco) supplemented with 10% heat-inactivated fetal bovine serum (FBS-Gibco), 100 IU mL⁻¹ of penicillin and 100 µg mL⁻¹ streptomycin (Gibco) at 37°C in a humidified incubator with 5% CO₂ and 95% air.

B16F10 cells (ATCC CRL-6475) were cultured in DMEM supplemented with 10% fetal bovine serum, 100 IU mL⁻¹ of penicillin and 100 µg mL⁻¹ streptomycin at 37°C in a humidified incubator with 5% CO₂ and 95% air.

3T3-L1 murine fibroblasts (ATCC CL-173) were grown until 80-100% confluency in DMEM supplemented with 10% heat-inactivated FBS and 100 IU mL⁻¹ of penicillin and 100 µg mL⁻¹ streptomycin, and then differentiated into adipocytes. The differentiation procedure consisted of 48 h of growth in differentiation medium 1 (DMEM supplemented with 10% FBS, 1.5 µM of insulin from bovine pancreas (Sigma-Aldrich), 1.0 µM dexamethasone (G-Biosciences)

and 0.5 mM iso-butylmethyl-xanthine (Sigma-Aldrich)). The differentiation medium was replaced with Adipocyte Maintenance Medium (DMEM supplemented with 10% FBS and 1.0 μ M bovine insulin (Sigma-Aldrich)). For full differentiation, Adipocyte Maintenance Medium was replaced every 72 h for 15 days after induction, until lipid droplets could be observed by Oil Red O staining (Sigma-Aldrich). The cells were cultured at 37°C in a humidified incubator with 5% CO₂ and 95% air.

H9c2 rat myoblasts (ATCC CRL-1446) were cultured in RPMI supplemented with 5% FBS, 100 IU mL⁻¹ of penicillin, 100 μ g mL⁻¹ streptomycin and 2 mM L-glutamine) at 37°C in a humidified incubator with 5% CO₂ and 95% air.

The CL Brener strain of *T. cruzi* expressing the *Photinus pyralis* luciferase mutant (Ppy RE9) was used for all experiments. Epimastigotes were cultivated at 28 °C in Liver Infusion broth supplemented with 4 g L⁻¹ NaCl, 0.4 g L⁻¹ KCl, 6.0 g L⁻¹ sodium bicarbonate anhydrous, 2 g L⁻¹ glucose, 5g L⁻¹ tryptose, 15 g L⁻¹ yeast extract, 25 mg L⁻¹ hemin, 10 mg L⁻¹ folic acid, and 10% heat-inactivated FBS, pH 7.2. After 15 days, a few trypomastigotes were observed in epimastigote culture flasks. H9c2 rat myoblasts were cultivated with a suspension of trypomastigotes/epimastigotes (10% v/v), at 37 °C, 5% CO₂, for 24 h. The cell flask was washed with PBS repeatedly to remove non-internalized parasites and incubated with DMEM with 2 mM L-Glutamine (Sigma-Aldrich) under the same conditions. After 5-7 days, trypomastigotes were observed in the supernatant. Trypomastigotes were purified from culture supernatants through standard centrifugation methods.²⁴⁵

4.3.6. MTT Assay

RAW 264.7 cells were seeded at a density of 30,000 cells in 100 μL of media per well in a 96-well plate and allowed to adhere overnight. 11 μL of nanocarriers at various concentrations were then added to each well for final nanocarrier concentrations of 0, 0.0625, 0.125, 0.25 and 0.5 mg mL^{-1} . For the free BNZ formulation, BNZ was dissolved in water with 1% DMSO. After 48 h, 12 μL of 5 mg mL^{-1} of MTT (thiazol blue tetrazolium bromide) was added per well, and the cells were incubated at 37°C for 4 h in the dark. The media was removed and 150 μL of DMSO was added to each well to dissolve the formazan crystals.²⁴⁶ The absorbance was measured at 570 nm. The absorbance of any cell debris at 630 nm was subtracted from the absorbance at 570 nm, and the percent cell viability was determined by normalizing the absorbance by the negative control (PBS-treated cells).

4.3.7. Determination of IC₅₀ for Intracellular Amastigotes

RAW 264.7 macrophages, H9c2 myoblasts, and 3T3-L1 adipocytes were seeded in 16 well Nunc Lab-Tek II (Thermo Fisher Scientific) chamber slides at a concentration of 30,000 live cells per well. After 24 h, the cells were infected by 1×10^6 *T. cruzi* trypomastigotes per well, incubated for another 24 h, then washed to remove non-internalized trypomastigotes. The infected cells were then incubated with different concentrations of nanocarriers and free BNZ dissolved in water and <1% DMSO for 48 h, and the slides were fixed with methanol (Sigma-Aldrich) and stained with 10% Giemsa stain (Gibco). Under a light microscope, 100 cells were counted and the number of infected cells and amastigotes were used to determine the Survival Index (percentage of infected cells x mean number of amastigotes/infected cell) for each sample, including the untreated

control.²⁴⁷ Non-linear regression in GraphPad Prism 9.2.0 was used to calculate the IC₅₀ based on a log concentration versus response curve.

4.3.8. Chagas Disease in vivo Study

Seven-week-old male BALB/c mice (The Jackson Laboratory) were fed a standard diet. All in vivo experiments were conducted according to protocols approved by the Institutional Animal Care and Use Committee at Northwestern University (IS00014998). The mice were injected with sterile BNZ-MC, blank MC, or free BNZ (2% DMSO) as indicated in Table 4-3. The mice were infected with 10⁴ trypomastigotes via intraperitoneal injection. The weights of the animals were measured weekly, and bioluminescence detection and blood collection for blood parasitemia measurement were completed 2 times a week. For bioluminescent detection, 15 mg mL⁻¹ D-luciferin potassium salt (Cayman Chemicals) was injected intraperitoneally into mice. Each animal received 150 mg D-luciferin/kg. After 15 min, the bioluminescence was detected on IVIS (PerkinElmer). Data was analyzed on Living Image Software (PerkinElmer) and the background was subtracted for each image. To estimate the blood parasitemia, 3 μL of blood were collected from the tail vein and analyzed under a light microscope using the Pizzy-Brener method.²⁴⁸ The mice were euthanized after 25 days and the serum, heart, spleen, liver, kidneys, large intestine, and adipose tissue were collected for bioluminescence detection by IVIS.

4.3.9. BNZ-loaded FM Hydrogel Formation

100 mg mL⁻¹ of BNZ-loaded FM were self-assembled as in Table 4-4, with 0.5 mg of BNZ added per 10 mg of polymer. 40 μL of BNZ-loaded FM sample were then mixed with 7.5 μL of 100 mg mL⁻¹ 8-arm PEG-vinyl sulfone (MW=10k) and 7.5 μL of 100 mg mL⁻¹ 8-arm PEG-SH

(MW=10k), and then placed in a Teflon mold. After incubation at 37°C for 30 minutes, the gels were removed from the mold.

4.3.10. Rheology Measurements on FM Hydrogels

Rheology was conducted using a dynamic oscillatory rheometer (HR-2 DHR, TA instruments) equipped with an 8 mm flat bottom cone and plate geometry. Frequency dependence of the storage and loss moduli were analyzed in oscillatory mode with an applied strain of 1%.

4.3.11. Fabrication of DiR-loaded Nanocarriers

0.5 weight % of DiR (50 μ g DiR/ 10 mg polymer) was added to the organic solvent during nanocarrier fabrication with either FNP (PS: 5 impingements in PBS, mPBI-FM-C: 1 impingement in water, BCN: 1 impingement in water) or TFH (MC and (-)PBI-FM rehydrated with PBS). After formation, the formulations were filtered in a Zeba spin column with 7k MW cutoff (Thermo Fisher Scientific) to remove free DiR. Nanocarrier fabrication and purification were performed under sterile conditions for in vivo studies.

4.3.12. Measurement of DiR Encapsulation Efficiency

Filtered and unfiltered samples were incubated with 0.1% sodium dodecyl sulfate for 30 minutes with shaking. The fluorescence intensity at an excitation wavelength of 750 and emission wavelength of 780 was measured with a Shimadzu RF-6000 Spectrofluorometer. The encapsulation efficiency was calculated as fluorescence of filtered sample/fluorescence of unfiltered sample multiplied by 100.

4.3.13. Cancer Biodistribution in vivo Study

Female 6-8 week old C57BL/6J mice (The Jackson Laboratory) were fed a standard diet. All in vivo experiments were conducted according to protocols approved by the Institutional

Animal Care and Use Committee at Northwestern University. The mice were injected subcutaneously in the right flank with 10^6 B16F10 melanoma cells. After 7 days, the mice received an intratumoral injection of 50 μ L of DiR-loaded nanocarriers (1 μ g of loaded DiR), PBS, or free DiR. Each group had 3 mice. At the designated time point for each group (24 h, 3 days, or 7 days after intratumoral injection), the mice were sacrificed. After whole-body perfusion with heparinized PBS, the liver, spleen, kidneys, lungs, tumor, and tumor-draining inguinal lymph node were collected into a petri dish for each mouse. The organs were imaged by the IVIS in vivo imaging system (PerkinElmer) with an excitation wavelength of 750 nm and emission wavelength of 780 nm.

IVIS data was analyzed using Living Image software (PerkinElmer). A circular region of interest (ROI) was drawn over each organ, and a background ROI was drawn in an empty area of the petri dish for each mouse. The radiant efficiency, RE, $((\text{p/s/cm}^2/\text{sr})/(\mu\text{W/cm}^2))$ was determined for each ROI. The adjusted radiant efficiency was obtained by subtracting from the radiant efficiency of the organ the radiant efficiency of the background, which was defined as average RE of the background ROI multiplied by the area of the organ ROI and a factor calculated as the radiant efficiency of the organ/(average radiant efficiency x area of the organ ROI). For the images of the organs or mice, the color scale minimum was adjusted until the plate autofluorescence disappeared for all images and the images were displayed with the same logarithmic color scale.

4.3.14. Statistical Analysis

Any pre-processing of data including background subtraction are described above in the relevant methods subsection. Unless otherwise noted in the figure captions, the mean was

presented with error bars representing the SEM. All statistical analyses used a 5% significance level and were performed with GraphPad Prism software (version 9.0.2).

4.4. Results and Discussion

4.4.1 Characterization of BNZ-loaded and Vitamin D-loaded Nanocarriers

I first aimed to assess the effect of nanocarrier morphology on BNZ drug delivery. BNZ-loaded nanocarriers with different morphologies were formed including MC, PS, mPBI-FM types C and D, and (-)PBI-FM, with 0.05 mg of BNZ added per mg of polymer during self-assembly. The encapsulation efficiencies of the nanocarriers are shown in **Figure 4-1**. MC and (-)PBI-FM had the highest encapsulation efficiencies of around 60%, and MC and FM formulations all had significantly higher encapsulation efficiencies compared to PS. mPBI-FM and (-)PBI-FM maintained their filamentous morphology after loading with BNZ (**Figure 4-2**). The nanocarriers all had a near-neutral or negative zeta-potential after BNZ loading (**Table 4-1**).

The active form of Vitamin D₃, also known as calcitriol, was also loaded into MC and used in these studies, as they are representative of MC released from FM hydrogels. The rationale was that if Vitamin D MCs, in combination with BNZ nanocarriers, are effective in reducing parasitemia while decreasing inflammation, then sustained release of BNZ-MC and Vitamin D-MC from a FM hydrogel system should be explored for Chagas disease treatment. The Vitamin D-MC had an average diameter of 20.7 nm with a low PDI of 0.1 as expected of PEG-*b*-PPS MC (Table 4-1).

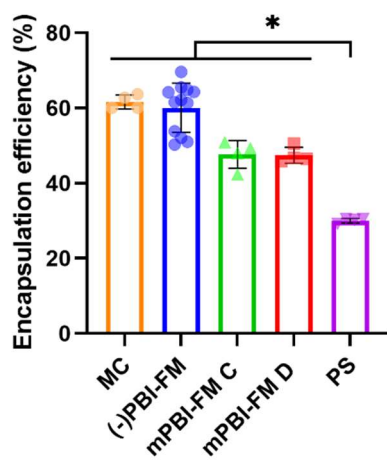


Figure 4-1. Encapsulation efficiency of BNZ-loaded nanocarriers. Statistical significance was determined by ANOVA with post hoc Tukey's test to correct for multiple comparisons with a 5 percent significance level (* $p < 0.05$). The mean is displayed together with error bars representing the SD ($n = 4-12$).

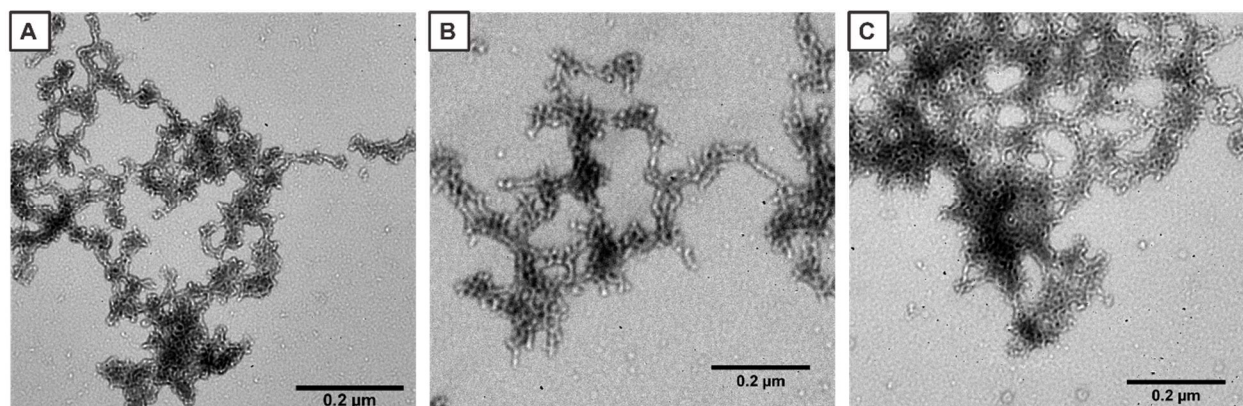


Figure 4-2. TEM images of BNZ-loaded FM formulations. a) (-)PBI-FM b) mPBI-FM-D c) mPBI-FM-C.

Table 4-1. Nanocarrier diameter measured by DLS and Zeta-potential.

	Diameter (nm±SD)	PDI	Zeta-Potential (mV±SD)
BNZ-MC (PEG ₄₅ - <i>b</i> -PPS ₄₀)	17.8 ±5.7	0.1	0.2±5.7
Vitamin D-MC (PEG ₄₅ - <i>b</i> - PPS ₄₀)	20.7 ±6.5	0.10	-2.4±4.0
BNZ (-)PBI-FM	N/A	N/A	-1.7±2.2
BNZ-mPBI-FM-C	N/A	N/A	-4.9±2.0
BNZ-PS (PEG ₁₇ - <i>b</i> -PPS ₃₄)	80.6 ±71.7	0.79	-4.9±0.8

4.4.2 Cytotoxicity of BNZ-loaded Nanocarriers

I next evaluated the cytotoxicity of BNZ-loaded and Vitamin D-loaded nanocarriers for RAW 264.7 macrophages and H9c2 rat cardiomyoblasts, two cell types known to be infected by parasites in Chagas disease. After 48 h of incubation with the nanocarriers at different concentrations up to 0.5 mg mL⁻¹, cell viability was assessed by the MTT assay. Blank nanocarriers were included for comparison. (-)PBI-FM formulations over a month old (Old (-)PBI-FM) were included to represent MCs released from FM over time, as after a month (-)PBI-FM transition to MC. All of the nanocarrier formulations were generally non-toxic in RAW 264.7 cells and H9c2 cells, with no dose-dependent toxicity observed (**Figure 4-3**).

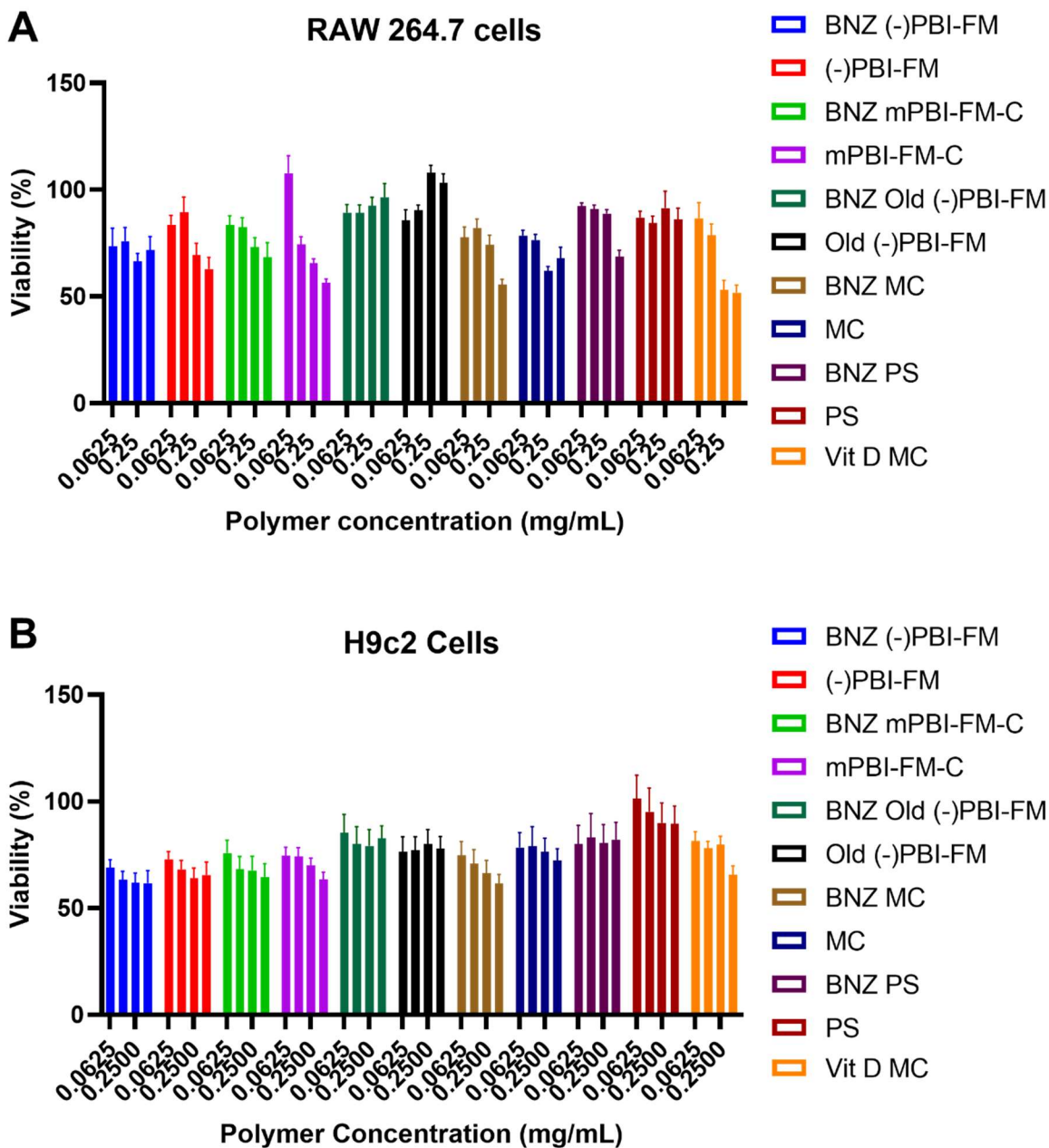


Figure 4-3. Cytotoxicity profiles of BNZ-loaded and Vitamin D-loaded nanocarriers. The nanocarriers were incubated with a) RAW 264.7 murine macrophages and b) H9c2 rat cardiomyoblasts for 48 h, and cytotoxicity was measured by the MTT assay. Blank nanocarriers

without BNZ were included as comparison. The viability was normalized to cells treated with PBS (100% viability). The polymer concentrations from left to right for each formulation were 0.0625 mg mL⁻¹, 0.125 mg mL⁻¹, 0.25 mg mL⁻¹, and 0.5 mg mL⁻¹. The mean is displayed together with error bars representing the SEM (n=8).

4.4.3. Trypanocidal Activity of BNZ-loaded Nanocarriers in vitro

The trypanocidal activity of BNZ-loaded nanocarriers in vitro was then assessed. The host cells of RAW 264.7 macrophages, H9c2 rat cardiomyoblasts, and differentiated 3T3-L1 adipocytes were infected with a bioluminescent CL Brener *T. cruzi* strain, which expresses the red-shifted *Photinus pyralis* luciferase gene (Ppy RE9). These cell types were chosen because macrophages and cardiomyocytes promote inflammatory responses after parasitic infection, especially in chronic Chagas Disease, and parasites have been shown to persist in adipose tissue for decades leading to chronic inflammation.^{249,250} The cells were then treated with 2.5 μM, 5 μM, 10 μM, or 20 μM of BNZ-loaded in nanocarriers for 48 h, the number of parasites in culture was counted, and the half-maximal inhibitory concentration (IC₅₀) was calculated. Free BNZ was included as a positive control. For RAW 264.7 macrophages, none of the nanocarriers had a significantly different IC₅₀ from free BNZ, except for BNZ loaded mPBI-FM-C, which had a significantly higher IC₅₀ (**Figure 4-4**). This is likely because of the lower uptake of these more rigid FM in RAW 264.7 macrophages as seen in Chapter 3. For the adipocytes and myoblasts, all of the nanocarriers had a comparable IC₅₀ for intracellular amastigotes compared to free BNZ. These results suggest that no specific nanocarrier morphology is better for intracellular delivery of BNZ to these three cell types in vitro, and that BNZ-MC have a similar IC₅₀ as BNZ-PS. In addition, the combination of Vitamin D-MC and BNZ-MC had similar IC₅₀ values compared to

BNZ-MC alone in macrophages and cardiac myoblasts, suggesting that the addition of an anti-inflammatory drug does not affect the parasite killing potential of BNZ. While the nanocarriers did not have an effect on the IC₅₀ in vitro, nanocarrier delivery of BNZ is still warranted for investigation in vivo as they alter the biodistribution of the drug, and facilitate delivery to immune cells through passive targeting.⁹⁴

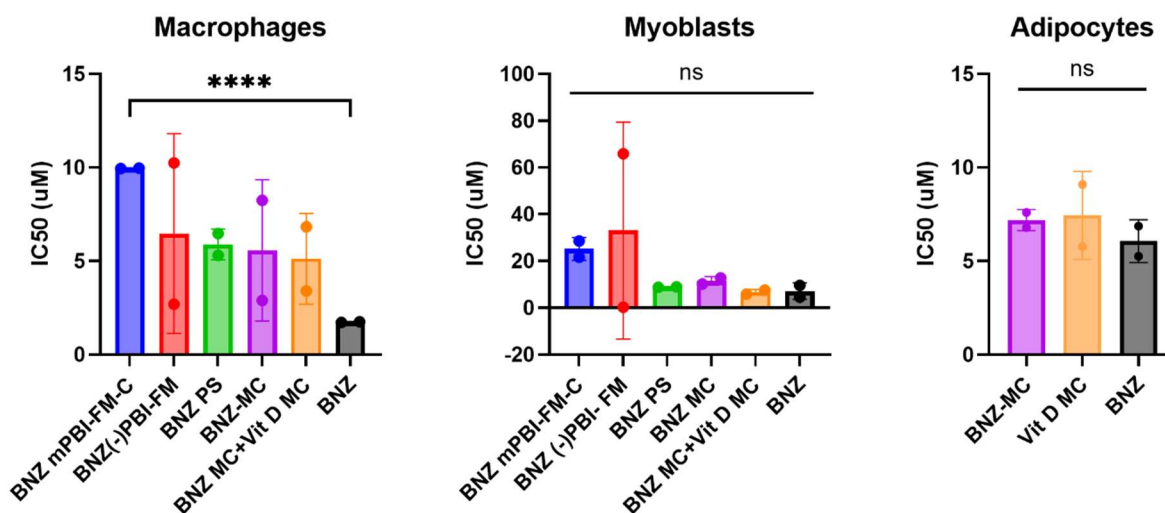


Figure 4-4. IC₅₀ of BNZ-loaded nanocarriers on intracellular amastigotes after 48 h of incubation with infected RAW 264.7 macrophages, H9c2 cardiomyoblasts, and 3T3-L1 adipocytes. Statistical significance was calculated with the Welch ANOVA test with post hoc Dunnett's T3 multiple comparisons test. The mean is displayed together with error bars representing the SD (n=2).

Table 4-2. IC50 values (μM) of BNZ-loaded nanocarriers after 48 h of incubation on intracellular amastigotes in RAW 264.7 macrophages, H9c2 cardiomyoblasts, and 3T3-L1 adipocytes.

	BNZ-MC	BNZ mPBI- FM-C	BNZ (-) PBI- FM	BNZ-PS	BNZ- MC+Vit D-MC	BNZ	Vit D- MC
Macrophages	5.56 \pm 3.78	9.96 \pm 0.02	6.47 \pm 5.3 3	5.89 \pm 0.82	5.12 \pm 2.43	1.74 \pm 0.03	
Cardiomyoblasts	11.47 \pm 1.86	25.13 \pm 4.8 8	33.02 \pm 46 .37	8.87 \pm 0.18	6.68 \pm 1.20	7.06 \pm 3.56	
Adipocytes	7.20 \pm 0.57					6.07 \pm 1.14	7.44 \pm 2.35

4.4.4. Effect of BNZ-loaded MC on Parasitemia and Parasite Load in vivo

PEG-*b*-PPS FM hydrogel systems have previously been utilized for the sustained delivery of Vitamin D-loaded MC to induce regulatory T cells in a mouse model of atherosclerosis.²⁵¹ To evaluate the potential of a sustained release hydrogel depot for BNZ to prevent or treat Chagas disease, I aimed to evaluate the efficacy of different injection regimens of BNZ-MC for prophylaxis of Chagas disease in a mouse model. As 1.5 mg/kg of BNZ encapsulated in PS administered weekly by intravenous injection was shown to be effective for suppressing parasitemia after infection previously,²¹⁷ I investigated whether BNZ-loaded MC at this dose could prevent parasitemia. The treatment groups for this study is summarized in **Table 4-3** and **Figure 4-5**. Subcutaneous (SC) administration of two doses of 1.5 mg/kg BNZ loaded in MC was included to mimic sustained release of MC from a subcutaneous FM depot. A retroorbital intravenous injection of 1.5 mg/kg BNZ loaded in MC one day before infection was included to

assess whether this dose is effective for Chagas disease prophylaxis. In group 3, 1.5mg/kg of BNZ loaded in MC was administered 7 days post injection(dpi) and 14 dpi for two weeks, in the same dosing regimen as reported previously with PS, to assess if this dose is also effective for Chagas disease treatment when encapsulated in a different nanocarrier morphology. 100 mg/kg of BNZ daily delivered through oral administration served as the gold standard BNZ treatment and positive control. Blank MC, 1.5 mg/kg of free BNZ, and a no treatment group were included as negative controls. BALB/c mice (n=3 for each group) were infected with the CL Brener strain of *T. cruzi*, which expresses the *Photinus pyralis* luciferase gene *Ppy RE9*, by intraperitoneal injection. A group of 3 mice was not infected and included as another control. The weight of the animals, blood parasitemia, and *T. cruzi* bioluminescence were measured over the course of 25 dpi. The mice were sacrificed 25 dpi, and the serum, heart, spleen, liver, kidneys, large intestine, and adipose tissue were collected and the bioluminescence of these organs was measured.

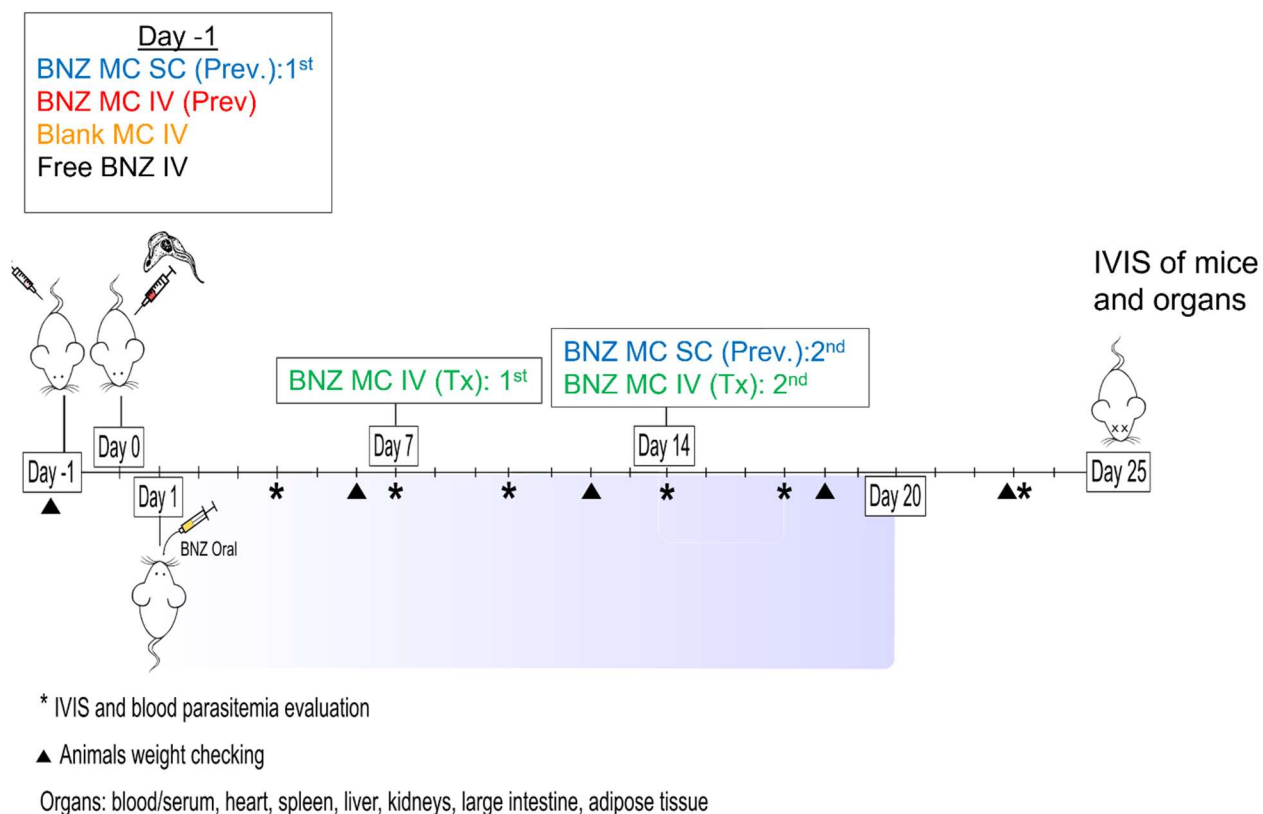


Figure 4-5. Schematic of experimental design of in vivo study to assess effect of BNZ-MC on preventing or treating Chagas disease. The injection schedule for the treatment groups is shown. The BALB/c mice (n=3) were infected with the CL Brener strain of *T. cruzi* on Day 0.

Table 4-3. Treatment groups to assess effect of BNZ-MC on preventing or treating *T. cruzi* infection in a Chagas disease mouse model.

Group	Dose	Timing	Method	Purpose
1	1.5 mg BNZ MC/kg	1 day before infection, day 14	SC	Mimic subcutaneous sustained release FM depot for prophylaxis

2	1.5 mg BNZ MC/kg	1 day before infection	IV	Assess prophylaxis dosage
3	1.5 mg BNZ MC/kg	Day 7 and 14	IV	Assess if BNZ-MC perform similarly to BNZ-PS in previous paper ²¹⁷
4	100 mg BNZ/kg	Day 1 (daily)	oral	Gold standard BNZ treatment
5	Blank MC	1 day before infection	IV	Negative control
6	1.5 mg/kg Free BNZ	1 day before infection	IV	Negative control
7	Infected, no treatment	N/A	N/A	Negative control
8	Uninfected	N/A	N/A	Control

No differences in weight were observed among the different infected groups, compared to the uninfected mice (**Figure 4-6**). The gold standard oral treatment of 100 mg/kg BNZ suppressed blood parasitemia (**Figure 4-7**). Large variability in blood parasitemia levels was observed in all the treatment groups besides the no treatment group and oral BNZ group. The only statistically significant difference in blood parasitemia detected for all the IV and SC treatment groups was in BNZ-MCs two doses IV (group 3) compared to the untreated group 14 dpi (Figure 4-7). On day 25 after infection, the parasite load in the heart, spleen, liver, kidneys, large intestine and adipose tissue was measured with IVIS. No significant differences in parasite load were observed between any of the groups in all the organs (**Figure 4-8**).

For total parasite load in the mice as measured by IVIS, again no parasites were detected in the body on IVIS after the oral BNZ treatment was started (**Figure 4-9**). Of note, the parasite load on day 0 after infection varied greatly for the different treatment groups (Figure 4-9) even though the same number of parasites (10^4) were injected intraperitoneally in each mouse. To adjust for the variability in parasite load on Day 0, the *T. cruzi* luminescence on day 0 was subtracted from subsequent time points, showing the parasite load after infection in relation to initial parasite load at infection (**Figure 4-10**). As expected, a significant difference in luminescence compared to the untreated group was seen for the control oral BNZ group 14, 17, 20, and 23 dpi (Figure 4-10). A significant difference in luminescence was also observed on day 20 for the BNZ-MC SC prophylaxis treatment compared to the untreated group (Figure 4-10). This suggests that subcutaneous injections of BNZ-MC have the potential to reduce parasite load, and that a subcutaneous hydrogel depot for sustained release of BNZ-MC warrants further investigation and optimization.

Some approaches to address the wide variability of parasitemia or parasite load within groups is to increase the sample size and to change the injection procedure, such as utilizing tail vein IV injections instead of retroorbital injections. The untreated group had the lowest intragroup variability, suggesting that mouse handling and anesthesia required for the injections in the treatment groups may be impacting the mice's immune responses leading to greater variability in parasitemia. An oral route of parasite infection can be compared with intraperitoneal infection to see whether the route of infection affects variance in parasitemia levels at day 1. A higher dose of BNZ-MCs and a more frequent schedule of SC BNZ-MC injections (Day before infection and 7 dpi instead of 14 dpi) can also be assessed.

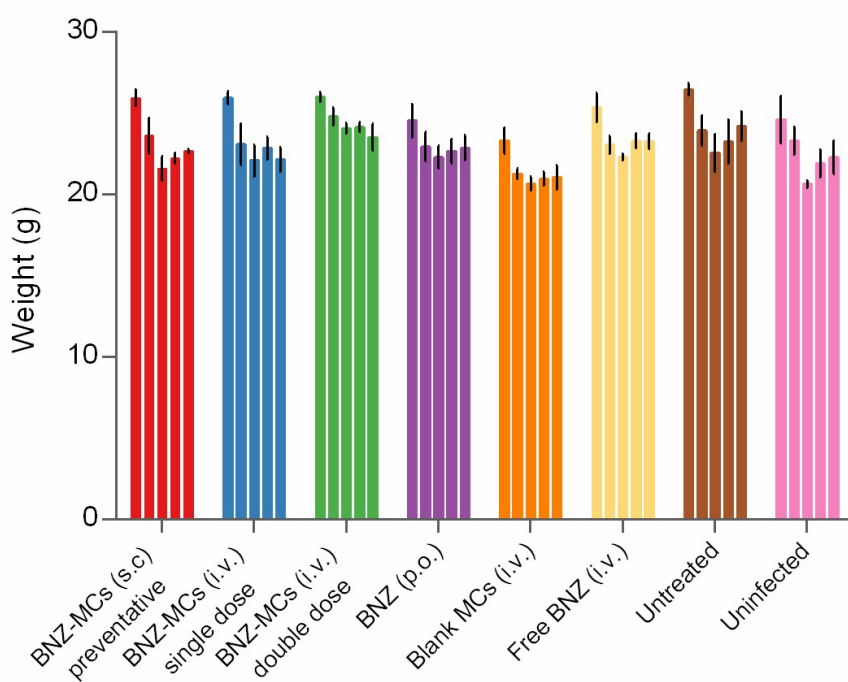


Figure 4-6. Weekly weights of the mice during the study. The weights of the BALB/c mice were measured once a week for a total of 5 timepoints (Day -1, Day 6, Day 12, Day 18, and Day 23) (n=3). The mean is displayed with error bars representing the SEM.

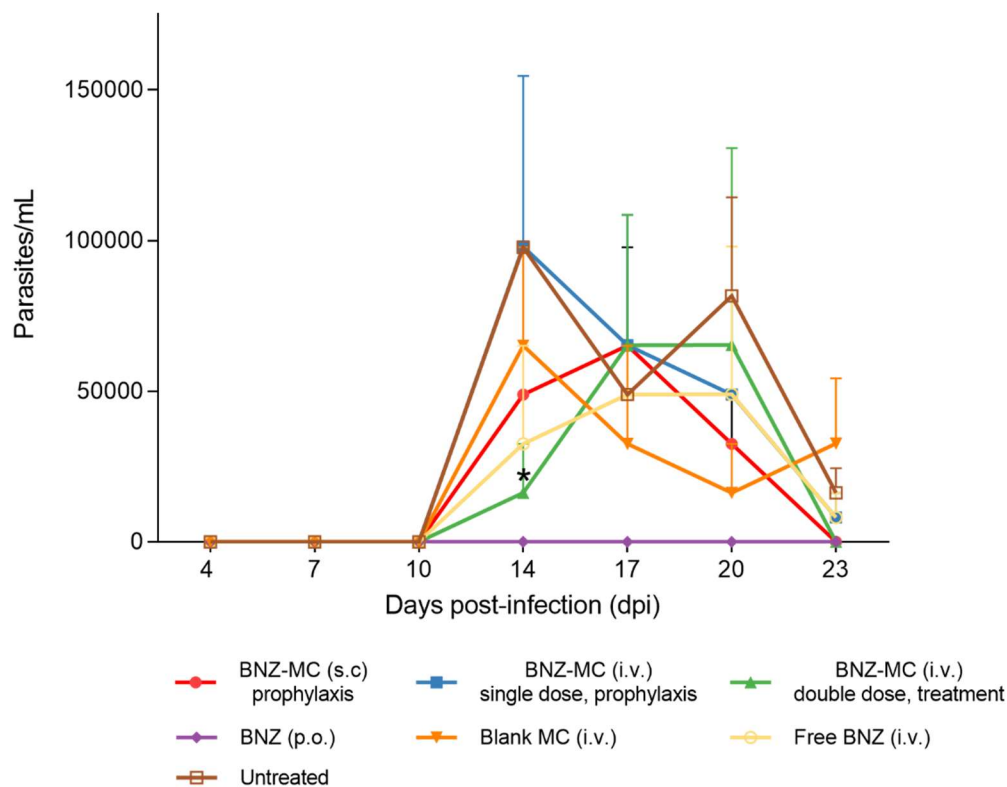


Figure 4-7. Blood parasitemia for different BNZ-MC regimens. Blood samples were collected twice a week on Day 4, Day 7, Day 10, Day 14, Day 17, Day 20, and Day 23. Blank MCs, free BNZ IV (1.5 mg/kg), and untreated mice served as negative controls, and 100 mg/kg oral BNZ daily served as the positive control. Statistical significance was determined by two-way ANOVA with post-hoc Dunnett's multiple comparison test. The mean is represented (n=3) and the error bar above each point represents the SEM.

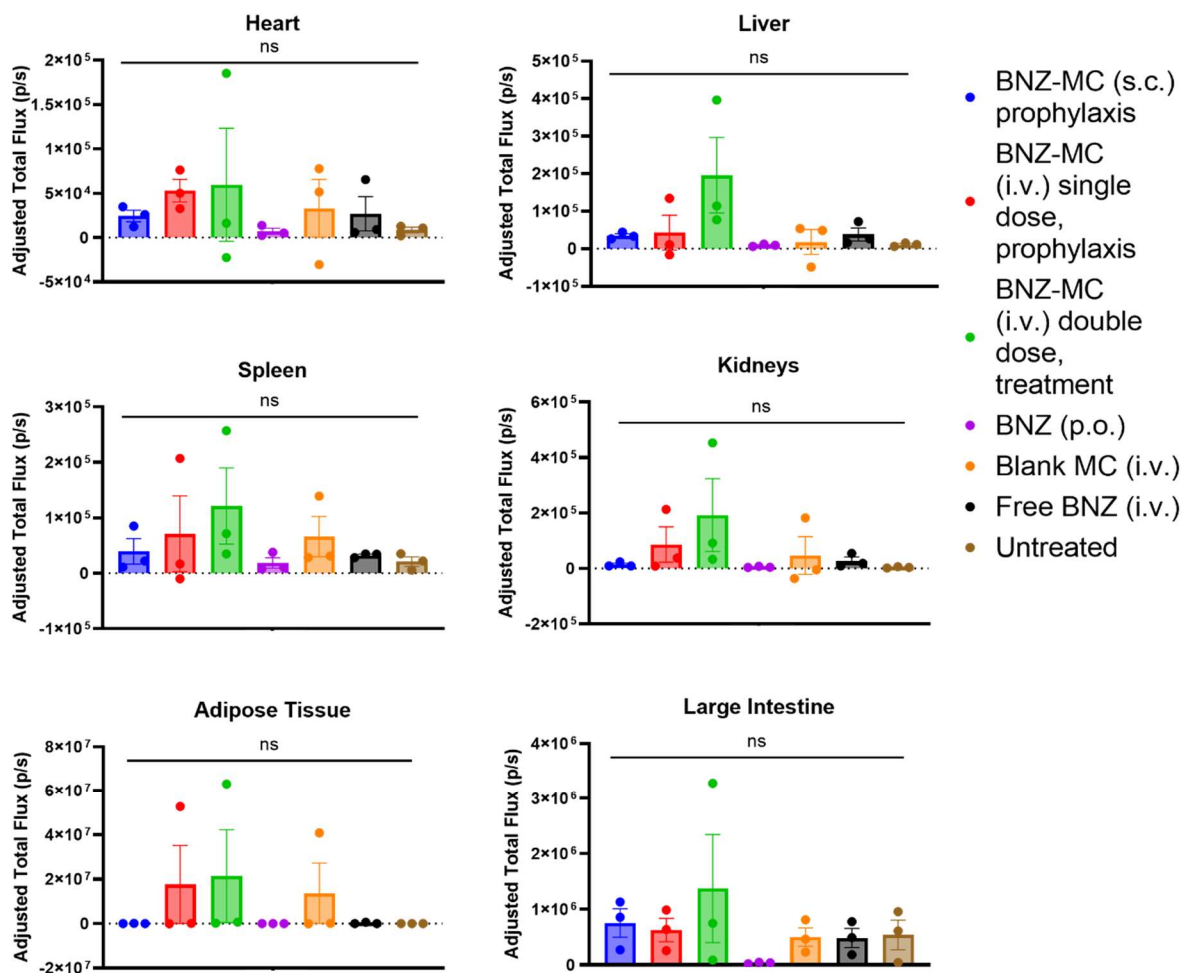


Figure 4-8. *T. cruzi* luminescence in the organs of BALB/C mice 25 days post infection for different BNZ-MC regimens. The background was subtracted from the total flux to obtain the adjusted total flux. Statistical significance was determined by one-way ANOVA with post-hoc Dunnett's test. The mean is represented (n=3) and the error bars represent the SEM.

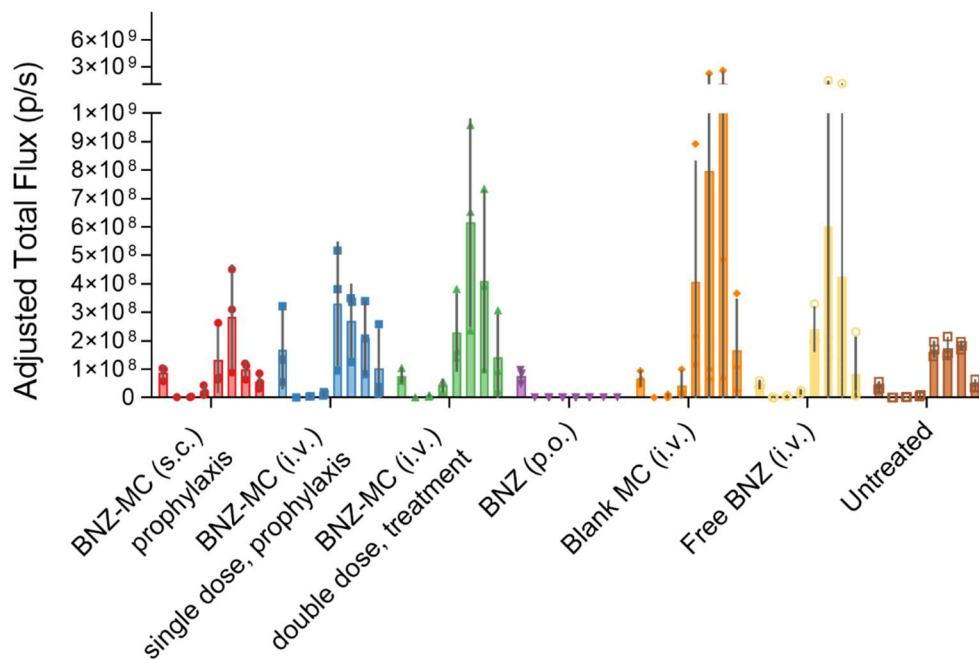


Figure 4-9. *T. cruzi* luminescence in BALB/c mice as measured on IVIS over 25 days for different BNZ-MC regimens. The luminescence was measured twice a week starting on the day of infection (Day 0). The mean is displayed with the error bars representing the SEM (n=3).

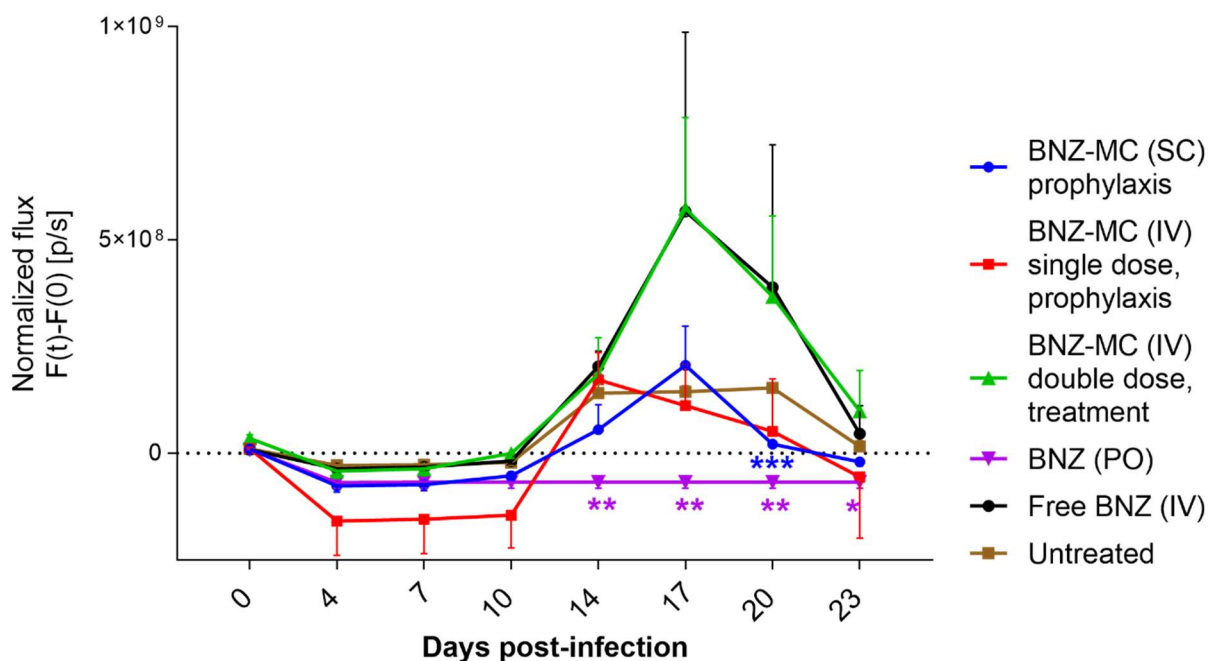


Figure 4-10. *T. cruzi* luminescence in BALB/C mice treated with different BNZ regimens over 25 days in relation to baseline parasite load on day 0. The mean of the total flux on day 0 was subtracted from the mean of the total flux for all subsequent timepoints to account for varying levels of parasite load for each animal upon infection. The blank MC group is not displayed as it had much larger flux values than the other groups. Statistical significance was determined by two-way ANOVA with post-hoc Dunnett's test (** $p < 0.01$, *** $p < 0.001$, * $p < 0.05$ compared to the untreated group). The mean is represented ($n=3$) and the error bar above each point represents the SEM.

4.4.5. Characterization of Novel BNZ-loaded PEG-*b*-PPS FM Hydrogel Platform

As a subcutaneous sustained release system for BNZ is promising for reducing parasitemia, I aimed to form a BNZ-loaded FM hydrogel system. In the (-)PBI-FM hydrogels previously

developed by the Scott Lab by Karabin *et al.*, the FM themselves were crosslinked through the reaction of 8-arm-PEG-thiol with vinyl sulfone-functionalized PEG-*b*-PPS FM (**Figure 4-11A**).³⁹ I hypothesized that a FM hydrogel can be formed without requiring crosslinking of the FM. I thus developed a new PEG-*b*-PPS FM hydrogel platform where high concentrations (100 mg/mL) of different BNZ-loaded FM are encapsulated within a scaffold or net of crosslinked 8-armed PEG-vinyl sulfone (MW 10K) and 8-arm PEG-thiol (MW 10K), as summarized in **Figure 4-11B**. The molar amount of the FM block copolymer was around 3 times greater than the molar amount of 8-armed PEG crosslinkers that encapsulated the FM (Table 4-4). The hydrogels are pictured in **Figure 4-12**. The encapsulation efficiency of the BNZ for the various FM formulations is shown in **Figure 4-13**, and the encapsulation efficiency of gel B (37%) was lower than that of the other gels, but was similar to mPBI-FM C and D (Figure 4-1). The greater EE observed for Gel C may be due to the formation method of FNP and also the incorporation of a PBI tetrablock copolymer with a longer hydrophobic PPS chain length.

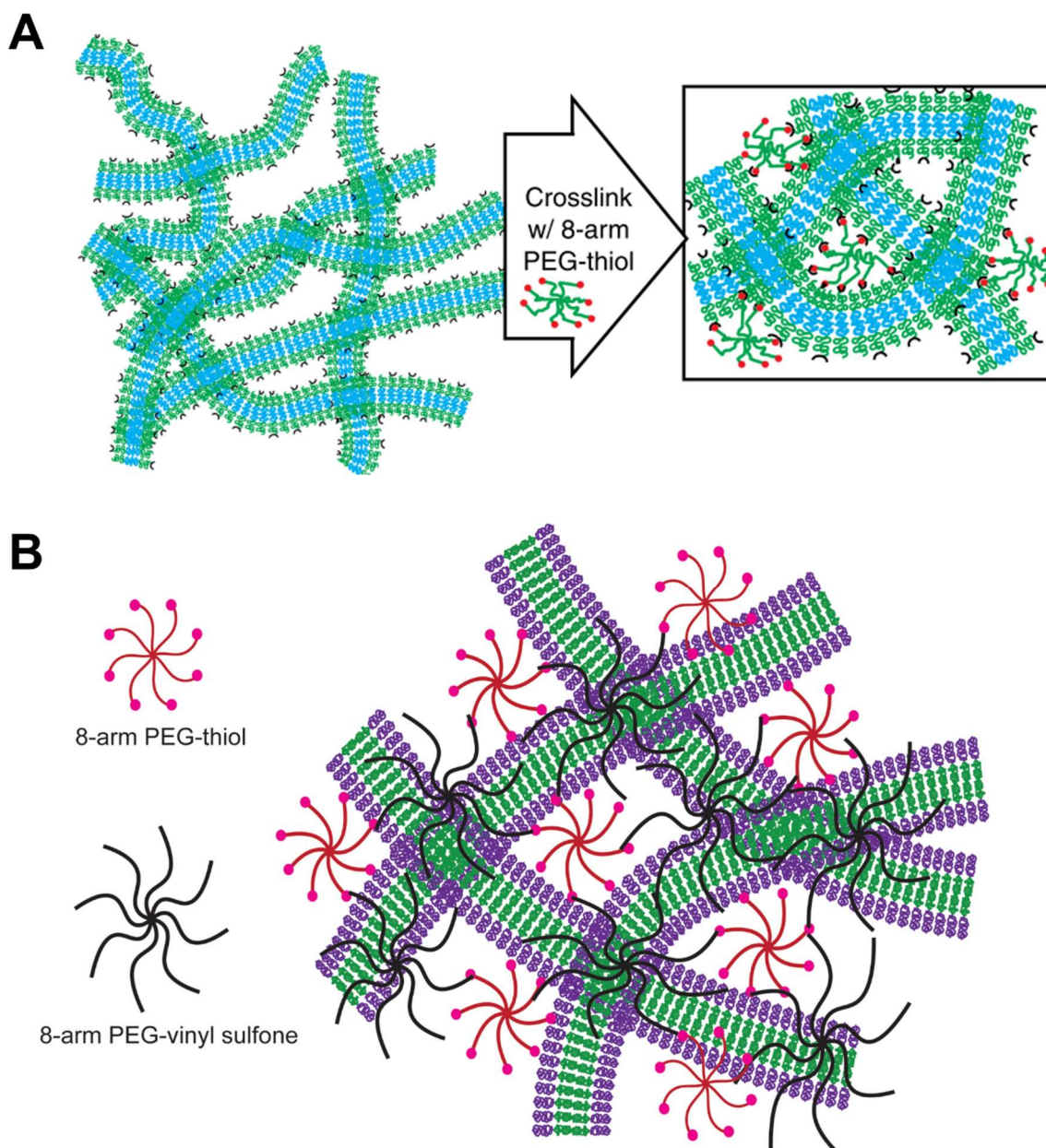


Figure 4-11. Schematic comparing the formation of distinct PEG-*b*-PPS FM hydrogel platforms. A) In the PEG-*b*-PPS FM hydrogels developed by Karabin *et al.*,³⁹ vinyl-sulfone functionalized PEG-*b*-PPS FM were crosslinked with 8-arm PEG-thiol to form a hydrogel in situ. Reprinted with permission from [39]. B) In the PEG-*b*-PPS FM hydrogels developed in this thesis

by Li, the FM themselves are not crosslinked. Instead, the FM are trapped in a PEG scaffold or net formed from the crosslinking of 8-arm PEG-thiol with 8-arm PEG-vinylsulfone.

I then assessed whether the incorporation of PBI tetrablock copolymer also affected the viscoelastic properties of the resulting FM hydrogels with dynamic oscillatory rheology. For the crosslinked FM hydrogels previously developed by Karabin *et al.*, viscoelastic gels were formed with storage moduli that increased as the percentage of vinyl-sulfone incorporated increased from 10% to 30%, demonstrating that the hydrogels exhibit more elastic behavior with increasing crosslinking density.³⁹ For the FM hydrogels that I developed, I found that for all the gels, the storage modulus was greater than the loss modulus, demonstrating that the gels are more elastic in nature (**Figure 4-14A**). A frequency dependence was observed, with both the storage and loss moduli increasing in the higher frequency range of 10 to 100 rad/s. The storage modulus also was greater in the mPBI-FM gels (Gels B and C) compared to (-)PBI-FM gel A for the lower frequencies of 0.1 to 10 rad/s (**Figure 4-14B**). Gel C, which was a mPBI-FM formulation formed from FNP, had the greatest storage modulus at the same angular frequency, most likely due to the increased rigidity of mPBI-FM formed from FNP compared to those of the same polymer composition formed from TFH (**Table 2-7**). These results demonstrate that PBI incorporation increases the elastic behavior of FM hydrogels compared to (-)PBI-FM hydrogels.

Table 4-4. Composition and formation method of BNZ-loaded FM hydrogels.

Gel	Composition	Formation method	Molar ratio of block copolymer to 8-armed PEG	Mass ratio of block copolymer to 8-armed PEG
A	PEG ₄₅ PPS ₄₅ benzyl	TFH in PBS	3.1	2.7
B	50 mol % PEG ₄₅ PPS ₄₅ benzyl and 50 mol% PEG ₁₇ PPS ₃₂ PBIPPS ₃₂ PEG ₁₇	TFH in PBS	2.7	2.7
C	50 mol % PEG ₄₅ PPS ₄₅ benzyl and 50 mol% PEG ₁₇ PPS ₃₂ PBIPPS ₃₂ PEG ₁₇	FNP in H ₂ O	2.7	2.7



Figure 4-12. Image of hydrogels formed by encapsulating BNZ-loaded FM in crosslinked PEG. From left to right: Gel A, Gel B, Gel C.

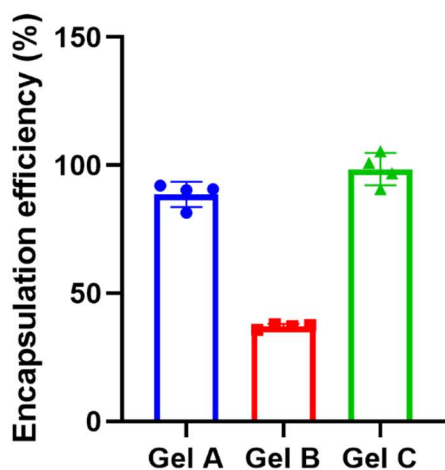


Figure 4-13. Encapsulation efficiency of BNZ for the FM formulations in Table 4-4.

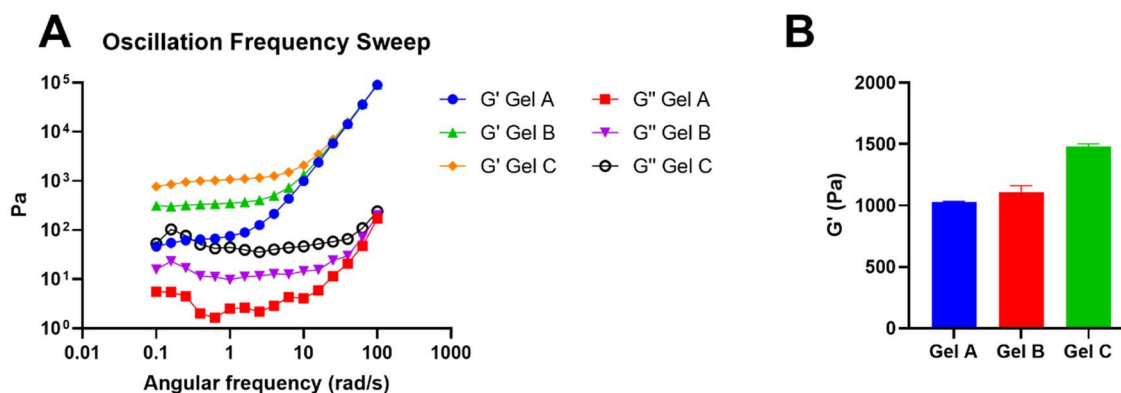


Figure 4-14. Rheology measurements of BNZ-loaded FM hydrogels. a) Storage modulus (G') and loss modulus (G'') as the angular frequency increased from 0.1 rad/s to 100 rad/s ($n=1$). b) G' when the angular frequency was held constant at 10 rad/s. The mean is shown with error bars representing SD ($n=20$ measurements).

I thus developed a new PEG-*b*-PPS FM hydrogel platform utilizing a net of crosslinked 8-arm PEG to entrap a high concentration of BNZ-loaded FM. This “net” method of hydrogel formation enables hydrogel formation without requiring functionalization of the FM. This simplifies FM hydrogel formation as separate synthesis of functionalized PEG-*b*-PPS or lipid tail constructs are not required, and the hydrogels can be formed from commercially available functionalized 8-arm PEG constructs. Other advantages of this new FM hydrogel platform include the ease of co-entrapment of different mPBI-FM and (-)PBI-FM formulations within the same scaffold for co-delivery of drugs. In addition, other crosslinkers, such as alginate, can potentially be used to form the net entrapping the FM. Bulk hydrogel properties can therefore be quickly modulated by changing the properties of the net, and FM can then be utilized for sustained nanocarrier delivery in other established hydrogel systems.

4.4.6. Characterization of DiR-loaded Nanocarriers for Cancer Biodistribution Study

In Chapter 3, I found that FM flexibility affected their biodistribution in vivo in C57Bl/6J mice. Thus, I aimed to investigate how FM flexibility affected their biodistribution after intratumoral injection in vivo in a B16F10 mouse disease model of melanoma. FM are of interest in cancer nanomedicine as summarized in Chapter 1 because of their increased circulation times and their ability to penetrate into tumors.³⁶

To compare the effect of nanocarrier morphology and FM flexibility, PEG-*b*-PPS nanocarriers of different morphologies (PS, MC, (-)PBI-FM, mPBI-FM-C, and bicontinuous nanospheres (BCN)) were loaded with the fluorescent dye DiR and characterized. The diameter

and PDI of spherical particles as measured by DLS and the DiR encapsulation efficiency is shown in **Table 4-5**.

Table 4-5. Average diameter and DiR encapsulation efficiency for various PEG-*b*-PPS nanocarrier morphologies.

Samples	Average diameter \pm SD (nm)	Polydispersity index (PDI)	DiR encapsulation efficiency \pm SD (%)
MC (PEG ₄₅ - <i>b</i> -PPS ₂₀)	62.3 \pm 50.7	0.293	101.0 \pm 2.7
PS (PEG ₁₇ - <i>b</i> -PPS ₃₂)	117.5 \pm 26.0	0.237	97.5 \pm 2.7
(-) <i>PBI</i> -FM	N/A	N/A	87.4 \pm 10.6
BCN (PEG ₁₇ - <i>b</i> -PPS ₇₅)	214.9 \pm 37.2	0.232	72.0 \pm 14.1
m <i>PBI</i> -FM-C	N/A	N/A	89.4 \pm 1.1

4.4.7. Nanocarrier Biodistribution after Intratumoral Injection

After 7 days of tumor growth in the right flank of C57Bl/6J mice, the DiR-loaded nanocarriers were injected into the tumor. A PBS and a free DiR group were included as controls. At 3 different timepoints (1 day, 3 days, and 7 days after intratumoral injection), the mice were sacrificed, the tumor, tumor-draining inguinal lymph node, liver, kidneys, spleen, and lungs were collected, and DiR fluorescence was measured by IVIS. Representative images of the organs are shown in **Figure 4-15**. In the tumor, significant nanocarrier uptake compared to the PBS control group was observed on Day 1 for PS and BCNs (**Figure 4-16**). For the tumor-draining lymph node, significant accumulation of MC and (-)*PBI*-FM were observed on Day 3, while significant

accumulation of PS, (-)PBI-FM, mPBI-FM-C, and DiR was seen on Day 7. For the other organs, MC traveled to the liver, kidneys, spleen, and lungs at the highest levels after intratumoral injection. Significant levels of FM were also observed in the liver, spleen, and lungs. In terms of FM flexibility, in general the more flexible (-)PBI-FM had greater accumulation in the liver and kidneys compared to the less flexible mPBI-FM-C. This trend was similar to the biodistribution data in Figure 3-6, where significantly less uptake was observed in the spleen and liver for mPBI-FM-C compared to (-)PBI-FM after intravenous administration. Similar levels of accumulation were observed for both FM formulations in the lungs. These results suggest that MC, (-)PBI-FM, and mPBI-FM-C are entering systemic circulation after intratumoral injection leading to significant levels of accumulation in the liver, kidney, and lungs compared to the PBS control, and thus have potential for targeting tumor metastases to these organs. PS, mPBI-FM-C, and (-)PBI-FM also exhibit passive targeting to the tumor-draining lymph node at the day 7 timepoint and so have potential to target immune cells in the lymph node for applications in cancer immunotherapy. Lastly, the effect of filament flexibility was again exhibited as differences in biodistribution were observed between the two FM formulations in this disease model.

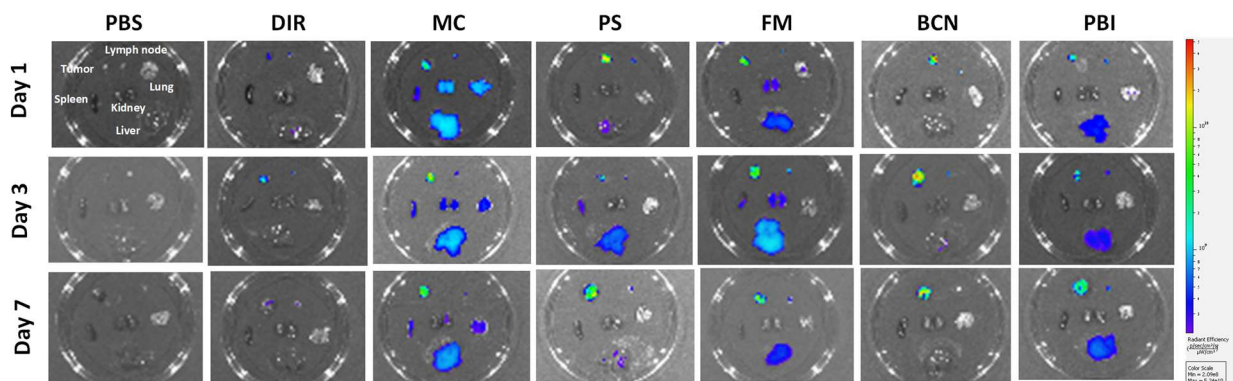


Figure 4-15. Representative fluorescence images of the tumor, tumor-draining inguinal lymph node, lung, spleen, kidney, and liver obtained via IVIS 1 day, 3 days, and 7 days after intratumoral injection in a B16F10 melanoma mouse model in C57BL/6J mice.

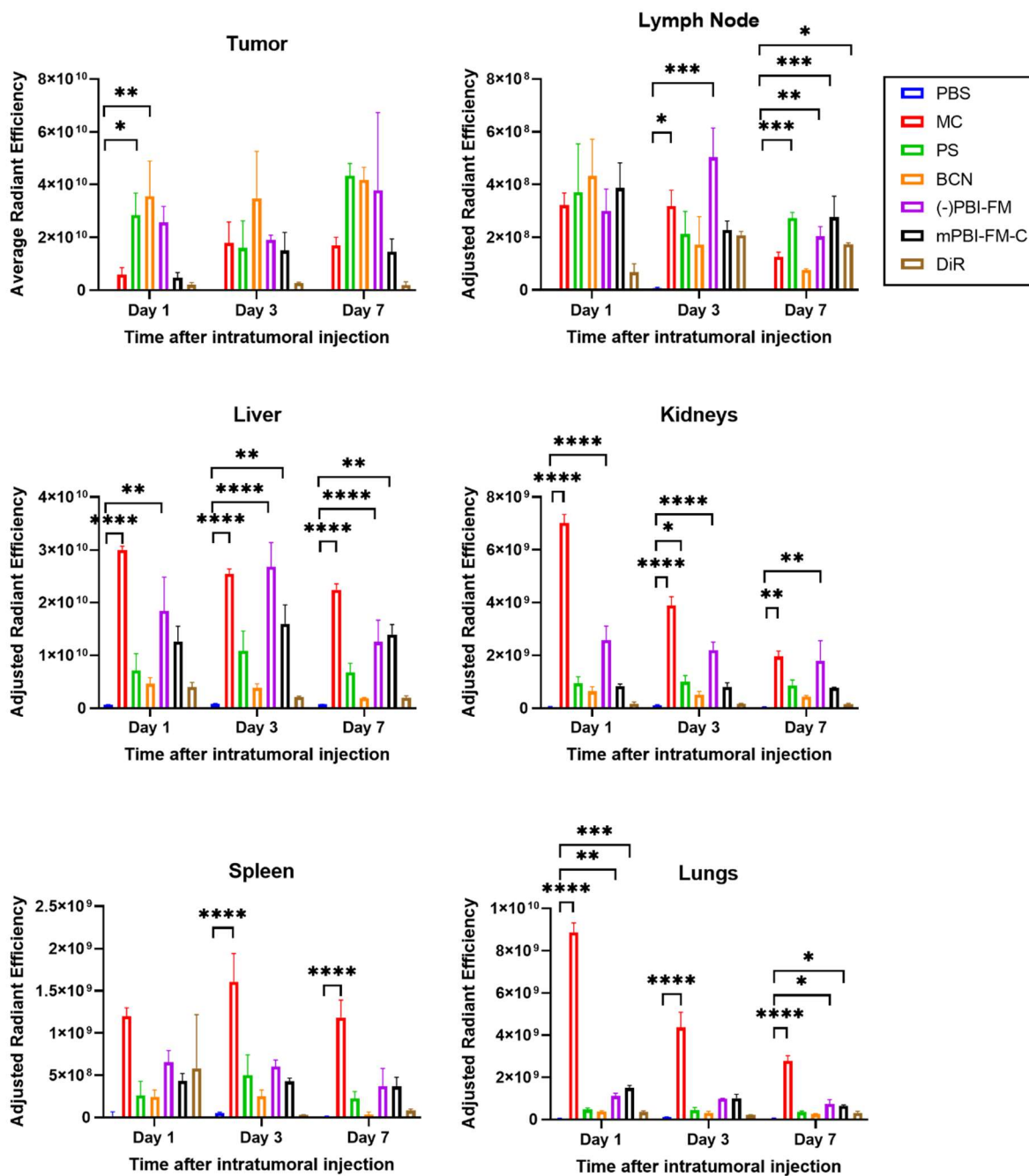


Figure 4-16. Organ-level biodistribution of DiR-loaded nanocarriers of various morphologies after intratumoral injection in a B16F10 melanoma mouse model in C57BL/6J

mice. Statistical significance was determined by ANOVA with post hoc Tukey's test to correct for multiple comparisons with a 5 percent significance level (* $p < 0.05$, ** $p < 0.01$, *** $p < 0.001$, **** $p < 0.0001$). The mean is displayed ($n=3$), with error bars representing the SEM.

4.5. Conclusions

In this chapter, I explored potential applications of FM in nanomedicine in Chagas disease and cancer. For Chagas disease, I found that PEG-*b*-PPS nanocarriers of different morphologies loaded with BNZ, an anti-parasitic drug, had similar cytotoxic and trypanocidal profiles. I then assessed the feasibility of FM hydrogel systems that enable controlled release of MC over time for Chagas disease prophylaxis. I formed and characterized BNZ-loaded FM hydrogels and found that 2 subcutaneous doses of BNZ-loaded MC significantly reduced parasite load in vivo 20 days after infection compared to untreated mice. This suggests that further exploration and development of a sustained release system for BNZ for the prevention of Chagas disease is warranted.

For the cancer biodistribution studies, I found that FM flexibility did affect organ level biodistribution after intratumoral injection in a B16F10 melanoma model. (-)PBI-FM, mPBI-FM-C, and PS all had significant accumulation in the tumor draining lymph node 7 days after the injection, demonstrating that these nanocarrier morphologies can passively target the lymph node for future applications in cancer vaccine development or cancer immunotherapy. In addition, MC, (-)PBI-FM, and mPBI-FM-C had significant accumulation in the liver and lungs, suggesting that these nanocarriers may be able to target metastases to these organs. This work led to better

understanding of the biodistribution of PEG-*b*-PPS FM nanocarriers in a cancer disease model that will enable future development of PEG-*b*-PPS FM in the therapeutic area of cancer nanomedicine.

4.6. Acknowledgements

I would like to thank Debora Scariot for all her guidance and help with the Chagas disease studies. I would also like to thank Sun-young Kim, Austeja Staneviciute, Yu-gang (Bryan) Liu, Sharan Bobbala, Stephanie Zelenetz, and Simseok (Andrew) Yuk for their assistance in conducting the animal studies for both Chagas disease and the melanoma model.

CHAPTER 5

5. Conclusions and Future Directions

5.1. Conclusions

In this thesis, I aimed to increase current knowledge on how chemical and physical properties of filamentous nanocarriers affect their biological performance, and take PEG-*b*-PPS filamentous nanocarriers, or PEG-*b*-PPS FM, further towards clinical translation. I have developed a new filamentous nanocarrier platform that utilizes pi-stacking to enhance the stability, scalability and reproducibility of formation, and control over flexibility of PEG-*b*-PPS FM. I have demonstrated that modulating PEG-*b*-PPS FM flexibility affects their cellular uptake and biodistribution and shown that the flexibility of FM can be controlled to increase their circulation time and decrease clearance by macrophages *in vivo*. This pi-stacking FM platform also undergoes “cylinder-to-sphere” morphological transitions under oxidative conditions, allowing for their use for sustained delivery of micellar nanocarriers. Lastly, I have demonstrated the potential utility of FM nanocarriers for drug delivery and laid the groundwork for future applications of these nanocarriers in the prevention and treatment of infectious disease and cancer.

5.1.1 Rapid, Scalable FM Formation with Tunable Flexibility

Previously in the Scott Lab, the formation of PEG-*b*-PPS FM was conducted through the thin film hydration method and required PEG₄₅-*b*-PPS with a narrow range of f_{PEG} (0.36-0.38). While the thin film hydration method is an established method for FM in the literature, it is difficult to scale and can lead to batch-to-batch variability, making it challenging to reproducibly form FM. The rapid and scalable technique of flash nanoprecipitation has been used extensively for the

formation of other PEG-*b*-PPS morphologies including polymersomes, micelles, and bicontinuous nanospheres; however, it was previously not used for FM self-assembly as it required the synthesis of PEG₁₇-*b*-PPS with a specific f_{PEG} of 0.21 and did not reproducibly form FM with the higher molecular weight PEG₄₅-*b*-PPS. I found that the co-assembly of a tetrablock pi-stacking polymer containing perylene bisimide (PBI) with the diblock PEG-*b*-PPS polymer led to more reproducible formation of FM by both self-assembly methods (thin film hydration and flash nanoprecipitation) and expanded the range of f_{PEG} that is amenable to FM formation. This mixed perylene bisimide FM (mPBI-FM) platform also enhanced stability in storage compared to PEG-*b*-PPS FM without PBI tetrablocks ((-)PBI-FM) and had tunable flexibility. I thus improved the process of PEG-*b*-PPS FM formation and demonstrated that a library of FM with varying lengths and flexibilities can be reproducibly formed with the incorporation of pi-stacking polymer in the mPBI-FM platform.

5.1.2. Fluorescence Tracking of “Cylinder-to-sphere” Morphological Transition

Previously, the kinetics of the “cylinder-to-sphere” morphological transition in PEG-*b*-PPS FM after oxidation had to be observed through techniques such as SAXS, which is time-intensive and requires specialized facilities. I demonstrated that the mPBI-FM maintained their ability to undergo oxidation-driven “cylinder-to-sphere” transitions for sustained drug delivery applications. In addition, because of the aggregation-dependent fluorescence of PBI, this morphological transition can now be tracked by monitoring the fluorescence of the solution, allowing more high-throughput characterization. I also demonstrated that mPBI-FM with different flexibilities had distinct “cylinder-to-sphere” transition kinetics, which can be useful in designing FM hydrogels with different rates of sustained release of micellar nanocarriers.

5.1.3. Investigation of the Effect of FM flexibility on Immune Cell Interactions

Because of the difficulties in forming FM with the same surface chemistry but with varying flexibilities, the effect of filament flexibility, particularly for polymeric FM, is not well understood. With my pi-stacking FM platform, I showed that FM flexibility affected their cytotoxicity and uptake in murine macrophages, with the most rigid FM exhibiting the most cytotoxicity, and FM in the medium range of flexibilities tested exhibiting reduced uptake by murine macrophages in vitro. FM in this medium range of flexibilities also had increased circulation time and different biodistribution in vivo on a cellular and organ level compared to the more flexible (-)PBI-FM, which is advantageous for drug delivery and for passive targeting of certain immune subtypes. I thus demonstrated the importance of FM flexibility as a parameter that can be optimized for rational design of therapeutic filamentous nanocarriers depending on the biomedical application.

5.1.4 Potential Utility of PEG-*b*-PPS FM for Drug Delivery

In previous work, PEG-*b*-PPS FM have been utilized for the sustained release of an anti-inflammatory agent for the treatment of atherosclerosis.⁸² I laid the groundwork for explorations of PEG-*b*-PPS FM as nanocarriers in the therapeutic area of Chagas disease, and demonstrated that subcutaneous delivery of micelles, mimicking a sustained release FM hydrogel platform, significantly decreased parasite load at 20 days post-infection compared to the untreated control group. These results suggest that further work in optimizing a sustained release platform for Chagas disease is warranted. In addition, I built on previous biodistribution studies in melanoma cancer models to demonstrate that FM flexibility affects their biodistribution after intratumoral injection, providing information for the future development of PEG-*b*-PPS FM cancer therapeutics.

5.2. Future Directions

My thesis work brings PEG-*b*-PPS FM closer toward the possibility of utilizing these filamentous nanocarriers for drug delivery in the clinic. While I have improved the process of PEG-*b*-PPS FM formation and addressed key questions on how FM flexibility affects nanocarrier biodistribution and circulation time, there are many potential future directions that can be pursued to further the rational design of PEG-*b*-PPS FM nanocarriers for biomedical applications.

5.2.1. Effect of mPBI-FM Flexibility on Immune Activation

There are very few studies on the effect of polymeric filament flexibility on immune cell activation. I found that FM flexibility had interesting effects on the immunological phenotype of RAW 264.7 murine macrophages. While the mPBI-FM formulations I tested did not lead to NF- κ B activation of RAW-Blue cells, upregulation of the co-stimulatory surface markers of CD80 and CD86 was observed after incubation with different FM formulations in vitro, particularly in the most rigid mPBI-FM formulations. In addition, no IL-10 cytokine release was detected, suggesting that the macrophages were not being polarized toward a M2 phenotype. mPBI-FM may therefore be activating murine macrophages to a more pro-inflammatory, M1-like phenotype. This effect is reminiscent of that of rigid carbon nanotubes, which are known to lead to macrophage activation, depending on their length.²⁵² Of note, mPBI-PS also led to upregulation of CD80 and MHC II compared to (-)PBI-PS, suggesting that the upregulation was not just due to the filamentous morphology. As mPBI-PS are much smaller in diameter and expected to be less flexible than (-)PBI-PS, this suggests that changing the elasticity of spherical nanostructures can also lead to macrophage activation. Alternatively, perhaps the presence of PBI, a potentially electroconductive material, is immunomodulatory. Conducting polymer nanostructures have been

found to induce proinflammatory genes in J774A.1 mouse alveolar macrophages at higher concentrations, so the presence of the pi-stacking polymer itself may have an immunological effect.²⁵³

However, further studies will be needed to characterize and better understand the immunophenotype of macrophages after incubation with FM of varying flexibility. Quantification of the secretion of proinflammatory cytokines such as TNF- α , IL-6, and IL-1 β , assessment of a wider range of cell surface markers, and assessment of nitric oxide production can provide more insight into whether the macrophage phenotype that was induced is more similar to a classical M1 phenotype or more representative of a mixed M1/M2 phenotype. RNAseq of the macrophages can also elucidate which transcriptional pathways are being activated and help explain how pro-inflammatory surface markers are being expressed. In addition, the effect of FM flexibility on the activation of other immune cell subtypes, such as dendritic cells, should be explored.

The ability to activate immune cells by modulating FM flexibility or by using mPBI-nanocarriers without loaded drugs has utility in many different immunoengineering applications, including in vaccine development and in cancer immunotherapy. mPBI-FM can be used as an adjuvant for antigen delivery or can be delivered to “cold” tumors to promote a pro-inflammatory tumor microenvironment.

5.2.2. mPBI-FM Hydrogels for Sustained Delivery of Micelles

My work showed that BNZ-FM hydrogels can be formed with a new crosslinking technique, where the FM are encapsulated in a “net” of cross-linked 8-armed PEG. As mPBI-FM themselves have different MC release rates in response to oxidation depending on their flexibility,

they have the potential to form hydrogels with distinct controlled release rates depending on the biomedical application. For example, mPBI-FM with different flexibilities can each be loaded with a unique drug, allowing for sustained release of each drug at different rates from the same hydrogel. Release studies *in vitro* and *in vivo* with different mPBI-FM formulations co-encapsulated in the same hydrogel can be conducted in order to develop and optimize mPBI-FM sustained release hydrogels. These hydrogels will then allow for possible drug release profiles with a burst release of FM as they diffuse out of the gel in the gel periphery alongside concomitant slower sustained release of MC nanocarriers.

While the incorporation of crosslinkers directly into mPBI-FM hydrogels, such as through a peptide lipid tail construct, to form crosslinked FM gels as previously described by Karabin *et al.*, should also be explored,³⁹ the hydrogel formation technique of encapsulation of FM in a “net” that I developed can be advantageous for the creation of innovative hydrogels. The FM can be encapsulated in different “nets,” including PEG-acrylate crosslinkers, fibrin gels, and crosslinked collagen gels. This approach may also be amenable to 3D printing of FM hydrogels, as the FM can be encapsulated in already characterized hydrogel inks for 3D-printing including Pluronics and alginate, to form customizable and advanced biomaterials.²⁵⁴

The *in vivo* study of BNZ-MC in a Chagas disease model also suggests that a subcutaneous sustained release system may be more effective than multiple intravenous injections for prevention of Chagas disease, so the efficacy of a BNZ-loaded mPBI-FM or (-) PBI-FM hydrogel depot should be explored after determination of the ideal dose of BNZ-MC needed to prevent parasitemia. My study demonstrated that a higher dose of BNZ is likely needed to reduce and eradicate the

parasite load. However, having more frequent subcutaneous injections in the week post infection may be a better mimic of a sustained release system with a burst release in the first day followed by a slower release profile, which is the release profile of (-) PBI-FM.³⁹ The release profiles of BNZ-loaded mPBI-FM in vitro combined with in vivo data from subcutaneous MC injections can then be used to optimize the sustained release system.

In addition, for the treatment of chronic Chagas disease, a combinatorial approach with delivery of an anti-inflammatory drug alongside delivery of BNZ is hypothesized to be more effective. I found that the combination treatment of Vitamin D-MC and BNZ-MC did not affect the trypanocidal activity of BNZ, and so Vitamin D may be a promising drug to pair with BNZ. In this case, a hydrogel with two different mPBI-FM formulations may be useful to allow for different release rates, as it may be beneficial to have a burst release of BNZ followed by release of low levels of an anti-inflammatory agent as the parasite load decreases.

5.2.3. Active Targeting of Immune cells

In my studies, I described how passive targeting based on changing FM flexibility led to preferential nanocarrier uptake in different cell types, such as enhanced targeting to liver dendritic cells. While this can be utilized for immunomodulation of specific immune subtypes, one of the advantages of filamentous nanocarriers is their enhanced avidity when targeting ligands are attached to the nanocarrier surface. Combined with their increased circulation time and reduced uptake by macrophages compared to (-)PBI-FM in vivo, mPBI-FM with targeting ligands may have enhanced cellular targeting. Clayton Rische in the Scott Lab and I have worked on the attachment of antibodies to PEG-*b*-PPS nanocarrier surfaces but have not been able to achieve

consistent, controlled, and specific antibody attachment via direct conjugation approaches using click chemistry and through noncovalent approaches (Fc binding peptide constructs). Peptide-lipid tail constructs already developed in the Scott Lab for MC and PS can be optimized for incorporation into FM and mPBI-FM. Lipid tail linkers that can pi-stack may allow for stable incorporation into mPBI-FM when mixed in with the block copolymers during self-assembly. In addition, the Mrksich lab has developed megamolecules that allow for the specific attachment of anti-CD3 F(ab) fragments to nanoparticles through the binding of an enzyme to an enzyme inhibitor attached to a lipid tail construct.²⁵⁵ These constructs have great potential as T cell targeting ligands and can allow for the investigation of how FM flexibility and avidity affect T cell internalization of nanocarriers.

Active targeting can be beneficial in other applications, such as in Chagas disease, where intracellular delivery of BNZ is crucial for parasite elimination. Targeting of specific cell types such as cardiomyocytes and adipocytes, such as through the LDL receptor, can improve the efficacy of BNZ, as the trypanosomes use these receptors to enter host cells.²⁵⁶ In addition, Debora Scariot and Austėja Staneviciute are working on developing nanocarriers that target the transferrin receptor expressed on the parasite in order to increase BNZ delivery to the parasite.

5.2.4. Applications of PEG-*b*-PPS FM in Cancer Nanomedicine

I have demonstrated that (-)PBI-FM and mPBI-FM are able to accumulate in the tumor-draining lymph node after intratumoral injection, suggesting that FM may have utility for drug delivery to immune cells in the lymph node for cancer immunotherapy, or delivery of chemotherapeutics to cancer metastases that arrive in the tumor-draining lymph node. FM also

accumulated in other organs including the lungs after intratumoral injection, which demonstrates that FM could potentially be used to target metastases to these organs. A folate-targeting lipid tail construct has been developed in the Scott Lab for targeting of B16F10 melanoma cells and can be utilized for the targeting of tumors and metastatic lesions. In future studies, PEG-*b*-PPS of different morphologies can also be loaded with immunomodulatory molecules, such as imiquimod, a TLR-7 agonist with antitumor activity, for applications in cancer immunotherapy. Multi-pronged approaches where circulating FM targeted to the tumor are combined with sustained release FM hydrogels with immunomodulatory activity can also be explored.

5.2.5. Evaluating Electrical Conductivity of mPBI-FM for Optoelectronics or Regenerative Engineering Applications

Perylene bisimide is a n-type semiconductor and thus has utility in optoelectronics applications, such as in organic field effect transistors (OFETs). As mPBI-FM have been shown to form stable rods after drying on a grid, their electroconductivity after incorporation into an OFET can be measured. Increasing the molar fraction of PBI tetrablock copolymer in the FM formulation may also enhance electroconductivity. Even if mPBI-FM are not conductive enough for use as transistors, mPBI-FM hydrogels may have some electroconductivity that can be beneficial for applications in regenerative engineering. Conducting polymers can influence cellular interactions with a material leading to cellular proliferation and differentiation of cell types including mesenchymal stem cells, Schwann cells, and neural stem cells, which can facilitate tissue regeneration.²⁵⁷

5.2.6. Characterization of FM in Large Animal Models

Finally, aside from a few peptide filaments and some viral filaments including M13 bacteriophage, most self-assembled filaments are in pre-clinical studies.²⁴ More studies of polymeric filamentous structures in vivo, especially in larger animal models, like non-human primates, are needed to better understand their biological performance and improve clinical translation. While PEG-*b*-PPS polymersomes have been evaluated in nonhuman primates, other morphologies including FM have not, so it is not known whether the increased circulation time compared to spherical nanostructures seen in mice models for FM is translatable to larger animal models.

REFERENCES

1. Goeijenbier, M.; Van Kampen, J.; Reusken, C.; Koopmans, M.; Van Gorp, E., Ebola virus disease: a review on epidemiology, symptoms, treatment and pathogenesis. *Neth J Med* **2014**, *72* (9), 442-8.
2. Rossman, J. S.; Leser, G. P.; Lamb, R. A., Filamentous Influenza Virus Enters Cells via Macropinocytosis. *Journal of Virology* **2012**, *86* (20), 10950-10960.
3. Tanaka, M.; Sawada, T.; Li, X.; Serizawa, T., Controlled assembly of filamentous viruses into hierarchical nano- to microstructures at liquid/liquid interfaces. *RSC Advances* **2020**, *10* (44), 26313-26318.
4. Booth, T. F.; Rabb, M. J.; Beniac, D. R., How do filovirus filaments bend without breaking? *Trends in Microbiology* **2013**, *21* (11), 583-593.
5. Shukla, S.; Eber, F. J.; Nagarajan, A. S.; Difranco, N. A.; Schmidt, N.; Wen, A. M.; Eiben, S.; Twyman, R. M.; Wege, C.; Steinmetz, N. F., The Impact of Aspect Ratio on the Biodistribution and Tumor Homing of Rigid Soft-Matter Nanorods. *Advanced Healthcare Materials* **2015**, *4* (6), 874-882.
6. Shukla, S.; Ablack, A. L.; Wen, A. M.; Lee, K. L.; Lewis, J. D.; Steinmetz, N. F., Increased Tumor Homing and Tissue Penetration of the Filamentous Plant Viral Nanoparticle Potato virus X. *Molecular Pharmaceutics* **2013**, *10* (1), 33-42.
7. Lee, K. L.; Uhde-Holzem, K.; Fischer, R.; Commandeur, U.; Steinmetz, N. F., Genetic Engineering and Chemical Conjugation of Potato Virus X. Humana Press: 2014; pp 3-21.

8. Sawada, T.; Murata, Y.; Marubayashi, H.; Nojima, S.; Morikawa, J.; Serizawa, T., Filamentous Virus-based Assembly: Their Oriented Structures and Thermal Diffusivity. *Scientific Reports* **2018**, *8* (1).
9. Sawada, T.; Serizawa, T., Filamentous Viruses as Building Blocks for Hierarchical Self-Assembly toward Functional Soft Materials. *Bull. Chem. Soc. Jpn.* **2018**, *91* (3), 455-466.
10. Wang, Y. A.; Yu, X.; Overman, S.; Tsuboi, M.; Thomas, G. J.; Egelman, E. H., The Structure of a Filamentous Bacteriophage. **2006**, *361* (2), 209-215.
11. Ott, A.; Magnasco, M.; Simon, A.; Libchaber, A., Measurement of the persistence length of polymerized actin using fluorescence microscopy. *Physical Review E* **1993**, *48* (3), R1642-R1645.
12. Gittes, F.; Mickey, B.; Nettleton, J.; Howard, J., Flexural rigidity of microtubules and actin filaments measured from thermal fluctuations in shape. *J. Cell Biol.* **1993**, *120* (4), 923-934.
13. Mücke, N.; Kreplak, L.; Kirmse, R.; Wedig, T.; Herrmann, H.; Aebi, U.; Langowski, J., Assessing the Flexibility of Intermediate Filaments by Atomic Force Microscopy. *J. Mol. Biol.* **2004**, *335* (5), 1241-1250.
14. Sun, Y.-L.; Luo, Z.-P.; Fertala, A.; An, K.-N., Direct quantification of the flexibility of type I collagen monomer. *Biochem. Biophys. Res. Commun.* **2002**, *295* (2), 382-386.
15. Yadavalli, V. K.; Svintradze, D. V.; Pidaparti, R. M., Nanoscale measurements of the assembly of collagen to fibrils. *Int. J. Biol. Macromol.* **2010**, *46* (4), 458-464.
16. Sivakumar, L.; Agarwal, G., The influence of discoidin domain receptor 2 on the persistence length of collagen type I fibers. *Biomaterials* **2010**, *31* (18), 4802-4808.

17. Mai, Y.; Eisenberg, A., Self-assembly of block copolymers. *Chem. Soc. Rev.* **2012**, *41* (18), 5969.
18. Deng, Z.; Liu, S., Emerging trends in solution self-assembly of block copolymers. *Polymer* **2020**, *207*.
19. Le, D. H. T.; Lee, K. L.; Shukla, S.; Commandeur, U.; Steinmetz, N. F., Potato virus X, a filamentous plant viral nanoparticle for doxorubicin delivery in cancer therapy. **2017**.
20. Kojima, S.; Kuriki, Y.; Yoshida, T.; Yazaki, K.; Miura, K.-I., Fibril Formation by an Amphipathic α -Helix-Forming Polypeptide Produced by Gene Engineering. *Proceedings of the Japan Academy. Ser. B: Physical and Biological Sciences* **1997**, *73* (1), 7-11.
21. Aggeli, A.; Bell, M.; Boden, N.; Keen, J. N.; Knowles, P. F.; McLeish, T. C. B.; Pitkeathly, M.; Radford, S. E., Responsive gels formed by the spontaneous self-assembly of peptides into polymeric β -sheet tapes. *Nature* **1997**, *386* (6622), 259-262.
22. Zhang, Y.; Gu, H.; Yang, Z.; Xu, B., Supramolecular Hydrogels Respond to Ligand–Receptor Interaction. *J. Am. Chem. Soc.* **2003**, *125* (45), 13680-13681.
23. Koutsopoulos, S., Self-assembling peptide nanofiber hydrogels in tissue engineering and regenerative medicine: Progress, design guidelines, and applications. *Journal of Biomedical Materials Research Part A* **2016**, *104* (4), 1002-1016.
24. Hainline, K. M.; Fries, C. N.; Collier, J. H., Progress Toward the Clinical Translation of Bioinspired Peptide and Protein Assemblies. *Advanced Healthcare Materials* **2018**, *7* (5), 1700930.
25. Hartgerink, J. D., Self-Assembly and Mineralization of Peptide-Amphiphile Nanofibers. *Science* **2001**, *294* (5547), 1684-1688.

26. Ke, W.; Lu, N.; Japir, A. A.-W. M. M.; Zhou, Q.; Xi, L.; Wang, Y.; Dutta, D.; Zhou, M.; Pan, Y.; Ge, Z., Length effect of stimuli-responsive block copolymer prodrug filomicelles on drug delivery efficiency. *J. Controlled Release* **2020**, *318*, 67-77.
27. Won, Y.-Y.; Davis, H. T.; Bates, F. S., Giant wormlike rubber micelles. *Science* **1999**, *283* (5404), 960-963.
28. Lin, Y.-A.; Kang, M.; Chen, W.-C.; Ou, Y.-C.; Cheetham, A. G.; Wu, P.-H.; Wirtz, D.; Loverde, S. M.; Cui, H., Isomeric control of the mechanical properties of supramolecular filament hydrogels. *Biomaterials Science* **2018**, *6* (1), 216-224.
29. Shukla, S.; Myers, J. T.; Woods, S. E.; Gong, X.; Czapar, A. E.; Commandeur, U.; Huang, A. Y.; Levine, A. D.; Steinmetz, N. F., Plant viral nanoparticles-based HER2 vaccine: Immune response influenced by differential transport, localization and cellular interactions of particulate carriers. *Biomaterials* **2017**, *121*, 15-27.
30. Lax, R., The future of peptide development in the pharmaceutical industry. *PharManufacturing: The international peptide review* **2010**, *2*, 10-15.
31. Shu, J. Y.; Panganiban, B.; Xu, T., Peptide-polymer conjugates: from fundamental science to application. *Annu. Rev. Phys. Chem.* **2013**, *64*, 631-657.
32. Truong, N. P.; Quinn, J. F.; Whittaker, M. R.; Davis, T. P., Polymeric filomicelles and nanoworms: two decades of synthesis and application. *Polymer Chemistry* **2016**, *7* (26), 4295-4312.
33. Sato, K.; Hendricks, M. P.; Palmer, L. C.; Stupp, S. I., Peptide supramolecular materials for therapeutics. *Chem. Soc. Rev.* **2018**, *47* (20), 7539-7551.

34. Qi, G.-B.; Gao, Y.-J.; Wang, L.; Wang, H., Self-Assembled Peptide-Based Nanomaterials for Biomedical Imaging and Therapy. *Adv. Mater.* **2018**, *30* (22), 1703444.
35. Shukla, S.; Hu, H.; Cai, H.; Chan, S.-K.; Boone, C. E.; Beiss, V.; Chariou, P. L.; Steinmetz, N. F., Plant Viruses and Bacteriophage-Based Reagents for Diagnosis and Therapy. *Annual Review of Virology* **2020**, *7*, 559-587.
36. Oltra, N. S.; Nair, P.; Discher, D. E., From Stealthy Polymersomes and Filomicelles to “Self” Peptide-Nanoparticles for Cancer Therapy. *Annual Review of Chemical and Biomolecular Engineering* **2014**, *5* (1), 281-299.
37. Allen, S.; Osorio, O.; Liu, Y.-G.; Scott, E., Facile assembly and loading of theranostic polymersomes via multi-impingement flash nanoprecipitation. *J. Controlled Release* **2017**.
38. Wang, L.; Huang, H.; He, T., Rayleigh Instability Induced Cylinder-to-Sphere Transition in Block Copolymer Micelles: Direct Visualization of the Kinetic Pathway. *ACS Macro Letters* **2014**, *3* (5), 433-438.
39. Karabin, N. B.; Allen, S.; Kwon, H.-K.; Bobbala, S.; Firlar, E.; Shokuhfar, T.; Shull, K. R.; Scott, E. A., Sustained micellar delivery via inducible transitions in nanostructure morphology. *Nature communications* **2018**, *9* (1), 624.
40. Israelachvili, J. N.; Mitchell, D. J.; Ninham, B. W., Theory of self-assembly of hydrocarbon amphiphiles into micelles and bilayers. *Journal of the Chemical Society, Faraday Transactions 2* **1976**, *72*, 1525.
41. Israelachvili, J. N., *Intermolecular and surface forces*. Academic press: 2011.
42. Dionzou, M.; Morère, A.; Roux, C.; Lonetti, B.; Marty, J. D.; Mingotaud, C.; Joseph, P.; Goudounèche, D.; Payré, B.; Léonetti, M.; Mingotaud, A. F., Comparison of methods for

the fabrication and the characterization of polymer self-assemblies: what are the important parameters? *Soft Matter* **2016**, *12* (7), 2166-2176.

43. Discher, D. E.; Eisenberg, A., Polymer vesicles. *Science* **2002**, *297* (5583), 967-973.
44. Lee, J. S.; Feijen, J., Polymersomes for drug delivery: Design, formation and characterization. *J. Controlled Release* **2012**, *161* (2), 473-483.
45. Szwarc, M., 'Living' Polymers. *Nature* **1956**, *178* (4543), 1168-1169.
46. Hadjichristidis, N.; Iatrou, H.; Pispas, S.; Pitsikalis, M., Anionic polymerization: high vacuum techniques. *J. Polym. Sci., Part A: Polym. Chem.* **2000**, *38* (18), 3211-3234.
47. Cai, S.; Vijayan, K.; Cheng, D.; Lima, E. M.; Discher, D. E., Micelles of Different Morphologies—Advantages of Worm-like Filomicelles of PEO-PCL in Paclitaxel Delivery. *Pharm. Res.* **2007**, *24* (11), 2099-2109.
48. Geng, Y.; Discher, D. E., Hydrolytic Degradation of Poly(ethylene oxide)-block-Polycaprolactone Worm Micelles. *J. Am. Chem. Soc.* **2005**, *127* (37), 12780-12781.
49. Nair, P. R.; Karthick, S.; Spinler, K. R.; Vakili, M. R.; Lavasanifar, A.; Discher, D. E., Filomicelles from aromatic diblock copolymers increase paclitaxel-induced tumor cell death and aneuploidy compared with aliphatic copolymers. *Nanomedicine* **2016**, *11* (12), 1551-1569.
50. Oltra, N. S.; Swift, J.; Mahmud, A.; Rajagopal, K.; Loverde, S. M.; Discher, D. E., Filomicelles in nanomedicine – from flexible, fragmentable, and ligand-targetable drug carrier designs to combination therapy for brain tumors. *Journal of Materials Chemistry B* **2013**, *1* (39), 5177.

51. Shen, X.; Liu, X.; Li, R.; Yun, P.; Li, C.; Su, F.; Li, S., Biocompatibility of filomicelles prepared from poly (ethylene glycol)-polylactide diblock copolymers as potential drug carrier. *Journal of Biomaterials science, Polymer edition* **2017**, *28* (15), 1677-1694.
52. Allen, S. D.; Liu, Y.-G.; Bobbala, S.; Cai, L.; Hecker, P. I.; Temel, R.; Scott, E. A., Polymersomes scalably fabricated via flash nanoprecipitation are non-toxic in non-human primates and associate with leukocytes in the spleen and kidney following intravenous administration. *Nano Research*, 1-15.
53. Le Devedec, F.; Won, A.; Oake, J.; Houdaihed, L.; Bohne, C.; Yip, C. M.; Allen, C., Postalkylation of a Common mPEG-b-PAGE Precursor to Produce Tunable Morphologies of Spheres, Filomicelles, Disks, and Polymersomes. *ACS Macro Letters* **2016**, *5* (1), 128-133.
54. Perrier, S., 50th Anniversary Perspective: RAFT Polymerization—A User Guide. *Macromolecules* **2017**, *50* (19), 7433-7447.
55. Qiu, L.; Xu, C.-R.; Zhong, F.; Hong, C.-Y.; Pan, C.-Y., Fabrication of Functional Nano-objects through RAFT Dispersion Polymerization and Influences of Morphology on Drug Delivery. **2016**, *8* (28), 18347-18359.
56. Geng, Y.; Dalhaimer, P.; Cai, S.; Tsai, R.; Tewari, M.; Minko, T.; Discher, D. E., Shape effects of filaments versus spherical particles in flow and drug delivery. *Nature nanotechnology* **2007**, *2* (4), 249.
57. Rajagopal, K.; Mahmud, A.; Christian, D. A.; Pajerowski, J. D.; Brown, A. E. X.; Loverde, S. M.; Discher, D. E., Curvature-Coupled Hydration of Semicrystalline Polymer Amphiphiles Yields flexible Worm Micelles but Favors Rigid Vesicles: Polycaprolactone-Based Block Copolymers. *Macromolecules* **2010**, *43* (23), 9736-9746.

58. Zhang, H., Thin-film hydration followed by extrusion method for liposome preparation. In *Liposomes*, Springer: 2017; pp 17-22.
59. Ghanbarzadeh, S.; Valizadeh, H.; Zakeri-Milani, P., Application of response surface methodology in development of sirolimus liposomes prepared by thin film hydration technique. *BioImpacts: BI* **2013**, 3 (2), 75.
60. Li, S.; Bobbala, S.; Vincent, M. P.; Modak, M.; Liu, Y.; Scott, E. A., Pi-Stacking Enhances Stability, Scalability of Formation, Control over Flexibility, and Circulation Time of Polymeric Filamentous Nanocarriers. *Advanced NanoBiomed Research* **2021**, 2100063.
61. He, W.-N.; Xu, J.-T., Crystallization assisted self-assembly of semicrystalline block copolymers. *Prog. Polym. Sci.* **2012**, 37 (10), 1350-1400.
62. Wang, X.; Guerin, G.; Wang, H.; Wang, Y.; Manners, I.; Winnik, M. A., Cylindrical Block Copolymer Micelles and Co-Micelles of Controlled Length and Architecture. *Science* **2007**, 317 (5838), 644-647.
63. Yu, W.; Foster, J. C.; Dove, A. P.; O'Reilly, R. K., Length Control of Biodegradable Fiber-Like Micelles via Tuning Solubility: A Self-Seeding Crystallization-Driven Self-Assembly of Poly(ϵ -caprolactone)-Containing Triblock Copolymers. *Macromolecules* **2020**, 53 (4), 1514-1521.
64. Lovett, J. R.; Ratcliffe, L. P. D.; Warren, N. J.; Armes, S. P.; Smallridge, M. J.; Cracknell, R. B.; Saunders, B. R., A Robust Cross-Linking Strategy for Block Copolymer Worms Prepared via Polymerization-Induced Self-Assembly. *Macromolecules* **2016**, 49 (8), 2928-2941.

65. Larue, I.; Adam, M.; Pitsikalis, M.; Hadjichristidis, N.; Rubinstein, M.; Sheiko, S. S., Reversible Morphological Transitions of Polystyrene-*b*-polyisoprene Micelles. *Macromolecules* **2006**, *39* (1), 309-314.
66. Truong, N. P.; Whittaker, M. R.; Anastasaki, A.; Haddleton, D. M.; Quinn, J. F.; Davis, T. P., Facile production of nanoaggregates with tuneable morphologies from thermoresponsive P(DEGMA-*co*-HPMA). *Polymer Chemistry* **2016**, *7* (2), 430-440.
67. Warren, N. J.; Derry, M. J.; Mykhaylyk, O. O.; Lovett, J. R.; Ratcliffe, L. P. D.; Ladmiral, V.; Blanazs, A.; Fielding, L. A.; Armes, S. P., Critical Dependence of Molecular Weight on Thermoresponsive Behavior of Diblock Copolymer Worm Gels in Aqueous Solution. *Macromolecules* **2018**, *51* (21), 8357-8371.
68. Yu, K.; Zhang, L.; Eisenberg, A., Novel Morphologies of “Crew-Cut” Aggregates of Amphiphilic Diblock Copolymers in Dilute Solution. *Langmuir* **1996**, *12* (25), 5980-5984.
69. Zhang, L.; Eisenberg, A., Thermodynamic vs Kinetic Aspects in the Formation and Morphological Transitions of Crew-Cut Aggregates Produced by Self-Assembly of Polystyrene-*b*-poly(acrylic acid) Block Copolymers in Dilute Solution. *Macromolecules* **1999**, *32* (7), 2239-2249.
70. Willner, L.; Poppe, A.; Allgaier, J.; Monkenbusch, M.; Richter, D., Time-resolved SANS for the determination of unimer exchange kinetics in block copolymer micelles. *Europhysics Letters (EPL)* **2001**, *55* (5), 667-673.
71. Lund, R.; Willner, L.; Stellbrink, J.; Lindner, P.; Richter, D., Logarithmic Chain-Exchange Kinetics of Diblock Copolymer Micelles. *Phys. Rev. Lett.* **2006**, *96* (6).

72. Lund, R.; Pipich, V.; Willner, L.; Radulescu, A.; Colmenero, J.; Richter, D., Structural and thermodynamic aspects of the cylinder-to-sphere transition in amphiphilic diblock copolymer micelles. *Soft Matter* **2011**, *7* (4), 1491-1500.
73. Zhulina, E. B.; Adam, M.; Larue, I.; Sheiko, S. S.; Rubinstein, M., Diblock Copolymer Micelles in a Dilute Solution. *Macromolecules* **2005**, *38* (12), 5330-5351.
74. Burke, S. E.; Eisenberg, A., Kinetics and Mechanisms of the Sphere-to-Rod and Rod-to-Sphere Transitions in the Ternary System PS310-b-PAA52/Dioxane/Water. *Langmuir* **2001**, *17* (21), 6705-6714.
75. La, Y.-H.; Edwards, E. W.; Park, S.-M.; Nealey, P. F., Directed Assembly of Cylinder-Forming Block Copolymer Films and Thermochemically Induced Cylinder to Sphere Transition: A Hierarchical Route to Linear Arrays of Nanodots. *Nano Lett.* **2005**, *5* (7), 1379-1384.
76. Vaidya, N. Y.; Han, C. D.; Kim, D.; Sakamoto, N.; Hashimoto, T., Microdomain Structures and Phase Transitions in Binary Blends Consisting of a Highly Asymmetric Block Copolymer and a Homopolymer. *Macromolecules* **2001**, *34* (2), 222-234.
77. Karabin, N. B.; Allen, S.; Kwon, H. K.; Bobbala, S.; Firlar, E.; Shokuhfar, T.; Shull, K. R.; Scott, E. A., Sustained micellar delivery via inducible transitions in nanostructure morphology. *Nat Commun* **2018**, *9* (1), 624.
78. Koppi, K. A.; Tirrell, M.; Bates, F. S.; Almdal, K.; Mortensen, K., Epitaxial growth and shearing of the body centered cubic phase in diblock copolymer melts. *J. Rheol.* **1994**, *38* (4), 999-1027.

79. Lund, R.; Willner, L.; Richter, D.; Lindner, P.; Narayanan, T., Kinetic Pathway of the Cylinder-to-Sphere Transition in Block Copolymer Micelles Observed in Situ by Time-Resolved Neutron and Synchrotron Scattering. *ACS Macro Letters* **2013**, *2* (12), 1082-1087.
80. Hartgerink, J. D.; Beniash, E.; Stupp, S. I., Peptide-amphiphile nanofibers: A versatile scaffold for the preparation of self-assembling materials. *Proceedings of the National Academy of Sciences* **2002**, *99* (8), 5133-5138.
81. Dalhaimer, P.; Bermudez, H.; Discher, D. E., Biopolymer mimicry with polymeric wormlike micelles: Molecular weight scaled flexibility, locked-in curvature, and coexisting microphases. *J. Polym. Sci., Part B: Polym. Phys.* **2004**, *42* (1), 168-176.
82. Yi, S.; Karabin, N. B.; Zhu, J.; Bobbala, S.; Lyu, H.; Li, S.; Liu, Y.; Frey, M.; Vincent, M.; Scott, E. A., An injectable hydrogel platform for sustained delivery of anti-inflammatory nanocarriers and induction of regulatory T cells in atherosclerosis. *Frontiers in Bioengineering and Biotechnology* **2020**, *8*, 542.
83. Larue, I.; Adam, M.; Da Silva, M.; Sheiko, S. S.; Rubinstein, M., Wormlike Micelles of Block Copolymers: Measuring the Linear Density by AFM and Light Scattering. *Macromolecules* **2004**, *37* (13), 5002-5005.
84. Simone, E. A.; Dziubla, T. D.; Discher, D. E.; Muzykantov, V. R., Filamentous Polymer Nanocarriers of Tunable Stiffness that Encapsulate the Therapeutic Enzyme Catalase. **2009**, *10* (6), 1324-1330.
85. Dalhaimer, P.; Engler, A. J.; Parthasarathy, R.; Discher, D. E., Targeted Worm Micelles. *Biomacromolecules* **2004**, *5* (5), 1714-1719.

86. Jelonek, K.; Li, S.; Kaczmarczyk, B.; Marcinkowski, A.; Orchel, A.; Musiał-Kulik, M.; Kasperczyk, J., Multidrug PLA-PEG filomicelles for concurrent delivery of anticancer drugs—The influence of drug-drug and drug-polymer interactions on drug loading and release properties. *International Journal of Pharmaceutics* **2016**, *510* (1), 365-374.
87. Frey, M.; Bobbala, S.; Karabin, N.; Scott, E., Influences of nanocarrier morphology on therapeutic immunomodulation. *Nanomedicine* **2018**, *13* (14), 1795-1811.
88. Geng, Y.; Dalhaimer, P.; Cai, S.; Tsai, R.; Tewari, M.; Minko, T.; Discher, D. E., Shape effects of filaments versus spherical particles in flow and drug delivery. *Nature Nanotechnology* **2007**, *2* (4), 249-255.
89. Dalhaimer, P.; Bates, F. S.; Discher, D. E., Single Molecule Visualization of Stable, Stiffness-Tunable, Flow-Conforming Worm Micelles. *Macromolecules* **2003**, *36* (18), 6873-6877.
90. Eliezar, J.; Scarano, W.; Boase, N. R. B.; Thurecht, K. J.; Stenzel, M. H., In Vivo Evaluation of Folate Decorated Cross-Linked Micelles for the Delivery of Platinum Anticancer Drugs. **2015**, *16* (2), 515-523.
91. Le, D. H. T.; Lee, K. L.; Shukla, S.; Commandeur, U.; Steinmetz, N. F., Potato virus X, a filamentous plant viral nanoparticle for doxorubicin delivery in cancer therapy. *Nanoscale* **2017**, *9* (6), 2348-2357.
92. Dasgupta, S.; Auth, T.; Gompper, G., Shape and Orientation Matter for the Cellular Uptake of Nonspherical Particles. *Nano Lett.* **2014**, *14* (2), 687-693.

93. Lock, L. L.; Reyes, C. D.; Zhang, P.; Cui, H., Tuning Cellular Uptake of Molecular Probes by Rational Design of Their Assembly into Supramolecular Nanoprobes. *J. Am. Chem. Soc.* **2016**, *138* (10), 3533-3540.
94. Yi, S.; Allen, S. D.; Liu, Y. G.; Ouyang, B. Z.; Li, X.; Augsornworawat, P.; Thorp, E. B.; Scott, E. A., Tailoring Nanostructure Morphology for Enhanced Targeting of Dendritic Cells in Atherosclerosis. *ACS Nano* **2016**, *10* (12), 11290-11303.
95. Allen, S.; Osorio, O.; Liu, Y.-G.; Scott, E., Facile assembly and loading of theranostic polymersomes via multi-impingement flash nanoprecipitation. *Journal of Controlled Release* **2017**, *262*, 91-103.
96. Karabin, N. B.; Vincent, M. P.; Allen, S. D.; Bobbala, S.; Frey, M. A.; Yi, S.; Yang, Y.; Scott, E. A., The Combination of Morphology and Surface Chemistry Defines the Biological Identity of Nanocarriers in Human Blood. *bioRxiv* **2020**, 2020.09.02.280404.
97. Soehnlein, O.; Steffens, S.; Hidalgo, A.; Weber, C., Neutrophils as protagonists and targets in chronic inflammation. *Nature Reviews Immunology* **2017**, *17* (4), 248-261.
98. Lecot, P.; Sarabi, M.; Pereira Abrantes, M.; Mussard, J.; Koenderman, L.; Caux, C.; Bendriss-Vermare, N.; Michallet, M.-C., Neutrophil Heterogeneity in Cancer: From Biology to Therapies. *Front Immunol* **2019**, *10* (2155).
99. Brostjan, C.; Oehler, R., The role of neutrophil death in chronic inflammation and cancer. *Cell Death Discovery* **2020**, *6* (1), 26.
100. Dowling, D. J.; Scott, E. A.; Scheid, A.; Bergelson, I.; Joshi, S.; Pietrasanta, C.; Brightman, S.; Sanchez-Schmitz, G.; Van Haren, S. D.; Ninković, J.; Kats, D.; Guiducci, C.; de Titta, A.; Bonner, D. K.; Hirosue, S.; Swartz, M. A.; Hubbell, J. A.; Levy, O., Toll-like

receptor 8 agonist nanoparticles mimic immunomodulating effects of the live BCG vaccine and enhance neonatal innate and adaptive immune responses. *Journal of Allergy and Clinical Immunology* **2017**, *140* (5), 1339-1350.

101. Shuvaev, V. V.; Ilies, M. A.; Simone, E.; Zaitsev, S.; Kim, Y.; Cai, S.; Mahmud, A.; Dziubla, T.; Muro, S.; Discher, D. E.; Muzykantov, V. R., Endothelial Targeting of Antibody-Decorated Polymeric Filomicelles. *ACS Nano* **2011**, *5* (9), 6991-6999.

102. Mandal, S.; Eksteen-Akeroyd, Z. H.; Jacobs, M. J.; Hammink, R.; Koepf, M.; Lambeck, A. J. A.; Van Hest, J. C. M.; Wilson, C. J.; Blank, K.; Figdor, C. G.; Rowan, A. E., Therapeutic nanoworms: towards novel synthetic dendritic cells for immunotherapy. **2013**, *4* (11), 4168.

103. Mandal, S.; Hammink, R.; Tel, J.; Eksteen-Akeroyd, Z. H.; Rowan, A. E.; Blank, K.; Figdor, C. G., Polymer-Based Synthetic Dendritic Cells for Tailoring Robust and Multifunctional T Cell Responses. *ACS Chemical Biology* **2015**, *10* (2), 485-492.

104. Hammink, R.; Mandal, S.; Eggermont, L. J.; Nooteboom, M.; Willems, P. H. G. M.; Tel, J.; Rowan, A. E.; Figdor, C. G.; Blank, K. G., Controlling T-Cell Activation with Synthetic Dendritic Cells Using the Multivalency Effect. *ACS Omega* **2017**, *2* (3), 937-945.

105. Serrano, C. M.; Freeman, R.; Godbe, J.; Lewis, J. A.; Stupp, S. I., DNA-Peptide Amphiphile Nanofibers Enhance Aptamer Function. *ACS Applied Bio Materials* **2019**, *2* (7), 2955-2963.

106. Chung, J.; Jung, Y.; Hong, C.; Kim, S.; Moon, S.; Kwak, E. A.; Jeung Hwang, B.; Park, S.-H.; Lin Seong, B.; Kweon, D.-H.; Chung, W.-J., Filamentous anti-influenza agents wrapping around viruses. *J. Colloid Interface Sci.* **2020**.

107. Zhang, Z.; Liu, C.; Li, C.; Wu, W.; Jiang, X., Shape Effects of Cylindrical versus Spherical Unimolecular Polymer Nanomaterials on in Vitro and in Vivo Behaviors. *Research* **2019**, *2019*, 2391486.
108. Qiu, L.; Xu, C.-R.; Zhong, F.; Hong, C.-Y.; Pan, C.-Y., Fabrication of Functional Nano-objects through RAFT Dispersion Polymerization and Influences of Morphology on Drug Delivery. *ACS Applied Materials & Interfaces* **2016**, *8* (28), 18347-18359.
109. Jelonek, K.; Kasperczyk, J.; Li, S.; Nguyen, T. H. N.; Orchel, A.; Chodurek, E.; Padiuszyński, P.; Jaworska-Kik, M.; Chrobak, E.; Bębenek, E.; Boryczka, S.; Jarosz-Biej, M.; Smolarczyk, R.; Foryś, A., Bioresorbable filomicelles for targeted delivery of betulin derivative – In vitro study. *Int. J. Pharm.* **2019**, *557*, 43-52.
110. Paranjpe, M.; Müller-Goymann, C. C., Nanoparticle-mediated pulmonary drug delivery: a review. *International journal of molecular sciences* **2014**, *15* (4), 5852-5873.
111. Mahmud, A.; Discher, D. E., Lung vascular targeting through inhalation delivery: insight from filamentous viruses and other shapes. *IUBMB life* **2011**, *63* (8), 607-612.
112. Mahmud, A.; Harada, T.; Rajagopal, K.; Christian, D. A.; Nair, P.; Murphy, R.; Discher, D. E., Spray stability of self-assembled filaments for delivery. *Journal of Controlled Release* **2017**, *263*, 162-171.
113. Esser, L.; Truong Phuoc, N.; Karagoz, B.; Moffat, B. A.; Boyer, C.; Quinn, J. F.; Whittaker, M. R.; Davis, T. P., Gadolinium-Functionalized Nanoparticles for Application as Magnetic Resonance Imaging Contrast Agents via Polymerization-Induced Self-Assembly. *Polym. Chem.* **2016**, *7*, 7325-7337.

114. Park, J.-H.; Von Maltzahn, G.; Zhang, L.; Schwartz, M. P.; Ruoslahti, E.; Bhatia, S. N.; Sailor, M. J., Magnetic Iron Oxide Nanoworms for Tumor Targeting and Imaging. *Advanced Materials* **2008**, *20* (9), 1630-1635.
115. Wang, G.; Inturi, S.; Serkova, N. J.; Merkulov, S.; McCrae, K.; Russek, S. E.; Banda, N. K.; Simberg, D., High-relaxivity superparamagnetic iron oxide nanoworms with decreased immune recognition and long-circulating properties. *ACS nano* **2014**, *8* (12), 12437-12449.
116. Ahmadi, Y.; Kostenich, G.; Oron-Herman, M.; Wadsak, W.; Mitterhauser, M.; Orenstein, A.; Mirzaei, S.; Knoll, P., In vivo magnetic resonance imaging of pancreatic tumors using iron oxide nanoworms targeted with PTR86 peptide. *Colloids and Surfaces B: Biointerfaces* **2017**, *158*, 423-430.
117. Chesson, C. B.; Huante, M.; Nusbaum, R. J.; Walker, A. G.; Clover, T. M.; Chinnaswamy, J.; Endsley, J. J.; Rudra, J. S., Nanoscale Peptide Self-assemblies Boost BCG-primed Cellular Immunity Against Mycobacterium tuberculosis. *Scientific Reports* **2018**, *8* (1), 12519.
118. Si, Y.; Wen, Y.; Kelly, S. H.; Chong, A. S.; Collier, J. H., Intranasal delivery of adjuvant-free peptide nanofibers elicits resident CD8⁺ T cell responses. *Journal of Controlled Release* **2018**, *282*, 120-130.
119. Rangel-Argote, M.; Claudio-Rizo, J. A.; Mata-Mata, J. L.; Mendoza-Novelo, B., Characteristics of Collagen-Rich Extracellular Matrix Hydrogels and Their Functionalization with Poly(ethylene glycol) Derivatives for Enhanced Biomedical Applications: A Review. *ACS Applied Bio Materials* **2018**, *1* (5), 1215-1228.

120. Zhang, Y. S.; Khademhosseini, A., Advances in engineering hydrogels. *Science* **2017**, *356* (6337), eaaf3627.
121. Annabi, N.; Nichol, J. W.; Zhong, X.; Ji, C.; Koshy, S.; Khademhosseini, A.; Dehghani, F., Controlling the Porosity and Microarchitecture of Hydrogels for Tissue Engineering. *Tissue Engineering Part B: Reviews* **2010**, *16* (4), 371-383.
122. Vasdekis, A. E.; Scott, E. A.; O'Neil, C. P.; Psaltis, D.; Hubbell, J. A., Precision Intracellular Delivery Based on Optofluidic Polymersome Rupture. *ACS Nano* **2012**, *6* (9), 7850-7857.
123. Authimoolam, S. P.; Lakes, A. L.; Puleo, D. A.; Dziubla, T. D., Layer-by-Layers of Polymeric Micelles as a Biomimetic Drug-Releasing Network. *Macromolecular Bioscience* **2016**, *16* (2), 242-254.
124. Canton, I.; Warren, N. J.; Chahal, A.; Amps, K.; Wood, A.; Weightman, R.; Wang, E.; Moore, H.; Armes, S. P., Mucin-Inspired Thermoresponsive Synthetic Hydrogels Induce Stasis in Human Pluripotent Stem Cells and Human Embryos. *ACS Central Science* **2016**, *2* (2), 65-74.
125. Redondo-Gómez, C.; Padilla-Lopategui, S.; Azevedo, H. S.; Mata, A., Host-Guest-Mediated Epitope Presentation on Self-Assembled Peptide Amphiphile Hydrogels. *ACS Biomaterials Science & Engineering* **2020**, *6* (9), 4870-4880.
126. Lewis, J. A.; Freeman, R.; Carrow, J. K.; Clemons, T. D.; Palmer, L. C.; Stupp, S. I., Transforming Growth Factor β -1 Binding by Peptide Amphiphile Hydrogels. *ACS Biomaterials Science & Engineering* **2020**, *6* (8), 4551-4560.

127. Freeman, R.; Han, M.; Álvarez, Z.; Lewis, J. A.; Wester, J. R.; Stephanopoulos, N.; McClendon, M. T.; Lynsky, C.; Godbe, J. M.; Sangji, H.; Luijten, E.; Stupp, S. I., Reversible self-assembly of superstructured networks. *Science* **2018**, *362* (6416), 808-813.
128. O'Donnell, M. J.; Zhou, C.; Scott, W. L., Solid-Phase Unnatural Peptide Synthesis (UPS). *Journal of the American Chemical Society* **1996**, *118* (25), 6070-6071.
129. Liang, P.; Zheng, J.; Zhang, Z.; Hou, Y.; Wang, J.; Zhang, C.; Quan, C., Bioactive 3D scaffolds self-assembled from phosphorylated mimicking peptide amphiphiles to enhance osteogenesis. *J Biomater Sci Polym Ed* **2019**, *30* (1), 34-48.
130. Chen, C. H.; Hsu, E. L.; Stupp, S. I., Supramolecular self-assembling peptides to deliver bone morphogenetic proteins for skeletal regeneration. *Bone* **2020**, *141*, 115565.
131. Arioiz, I.; Erol, O.; Bakan, G.; Dikecoglu, F. B.; Topal, A. E.; Urel, M.; Dana, A.; Tekinay, A. B.; Guler, M. O., Biocompatible Electroactive Tetra(aniline)-Conjugated Peptide Nanofibers for Neural Differentiation. *ACS Appl Mater Interfaces* **2018**, *10* (1), 308-317.
132. Berns, E. J.; Álvarez, Z.; Goldberger, J. E.; Boekhoven, J.; Kessler, J. A.; Kuhn, H. G.; Stupp, S. I., A tenascin-C mimetic peptide amphiphile nanofiber gel promotes neurite outgrowth and cell migration of neurosphere-derived cells. *Acta Biomater* **2016**, *37*, 50-8.
133. Hainline, K. M.; Gu, F.; Handley, J. F.; Tian, Y. F.; Wu, Y.; De Wet, L.; Vander Griend, D. J.; Collier, J. H., Self-Assembling Peptide Gels for 3D Prostate Cancer Spheroid Culture. *Macromolecular Bioscience* **2019**, *19* (1), 1800249.
134. Matsuoka, A. J.; Sayed, Z. A.; Stephanopoulos, N.; Berns, E. J.; Wadhwani, A. R.; Morrissey, Z. D.; Chadly, D. M.; Kobayashi, S.; Edelbrock, A. N.; Mashimo, T.; Miller, C.

- A.; McGuire, T. L.; Stupp, S. I.; Kessler, J. A., Creating a stem cell niche in the inner ear using self-assembling peptide amphiphiles. *PLOS ONE* **2017**, *12* (12), e0190150.
135. Shah, R. N.; Shah, N. A.; Del Rosario Lim, M. M.; Hsieh, C.; Nuber, G.; Stupp, S. I., Supramolecular design of self-assembling nanofibers for cartilage regeneration. *Proceedings of the National Academy of Sciences* **2010**, *107* (8), 3293-3298.
136. Edelbrock, A. N.; Álvarez, Z.; Simkin, D.; Fyrner, T.; Chin, S. M.; Sato, K.; Kiskinis, E.; Stupp, S. I., Supramolecular Nanostructure Activates TrkB Receptor Signaling of Neuronal Cells by Mimicking Brain-Derived Neurotrophic Factor. *Nano Letters* **2018**, *18* (10), 6237-6247.
137. Thoenen, H.; Sendtner, M., Neurotrophins: from enthusiastic expectations through sobering experiences to rational therapeutic approaches. *Nat Neurosci* **2002**, *5 Suppl*, 1046-50.
138. Charcosset, C.; Juban, A.; Valour, J.-P.; Urbaniak, S.; Fessi, H., Preparation of liposomes at large scale using the ethanol injection method: Effect of scale-up and injection devices. *Chem. Eng. Res. Des.* **2015**, *94*, 508-515.
139. Elzainy, A. A.; Gu, X.; Simons, F. E. R.; Simons, K. J., Hydroxyzine-and cetirizine-loaded liposomes: effect of duration of thin film hydration, freeze-thawing, and changing buffer pH on encapsulation and stability. *Drug Dev. Ind. Pharm.* **2005**, *31* (3), 281-291.
140. Saad, W. S.; Prud'Homme, R. K., Principles of nanoparticle formation by flash nanoprecipitation. *Nano Today* **2016**, *11* (2), 212-227.
141. Allen, S.; Vincent, M.; Scott, E., Rapid, Scalable Assembly and Loading of Bioactive Proteins and Immunostimulants into Diverse Synthetic Nanocarriers Via Flash Nanoprecipitation. *Journal of Visualized Experiments* **2018**, (138), e57793.

142. Johnson, B. K.; Prud'homme, R. K., Flash nanoprecipitation of organic actives and block copolymers using a confined impinging jets mixer. *Aust. J. Chem.* **2003**, *56* (10), 1021-1024.
143. Han, J.; Zhu, Z.; Qian, H.; Wohl, A. R.; Beaman, C. J.; Hoye, T. R.; Macosko, C. W., A simple confined impingement jets mixer for flash nanoprecipitation. *J. Pharm. Sci.* **2012**, *101* (10), 4018-4023.
144. Bobbala, S.; Allen, S. D.; Scott, E. A., Flash nanoprecipitation permits versatile assembly and loading of polymeric bicontinuous cubic nanospheres. *Nanoscale* **2018**.
145. Tang, C.; Amin, D.; Messersmith, P. B.; Anthony, J. E.; Prud'Homme, R. K., Polymer Directed Self-Assembly of pH-Responsive Antioxidant Nanoparticles. *Langmuir* **2015**, *31* (12), 3612-3620.
146. Grundy, L. S.; Lee, V. E.; Li, N.; Sosa, C.; Mulhearn, W. D.; Liu, R.; Register, R. A.; Nikoubashman, A.; Prud'Homme, R. K.; Panagiotopoulos, A. Z.; Priestley, R. D., Rapid Production of Internally Structured Colloids by Flash Nanoprecipitation of Block Copolymer Blends. *ACS Nano* **2018**, *12* (5), 4660-4668.
147. Wang, M.; Xu, Y.; Liu, Y.; Gu, K.; Tan, J.; Shi, P.; Yang, D.; Guo, Z.; Zhu, W.; Guo, X.; Cohen Stuart, M. A., Morphology Tuning of Aggregation-Induced Emission Probes by Flash Nanoprecipitation: Shape and Size Effects on in Vivo Imaging. *ACS Applied Materials & Interfaces* **2018**, *10* (30), 25186-25193.
148. Anselmo, A. C.; Mitragotri, S., Impact of particle elasticity on particle-based drug delivery systems. *Advanced Drug Delivery Reviews* **2017**, *108*, 51-67.
149. Pawley, J., *Handbook of biological confocal microscopy*. Springer Science & Business Media: 2006; Vol. 236.

150. Schermelleh, L.; Ferrand, A.; Huser, T.; Eggeling, C.; Sauer, M.; Biehlmaier, O.; Drummen, G. P. C., Super-resolution microscopy demystified. *Nature Cell Biology* **2019**, *21* (1), 72-84.
151. Valades Cruz, C. A.; Shaban, H. A.; Kress, A.; Bertaux, N.; Monneret, S.; Mavrakis, M.; Savatier, J.; Brasselet, S., Quantitative nanoscale imaging of orientational order in biological filaments by polarized superresolution microscopy. *Proceedings of the National Academy of Sciences* **2016**, *113* (7), E820-E828.
152. Kolpe, A.; Arista-Romero, M.; Schepens, B.; Pujals, S.; Saelens, X.; Albertazzi, L., Super-resolution microscopy reveals significant impact of M2e-specific monoclonal antibodies on influenza A virus filament formation at the host cell surface. *Scientific Reports* **2019**, *9* (1).
153. Wu, Y.; Shroff, H., Faster, sharper, and deeper: structured illumination microscopy for biological imaging. *Nature Methods* **2018**, *15* (12), 1011-1019.
154. Li, D.; Shao, L.; Chen, B. C.; Zhang, X.; Zhang, M.; Moses, B.; Milkie, D. E.; Beach, J. R.; Hammer, J. A.; Pasham, M.; Kirchhausen, T.; Baird, M. A.; Davidson, M. W.; Xu, P.; Betzig, E., Extended-resolution structured illumination imaging of endocytic and cytoskeletal dynamics. *Science* **2015**, *349* (6251), aab3500-aab3500.
155. Schoonbeek, F. S.; Van Esch, J. H.; Wegewijs, B.; Rep, D. B.; De Haas, M. P.; Klapwijk, T. M.; Kellogg, R. M.; Feringa, B. L., Efficient intermolecular charge transport in self-assembled fibers of mono- and bithiophene bisurea compounds. *Angew. Chem. Int. Ed.* **1999**, *38* (10), 1393-1397.

156. Yagai, S.; Monma, Y.; Kawauchi, N.; Karatsu, T.; Kitamura, A., Supramolecular Nanoribbons and Nanoropes Generated from Hydrogen-Bonded Supramolecular Polymers Containing Perylene Bisimide Chromophores. *Org. Lett.* **2007**, *9* (6), 1137-1140.
157. Zhang, X.; Chen, Z.; Würthner, F., Morphology control of fluorescent nanoaggregates by co-self-assembly of wedge-and dumbbell-shaped amphiphilic perylene bisimides. *J. Am. Chem. Soc.* **2007**, *129* (16), 4886-4887.
158. Du, F.; Liu, Y.-G.; Scott, E. A., Immunotheranostic Polymersomes Modularly Assembled from Tetrablock and Diblock Copolymers with Oxidation-Responsive Fluorescence. *Cellular and molecular bioengineering* **2017**, *10* (5), 357-370.
159. Bobbala, S.; Allen, S. D.; Yi, S.; Vincent, M.; Frey, M.; Karabin, N. B.; Scott, E. A., Employing bicontinuous-to-micellar transitions in nanostructure morphology for on-demand photo-oxidation responsive cytosolic delivery and off-on cytotoxicity. *Nanoscale* **2020**, *12* (9), 5332-5340.
160. Modak, M.; Bobbala, S.; Lescott, C.; Liu, Y.-G.; Nandwana, V.; Dravid, V. P.; Scott, E. A., Magnetic Nanostructure-Loaded Bicontinuous Nanospheres Support Multicargo Intracellular Delivery and Oxidation-Responsive Morphological Transitions. *ACS Applied Materials & Interfaces* **2020**, *12* (50), 55584-55595.
161. Kaiser, E.; Colecott, R.; Bossinger, C.; Cook, P., Color test for detection of free terminal amino groups in the solid-phase synthesis of peptides. *Anal. Biochem.* **1970**, *34* (2), 595-598.
162. Vincent, M. P.; Karabin, N. B.; Allen, S. D.; Bobbala, S.; Frey, M. A.; Yi, S.; Yang, Y.; Scott, E. A., The Combination of Morphology and Surface Chemistry Defines the

- Immunological Identity of Nanocarriers in Human Blood. *Advanced Therapeutics* **2021**, 2100062.
163. Greim, H.; Bury, D.; Klimisch, H. J.; Oeben-Negele, M.; Ziegler-Skylakakis, K., Toxicity of aliphatic amines: Structure-activity relationship. *Chemosphere* **1998**, *36* (2), 271-295.
164. Velluto, D.; Bojadzic, D.; De Toni, T.; Buchwald, P.; Tomei, A. A., Drug-Integrating Amphiphilic Nanomaterial Assemblies: 1. Spatiotemporal control of cyclosporine delivery and activity using nanomicelles and nanofibrils. *J. Controlled Release* **2021**, *329*, 955-970.
165. Brubaker, C. E.; Velluto, D.; Demurtas, D.; Phelps, E. A.; Hubbell, J. A., Crystalline Oligo(ethylene sulfide) Domains Define Highly Stable Supramolecular Block Copolymer Assemblies. *ACS Nano* **2015**, *9* (7), 6872-6881.
166. Górecki, R.; Antenucci, F.; Norinkevicius, K.; Elmstrøm Christiansen, L.; Myers, S. T.; Trzaskus, K.; Hélix-Nielsen, C., Effect of Detergents on Morphology, Size Distribution, and Concentration of Copolymer-Based Polymersomes. *Langmuir* **2021**, *37* (6), 2079-2090.
167. Wurthner, F., Perylene bisimide dyes as versatile building blocks for functional supramolecular architectures. *Chem. Commun.* **2004**, (14), 1564-1579.
168. Backes, C.; Schmidt, C. D.; Hauke, F.; Böttcher, C.; Hirsch, A., High Population of Individualized SWCNTs through the Adsorption of Water-Soluble Perylenes. *J. Am. Chem. Soc.* **2009**, *131* (6), 2172-2184.
169. Xu, Z.; Cheng, W.; Guo, K.; Yu, J.; Shen, J.; Tang, J.; Yang, W.; Yin, M., Molecular Size, Shape, and Electric Charges: Essential for Perylene Bisimide-Based DNA Intercalator to Localize in Cell Nuclei and Inhibit Cancer Cell Growth. **2015**, *7* (18), 9784-9791.

170. Xu, Z.; Guo, K.; Yu, J.; Sun, H.; Tang, J.; Shen, J.; Müllen, K.; Yang, W.; Yin, M., A Unique Perylene-Based DNA Intercalator: Localization in Cell Nuclei and Inhibition of Cancer Cells and Tumors. **2014**, n/a-n/a.
171. Müllner, M.; Dodds, S. J.; Nguyen, T.-H.; Senyschyn, D.; Porter, C. J. H.; Boyd, B. J.; Caruso, F., Size and Rigidity of Cylindrical Polymer Brushes Dictate Long Circulating Properties In Vivo. *ACS Nano* **2015**, *9* (2), 1294-1304.
172. Wang, Y.; Smith, W.; Hao, D.; He, B.; Kong, L., M1 and M2 macrophage polarization and potentially therapeutic naturally occurring compounds. *International Immunopharmacology* **2019**, *70*, 459-466.
173. Nonnenmacher, Y.; Hiller, K., Biochemistry of proinflammatory macrophage activation. *Cellular and Molecular Life Sciences* **2018**, *75* (12), 2093-2109.
174. Mosser, D. M.; Gonçalves, R., Activation of Murine Macrophages. *Current Protocols in Immunology* **2015**, *111* (1).
175. Ke, X.; Howard, G. P.; Tang, H.; Cheng, B.; Saung, M. T.; Santos, J. L.; Mao, H. Q., Physical and chemical profiles of nanoparticles for lymphatic targeting. *Adv Drug Deliv Rev* **2019**, *151-152*, 72-93.
176. Park, E.-J.; Kim, S. N.; Kang, M.-S.; Lee, B.-S.; Yoon, C.; Jeong, U.; Kim, Y.; Lee, G.-H.; Kim, D.-W.; Kim, J. S., A higher aspect ratio enhanced bioaccumulation and altered immune responses due to intravenously-injected aluminum oxide nanoparticles. *Journal of Immunotoxicology* **2016**, *13* (4), 439-448.

177. Li, Z.; Sun, L.; Zhang, Y.; Dove, A. P.; O'Reilly, R. K.; Chen, G., Shape Effect of Glyco-Nanoparticles on Macrophage Cellular Uptake and Immune Response. *ACS Macro Letters* **2016**, *5* (9), 1059-1064.
178. Sato, Y.; Yokoyama, A.; Shibata, K.-I.; Akimoto, Y.; Ogino, S.-I.; Nodasaka, Y.; Kohgo, T.; Tamura, K.; Akasaka, T.; Uo, M.; Motomiya, K.; Jeyadevan, B.; Ishiguro, M.; Hatakeyama, R.; Watari, F.; Tohji, K., Influence of length on cytotoxicity of multi-walled carbon nanotubes against human acute monocytic leukemia cell line THP-1 in vitro and subcutaneous tissue of rats in vivo. *Molecular BioSystems* **2005**, *1* (2), 176.
179. Cohen, A. E.; Mahadevan, L., Kinks, rings, and rackets in filamentous structures. *Proceedings of the National Academy of Sciences* **2003**, *100* (21), 12141-12146.
180. Nagai, H.; Okazaki, Y.; Chew, S. H.; Misawa, N.; Yamashita, Y.; Akatsuka, S.; Ishihara, T.; Yamashita, K.; Yoshikawa, Y.; Yasui, H.; Jiang, L.; Ohara, H.; Takahashi, T.; Ichihara, G.; Kostarelos, K.; Miyata, Y.; Shinohara, H.; Toyokuni, S., Diameter and rigidity of multiwalled carbon nanotubes are critical factors in mesothelial injury and carcinogenesis. *Proceedings of the National Academy of Sciences* **2011**, *108* (49), E1330-E1338.
181. Francis, A. P.; Devasena, T., Toxicity of carbon nanotubes: A review. *Toxicology and Industrial Health* **2018**, *34* (3), 200-210.
182. Zhao, Z.; Ukidve, A.; Krishnan, V.; Mitragotri, S., Effect of physicochemical and surface properties on in vivo fate of drug nanocarriers. *Advanced Drug Delivery Reviews* **2019**, *143*, 3-21.
183. Huo, M.; Yuan, J.; Tao, L.; Wei, Y., Redox-responsive polymers for drug delivery: from molecular design to applications. *Polym. Chem.* **2014**, *5* (5), 1519-1528.

184. Tavares, A. J.; Poon, W.; Zhang, Y.-N.; Dai, Q.; Besla, R.; Ding, D.; Ouyang, B.; Li, A.; Chen, J.; Zheng, G.; Robbins, C.; Chan, W. C. W., Effect of removing Kupffer cells on nanoparticle tumor delivery. *Proceedings of the National Academy of Sciences* **2017**, *114* (51), E10871-E10880.
185. Swirski, F. K.; Nahrendorf, M.; Etzrodt, M.; Wildgruber, M.; Cortez-Retamozo, V.; Panizzi, P.; Figueiredo, J.-L.; Kohler, R. H.; Chudnovskiy, A.; Waterman, P.; Aikawa, E.; Mempel, T. R.; Libby, P.; Weissleder, R.; Pittet, M. J., Identification of Splenic Reservoir Monocytes and Their Deployment to Inflammatory Sites. *Science* **2009**, *325* (5940), 612-616.
186. Ishibashi, H.; Nakamura, M.; Komori, A.; Migita, K.; Shimoda, S., Liver architecture, cell function, and disease. *Seminars in Immunopathology* **2009**, *31* (3), 399-409.
187. Soysa, R.; Wu, X.; Crispe, I. N., Dendritic cells in hepatitis and liver transplantation. *Liver Transplantation* **2017**, *23* (11), 1433-1439.
188. Saraiva, M.; O'Garra, A., The regulation of IL-10 production by immune cells. *Nature Reviews Immunology* **2010**, *10* (3), 170-181.
189. Scott, E. A.; Stano, A.; Gillard, M.; Maio-Liu, A. C.; Swartz, M. A.; Hubbell, J. A., Dendritic cell activation and T cell priming with adjuvant-and antigen-loaded oxidation-sensitive polymersomes. *Biomaterials* **2012**, *33* (26), 6211-6219.
190. Allen, S. D.; Liu, Y.-G.; Bobbala, S.; Cai, L.; Hecker, P. I.; Temel, R.; Scott, E. A., Polymersomes scalably fabricated via flash nanoprecipitation are non-toxic in non-human primates and associate with leukocytes in the spleen and kidney following intravenous administration. *Nano Research* **2018**, *11* (10), 5689-5703.

191. Anselmo, A. C.; Zhang, M.; Kumar, S.; Vogus, D. R.; Menegatti, S.; Helgeson, M. E.; Mitragotri, S., Elasticity of Nanoparticles Influences Their Blood Circulation, Phagocytosis, Endocytosis, and Targeting. *ACS Nano* **2015**, *9* (3), 3169-3177.
192. Pérez-Molina, J. A.; Molina, I., Chagas disease. *Lancet* **2018**, *391* (10115), 82-94.
193. Ventura-Garcia, L.; Roura, M.; Pell, C.; Posada, E.; Gascón, J.; Aldasoro, E.; Muñoz, J.; Pool, R., Socio-Cultural Aspects of Chagas Disease: A Systematic Review of Qualitative Research. *PLoS Neglected Tropical Diseases* **2013**, *7* (9), e2410.
194. Health, C. C. f. G. Epidemiology and Risk Factors.
<https://www.cdc.gov/parasites/chagas/epi.html>.
195. Bern, C.; Messenger, L. A.; Whitman, J. D.; Maguire, J. H., Chagas Disease in the United States: a Public Health Approach. *Clinical Microbiology Reviews* **2019**, *33* (1).
196. López-Vélez, R.; Norman, F.; Bern, C., American trypanosomiasis (Chagas disease), p 762–765. *Hunter's tropical medicine and emerging infectious disease, 10th ed. Elsevier, London, United Kingdom* **2019**.
197. Tyler, K. M.; Engman, D. M., The life cycle of *Trypanosoma cruzi* revisited. *International Journal for Parasitology* **2001**, *31* (5-6), 472-481.
198. Caradonna, K. L.; Burleigh, B. A., Mechanisms of Host Cell Invasion by *Trypanosoma cruzi*. Elsevier: 2011; pp 33-61.
199. Carter, Y. L.; Juliano, J. J.; Montgomery, S. P.; Qvarnstrom, Y., Acute Chagas Disease in a Returning Traveler. *The American Journal of Tropical Medicine and Hygiene* **2012**, *87* (6), 1038-1040.

200. Andrade, D. V.; Gollob, K. J.; Dutra, W. O., Acute Chagas Disease: New Global Challenges for an Old Neglected Disease. *PLoS Neglected Tropical Diseases* **2014**, *8* (7), e3010.
201. Acquatella, H.; Asch, F. M.; Barbosa, M. M.; Barros, M.; Bern, C.; Cavalcante, J. L.; Echeverria Correa, L. E.; Lima, J.; Marcus, R.; Marin-Neto, J. A.; Migliore, R.; Milei, J.; Morillo, C. A.; Nunes, M. C. P.; Campos Vieira, M. L.; Viotti, R., Recommendations for Multimodality Cardiac Imaging in Patients with Chagas Disease: A Report from the American Society of Echocardiography in Collaboration With the InterAmerican Association of Echocardiography (ECOSIAC) and the Cardiovascular Imaging Depa. *Journal of the American Society of Echocardiography* **2018**, *31* (1), 3-25.
202. Barreto-De-Albuquerque, J.; Silva-Dos-Santos, D.; Pérez, A. R.; Berbert, L. R.; Santana-Van-Vliet, E. D.; Farias-De-Oliveira, D. A.; Moreira, O. C.; Roggero, E.; Carvalho-Pinto, C. E. D.; Jurberg, J.; Cotta-De-Almeida, V.; Bottasso, O.; Savino, W.; Meis, J. D., Trypanosoma cruzi Infection through the Oral Route Promotes a Severe Infection in Mice: New Disease Form from an Old Infection? *PLOS Neglected Tropical Diseases* **2015**, *9* (6), e0003849.
203. Benck, L.; Kransdorf, E.; Patel, J., Diagnosis and Management of Chagas Cardiomyopathy in the United States. *Current Cardiology Reports* **2018**, *20* (12).
204. De Oliveira, R., Gastrointestinal manifestations of chagas' disease. *The American Journal of Gastroenterology* **1998**, *93* (6), 884-889.
205. Arrúa, E. C.; Seremeta, K. P.; Bedogni, G. R.; Okulik, N. B.; Salomon, C. J., Nanocarriers for effective delivery of benznidazole and nifurtimox in the treatment of chagas disease: A review. *Acta Tropica* **2019**, *198*, 105080.

206. Lascano, F.; Altcheh, J., An evaluation of nifurtimox for Chagas disease in children. *Expert Opinion on Orphan Drugs* **2021**, *9* (5), 139-149.
207. Viotti, R.; Vigliano, C.; Lococo, B.; Alvarez, M. G.; Petti, M.; Bertocchi, G.; Armenti, A., Side effects of benznidazole as treatment in chronic Chagas disease: fears and realities. *Expert review of anti-infective therapy* **2009**, *7* (2), 157-163.
208. Stass, H.; Feleder, E.; Garcia-Bournissen, F.; Nagelschmitz, J.; Weimann, B.; Yerino, G.; Altcheh, J., Biopharmaceutical Characteristics of Nifurtimox Tablets for Age- and Body Weight-Adjusted Dosing in Patients With Chagas Disease. *Clinical Pharmacology in Drug Development* **2021**, *10* (5), 542-555.
209. Bern, C., Chagas' Disease. *N Engl J Med* **2015**, *373* (5), 456-66.
210. Maximiano, F. P.; Costa, G. H. Y.; Souza, J. d.; Cunha-Filho, M. S. S. d., Caracterização físico-química do fármaco antichagásico benznidazol. *Quim. Nova* **2010**, *33*, 1714-1719.
211. Kasim, N. A.; Whitehouse, M.; Ramachandran, C.; Bermejo, M.; Lennernäs, H.; Hussain, A. S.; Junginger, H. E.; Stavchansky, S. A.; Midha, K. K.; Shah, V. P.; Amidon, G. L., Molecular Properties of WHO Essential Drugs and Provisional Biopharmaceutical Classification. *Molecular Pharmaceutics* **2004**, *1* (1), 85-96.
212. Quijia Quezada, C.; Azevedo, C. S.; Charneau, S.; Santana, J. M.; Chorilli, M.; Carneiro, M. B.; Bastos, I. M. D., <p>Advances in nanocarriers as drug delivery systems in Chagas disease</p>. *International Journal of Nanomedicine* **2019**, *Volume 14*, 6407-6424.

213. Sur, S.; Rathore, A.; Dave, V.; Reddy, K. R.; Chouhan, R. S.; Sadhu, V., Recent developments in functionalized polymer nanoparticles for efficient drug delivery system. *Nano-Structures & Nano-Objects* **2019**, *20*.
214. Shields, C. W.; Wang, L. L. W.; Evans, M. A.; Mitragotri, S., Materials for Immunotherapy. *Adv. Mater.* **2020**, *32* (13), 1901633.
215. Baptista, P. V.; McCusker, M. P.; Carvalho, A.; Ferreira, D. A.; Mohan, N. M.; Martins, M.; Fernandes, A. R., Nano-Strategies to Fight Multidrug Resistant Bacteria-"A Battle of the Titans". *Front Microbiol* **2018**, *9*, 1441.
216. Rial, M. S.; Scalise, M. L.; Arrúa, E. C.; Esteva, M. I.; Salomon, C. J.; Fichera, L. E., Elucidating the impact of low doses of nano-formulated benznidazole in acute experimental Chagas disease. *PLOS Neglected Tropical Diseases* **2017**, *11* (12), e0006119.
217. Li, X.; Yi, S.; Scariot, D. B.; Martinez, S. J.; Falk, B. A.; Olson, C. L.; Romano, P. S.; Scott, E. A.; Engman, D. M., Nanocarrier-enhanced intracellular delivery of benznidazole for treatment of *Trypanosoma cruzi* infection. *JCI Insight* **2021**, *6* (9).
218. Morillo, C. A.; Marin-Neto, J. A.; Avezum, A.; Sosa-Estani, S.; Rassi, A.; Rosas, F.; Villena, E.; Quiroz, R.; Bonilla, R.; Britto, C.; Guhl, F.; Velazquez, E.; Bonilla, L.; Meeks, B.; Rao-Melacini, P.; Pogue, J.; Mattos, A.; Lazdins, J.; Rassi, A.; Connolly, S. J.; Yusuf, S., Randomized Trial of Benznidazole for Chronic Chagas' Cardiomyopathy. *New England Journal of Medicine* **2015**, *373* (14), 1295-1306.
219. Hasslocher-Moreno, A. M.; Saraiva, R. M.; Sangenis, L. H. C.; Xavier, S. S.; De Sousa, A. S.; Costa, A. R.; De Holanda, M. T.; Veloso, H. H.; Mendes, F. S. N. S.; Costa, F. A. C.; Boia, M. N.; Brasil, P. E. A. A.; Carneiro, F. M.; Da Silva, G. M. S.; Mediano, M. F. F.,

Benznidazole decreases the risk of chronic Chagas disease progression and cardiovascular events: A long-term follow up study. *EClinicalMedicine* **2021**, *31*, 100694.

220. Rassi Jr, A.; Marin Neto, J. A.; Rassi, A., Chronic Chagas cardiomyopathy: a review of the main pathogenic mechanisms and the efficacy of aetiological treatment following the BENznidazole Evaluation for Interrupting Trypanosomiasis (BENEFIT) trial. *Memórias do Instituto Oswaldo Cruz* **2017**, *112* (3), 224-235.

221. Stano, A.; Scott, E. A.; Dane, K. Y.; Swartz, M. A.; Hubbell, J. A., Tunable T cell immunity towards a protein antigen using polymersomes vs. solid-core nanoparticles. *Biomaterials* **2013**, *34* (17), 4339-4346.

222. Yi, S.; Zhang, X.; Sangji, M. H.; Liu, Y.; Allen, S. D.; Xiao, B.; Bobbala, S.; Braverman, C. L.; Cai, L.; Hecker, P. I., Surface Engineered Polymersomes for Enhanced Modulation of Dendritic Cells During Cardiovascular Immunotherapy. *Adv. Funct. Mater.* **2019**, 1904399.

223. Allen, S. D.; Liu, Y.-G.; Kim, T.; Bobbala, S.; Yi, S.; Zhang, X.; Choi, J.; Scott, E. A., Celastrol-loaded PEG-b-PPS nanocarriers as an anti-inflammatory treatment for atherosclerosis. *Biomaterials science* **2019**, *7* (2), 657-668.

224. Luo, D.; Carter, K. A.; Lovell, J. F., Nanomedical engineering: shaping future nanomedicines. *Wiley Interdisciplinary Reviews: Nanomedicine and Nanobiotechnology* **2015**, *7* (2), 169-188.

225. Barenholz, Y., Doxil® — The first FDA-approved nano-drug: Lessons learned. *J. Controlled Release* **2012**, *160* (2), 117-134.

226. Shi, Y.; van der Meel, R.; Chen, X.; Lammers, T., The EPR effect and beyond: Strategies to improve tumor targeting and cancer nanomedicine treatment efficacy. *Theranostics* **2020**, *10* (17), 7921-7924.
227. Iqbal, J.; Abbasi, B. A.; Ahmad, R.; Mahmood, T.; Ali, B.; Khalil, A. T.; Kanwal, S.; Shah, S. A.; Alam, M. M.; Badshah, H.; Munir, A., Nanomedicines for developing cancer nanotherapeutics: from benchtop to bedside and beyond. *Appl. Microbiol. Biotechnol.* **2018**, *102* (22), 9449-9470.
228. Van Der Meel, R.; Sulheim, E.; Shi, Y.; Kiessling, F.; Mulder, W. J. M.; Lammers, T., Smart cancer nanomedicine. *Nature Nanotechnology* **2019**, *14* (11), 1007-1017.
229. Roh, J. S.; Sohn, D. H., Damage-Associated Molecular Patterns in Inflammatory Diseases. *Immune Network* **2018**, *18* (4).
230. Kawai, T.; Akira, S., The role of pattern-recognition receptors in innate immunity: update on Toll-like receptors. *Nature Immunology* **2010**, *11* (5), 373-384.
231. He, X.; Yu, H.; Bao, X.; Cao, H.; Yin, Q.; Zhang, Z.; Li, Y., pH-Responsive Wormlike Micelles with Sequential Metastasis Targeting Inhibit Lung Metastasis of Breast Cancer. *Advanced Healthcare Materials* **2016**, *5* (4), 439-448.
232. Zeng, L.; Zou, L.; Yu, H.; He, X.; Cao, H.; Zhang, Z.; Yin, Q.; Zhang, P.; Gu, W.; Chen, L.; Li, Y., Treatment of Malignant Brain Tumor by Tumor-Triggered Programmed Wormlike Micelles with Precise Targeting and Deep Penetration. *Adv. Funct. Mater.* **2016**, *26* (23), 4201-4212.
233. Wan, X.; Min, Y.; Bludau, H.; Keith, A.; Sheiko, S. S.; Jordan, R.; Wang, A. Z.; Sokolsky-Papkov, M.; Kabanov, A. V., Drug Combination Synergy in Worm-like Polymeric

Micelles Improves Treatment Outcome for Small Cell and Non-Small Cell Lung Cancer. *ACS Nano* **2018**, *12* (3), 2426-2439.

234. Peng, J.; Chen, J.; Xie, F.; Bao, W.; Xu, H.; Wang, H.; Xu, Y.; Du, Z., Herceptin-conjugated paclitaxel loaded PCL-PEG worm-like nanocrystal micelles for the combinatorial treatment of HER2-positive breast cancer. *Biomaterials* **2019**, *222*, 119420.

235. Sainte-Marie, G., The Lymph Node Revisited: Development, Morphology, Functioning, and Role in Triggering Primary Immune Responses. *The Anatomical Record: Advances in Integrative Anatomy and Evolutionary Biology* **2010**, *293* (2), 320-337.

236. Schudel, A.; Francis, D. M.; Thomas, S. N., Material design for lymph node drug delivery. *Nature Reviews Materials* **2019**, *4* (6), 415-428.

237. Singh, I.; Swami, R.; Khan, W.; Sistla, R., Delivery Systems for Lymphatic Targeting. Springer US: 2014; pp 429-458.

238. Rohner, N. A.; Thomas, S. N., Flexible Macromolecule versus Rigid Particle Retention in the Injected Skin and Accumulation in Draining Lymph Nodes Are Differentially Influenced by Hydrodynamic Size. *ACS Biomaterials Science & Engineering* **2017**, *3* (2), 153-159.

239. Rohner, N. A.; Thomas, S. N., Melanoma growth effects on molecular clearance from tumors and biodistribution into systemic tissues versus draining lymph nodes. *J Control Release* **2016**, *223*, 99-108.

240. Kaplan, D. H., In vivo function of Langerhans cells and dermal dendritic cells. *Trends Immunol* **2010**, *31* (12), 446-51.

241. Kopf, M.; Schneider, C.; Nobs, S. P., The development and function of lung-resident macrophages and dendritic cells. *Nature Immunology* **2015**, *16* (1), 36-44.

242. Huang, F.-P.; Platt, N.; Wykes, M.; Major, J. R.; Powell, T. J.; Jenkins, C. D.; Macpherson, G. G., A Discrete Subpopulation of Dendritic Cells Transports Apoptotic Intestinal Epithelial Cells to T Cell Areas of Mesenteric Lymph Nodes. *Journal of Experimental Medicine* **2000**, *191* (3), 435-444.
243. Tang, L.; Zheng, Y.; Melo, M. B.; Mabardi, L.; Castaño, A. P.; Xie, Y.-Q.; Li, N.; Kudchodkar, S. B.; Wong, H. C.; Jeng, E. K.; Maus, M. V.; Irvine, D. J., Enhancing T cell therapy through TCR-signaling-responsive nanoparticle drug delivery. *Nat. Biotechnol.* **2018**, *36* (8), 707-716.
244. Chung, M. K.; Do, I.-G.; Jung, E.; Son, Y.-I.; Jeong, H.-S.; Baek, C.-H., Lymphatic Vessels and High Endothelial Venules are Increased in the Sentinel Lymph Nodes of Patients with Oral Squamous Cell Carcinoma Before the Arrival of Tumor Cells. *Annals of Surgical Oncology* **2012**, *19* (5), 1595-1601.
245. Vatarunakamura, C.; Ueda-Nakamura, T. N.; Souza, W., Visualization of the cytostome in *Trypanosoma cruzi* by high resolution field emission scanning electron microscopy using secondary and backscattered electron imaging. *FEMS Microbiol. Lett.* **2005**, *242* (2), 227-230.
246. Mosmann, T., Rapid colorimetric assay for cellular growth and survival: application to proliferation and cytotoxicity assays. *Journal of immunological methods* **1983**, *65* (1-2), 55-63.
247. Peron, F.; Lazzarin-Bidóia, D.; Ud Din, Z.; Rodrigues-Filho, E.; Ueda-Nakamura, T.; Silva, S. D. O.; Nakamura, C. V., Effects of (1E,4E)-2-Methyl-1,5-bis(4-nitrophenyl)penta-1,4-dien-3-one on *Trypanosoma cruzi* and Its Combinational Effect with Benznidazole, Ketoconazole, or Fluconazole. *BioMed Research International* **2017**, *2017*, 1-11.

248. Brener, Z., Therapeutic activity and criterion of cure on mice experimentally infected with *Trypanosoma cruzi*. *Rev Inst Med Trop Sao Paulo* **1962**, *4*, 389-96.
249. Matos Ferreira, A. V.; Segatto, M.; Menezes, Z.; Macedo, A. M.; Gelape, C.; De Oliveira Andrade, L.; Nagajyothi, F.; Scherer, P. E.; Teixeira, M. M.; Tanowitz, H. B., Evidence for *Trypanosoma cruzi* in adipose tissue in human chronic Chagas disease. *Microbes and Infection* **2011**, *13* (12-13), 1002-1005.
250. Lopez, M.; Tanowitz, H. B.; Garg, N. J., Pathogenesis of Chronic Chagas Disease: Macrophages, Mitochondria, and Oxidative Stress. *Current Clinical Microbiology Reports* **2018**, *5* (1), 45-54.
251. Yi, S.; Karabin, N. B.; Zhu, J.; Bobbala, S.; Lyu, H.; Li, S.; Liu, Y.; Frey, M.; Vincent, M.; Scott, E. A., An Injectable Hydrogel Platform for Sustained Delivery of Anti-inflammatory Nanocarriers and Induction of Regulatory T Cells in Atherosclerosis. *Frontiers in Bioengineering and Biotechnology* **2020**, *8*.
252. Meng, J.; Li, X.; Wang, C.; Guo, H.; Liu, J.; Xu, H., Carbon Nanotubes Activate Macrophages into a M1/M2 Mixed Status: Recruiting Naïve Macrophages and Supporting Angiogenesis. *ACS Applied Materials & Interfaces* **2015**, *7* (5), 3180-3188.
253. Oh, W.-K.; Kim, S.; Yoon, H.; Jang, J., Shape-Dependent Cytotoxicity and Proinflammatory Response of Poly(3,4-ethylenedioxythiophene) Nanomaterials. *Small* **2010**, *6* (7), 872-879.
254. Highley, C. B.; Rodell, C. B.; Burdick, J. A., Direct 3D Printing of Shear-Thinning Hydrogels into Self-Healing Hydrogels. *Adv. Mater.* **2015**, *27* (34), 5075-5079.

255. Modica, J. A.; Iderzorig, T.; Mrksich, M., Design and Synthesis of Megamolecule Mimics of a Therapeutic Antibody. *J. Am. Chem. Soc.* **2020**, *142* (32), 13657-13661.
256. Nagajyothi, F.; Weiss, L. M.; Silver, D. L.; Desruisseaux, M. S.; Scherer, P. E.; Herz, J.; Tanowitz, H. B., Trypanosoma cruzi Utilizes the Host Low Density Lipoprotein Receptor in Invasion. *PLoS Neglected Tropical Diseases* **2011**, *5* (2), e953.
257. Petty, A. J.; Keate, R. L.; Jiang, B.; Ameer, G. A.; Rivnay, J., Conducting Polymers for Tissue Regeneration in Vivo. *Chem. Mater.* **2020**, *32* (10), 4095-4115.

CURRICULUM VITAE**Sophia Li**sophia.li@northwestern.edu

Education*Northwestern University, Evanston, IL**Expected*

MD/PhD Candidate in Biomedical Engineering, GPA: 3.97/4.0

May 2023

Relevant Coursework: Advances in Biotechnology, Biomaterials, Tissue

Engineering, Drug Delivery, Virology, Experimental Design and

Measurement, Biological Performance of Materials

*Massachusetts Institute of Technology (MIT), Cambridge, MA**June 2015*

Bachelor of Science in Biological Engineering, GPA: 4.9/5.0

Relevant Coursework: Organic Chemistry I and II, Differential Equations,

Thermodynamics of Biological Systems, Intro. to Programming, Seminar

(Products from Microbes), Biochemistry, Genetics, Cell Biology,

Biomechanics, Biomaterials, Immunology

Analysis of Biomolecular Systems, Lab Fundamentals in Biological

Engineering

Study Abroad in Madrid, Spain (Spanish II)

*La Cueva High School, Albuquerque, NM**May 2011*

Valedictorian: Rank 1 in class of 498 students

Awards/Honors

Northwestern Biotechnology Training Program Trainee	<i>Sept 2018-</i>
Awarded two years of NIH funding	<i>Sept 2020</i>
Fannie and John Hertz Foundation Fellowship Semifinalist	<i>2018</i>
Member of Tau Beta Pi Engineering Honor Society	<i>2015</i>
Fung Scholar, Victor and William Fung Foundation	<i>2014</i>
\$2000 National Merit Finalist and Scholarship Winner	<i>2011</i>
\$11,000 Woodcock Foundation Scholarship	<i>2011</i>
U.S. Presidential Scholar Semifinalist	<i>2011</i>

Research Experience

PhD Candidate in Evan Scott Laboratory, Northwestern University	<i>July 2017-Sept</i>
Developed and characterized novel filamentous polymeric nanocarriers for drug delivery to immune cells	<i>2021</i>
Enhanced stability, scalability of formation, control over flexibility and circulation times of filamentous nanocarriers	

Assessed nanocarrier uptake in vitro in mouse macrophages and nanocarrier immune cell biodistribution in vivo in mice

Undergraduate Researcher in Sinsky Laboratory, MIT

June 2012-

Engineered bacteria to express organelle-like structures to improve their carbon fixation efficiency for biofuel production

May 2015

Performed enzyme assays to determine efficiency of carbon fixation in bacteria

Summer Intern at National Taiwan University Hospital, Taipei, Taiwan

June-Aug

Genotyped and analyzed 932 patient DNA samples to confirm if 2 genetic variations are associated with liver cancer in chronic Hepatitis B patients

2013

Validated the association of a genetic factor with higher risk of liver cancer

Job Experience

Medical Safety Evaluation Intern, Abbvie

June 2021-

- Compiled and evaluated safety data for Medical Safety Physicians in the Botox and Neurotoxins division, Pharmacovigilance and Patient Safety department

Aug 2021

- Medical Student Tutor**, *Northwestern University Feinberg School of Medicine* *Sept 2017-*
- Conducted review sessions and created question banks for first year medical students *June 2020*
- Work-study Tutor**, *East End House, Cambridge, MA* *Feb-May*
- Tutored elementary school students in math, science, and reading for 2 hours/week *2015*
- Problem Set Grader**, *MIT* *Sept-Dec 2012*
- Corrected and recorded grades for 25 problem sets every 2 weeks
- Admissions Caller**, *MIT* *June-August*
- Informed prospective students about life at MIT *2012*
 - Called 130 prospective applicants to guide them through the college application process

Publications

Li, S., Bobbala, S., Vincent, M.P., Liu, Y., & Scott, E.A. (2021) Pi-stacking enhances stability, scalability of formation, control over flexibility and circulation time of polymeric filamentous nanocarriers. *Advanced NanoBiomed Research*, 2100063.

Soni, D., Bobbala, S., **Li, S.**, Scott, E. A., & Dowling, D. J. (2020). The sixth revolution in pediatric vaccinology: immunoengineering and delivery systems. *Pediatric Research*, 1-10.

Yi, S., Karabin, N. B., Zhu, J., Bobbala, S., Lyu, H., **Li, S.**, ... & Scott, E. A. (2020). An injectable hydrogel platform for sustained delivery of anti-inflammatory nanocarriers and induction of regulatory T cells in atherosclerosis. *Frontiers in Bioengineering and Biotechnology*, 8.

Lu, J., Brigham, C. J., **Li, S.**, & Sinskey, A. J. (2016). *Ralstonia eutropha* H16 as a platform for the production of biofuels, biodegradable plastics, and fine chemicals from diverse carbon resources. In *Biotechnology for Biofuel Production and Optimization* (pp. 325-351). Elsevier.

Allen, M., Golding, A., Rus, V., Karabin N.B., **Li, S.**, Lescott, C.J., Bobbala, S., Scott, E.A., & Szeto, G.L. Targeted delivery of chloroquine to plasmacytoid dendritic cells enhances inhibition of the type I interferon response. (submitted)

Li, S., Bobbala,S., Rische, C., Modak, M., Scott, E.A. Engineering synthetic self-assembled polymeric nanofilaments for biomedical applications. (in preparation)

Presentations

“A Pi-stacking Moiety Enhances Scalable Filomicelle Fabrication via Flash Nanoprecipitation.” **S.Li**, S. Bobbala, E. Scott. E-Poster Presentation at Biomedical Engineering Society Annual Meeting. October 14-17, 2020.

“Development and Characterization of Filomicelles with Endocytosis-Responsive Fluorescence to Investigate Morphology-dependent Intracellular Delivery.” **S.Li**, S. Bobbala, E. Scott. Poster Presentation in the “Targeted or Responsive Delivery Systems” Session as part of the Drug Delivery track at Biomedical Engineering Society Annual Meeting in Philadelphia, PA. October 17, 2019.

“Targeting the Latent HIV Reservoir Via HIV-1-mimetic Nanocarriers.” **S. Li**, J. Park, N. Karabin, S. Allen, J. Choi, T. Hope, E. Scott. Oral Presentation in the “Nanotechnologies for Drug and Nucleic Acid Delivery and Immunotherapy” Session at Biomedical Engineering Society Annual Meeting in Atlanta, GA. October 19, 2018.

“Targeting the Latent HIV Reservoir Via HIV-1-mimetic Nanocarriers.” **S. Li**, J. Park, N. Karabin, S. Allen, J. Choi, T. Hope, E. Scott. Poster at Third Coast Center for AIDS Research Annual Symposium in Chicago, IL. November 1, 2018.

“Improving Carbon Fixation in *Ralstonia eutropha* through Carbon-concentrating Microcompartments.” **S. Li**, C. Brigham, C. Gai, J. Lu, A. Sinskey. Lightning Presentation at US Clean Energy Education and Empowerment, Women in Clean Energy Symposium in Cambridge, MA. September 16, 2014.

“Heterologous Expression of Carboxysomes in *Ralstonia eutropha* Re2061 to Improve Carbon Fixation.” **S. Li**, C. Brigham, C. Gai, J. Lu, A. Sinskey. MIT MURJ Undergraduate Poster Session in Cambridge, MA. April 12, 2014.

“Heterologous Expression of Carboxysomes in *Ralstonia eutropha* Re2061 to Improve Carbon Fixation.” **S. Li**, C. Brigham, C. Gai, J. Lu, A. Sinskey. MIT Koch Institute Undergraduate Poster Session in Cambridge, MA. April 18, 2013.

Teaching/Mentoring Experience

Teaching Assistant in Biomedical Engineering, *Northwestern University* *Fall 2019*

Coached 27 students in Biological Performance of Materials course

Delivered 2 lectures, held weekly office hours with students, delivered 2 exam review sessions

Graded journal critique assignments and problem sets

Earned a teaching evaluation of 5.4/6

Research Mentoring *Summer*

Mentored 1 summer undergraduate student and 1 graduate rotation student *2018, Fall*

2020

Associated Advisor in Dept. of Biological Engineering, MIT *Sept 2013-*
 Assisted Biological Engineering faculty member in guiding and mentoring 3
 sophomore advisees *May 2014*

Leadership Experience

Northwestern Biotechnology Training Program Steering Committee *Sept 2019-*

Member, Northwestern University *Sept 2020*

Elected as student representative for Biotechnology Training Program

Approved and provided feedback on changes to course requirements

Northwestern Biotechnology Training Program Practicum Committee *Sept 2018-*

Member, Northwestern University *August 2019*

Organized 1-day Data Visualization Practicum Speaker series for over 100
 attendees

Northwestern Medical Orchestra Concertmaster and Librarian, *Jan 2020-Jan*

Northwestern Feinberg School of Medicine *2022*

Printed, bought and distributed sheet music for 50+ orchestra members

Organized livestreamed chamber music concerts for 200+ attendees

Phi Rho Sigma Medical Society Social and Philanthropy Chair, Chicago, IL *Jan 2016-Jan*

Planned annual initiation dinner for new members *2019*

Organized monthly free movie events for medical student members

Coordinated volunteer opportunities at Halloween Parade and Hustle at the Hancock for medical student members

Chinatown Clinic Translation Services Coordinator, Chicago, IL *Jan 2016-Jan*

Organized and recruited undergraduate translators for free clinic every Sunday *2017*

Assisted attending physician at the free clinic once a month

Team Hepatitis B Virus, MIT President, National Recruitment and Training Advisor, Cambridge, MA *May 2012-May 2015*

Organized conference calls to oversee recruitment and training of members in 20 Team HBV chapters across US

Educated MIT and Boston community about Hepatitis B through presentations, Hepatitis B Awareness week, and poster campaigns and provided one free screening per semester

Promoted Hepatitis B awareness, especially to Boston immigrant population, at balloon-animal booths at 2 health or community fairs

Organized national conference at MIT with 30+ attendees

- MIT Symphony Orchestra Social Chair and Violinist, Cambridge, MA** *Aug 2012-*
 Collected funds and distributed snacks at each rehearsal *May 2015*
 Organized annual barbecue and gingerbread house making events for
 70+members
- MIT Chinese Ensemble President, Erhu (Chinese violin) player and
 instructor, Cambridge, MA** *Feb 2013-*
May 2015
 Organized concert every semester and led weekly rehearsals
- MIT Chapter of National Society of Collegiate Scholars Treasurer,
 Cambridge, MA** *Aug 2013-*
May 2014
 Managed budget of over \$1000/semester
 Planned Induction Ceremony for new members of this honor society
- MIT Society of Women Engineers Internal Mentorship Chair, Cambridge,
 MA** *Feb 2012-Jan*
2014
 Promoted mentorship of women engineering students by organizing 5 bonding
 events each year with 25+ attendees at each event. Managed a budget of
 \$1400 each semester

Activities

- Medical Scientist Training Program Diversity Committee Member,** *Fall 2020-*
Northwestern University Feinberg School of Medicine *present*
- Review literature to provide evidence-based recommendations for improving admissions and training of MD/PhD students
- MIT Educational Counselor, Chicago, IL** *Sept 2017-*
- Interviewed 10+ high school applicants/year for undergraduate admission *Sept 2021*
- Medical Scientist Training Program Admissions Committee Member,** *Aug 2017-*
Northwestern University Feinberg School of Medicine *present*
- Screen and interview MD/PhD applicants for admission
- Music Matters Volunteer** *August 2018-*
- Performed violin music for patients at Northwestern Memorial Hospital *August 2019*
- Kpoptosis Dance Group, Northwestern University Feinberg School of Medicine** *Sept 2015-Jan*
2017
- Performed Korean pop dances 2 times/year

Volunteer at Brigham and Women's Hospital*Sept 2013-Jan*

Guided patients around the hospital for 30 hours

2015

Transferred blood, patient samples and belongings around hospital for 30
hours

Volunteered in Ambulatory Radiology Department for 20+ hours Managed
budget of over \$1000/semester